4-5-2013

A Better Looking Brain: Image Pre-Processing Approaches for fMRI Data

Siddharth Khullar

A BETTER LOOKING BRAIN: IMAGE PRE-PROCESSING APPROACHES FOR fMRI DATA

A dissertation presented to
the dissertation committee

by

Siddharth Khullar

In Partial Fulfillment of the Requirements for the
Degree of *Doctor of Philosophy* in Imaging Science

at

Rochester Institute of Technology
College of Science
Chester F. Carlson Center for Imaging Science
Rochester, New York, USA

April 5 2013

Signature of the Author _____

Accepted by _____

Prof. John Kerekes, Coordinator, Ph.D Degree Program Date

Chester F. Carlson Center for Imaging Science
Rochester Institute of Technology
Rochester, New York, USA

CERTIFICATE OF APPROVAL

Ph.D. Degree Dissertation

The Ph.D Degree Dissertation of Siddharth Khullar has been examined and approved by the following dissertation committee as satisfactory for a Ph.D degree in Imaging Science

Prof. Stefi A. Baum, Dissertation Advisor	Date
Prof. Vince D. Calhoun, Dissertation Advisor	Date
Dr. Nathan D. Cahill, Committee Member	Date
Prof. Maria Helguera, Committee Member	Date
Prof. Hans-Peter Bischof, Committee Chair	Date

Dedication

This work is dedicated to my family and mentors, who all have consistently shared
and supported me in the pursuit of
unmitigated truth and unrelenting respect.

Acknowledgments

On August 22, 2007, I traveled 11,654 km from New Delhi, India, to Rochester, NY to join the Rochester Institute of Technology first as a Masters' student and then as a PhD student. Every mile has been worth it. As most 21 year olds, I had little direction in life and was trying to figure out what to do with it. The RIT community helped me find my passion for science and has been a home away from home where I feel secure, confident and protected when required. It has instilled in me the core value of scientific research - "Ask the right questions first, then the right answers will follow," and empowered me to take up long-standing research problems in a systematic manner as well as perceive and execute solutions as optimally as possible.

I would like to thank my advisor Dr. Stefi Baum, who has been more like another parent to me than an academic advisor. She has mentored and advised me at making several crucial decisions regarding my career and sometimes my personal life. I owe this degree to her confidence in me and her courage to bring me in as her disciple. Thank you Stefi, you are amazing!

I'm grateful to Dr. Vince Calhoun who has always shown trust in my research ideas and solutions and without his guidance, this thesis would not have been possible. He has been a great mentor to a student like me, who knew nothing about functional brain imaging. I could not have asked for anything better for a starting point to kickstart a career in the field of medical imaging.

I'd like to thank my best friend who also happens to be my wife, Shilpa Tyagi who not only makes every day of my life amazing, but also without whom I would not have been motivated enough to pursue a career in scientific research. For the past 10 years, she has shown never ending courage in putting up with my odd schedules and always supported me in every endeavor of life.

My parents have been a constant source of support ever since my first day at school (I was 3 years old). It goes without saying, their belief in me and the never-ending encouragement, has helped become the person I am today and follow my self-defined principles with utmost respect and ethic.

I thank all the professors at the Center for Imaging Science. As advisors, professors, motivators, and teachers, I could not have asked for anything better. I would also like to thank my friends and colleagues at RIT - Dr. Eli Saber, Dr. Jeff Pelz, and my friends Tommy P. Keane, Udayan Sharma, Rohan Mehalwal and Dipak A. Kadam for supporting me through these enduring years. A special thanks to Dr. Andrew Michael for being the best academic brother any one can ask for, and being the most valuable critic of my research work.

Abstract

Researchers in the field of functional neuroimaging have faced a long standing problem in pre-processing low spatial resolution data without losing meaningful details within. Commonly, the brain function is recorded by a technique known as echo-planar imaging that represents the measure of blood flow (BOLD signal) through a particular location in the brain as an array of intensity values changing over time. This approach to record a movie of blood flow in the brain is known as functional magnetic resonance imaging (fMRI). The neural activity is then studied from the temporal correlation patterns existing within the fMRI time series. However, the resulting images are noisy and contain low spatial detail, thus making it imperative to pre-process them appropriately to derive meaningful activation patterns. Two of the several standard preprocessing steps employed just before the analysis stage are denoising and normalization. Fundamentally, it is difficult to perfectly remove noise from an image without making assumptions about signal and noise distributions. A convenient and commonly used alternative is to smooth the image with a Gaussian filter, but this method suffers from various obvious drawbacks, primarily loss of spatial detail. A greater challenge arises when we attempt to derive average activation patterns from fMRI images acquired from a group of individuals. The brain of one individual differs from others in a structural sense as well as in a functional sense. Commonly, the inter-individual differences in anatomical structures are compensated for by co-registering each subject's data to a common normalization space, known as spatial normalization. However, there are no existing methods to compensate for the differences in *functional organization* of the brain. This work presents first steps towards data-driven robust algorithms for fMRI image denoising and multi-subject image normalization by utilizing inherent information within fMRI data. In addition, a new validation approach based on spatial shape of the activation regions is presented to quantify the effects of preprocessing and also as a tool to record the differences in activation patterns between individual subjects or within two groups such as healthy controls and patients with mental illness. Qualititative and quantitative results of the proposed framework compare favorably against existing and widely used model-driven approaches such as Gaussian smoothing and structure-based spatial normalization. This work is intended to provide neuroscience researchers tools to derive more meaningful activation patterns to

accurately identify imaging biomarkers for various neurodevelopmental diseases and also maximize the specificity of a diagnosis.

Contents

List of Figures

List of Tables

List of Acronyms

fMRI functional magnetic resonance imaging

DTI diffuse tensor imaging

sMRI structural magnetic resonance imaging

BOLD blood oxygen level dependent

EPI echo-planar imaging

CNR contrast to noise ratio

SNR signal to noise ratio

MNI Montreal neurological institute

ICBM international consortium for brain mapping

EEG electroencephalography

ICA independent component analysis

FWHM full width half maximum

RF radio frequency

NMR nuclear magnetic resonance

TE echo time

TR time of repitition

FT Fourier transform

STFT short-time Fourier transform

FFT fast Fourier transform

DWT discrete wavelet transform

DWT continuous wavelet transform

SOA stimulus onset asynchrony

TIM total imaging matrix

FOV field of view

HC healthy controls

SZ schizophrenia patients

AOD auditory oddball design

REST resting state fMRI

NIfTI Neuroimaging informatics technology initiative

SPM statistical parametric mapping

GLM general linear model

HRF hemodynamic response function

FSL fMRI software library

ROI region of interest

SST study specific template

VBM voxel based morphometry

FT functional templates

RSN resting state network

DMN default mode network

TL temporal lobe network

DCT discrete cosine transform

GICA group ICA

FDR false discovery rate

DMN$_{rest}$ default mode network from rest data

TL$_{rest}$ temporal lobe network from rest data

DMN$_{AOD}$ default mode network from AOD data

TL$_{AOD}$ temporal lobe network from AOD data

ED euclidean distance

mnFT multi-network functional templates

SWT stationary wavelet transform

PCA principal component analysis

GIFT group ICA for fMRI toolbox

FPR false positive ration

TPR true positive ratio

ROC region operating characteristics

PSNR peak signal to noise ratio

MSE mean squared error

Chapter 1: Introduction

In the past two decades, functional magnetic resonance imaging, hereafter fMRI, has been extensively utilized to understand various mysteries related to the brain. This technology has enabled scientists to map physical and cognitive actions to different regions responsible within the brain. It has been used to study the effects of using alcohol, smoking and drug abuse, effects of increasing age, gender, and demographic associations. Also, the development cycle of the brain, from infancy to adulthood has been investigated through longitudinal studies on the same set of individuals. This has facilitated our understanding of the brain and some of the most impacting factors that govern its development. However, the primary area of research that continues to profoundly depend on fMRI has been classification of various neurodevelopmental and psychological disorders through the use of imaging biomarkers. A considerable fraction of the world population is affected by disorders such as schizophrenia, bipolar personality disorder, autism and so on. Through the combined use of advanced classification methods and fMRI, it is now possible for clinicians to identify brain regions that show significant differences, based on activation patterns to certain audio and visual stimuli, between patients and healthy individuals. In addition, fMRI is being utilized to enable examination of joint information between tasks that probe different functional domains in patients and healthy controls. For example, findings show that interesting relationships exist between brain at rest and brain at task for the same set of subjects (Calhoun et al., 2008, Smith et al., 2009). In addition to fMRI, other brain imaging modalities such as diffusion tensor imaging (DTI) and structural MRI (sMRI) are being jointly utilized to investigate similarities and differences in function and structure of the brain.

Since the results from the first Functional Magnetic Resonance Imaging (fMRI) human-based studies were reported in 1992 by two different groups (Bandettini et al., 1992, Ogawa et al., 1992), a plethora of research has emerged using fMRI, revealing the cornerstones of everything from motor and sensory processes to foundations of social cognition in humans. A variety of signal processing algorithms are sequentially applied to the imaging data in order to extract indirect

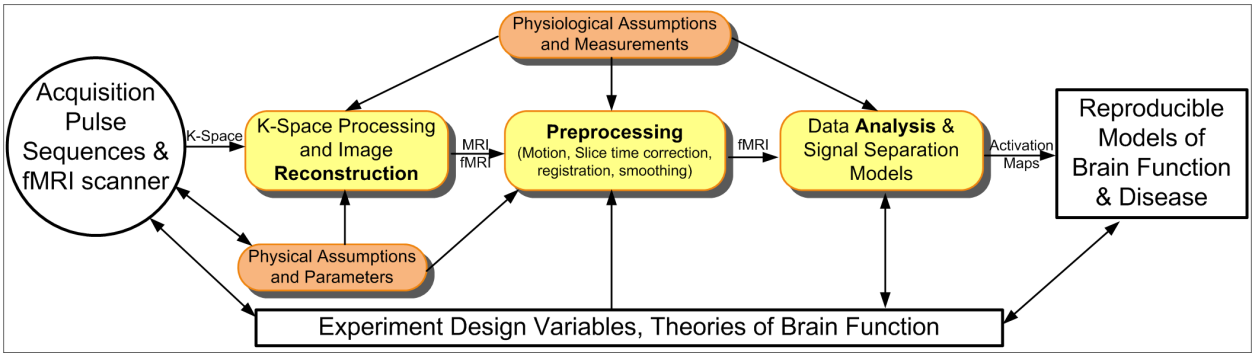

Figure 1.1: A schematic illustration (redrawn from Strother (2006) with permission) of the data flow through fMRI processing pipeline comprised of following steps after the acquisition of raw k-space data: 1) Computation of magnitude and phase images followed by **Reconstruction** using inverse Fourier transform; 2) **Preprocessing** (motion correction, registration etc.); 3) Data **Analysis** to generate activation maps also defined as statistical parametric images.

measurements of neuronal activity within the brain. These algorithms can be broadly classified in to three categories: (1) Reconstruction, (2) Preprocessing, and (3) Analysis. The schematic shown (redrawn from Strother (2006)) in Figure 1.1, depicts various relationships between numerous steps involved in fMRI acquisition to processing to forming models for brain function. All three steps are strongly associated with one or more type of assumptions that influence the choice of methods used to perform these operations. These assumptions, independently or collectively, have varying degrees of impact on the final results and inference. The purpose of this thesis is - a) to understand, compare and question the applicability of various fMRI image preprocessing pipelines in use today and, b) to present new algorithms that, when used independently or together, can compensate for some of the irregularities introduced in the data and reveal additional information within the data, leading to improvement in detection sensitivity of activation patterns.

1.1 What is fMRI?

Functional brain imaging is widely being used to enhance identification of neuropsychological disorders such as schizophrenia, psychosis, and bipolar personality disorder that are currently diagnosed on the basis of patients' self reported experiences and observed behavior. A type of specialized

imaging technique known as functional MRI (fMRI) is used to measure indirect level of brain activity associated with a physical or mental action. Intuitively, brain activity refers to transfer of electrical and chemical energy between neurons in different parts of the brain. However, fMRI measures changes in deoxy-hemoglobin concentrations in nearby (to neurons) blood vessels. This is known as blood-oxygen-level-dependent or BOLD activity.

The neurovascular linkage between networks of neurons and blood vessels (Huettel et al., 2004) results in exchange of energy that further causes change in oxygenated hemoglobin. BOLD activations are considered an acceptable indicator of *bundled* neural activity by scientists as the spatial resolution of fMRI images is many orders greater than the size of a neuron. Images acquired through fMRI can help decipher intensity and boundaries of simultaneous activity across different brain regions, thus making such recordings a viable measure to study and label underlying relationships that link complex external stimuli to corresponding brain functions.

During an fMRI experiment, a subject is asked to perform a task, e.g. pressing a button, while the MRI scanner records the BOLD changes within the brain. Several volumetric images of brain are acquired using a rapid pulse sequence firing technique known as echo-planar imaging (EPI) (Huettel et al., 2004).

1.2 Preprocessing: An Imperative Requirement

The pivotal role of preprocessing steps in the fMRI analysis is evident from its central position seen in Figure 1.1. These algorithms interact with almost every decision made in designing, performing and analyzing results from an fMRI experiment. In addition, the theories of brain function and disease determine the experimental design variables (event-related, block design or both), which in turn guide the choice of scanner pulse sequences. Independent of these attributes, the field strength of the scanner governs the contrast-to-noise ratio (CNR) of the resulting images. Higher field strength (measure in Tesla (1.5T, 3T etc.)) results in higher CNR. However, this advantage is somewhat diminished by higher sensitivity to physiological noise, greater artifacts at air-tissue

boundaries, and reduced decay times, thus making choice of preprocessing methods a pivotal decision in fMRI analysis (Strother, 2006). With the ever-expanding collection of algorithms and software tools for preprocessing, one of the primary challenges facing researchers and clinicians is *How to choose from among this plethora of possible pipelines?*. The most convenient and widely adopted resolution for this concern is based on a method's availability, familiarity, and ease of use. This is not always, medically or scientifically, a robust choice.

The functional properties of the brain stored in the form of fMRI data need to be analyzed by appropriate statistical methods. Due to the inherent system properties of the techniques used for acquiring fMRI, the resulting images are of low spatial resolution and have little anatomical contrast in addition to suffering from geometric (head motion) and intensity distortions (magnetic field homogeneity). These limitations may be tolerable when investigating fMRI data for a single subject. However, in many experiments, researchers want to address two important questions:

- *How does BOLD activity map (spatially) on to the corresponding anatomical brain regions?*
- *How consistent (or different) is this mapping across a sample population (healthy or patients)?*

Both these questions are substantially dependent on the the spatial quality of fMRI images that are tested for activity which in turn depends on the signal-to-noise ratio (SNR) of the data. Thus, it becomes imperative to map the data onto relatively high resolution and high contrast structural images through co-registration of fMRI and sMRI data from the same subject. Nevertheless, there remains a problem of comparing activity across individuals within a study or across different studies. There is a wide variation in size, shape, orientation, and gyral anatomy of the brain across different individuals. Therefore, inter-subject comparisons are performed after warping each subject's data to a common coordinate space using a brain template so that their brains at least have the same size and shape as all of the others. This process is known as spatial normalization, and is the first of the last two preprocessing stages prior to statistical analysis of fMRI.

The last stage in fMRI preprocessing is spatial smoothing and is typically the most common data preparation step in a variety of fMRI analysis pipelines used worldwide. Clinical decisions

based on BOLD activation patterns are highly influenced by the spatial quality and signal-to-noise-ratio (SNR) of fMRI images. If the image is extremely noisy, some of most intricate details associated with the BOLD signal may get obscured or even misrepresented to a great extent during the statistical analysis. As a solution, spatial filtering is done to improve the functional SNR, reduce apparent noise, and increase the validity of comparisons across subjects. Prior to spatial smoothing, some studies also apply temporal filtering to reduce scanner drift and physiological noise.

Apart from registration and smoothing, a number of other steps are common amongst different preprocessing pipelines for fMRI. These include - slice artifact removal due to timing errors and radio frequency spikes, and slice time acquisition correction. The severity of errors due to these resources has considerably diminished due to the ever evolving scanning and data acquisition and equipment and practices.

1.3 Motivation for Change

An ever-expanding collection of techniques and software tools is available to the functional neuroimaging community to assemble and apply different preprocessing pipelines to fMRI data sets (Strother, 2006). Neuroimaging studies often comprise $10-20$ or more subjects who undergo an experimental paradigm. The initial few preprocessing steps operate on temporal information stored in a single dimension whereas later stages such as registration, spatial normalization and smoothing utilize complex 3-D brain structures. Thus, the validation of this class of spatial algorithms is not a trivial task due to a number of questions that consequently reveal commonly ignored limitations in reliability and reproducibility.

1.3.1 Template-to-Structure Correspondence

Brain templates are normally used as references for mapping different brains in a group analysis study. Normally, a brain template is constructed by averaging images that are premapped to a standard coordinate space. There are two main reasons to use brain templates: 1) to obtain a

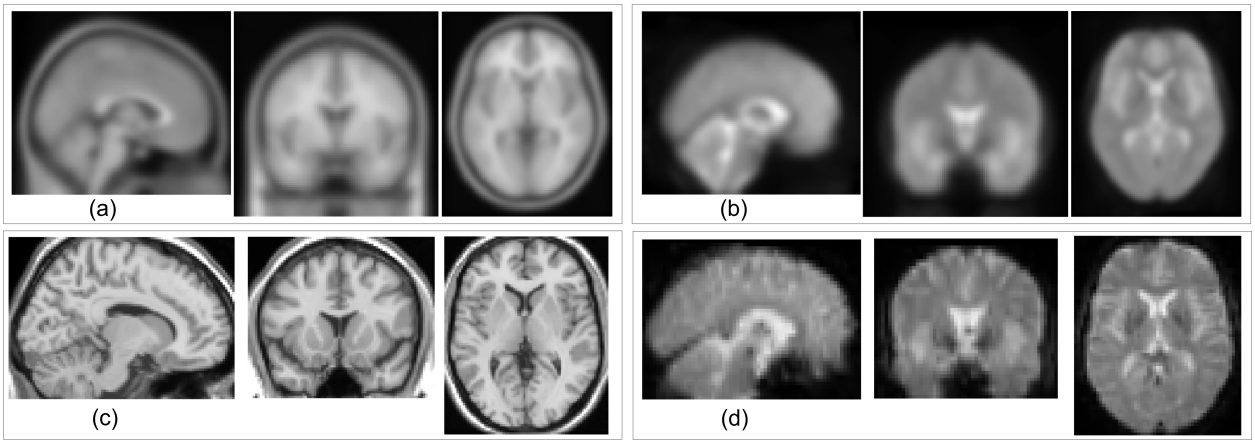

Figure 1.2: **Contrast and CNR Comparison:** MNI-305 standard average templates as obtained from the SPM5 library are compared side-by-side with single subject T1 and EPI images: (a) $T1$ contrast template; (b) Echo Planar Imaging (EPI) template; (c) single subject T1 image; (d) single subject EPI image. These images are all mapped to the Talairach coordinates and correspond to the same physical location in the brain. The contrast difference around the ventricle regions is most notable across all four images. The templates ((a)-(b)) are more blurred than their single-subject counterparts ((c)-(d)) due to the averaging effect. Each image is arranged as Sagittal (Left), Coronal (Center) and Axial (Right) geometries.

standard basis for functional activation labeling, 2) to compensate for anatomical variations across subjects. The role of brain atlases and templates has been thoroughly reviewed by some of the most prominent studies in this field such as Mazziotta et al. (2001), Toga and Thompson (2001). However, *there is substantial doubt as to whether there exists a perfect correspondence between a subject's anatomical image and a template.* Numerous studies of anatomical variability in normal (Rivičre et al., 2002, Roland et al., 1997) and lesioned brains (Ripollés et al., 2012, Thompson et al., 1997) have suggested that alternate methods be considered. Techniques for construction and application of brain templates depending on class of subjects under investigation, such as disease-specific atlases, are a viable option to study the differences between diseased and normal populations (Toga and Mazziotta, 2002). The question raised by many researchers is even if such correspondence does exist with minimal errors in certain specific studies, *how do we measure the accuracy of the transformation estimate*? Several studies have shown that residual variability is of the order of several millimeters (Brett et al., 2002) with an average isotropic voxel's size $\approx 27mm^3$.

In a series of studies, the Montreal Neurological Institute (MNI) created a brain template called MNI305 (see Figure 1.2) by averaging a large number of normal MRI brain images (Evans et al., 1993). The International Consortium for Brain Mapping (ICBM) adopted the MNI template by registering 152 normal brains to the MNI template and named the new template $ICBM152$ (Mazziotta et al., 1995). These are the two most commonly used templates for spatial normalization of fMRI data sets and have been incorporated in to several computer analysis packages. These standard *templates* are representative of the brain size and shape, whereas the cortical structures are difficult to identify and blurred in these atlases due to the obvious low pass filtering effect caused by averaging. The classical brain *atlas* (anatomical) of Talairach and Tournoux (Talairach and Tournoux, 1988) is universally used as an anatomical reference standard by the neuroimaging community. Note that, the results from analysis done post-mapping (using $ICBM152$ or $MNI305$) are reported in the Talairach coordinate system.

Given the limited power of Talairach transformation in accounting for anatomical variability across different brains, the spatial locations in template (from MNI or ICBM) and atlas space do not exactly overlap, the most extreme case being the temporal lobes in MNI space extending $10mm$ below the temporal lobes in Talairach brain (Toga and Thompson, 2001). As a remedy, an affine transformation to improve the registration between the two spaces (Carmack et al., 2004) and is intensively used by those who follow the aforementioned approach for reporting results. Nevertheless, the inaccuracies introduced due to the differences between the template used and the reference coordinate space, clearly pose substantial re-alignment requirements.

1.3.2 Function-to-Structure Correspondence

Intrinsically, an exact correspondence does exist between functional and anatomical images of a subject, but usually these are not visible when both modalities are compared side-by-side. Factors such as spatial resolution, signal-to-noise ratio (SNR), difference in sources of contrast, cause the brain structures to appear vague in fMRI images as illustrated in Figure 1.2.

Current methods for anatomical alignment rely on anatomical features that are identified through high-resolution structural MRI scans. However, a crucial precursor for developing models

of brain organization and activity is to identify functional neuro-anatomical markers that assist in realignment of boundaries corresponding to BOLD activity across various individuals in a population. A precision of less than $5-10mm$ in anatomical correspondence between structural (MRI) and functional images (fMRI) is usually difficult to achieve due to the distortions of echo-planar imaging (EPI) (Thirion et al., 2006). Sequential acquisition of multiple signals from a single excitation pulse result in signal loss due to $T2^*$ effects. This leads to visible pockets spatial intensity distortions, in addition to the low spatial resolution due to rapid acquisition sequences. The primary limitation faced by EPI-based fMRI analysis techniques is handling correspondence between structural and functional data. For current methods, this correspondence problem is largely overlooked, especially in the case of spatial normalization where the data is mapped to a template-based coordinate space, in this case known as the MNI-coordinate space. So the question arises, even if we can construct a viable structural template, how accurate will its correspondence be to functional data, that is the domain of interest in context to the present analysis. We discuss the different classes of currently used methods for establishing structure-to-function correspondence and propose a new technique for functional normalization in the upcoming chapters.

1.3.3 Inter-Subject Variability

There is enough evidence to support the fact that the size, shape, and position of brain structures are anatomically non-uniform for individuals and show significant differences associated with race, age, gender, or state of healthiness (Dougherty et al., 2003, Dubb et al., 2003, Good et al., 2001a, Jang et al., 2005, Park et al., 2004, Rademacher et al., 1993, Raz et al., 2005, Sabuncu et al., 2010, Thompson et al., 1997, Toga and Thompson, 2001). However, these structural differences do not account for any functional variability across subjects. More work is required to further develop inter-subject registration and spatial normalization techniques for group-based fMRI studies. During the past decade, methods targeting group-analysis such as using study-specific templates (Good et al., 2001b, Huang et al., 2010), and cross-task functional re-alignment (Sabuncu et al., 2010) are gaining popularity and show substantial promise in reducing post-analysis artifacts due to inter-subject morphometric differences and even reveal new and improved statistical relationships across different

regions of the brain. These studies can be seen as compelling evidence that anatomical variations within a group as well as differences in scanners (sequences, other errors) used for acquisition of various templates or subjects' images can cause considerable spatial distortion when mapping data to a common co-ordinate space. Eventually, such distortions cause the statistics to change significantly, and lead to partially incorrect spatial maps showing patterns of cognitive activity.

One of the primary challenges researchers have repeatedly pointed out for future research is the effect of spatial normalization on functional maps in group studies. With the advent of MRI systems that provide higher fMRI resolution and localization of brain activity, a parallel effort in advancing high resolution template construction and hybrid spatial normalization methods is called for. Identification of functional biomarkers signifying good health or disease at an individual level are being given prominent importance in studies which will eventually help in advancement of personalized drug discovery, and use of patient and disease specific medicine.

1.3.4 Gaussian Smoothing: Brain is not Isotropic

Interestingly, the smoothing and spatial normalization steps share a very close relationship, specifically in terms of their sequential application within the preprocessing pipeline. The concerns raised in Sections 1.3.1-1.3.3 earlier have long been known, and have been discussed before by Brett et al. (2002), Nieto-Castanon et al. (2003) along with illustrative examples. The first and classical solution to address these has been to sacrifice the spatial resolution of fMRI to increase robustness against registration and normalization errors. The most commonly utilized method for this task is to smooth the fMRI image with full-width half-maximum volumetric Gaussian kernels (Poline et al., 1997). It is not unusual to apply an 3-D $8-10mm$ smoothing kernel to fMRI datasets (with isotropic voxel size up to 3mm) before performing a group analysis.

Two straightforward implications of such an approach for smoothing can be realized as follows:

- *Isotropic smoothing kernels are not optimal for neuro-scientific observations since they do not necessarily address the underlying variations in shapes and sizes of the anatomical regions or the functional clusters.*

- *This method also overlooks the spatial variations across subjects. These differences may be subtle structurally, but due to the variability in genetic and epigenetic factors across subjects, functional variability plays a major role in group analysis as also depicted by Hellier et al. (2003).*

The Gaussian smoothing methodology is also widely applied as it suppresses high-frequency noise. Furthermore, it is simple to implement and most importantly increases the overall signal-to-noise ratio (SNR). The drawbacks of Gaussian smoothing in the signal domain include considerable change in true intensity values (as a function of the size of the smoothing kernel), and the long-standing issue that the noise is averaged along with the signal. These effects make it more difficult to accurately separate signal and noise during the later stages of analysis, particularly when the noise is spatially or temporally varying. In addition to the above, the Gaussian smoothing approach suppresses the edge details and other medium-frequency information present in the original image.

1.4 Research Goals & Broader Impact

Neuroimaging researchers continue to pursue methods that may assist in overcoming the shortcomings discussed above. The goals of this doctoral study are to identify specific properties of existing spatial preprocessing methods and subsequent effects on the data, and develop new techniques that may tie together and help alleviate some of the undesirable effects of the normalization-smoothing pair applied just before analysis of fMRI data. In this thesis, an argument detailing the method and its need for function-specific templates and a novel normalization framework is presented. In addition, an adaptive wavelet-based denoising technique is proposed that proves to be a viable alternative to Gaussian smoothing. The wavelet-based method is exercised for its ability to address issues discussed above, specifically improving the specificity of activation contours and preserving the true shape of activations. This approach weaves in with our proposed functional normalization framework and provides a basis for answering questions raised above that mostly revolve around inter-subject variability and other problems relating group fMRI preprocessing pipelines. The contributions of this doctoral work are briefly listed and discussed as follows:

1. We present a framework for spatial normalization for a group of subjects by utilizing their intrinsic functional boundaries in contrast to other existing methods which use structure as a reference (Khullar et al., 2011a,d). We enable our framework by a method for constructing a functional template that represents default boundaries of various regions involved in performing various functions of the brain. This template can be modified to comprise one or more networks available from analysis of resting-state fMRI data. The number and class of networks depends on the nature of the cognitive task that the target data set corresponds to in addition to brain regions activated during the task.

2. We developed a novel 3-D wavelet-based fMRI denoising framework to improve the quality of images while reducing spatial noise (Khullar et al., 2011b,c,e). This is a flexible smoothing method that is independent of its point of application, that is, it may be applied before or after spatial normalization. Our proposed technique is able to preserve the edges, and other spatial details within the brain images while maintaining the homogeneity of the original BOLD signal values across the brain. The denoising method has been repeatedly verified using simulated as well as real data and compared favorably against the currently used methods for denoising. The algorithm is available for download on the web(`http://mialab.mrn.org/software/waveidiot/index.html`) as a MATLAB-based software toolbox.

3. The third and final contribution of this work is a validation method to quantify the 3-D spatial shape of BOLD activity within the brain. This technique focuses on comparing two 3-D activation clusters based on shape, size and anatomical location finally resulting in a single number or metric that represents this difference. This metric utilizes slice-wise measurements of 3-D shape in order to create a metric for comparing two shapes. This algorithm has been validated on multiple group fMRI data sets and presented as a validation method in our recent work (Khullar et al., 2011b,c,e). Other applications of this metric were also identified during its development such as understanding the spatial dynamics of brain activity during rest. This application is discussed with examples in later chapters. The metric has been incorporated in to a MATLAB-based toolbox for ease of use and application.

1.5 Perspective

I hope this doctoral work will help alert researchers to important concerns regarding current preprocessing approaches in fMRI and help them to select the methods best suited for their research. Some of the pivotal features of this doctoral work that, in my opinion, may leave a lasting impact on the field of neuroimaging, specifically fMRI analysis, are listed below:

- Preprocessing of images substantially governs the outcome of fMRI analysis, with direct implications from the use of fMRI data for diagnosis and discerning brain function. With better techniques available, diagnosis can be more specific and new hidden imaging biomarkers can be identified. The methods proposed in this thesis may help in reduction of false positives and improve the functional localization of brain activity.

- Methods developed in this work offer increased flexibility in terms of point of application of various preprocessing methods. For example, if smoothing is independent of its association with normalization, it may be applied at the beginning of preprocessing (before motion correction). This added flexibility, if validated with proper methods, can help remove other sources of noise that may have been amplified by other steps such as motion correction and realignment.

- The role of some unexplored regions in the brain that are obscured due to nonadaptive processing can be more clearly understood. Better functional localization of brain activity may reveal additional relationships between spatial dynamics across various sub-regions of an activation region. Undesired effects such as intensity leakage from inactive neighboring voxels may be reduced, thus improving the statistical significance of the active clusters and revealing relatively small regional activity that may have been averaged out before.

- Use of multiple states of the brain (at rest or during a cognitive task) can be used collectively to form a stronger foundation for understanding of a normal brain as well as that of a patient with certain neuropsychological disorders such as schizophrenia.

- Shape Metric may assist in quantification of the spatial structure of activation maps and related variability within a group (subject-to-subject) or across groups (health-to-patient). Clustering subjects based on their similarity in shape of activation can provide powerful priors for data fusion (fMRI,EEG etc.) and subsequent analysis where subjects with largely different activations can be segregated from the fusion study and examined separately.

- Resting state dynamics of the human brain have been under increased investigation within the fMRI brain imaging community but are still not largely understood in terms of spatial modulations over smaller units of time. With the help of adaptive signal separation, spatial activity corresponding to the parcellated time axis can be compared based on shape and the amount of change in shape over time. Metrics proposed in this thesis can be used to investigate these dynamics in healthy controls, the patients and help to identify the region-specific relationships separating these two groups.

1.6 Organization

The rest of this dissertation describes concepts, techniques, and results I have implemented and analyzed in the course of developing the proposed data-driven fMRI preprocessing framework. This research is an important building block towards adaptive data preprocessing for better understanding functional organization in the brain. In Chapter 2, I have briefly described some of the building blocks of this thesis including fMRI mechanism, wavelet transforms, independent component analysis, and different experimental paradigms used to collect fMRI data.

Chapter 3 describes a novel fMRI image normalization method using functional networks as templates derived from resting state fMRI data. I present the intricate details of the framework through theoretical explanations followed by its application on a task-related group fMRI data set. I describe the advantages of using functional information for normalization and present supporting results using variety of spatial and statistical comparisons against widely used spatial normalization methodologies. Next in Chapter 4, I describe the initial steps towards using multiple resting-state networks as a single fusion template for functional normalization. A simple wavelet-based image

fusion approach is presented in order to evaluate the feasibility of combining multiple functional networks. Furthermore, I discuss the advantages and limitations of such an approach and share my insight on future direction for extending and validating this methodology.

We describe a new image denoising approach in Chapter 5. We present a novel wavelet-based 3-D technique to remove noise in fMRI data while preserving the spatial features in the component maps obtained through group independent component analysis (ICA). The proposed method enables the preservation of shape of the actual activation regions associated with the BOLD activity. In addition it is able to achieve high specificity as compared to the conventionally used FWHM (full width half maximum) Gaussian kernels for smoothing fMRI data. This metric presents a potential feature that would help explain the dynamics of fMRI activity across different subjects in a single study or across different studies.

Chapter 2: Background

Brief History of Nuclear Imaging

A series of astounding accomplishments over the last four decades are responsible for the synthesis of beautiful images of the brain using MRI. The foremost of them being the detection of spin properties of subatomic particles in bulk matter using radio frequency (RF) energy, with the wavelengths of the order of tens of centimeters. The first measurements of the spin resonance, shown by Otto Stern and I.I. Rabi in 1920s (Pekar, 2006), demonstrated the ability of sub-atomic particles to absorb RF energy when traveling in a vacuum under the influence of strong magnetic fields. About 20 years later, the phenomenon known as Nuclear Magnetic Resonance (NMR), describing spin resonance amongst nuclear particles was discovered by Felix Bloch and Edward Mills Purcell, winning them the Nobel Prize in Physics in 1952. Since then, NMR has primarily found applications in fields of chemistry and life sciences. Arguably, its most seminal application in the field of physics was shown by Paul Lauterbur in 1973 (Lauterbur et al., 1974), where he linked the resonance frequency of nuclei with its spatial location using a spatial gradient of the static magnetic field. The result was a spatial representation of the bulk matter, also described as an ***image***. This idea was matured in to the field of incidental medical imaging by Peter Mansfield (Stehling et al., 1991) who accelerated the process by proposing snapshot MRI in a fraction of a second. Ironically, the Nobel Prize (Chemistry) for inventing a Fourier-based mathematical encoding framework for MR images (Ernst and Anderson, 1966) was first awarded to Richard Ernst in 1991, that is, even before Mansfield and Lauterbur were jointly recognized in 2004 for their contribution in Physiology and Medicine.

With advancing trends in modalities applied for imaging the human body, fMRI is rapidly moving from a technical interest to wide clinical application. A variety of concepts from the fields of physics, chemistry, biology, and mathematics are employed throughout the process of analyzing fMRI data. Some of the most widely applied techniques for fMRI acquisition and analysis proposed over the years by researchers in neuroimaging and related fields are also discussed. In addition, a few selected concepts behind chemical phenomenon underlying BOLD activity are explained in

this chapter.

2.1 fMRI BOLD Mechanism

Functional MRI is a noninvasive imaging modality that is widely employed to understand brain function and related cognitive processes in healthy and diseased brains. MRI utilizes the magnetic moments associated with the nuclear spin properties of the atom while the object to be imaged is placed along a strong static magnetic field. Randomly oriented nuclear spins are aligned along the direction of the strong magnetic field and then perturbed by a radio wave at resonant frequency. The perturbed atoms naturally get back to their initial orientation after different relaxation times depending on the type of tissue they belong to. This difference can be captured into an MRI structural image. In order to retrieve the spatial information and structures, resonant frequencies are changed by placing magnetic field gradients on the axial plane of the brain. Scanning different axial planes facilitates formation of a three dimensional image of the whole brain.

Functional MRI utilizes all of the above and goes a step further by recording the hemodynamic response in different regions simultaneously due to neural activity. As the neural signals start to travel within a certain region in the brain, there is an increase in blood supply due to the increase in oxygen consumption. The increased blood supply overcompensates for oxygen intake and causes a drop in deoxygenated hemoglobin concentration as illustrated in Fig. 2.1. The change in level of oxygen is detected by the scanner as a change in magnetic properties around that particular brain region. Note that, fMRI measures the hemodynamic dynamics and not the neuronal firing responsible for it. These *pictures of the mind* have been produced over the past two decades to illustrate the relationships between various regions of the brain and corresponding physical and mental actions. Experiments presented by Malonek and Grinvald (1996) show that evoked changes in hemoglobin and deoxygenated hemoglobin are quite distinct. As seen in Fig. 2.2 (taken from (Huettel et al., 2004) - Fig. 7.5), the concentration of deoxygenated hemoglobin increases rapidly at stimulus onset, peaking at about 2s, and then declines to a minimum value about 6s after onset. Whereas, oxygenated hemoglobin signal shows no decline, but begins rising shortly after stimulus

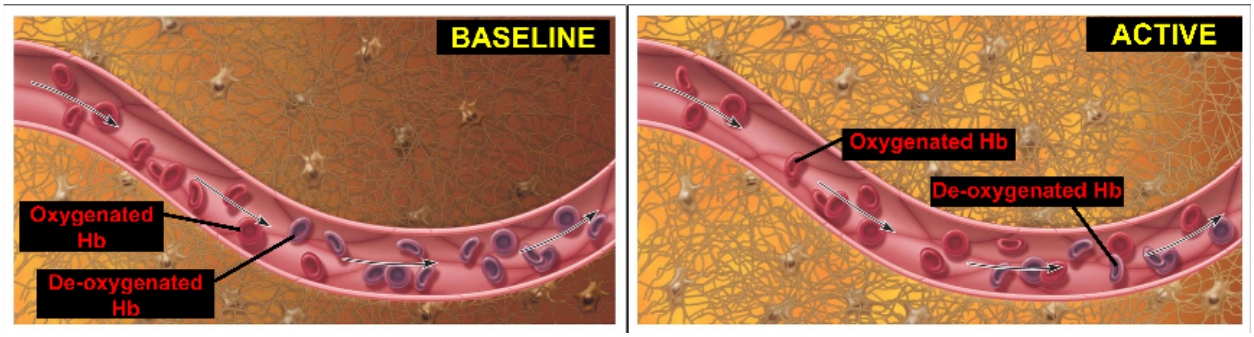

Figure 2.1: Summary of BOLD signal generation.

onset and reaches a peak at about 5 to 6s, with a slow decline to about 10s (Malonek and Grinvald, 1996). The results of the experiments in Malonek and Grinvald (1996) reported exquisite spatial correspondence of known anatomical structures with initial increase in deoxygenated hemoglobin (Deoxy-Hb) signal. In contrast, the spatial pattern of oxygenated hemoglobin did not reflect the expected pattern of neuronal activity. It extended to regions where there should have been no neuronal activity. This behavior of the so called BOLD signal indicates that the regulation of blood flow and oxygen delivery to the cortex is on a coarse spatial scale and mismatches metabolic needs (Huettel et al., 2004).

An important point to note here is that neuronal activity does not have a one-to-one correspondence with the activity shown in an fMRI image. The phenomenon responsible for neuronal activity also causes local increases in perfusion (blood flow). Thus, BOLD measure is a good proxy for regional changes in brain activity without making direct measurements of the various elements of brain function such as action potentials in axons, synaptic processes and energy transfer among neuronal cell bodies.

2.2 BOLD Image Formation

It is quite spectacular how simply the deoxygenation of hemoglobin is recorded as a change in gray intensity values across the brain. The phenomenon can be simply explained by magnetic interactions between the blood molecules and the strong magnetic field surrounding the brain. The deoxygenated hemoglobin is paramagetic, which causes a change in the homogeneity of a static

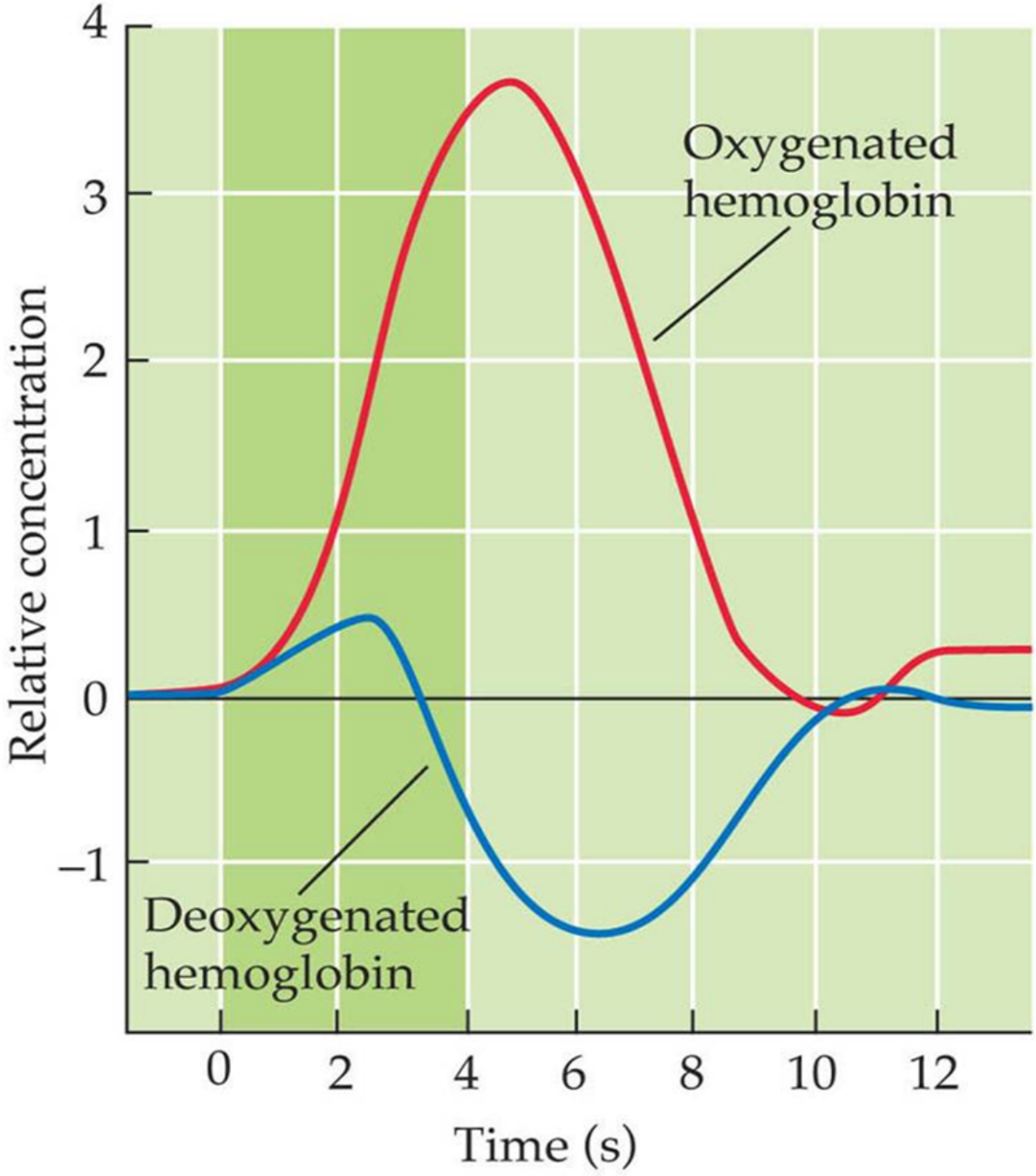

Figure 2.2: Changes in oxygenated and deoxygenated hemoglobin following neuronal stimulation. Neural activity increase, blood increases, deoxyhemoglobin concentration decreases, magnetic field homogeneity increases, gradient echo signal increases, this is transformed in to an intensity value observed within recorded imagery.

magnetic field depending on Deoxy-Hb's concentration, which results an increase in the gradient-echo signal. The brain is a 3-D volume and for efficiency reasons, the image data is acquired slice-wise using Mansfield's (Stehling et al., 1991) instantaneous single-shot echo-planar imaging (EPI) method.

If an excitation RF pulse is applied at a fixed frequency in the presence of a gradient magnetic field, only spins at the corresponding location in the field are affected by the pulse and become rotated in to the transverse place. This position corresponds to frequency and can be selected easily and more importantly instantaneously leading to fast slice acquisition. Once the field is turned off, spins from different locations are then encoded along the dimensions of the slice using rapidly switched magnetic field gradients. These field gradients are applied in three different directions, causing spin frequencies to vary along the three axis of the brain volume. The gradient encoding along various directions is interpreted as combined 2-D projections in the Fourier space. This untransformed raw data can then be converted in to an image of the slice under consideration using a 2-D Fourier transform. A simple illustration showing the process along with a single slice transform-image pair from our data set is presented in Fig. 2.3. The difference in magnetic susceptibility of the two hemoglobin molecules (oxy- and deoxy-hemoglobin) causes regional distortion of an MR decaying parameter T_2^*, leading to changes in the intensity of an MR image. The localized signal changes observed through this BOLD contrast occur in the range of several seconds, thus rapid image acquisition (explained below) allows for recording and subsequent analysis of intriguing brain dynamics.

In practical terms, a single slice can be acquired in approximately $50ms$, known as the *echo time* (TE). This is rapidly repeated for about 30-40 slices to cover the whole volume within the allotted *time of repetition* (TR), after which the process is repeated. Typically, the TR varies between $1.5 - 2s$, in this case, if TR $= 2s$, and we acquire 150 volumes corresponding to each TR, then the total time of acquisition is computed to be $300s$ (or 5 minutes). A task that plays out during this duration can be designed specifically for the above scanning parameters. In simple terms, the temporal resolution of such a data set is $2s$.

More information about MRI contrasts, types of pulse sequences, k-space sampling grids, and

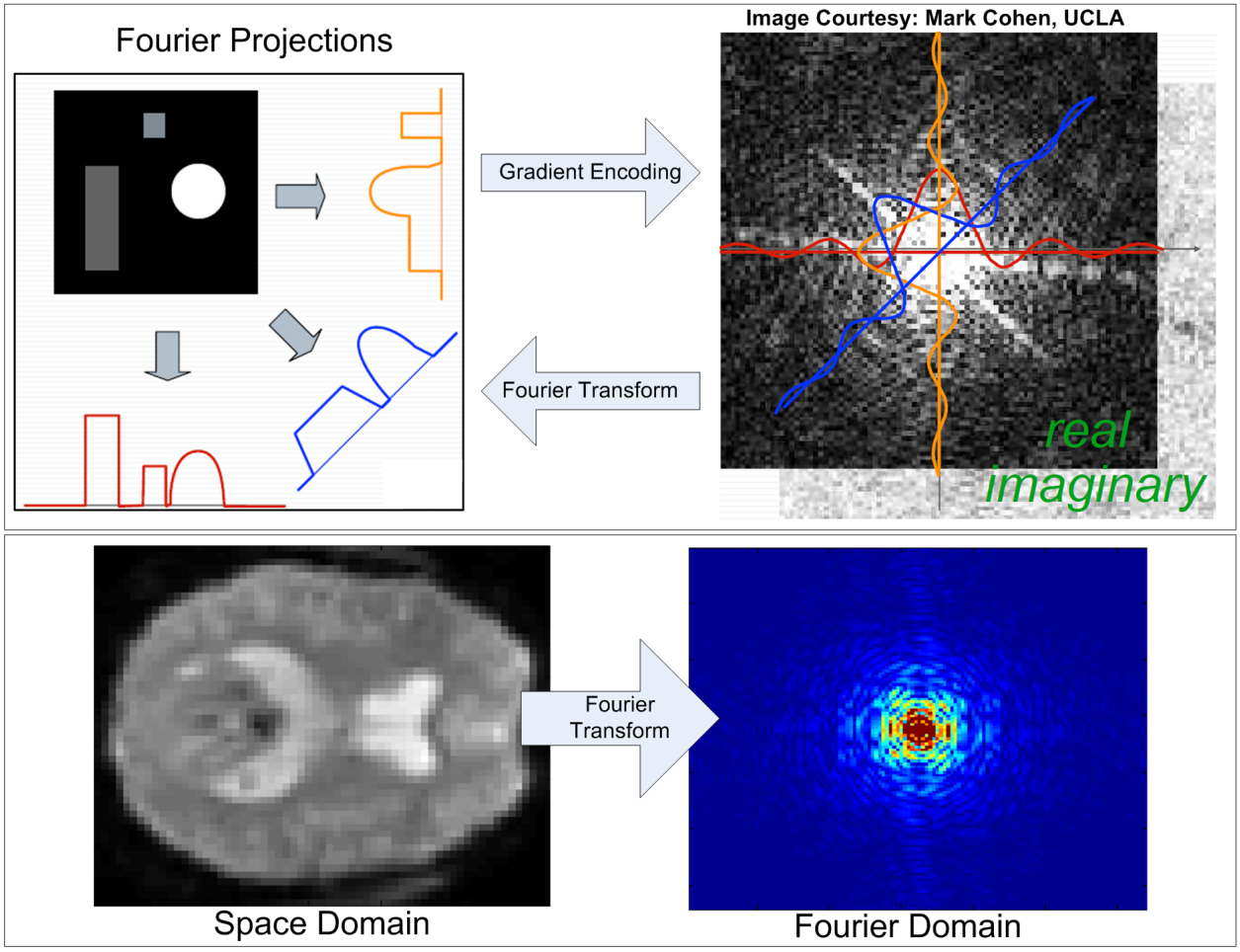

Figure 2.3: **MR Image Formation:** Examples illustrating gradient encoding and image reconstruction are presented here. (Top): Encoding of Fourier projects of known spatial shapes

other important details are explained in a seminal book on fMRI by Huettel and colleagues (Huettel et al., 2004).

2.3 Wavelet Transforms

2.3.1 Wavelet Definition

By definition, a 'wavelet' is a small wave which has its energy concentrated in time. It exhibits an oscillating wavelike characteristic but has the ability to allow simultaneous time and frequency analysis. The need for simultaneous representation and localization of both time and frequency

for non-stationary signals (e.g. music, speech, images etc.) led to the evolution of the wavelet transform from the popular Fourier Transform (Mallat, 1989). The idea of looking at signals at various scales and analyzing it at various resolution levels has emerged independently in many different fields of mathematics, physics and engineering (Daubechies, 1996). The wavelet serves as a set of basis functions for generation and analysis of natural (non-stationary) signals. This pivotal characteristic provides better time-frequency representation with wavelike signals, which is not possible to get with conventional Fourier analysis.

2.3.2 Fourier Transform

The Fourier Transform (FT) is a well-known mathematical tool to transform time or spatial domain signals to the corresponding frequency domain. The Fourier transform enables efficient extraction and representation of information. In addition, due to the nature of the complex exponential basis functions used, it is a reversible transform. For a signal $x(t)$, the FT and the inverse is given by:

$$Forward : X(f) = \int_{-\infty}^{\infty} x(t) e^{-j2\pi ft}\, \mathrm{d}t \qquad Inverse : x(t) = \int_{-\infty}^{\infty} X(f) e^{j2\pi ft}\, \mathrm{d}f \tag{2.1}$$

As per the Eqn. 2.1, any abrupt change in time domain for a non-stationary signal $x(t)$ is spread throughout the frequency axis in $X(f)$. In signal processing terms, a signal $x(t)$ when sampled with a train of Dirac-delta functions (through convolution) is highly localized in the time domain but spills over the entire frequency band and vice-versa. Thus, the FT is unable to offer simultaneous localization in time and frequency domains.

Gabor (Gabor, 1946) uses the first to introduce the concept of short-time Fourier transform (STFT), which assumes a non-stationary signal to be approximately stationary over an arbitrary but-fixed length window $g(t)$ for analysis. Thus, a two dimensional time-frequency representation $S(\tau, f)$ is obtained by STFT implemented using a sliding window $g(t)$ at different times τ. This is defined in mathematical terms below:

$$Forward : STFT_x(\tau, f) = \int_{-\infty}^{\infty} x(t) g^*(t-\tau) e^{-j2\pi ft}\, \mathrm{d}t \tag{2.2}$$

An obvious drawback that still exists with STFT is that once the window has been chosen for STFT, the time-frequency resolution is fixed over the entire time-frequency plane.

2.3.3 Wavelet Analysis and Theory

The conventional wavelet analysis procedure remains unchanged even though several different variants have been proposed over the past couple of decades. A wavelet prototype function, known as the *mother wavelet* is contracted and dilated to obtain a high and low frequency version respectively. The high frequency (contracted) wavelet is used for temporal analysis while the low frequency (dilated) is applied for frequency analysis. Fast filter-bank algorithms are implemented for efficient application of wavelet transforms, and known as Discrete Wavelet Transforms (DWT). This is inspired from the concept of the Fast Fourier Transform (FFT) algorithm formulated for simplified implementation of the computationally expensive Fourier transform.

For images, wavelets act as powerful tools capable of dividing data into various frequency bands describing, in general, a low frequency band termed as approximation, and three high-frequency bands depending on the direction of embedded high-frequency information termed as - horizontal (H), vertical (V), and diagonal (D) spatial frequency characteristics of the data. A detailed mathematical analysis of initial multi-resolution image representation models and its application to wavelet transform is given in Mallat (1989).

Continuous Wavelet Transform

Wavelet transforms come in essentially two distinct classes: the continuous wavelet transform (CWT) and the discrete wavelet transform (DWT). In contrast to the STFT explained in section 2.3.2, the CWT allows localization of high-frequency signal features in the time domain. This is achieved by applying a variable window width that directly relates to the scale of observation. This further allows for the distinct separation of high-frequency and low-frequency features. The continuous wavelet transform is mathematically defined as:

$$T(a,b) = \frac{1}{\sqrt{a}} \int_{-\infty}^{\infty} x(t)\, \psi^* \left(\frac{t-b}{a} \right) \mathrm{d}t \tag{2.3}$$

where $\psi^*(t)$ is the complex conjugate of the *mother wavelet* or the analysis filter - $\psi(t)$, a is the dilation parameter (scaling) of the wavelet, and b is the location (shifting) parameter. A function can be classified as a wavelet if it satisfies the following conditions (Addison, 2002):

1. The function must have a finite integral:

$$E = \int_{-\infty}^{\infty} |\psi(t)|^2 \mathrm{d}t < \infty \tag{2.4}$$

2. If $\hat{\psi}(f)$ is the Fourier transform of $\psi(t)$, given by:

$$\hat{\psi}(f) = \int_{-\infty}^{\infty} \psi(t) e^{-j2\pi ft}\, \mathrm{d}t, \tag{2.5}$$

then the following *admissibility* condition must hold

$$C_g = \int_0^{\infty} \frac{|\psi(f)|^2}{f}\, \mathrm{d}f \; < \infty \tag{2.6}$$

where C_g is the admissibility constant. It is clear from Eqn. 2.6 that the wavelet must have a zero mean i.e., D.C. value $\hat{\psi}(f) = 0$. In other words, the wavelet must exhibit a band pass behavior.

In more intuitive terms, the wavelet - $\psi\left(\frac{t-b}{a}\right)$ in Eqn. 2.3 can be seen as a filterbank with certain impulse response. The function dilates in time with increase in the scaling factor a and vice versa. A common notion related with scale is resolution. However, scale changes of a continuous signal do not have an effect on the resolution (Mallat, 1989). Lastly, the function $x(t)$ can be recovered from its transform $T(a, b)$, just as in case of the Fourier Transform (Addison et al., 2009). This is achieved using the *mother wavelet* in the following reconstruction formula:

$$x(t) = \frac{1}{C_g} \int_{-\infty}^{\infty} \int_{-\infty}^{\infty} T(a, b) \psi_{a,b}(t)\, \frac{\mathrm{d}a\, \mathrm{d}b}{a^2} \tag{2.7}$$

Discrete Wavelet Transform

The fundamental property of the discrete wavelet transform (DWT) that is different from CWT, is the implementation of dyadic grid (integer power of two) with orthonormal wavelet basis functions

that exhibits zero redundancy. The transform integral from Eqn. 2.3 still remains the same for DWT but is determined on a discretized grid of a scales and b locations. Most implementations of DWT use a logarithmic discretization of a and b where $a = a_0^m$ and $b = na_0^m b_0$ for $m, n \in Z$ and the family of wavelets is give by

$$\psi_{m,n}(t) = \frac{1}{\sqrt{a_0^m}} \psi\left(\frac{t - na_0^m b_0}{a_0^m}\right) \tag{2.8}$$

where m controls the dilation and n controls the translation as shown in Fig. 2.4. Here, $a_0 > 1$ and $b_0 > 0$. A common choice for parameters a_0 and b_0 is 2 and 1, respectively, thus implying the dyadic arrangement. The selection of $\psi(t)$ is made such that the basis function set - $\psi_{m,n}(t)$ constitutes an orthonormal basis such that:

$$\int_{-\infty}^{\infty} \psi_{m,n}(t)\psi_{m',n'}(t) = \begin{cases} 1 & \text{if } m = m' \text{ and } n = n', \\ 0 & \text{otherwise.} \end{cases} \tag{2.9}$$

Using the above orthonormal set of wavelets, the wavelet decomposition of signal $x(t)$ can be written as a summation of weighted wavelet basis functions. In other words, the signal can be completely recovered depending on the wavelet basis parameters. The weights for the wavelet basis are also commonly known as the wavelet coefficients:

$$x(t) = \sum_m \sum_n D_x(m, n)\psi_{m,n}(t) \tag{2.10}$$

where the wavelet coefficients can be represented as the inner product of the wavelet basis and the signal $x(t)$:

$$D_x(m, n) = \int_{-\infty}^{\infty} \psi^*_{m,n}(t)x(t) = \langle \psi_{m,n}(t)\, x(t) \rangle \tag{2.11}$$

Several wavelet basis sets such as Daubechies, Coiflets etc. can be found in the literature (Addison, 2002) to evaluate $x(t)$ using the summation of a finite basis set, $\psi_{m,n}(t)$, over the parameters m and n with finite DWT coefficients, $D_x(m, n)$, with minimal error against the original signal $x(t)$.

2-D DWT Implementation

Image processing applications require a 2-D (or higher for volumetric images) implementation of the DWT. It is also referred to as the *multidimensional* wavelet transform in the literature (Addison, 2002, Mallat, 1989). Image compression and encoding algorithms have largely benefited from the dyadic implementation of the 2-D DWT. The relatively recent image compression standard called the *JPEG2000* (Christopoulos et al., 2000) developed using the DWT offers the highest compression ratio and very high reconstructed image quality. It is most widely used in the motion picture industry.

The interesting thing to note about the implementation of 2-D DWT is that it is an extension of the 1-D DWT applied sequentially on the rows and columns of an image. The implementation schematic is presented in Fig. 2.4. Note that this filterbank can be extended to achieve higher dimensional wavelet decomposition. A multidimensional decomposition hierarchy is also demonstrated with an example image in Fig. 2.4. The analysis filters h_0 and h_1 are 1-D lowpass and highpass filter coefficients respectively. The synthesis or reconstruction filters are applied in a similar filterbank implementation, but in the reverse order to obtain the original signal.

The 2-D DWT filters can be constructed using tensor products of the one-dimensional separable wavelet and scaling functions as below:

$$\begin{aligned} \phi^{A(x,y)} &= \phi(x)\,\phi(y) \quad \text{LL subband} \\ \psi^{V(x,y)} &= \phi(x)\,\psi(y) \quad \text{LH subband} \\ \psi^{H(x,y)} &= \psi(x)\,\phi(y) \quad \text{HL subband} \\ \psi^{D(x,y)} &= \psi(x)\,\psi(y) \quad \text{HH subband} \end{aligned} \tag{2.12}$$

Non-separable wavelet filters offer an advantage for multidimensional processing through adaptable filter design, non-uniform grid sub-sampling, and linear phase (Addison, 2002). In this thesis, we utilize a different type of wavelet transform specifically useful for the applications presented here.

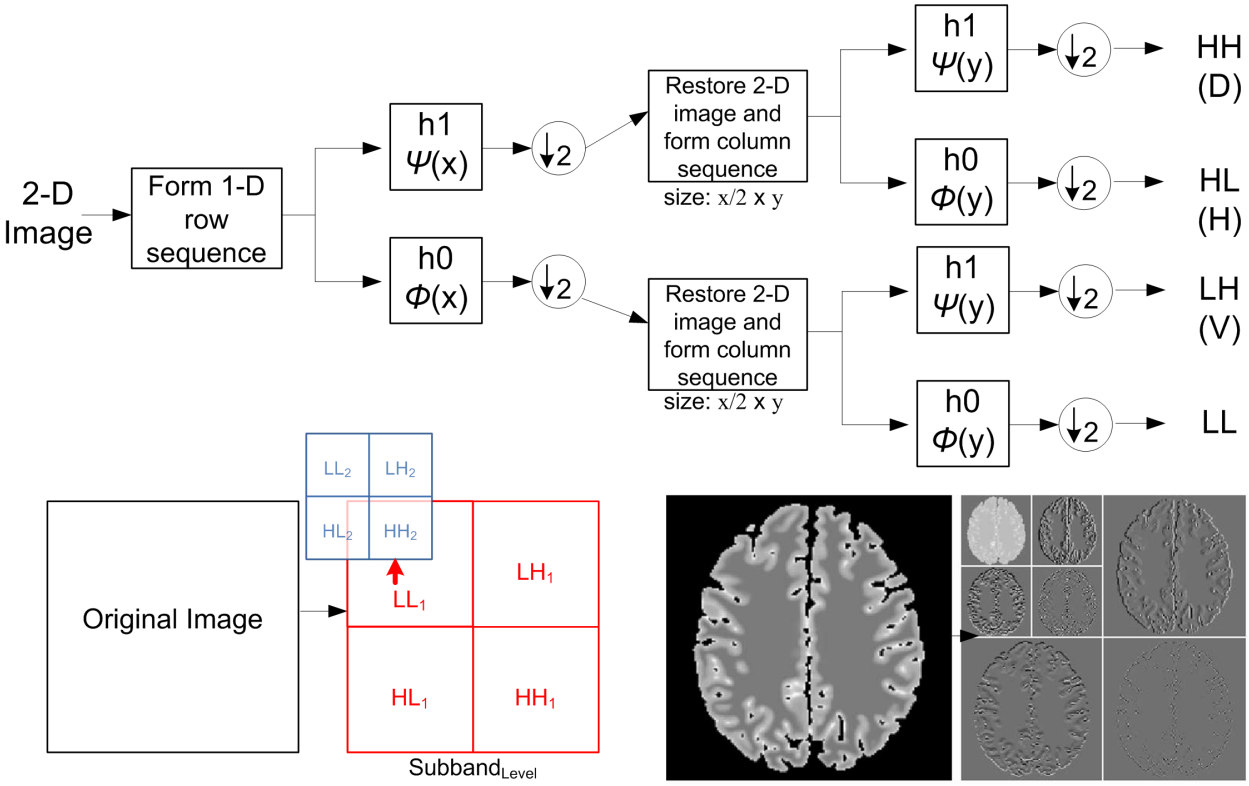

Figure 2.4: **Discrete Wavelet Transform:** (Top) Single level analysis filterbank for a 2-D Discrete Wavelet Transform. (Bottom) Schematic illustration of a 2-D DWT and arrangement of different subbands at different levels. An example image alongside its decomposed subbands shown on the right.

Stationary Wavelet Transform

The standard DWT discussed in Section 2.3.3 is non-redundant representation of the signal in the transform domain. The decimation step after filtering makes most implementations of the DWT shift-variant. On the contrary, the stationary wavelet transform (SWT) has a similar tree structured implementation, but without the decimation step. The SWT is also commonly referred to as redundant, non-decimated, or shift-invariant wavelet transform.

The tree implementation of the SWT is illustrated in Fig. 2.5. Elements h_0 and h_1 are the lowpass and highpass filters respectively whereas c_0 is the initial input signal. Elements $c_1 - c_3$ and $d_1 - d_3$ are the approximation and detail coefficients at three levels of decomposition respectively. The perfect reconstruction property is preserved by level adaptive zero-padding interpolation of

the respective highpass and lowpass as illustrated in Fig. 2.5. This process is based on the *A Trous* algorithm for inserting holes in a filter, and explained by Shensa (Shensa, 1992) in context to its application to DWT.

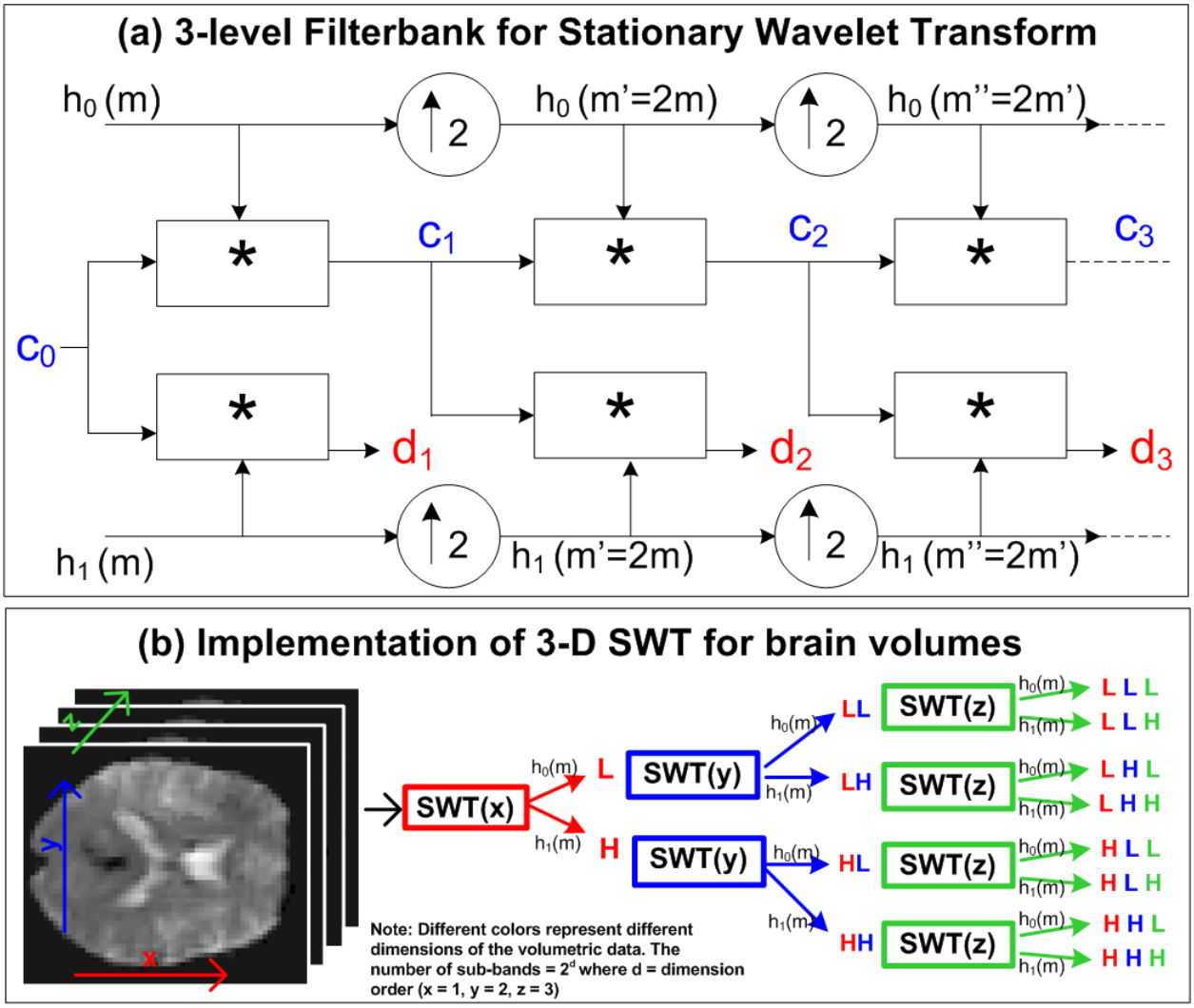

Figure 2.5: **SWT:** (a) A tree structure implementation of a 3 level SWT decomposition. (b) An illustration of the 3-D SWT applied to volumetric data set. The two filters $h_0(m)$ and $h_1(m)$ are applied on the intermediate results from the preceding dimension as indicated. A total of 8 volumetric sub-bands are obtained for each volumetric image.

The redundant representation of data by the SWT makes it suitable for several image processing applications such as denoising and data fusion. A simple illustration of the application of a multidimensional SWT is shown in Fig. 2.5. Although the implementation is computationally

expensive, the property of shift-invariance inherent to SWT is indispensable when used for such applications. Another important reason for this choice is the low spatial resolution of fMRI data. The non-decimated wavelet transform results in equal number of coefficients at each resolution scale (Lang et al., 1996), thus leaving more data points to model the signal and noise distributions of the data at hand.

2.4 fMRI Datasets

During an fMRI experiment, the subject is requested to perform a task while the scanner captures the hemodynamic response from different brain regions as neural activity. It is analogous to recording a movie of the brain where we are interested in deciphering the information representing BOLD signal change as explained in section 2.1. With efficient imaging parameters (pulse sequences) it is possible to scan the whole brain within a few seconds. Fig. 2.6 shows activation regions (green-lowest activation, orange-highest activation) derived from data collected during an fMRI task, overlaid on co-registered structural scans (gray). This image was derived from a data set where the subjects heard a sound and pressed a button in response. The most task-modulated region in the brain is found to be the temporal lobe (as seen here) where most of the initial auditory processing takes place. Most fMRI activation maps show high intensity near the central regions of spatially connected activation clusters. This is a major caveat in interpreting fMRI data, since this could be a direct consequence of poor preprocessing such as smoothing with a Gaussian, thus resulting in high intensities around the nucleus of the activations.

We propose to validate our algorithms on multiple data sets acquired using similar scanning parameters (different scanners). The nature of tasks and demographics of different fMRI data sets are briefly explained in this section. Each preprocessing algorithm proposed in this work is validated on each of these data sets. It is important to note that the algorithms proposed in this thesis are independent of the cognitive nature of task design, since each preprocessing technique spatially manipulates, while enhancing or improving the ability to extract meaningful information from fMRI imagery. However, to validate the functional normalization algorithm, we require two

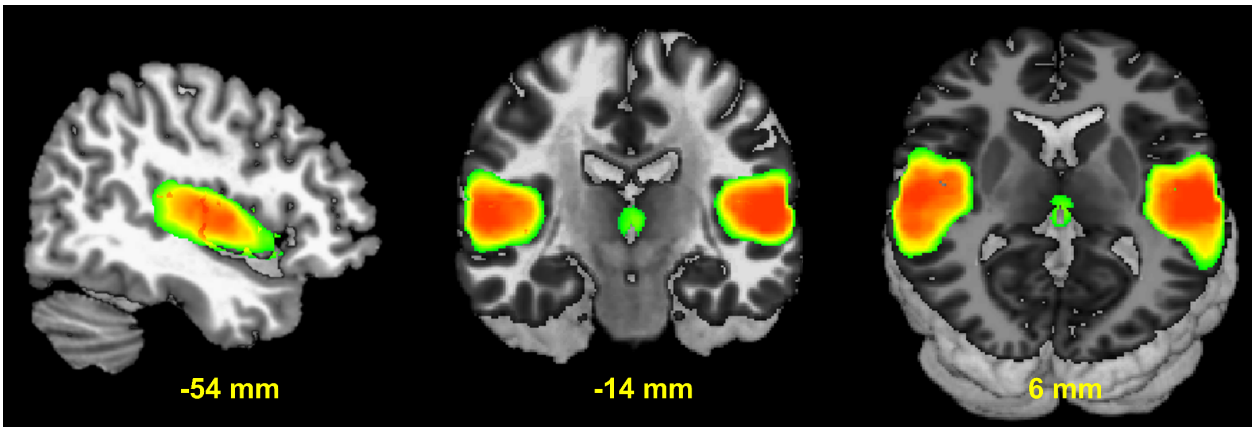

Figure 2.6: Brain activation captured by fMRI overlaid on structural images. Green regions indicate minimal spatial activity, in this case Z-scores. Whereas, the central orange regions indicate highest activity.

independently acquired fMRI data sets scanned (for each subject) during different sessions, where each subject performs a cognitive task during one session and is in rest (with eyes open) during the other session. Needless to say, our choice of tasks is not dependent on the work proposed in this thesis except the need for rest-task combination data set to illustrate the use of functional normalization.

Hereafter, we present two data sets acquired using different task designs (see Fig. 2.7). The first study consisted of a single group of 20 healthy subjects whereas the second study comprised 55 subjects divided further in two groups - Healthy Controls (28) and Schizophrenia patients (27). In order to widely use the techniques to be developed in this work, the diverse nature of data sets selected for validation will add to its robustness and stability and also assist in comparing the proposed algorithms against existing work in a more efficient manner. Most clinical-based neuroimaging studies have a common goal to explore differences in activation patterns and statistics between a healthy group and a diseased group of subjects. In this thesis, we will investigate and present the effects of the proposed techniques on these inter-group comparisons and discuss how that may modify the clinical and research decisions made on the basis of imaging biomarkers derived from fMRI studies.

2.4.1 TASK-1: Motor-Tapping Design: 1 group; 20 subjects

Participants

For this experiment, 20 healthy subjects in the age group between 18 and 62 years, participated in a motor tapping experiment, 17 subjects were right-handed, and 3 subjects were left-handed. There were 12 male subjects and 8 female subjects. IRB-approved informed consent at the University of New Mexico was obtained from all the participants.

Experimental Design

The data were recorded for all subjects performing a finger-tapping experiment designed as a block-design (on/off) with periods of 30 s off and 30 s on. During the on-block, 200ms tones were presented with a 500ms stimulus onset asynchrony (SOA). There were eight different tones with different pitches along a scale. These tones were presented in ascending and descending cycles as illustrated in Fig. 2.7a. The subjects tapped their right-hand fingers during the on period and rested during the off cycle. A single run of the experiment comprised of five and half cycles of on-off transitions($5\frac{1}{2}$ minutes), starting with an off and ending with an off period. For each subject, 165 whole head fMRI images were collected while they performed a single run of the experiment inside the scanner. Steps were taken to ensure that all participants could hear the stimuli and discriminate them from the background scanner noise.

fMRI Imaging Parameters

All imaging was performed on a 3-T Siemens Total Imaging Matrix (TIM) system with a 12-channel radio frequency (RF) coil. The scanning parameters are as follows: field of view (FOV) = 24 cm, slice thickness = 3.5 mm, slice gap = 1 mm, number of slices = 32, matrix size = 64×64, TE = 29 ms, TR = 2s, flip angle = $70\,^{\circ}$. About 165 whole head fMRI images were acquired and analyzed for each on or off period. The first 6 images were discarded to allow for stabilization of T1 effects.

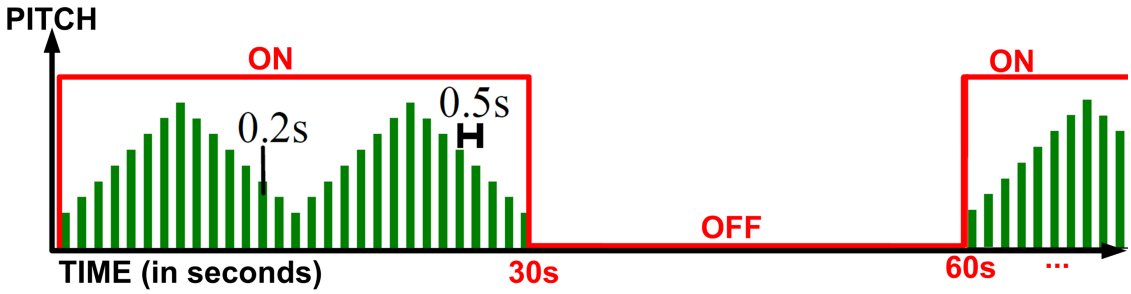

(a) Motor

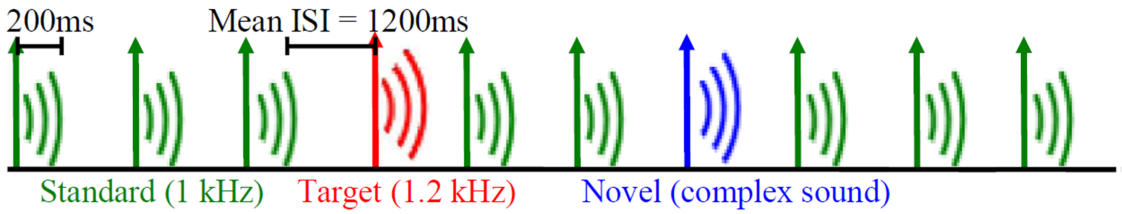

(b) AOD

Figure 2.7: (a) Motor-tapping Paradigm and the, (b) Auditory Oddball Design Paradigm.

2.4.2 TASK-2: Auditory Oddball Design and Resting State: 2 groups; 55 subjects

Participants

Subjects in this study consisted of 28 healthy control (HC) adults, and 27 chronic schizophrenia (SZ) patients, all of whom gave written, informed, IRB approved consent at Hartford Hospital, CT and were compensated for their participation. Schizophrenia was diagnosed according to the DSM-IV TR criteria on the basis of a structured clinical interview administered by a research nurse and review of the medical file (First et al., 1995). Patients were slightly older than controls (SZ age = 39.7 ± 10.1; HC age = 31.46 ± 10.9; Percent Male: HC - 73, SZ - 72).

Experimental Design

All subjects were scanned once (lasting 5-min) while at rest and twice (each lasting 8-min) while performing the auditory oddball task (AOD). The AOD task stimulates a subject with three kinds

of sounds: "standard" stimuli (1000 Hz tones with probability $p = 0.8$), infrequent *target* stimuli (1200 Hz tones, $p = 0.1$) and infrequent *novel* stimuli (computer generated complex tones, $p = 0.1$). The auditory stimuli were presented to each participant by a computer stimulus presentation system called *visual and audio presentation package* (VAPP:`http://nrc-iol.org/vapp/`) via insert earphones attached within a pair of 30-dB noise-canceling MR compatible headphones. Stimuli were presented sequentially in pseudo-random order for 200ms each with inter-stimulus interval varying randomly from 500 to 2000ms across trials, with a mean of 1200ms as illustrated in Fig. 2.7b. In order to enable the participants to decipher stimulus tones from scanner noise, all stimuli were presented about 80dB above the standard threshold of hearing. Each participant performed a practice block of 10 trials prior to entering the scanner. The participants were instructed to respond as quickly and accurately as possible with their right index fingers every time they heard the target stimulus (1000 Hz) and not respond at all if they heard any of the other two tones (standard or novel). The behavioral responses were recorded using an MRI compatible fiber-optic response device (Lightwave Medical, Vancouver, BC). The resting state scans (REST) were acquired while the participants rested quietly (with their eyes open) for 5 minutes without falling asleep inside the scanner.

fMRI Imaging Parameters

All scans were acquired at a single site - Olin Neuropsychiatry Research Center at the Institute of Living/Hartford Hospital on a Siemens Allegra 3T dedicated head scanner equipped with 40 mT/m gradients and a standard quadrature head coil. Following parameters were set for acquiring the functional scans trans-axially with gradient-echo EPI: repeat time (TR) = 1.50s, echo time (TE) = 27ms, field f view = 24 cm, acquisition matrix = 64×64, flip angle = $70\,^{\circ}$, voxel size = $3.75 \times 3.75 \times 4mm^3$, slice thickness = 4 mm, gap = 1 mm, 29 slices, ascending acquisition).

2.5 Preprocessing

The magnitude of fMRI images (initially recorded as real and imaginary parts separately) were estimated and written as 4-D NIfTI (Neuroimaging Informatics Technology Initiative) files for further analysis. Initial preprocessing of the data was done using the SPM5 software package (`http://www.fil.ion.ucl.ac.uk/spm/software/spm5/`). The data were (a) motion corrected using an approach which minimizes the impact of local signal variations using the INRIalign algorithm (Freire et al., 2002); (b) spatially normalized (Ashburner and Friston, 1999) into the MNI space (see Section 1.3.1 for definition) using the EPI template provided with SPM5; and (c) slightly re-sampled (bi-linear interpolation) from $3.75 \times 3.75 \times 3.75$ mm^3 to a voxel size of $3 \times 3 \times 3$ mm^3 resulting in $53 \times 63 \times 46$ voxels per volume. Conventionally, the last step is to spatially smooth the data using a full width half-maximum Gaussian kernel (ranging from $6 \times 6 \times 6$ mm^3 to $10 \times 10 \times 10$ mm^3).

As mentioned before, the first objective of this work is to introduce new preprocessing algorithms for fMRI. We introduce an alternate approach to smooth data, and an addition preprocessing step to re-normalize or functionally realign the data.

2.6 Signal Separation Methods

For almost two decades, meaningful information explaining functional properties of the brain has been extracted from fMRI data by applying various statistical signal processing methods. The most common approach is to use a linear regression model to detect voxels that fit closely to the fMRI task paradigm (Friston et al., 1994). This method is widely known as the general linear model (GLM). Recent literature has shown that a long standing signal separation approach known as independent component analysis (ICA) can consistently and efficiently assist in separating whole-brain fMRI data as multiple functional networks where each of these is a set of voxels correlated to each other but maximally independent to other networks (Calhoun et al., 2001b,c, McKeown et al., 1998). Both signal separation methods, ICA and GLM, are applied to provide generality and demonstrate capability in context to application of preprocessing algorithms proposed in this

work. Both approaches are briefly explained in this section.

2.6.1 General Linear Model (GLM)

GLM is a multiple regression analysis method to find task related activations in the brain. If an investigator is interested in finding spatial locations of the neural activations in the brain and is not interested in changes in the time domain, this method can be employed. For the AOD task regressors were created by modeling the target, novel, and standard stimuli as delta functions convolved with the default SPM5 hemodynamic response function (HRF) in addition to their temporal derivative. The motor-tapping study was modeled as a block design where each 'on' block was convolved with the HRF resulting in the appropriate regressors required. The regression coefficients for each voxel are then found using Equation 2.13.

$$y(j) = \beta_0 + \sum_{i=1}^{n} \beta_i x_i(j) + e(j) \tag{2.13}$$

where y is the time course of the observed image, β are the regression coefficients, m is the number of regressors, x_i are the regressors (made by convolving the HRF with different task time course) and e is the error. Spatial activation maps corresponding to each stimulus in a task are derived using the regression coefficients. An illustration depicting the application of GLM to fMRI data is presented in Fig. 2.8 For example, in case of the AOD task it is possible to create three activation maps corresponding to the target, novel and standard stimuli. Whereas in the case of MT task, we are able to obtain a single spatial map that corresponds to the 'on' condition.

The GLM approach is a widely used method due to its simplicity and low implementation and computational requirements. However, it suffers from two main drawbacks that translate as a handicap for researchers looking to gain more than just spatial information from fMRI data. The assumption that all voxels for all different tasks have the same HRF for all subjects is unlikely. The other limitation is that only task related activation regions can be found with this method since regressors used are derived from task time courses. Many non-task related activations occur

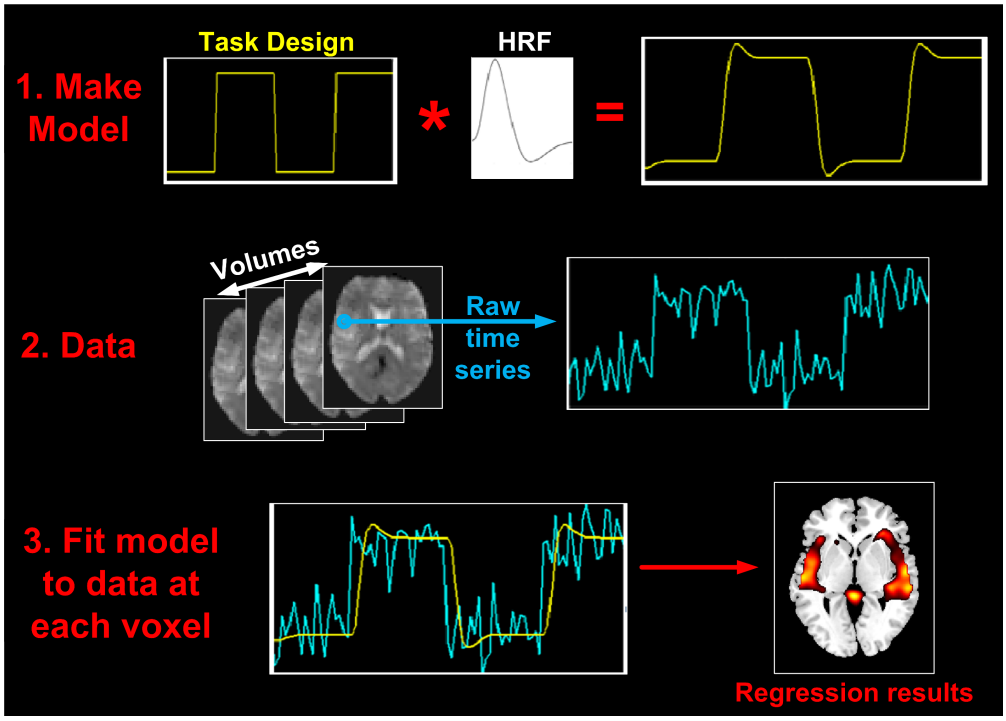

Figure 2.8: Application of GLM to fMRI data.

in the brain and it is not possible to map such networks or regions with this method. A detailed explanation of the aforementioned differences can be found in (Calhoun et al., 2001a) where the authors provide real-world examples and compare the results from application of each approach.

2.6.2 Independent Component Analysis (ICA)

Independent Component Analysis is a data-driven approach that is widely used for task-related (Calhoun et al., 2001a,b,c, 2004, McKeown et al., 1998) as well as resting-state fMRI data (Beckmann et al., 2005, Biswal et al., 1995, Calhoun et al., 2008, Damoiseaux et al., 2006, Sorg et al., 2007). This approach identifies components, a cluster of voxels in this case, which are maximally independent and linearly mixed; hence each component reflects brain regions which exhibit temporal coherence (functional connectivity). The foremost advantage of ICA is its applicability to detect cognitive patterns for which an a priori temporal model is unavailable. ICA has proven to help reveal inter-subject and inter-event differences in temporal dynamics as well as detect changes with respect to spatially distributed brain networks (Beckmann et al., 2005, Calhoun et al., 2001a,b,c,

2009b, McKeown et al., 1998). By far the most common application of ICA is extraction of spatially independent brain regions (spatial ICA) although temporal ICA is also possible (Calhoun et al., 2001c). Mathematically, ICA can be represented using a simple expression presented in Equation 2.14.

$$X = \hat{A}\hat{S} \tag{2.14}$$

where $\hat{A}$ is the $N \times N$ mixing matrix and $\hat{S}$ is the $N \times V$ spatial component map and X is the fMRI data from all subjects, concatenated along the temporal dimension as shown in Fig. 2.9a.

A group level ICA analysis is made possible by finding the activation maps that contain voxels that are correlated to each other but are maximally independent of other set of voxels. Each subject's data is stacked along the rows of matrix **X** and decomposed in to a mixing matrix **A** and a spatial component matrix **S** as illustrated in Fig. 2.9a. In the interest of brevity and to focus on the novel contributions, details of ICA and its implementation are not covered here and covered in Calhoun et al. (2001b).

The theoretical calculations and related equations can be found in Calhoun et al. (2001b). Through ICA, we can also obtain each subject's spatial activation patterns by back-reconstruction through inversion as illustrated in Fig. 2.9b). The data reduction, ICA estimation and computation of single-subject maps and time courses is mathematically presented in the appendix of Calhoun et al. (2001b) through matrix manipulations.

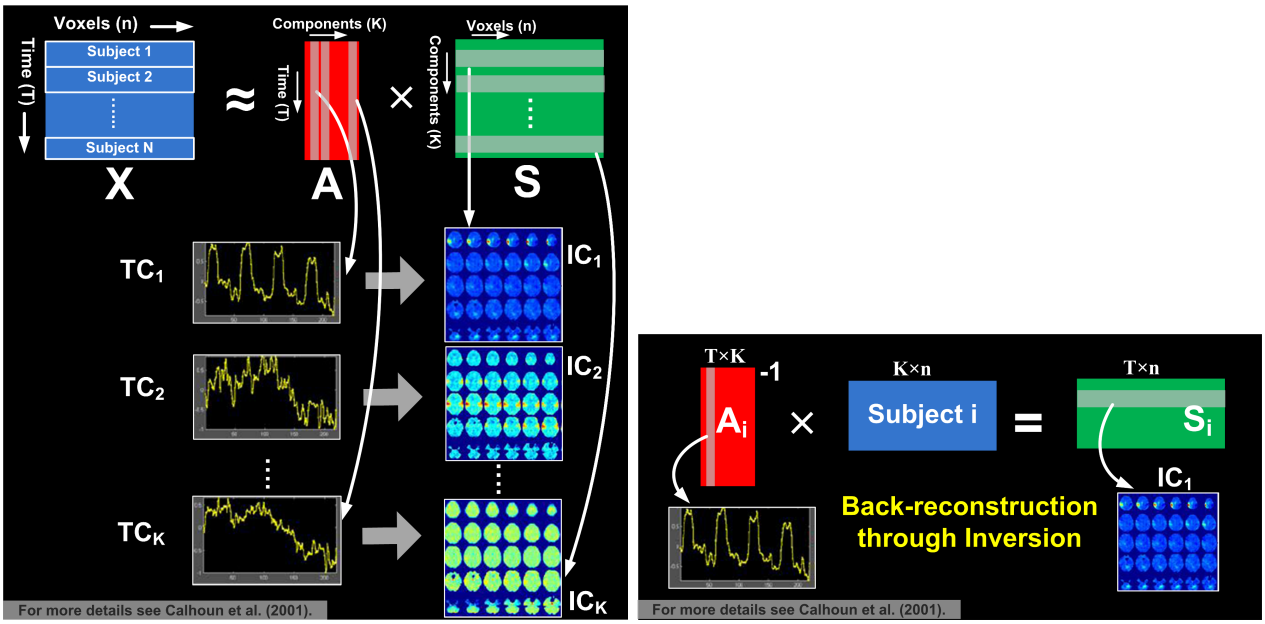

Figure 2.9: Application of ICA to multi-subject fMRI data (a) forward estimation and the, (b) back-reconstruction using inversion (Calhoun et al., 2001b).

Chapter 3: Functional Normalization with Resting Networks

3.1 Spatial Normalization of fMRI

An initial requirement for analyzing fMRI data from a group of subjects is registration of multi-subject fMRI scans to a common spatial coordinate space. This requirement is incorporated as a fundamental step in almost every pre-processing software package designed for the analysis of fMRI data. To date, one of the most common approaches used is transforming subjects' images to the MNI coordinate space utilizing a template created by averaging echo-planar imaging (EPI) MRI scans (Collins et al., 1994). Needless to say, all normalization methods, in a strict sense, map the fMRI data to a common space using information from structure. The structure (across subjects) is different due to magnetic field homogeneities in addition to individual biological variability. A commonly used approach implemented within most preprocessing software packages such as FSL (Jenkinson, 2003) and SPM (Andersson et al., 2001), uses field maps to correct for the field inhomogeneities. This enables correction for warping in the data due to magnetic susceptibility at an individual level, but the biological variability across different subjects seen as morphological differences in structural boundaries still poses a problem.

The differences between functional and structural anatomy of the human brain have been discussed since well before the advent of fMRI. In the past, several studies have initiated efforts to try and compensate for these differences at a macroscopic as well as microscopic level. Proposals and reviews such as those by (Brett et al., 2002, Mazziotta et al., 2001) have re-iterated the importance of functional localization and incorporating cyto- and chemo-architecture knowledge into algorithms and methods that are applied for re-alignment and segmentation of neuroimaging data sets. Their experiments involving superimposition of cytoarchitechtonic areas describe the inter-subject variability in extent and position of Brodmann areas 44 and 45.

Early fMRI studies focused on studying activations in sensorimotor areas and the visual cortex,

for which labeling activation regions is relatively straightforward. Concurrent studies conducted around the same time presented compelling evidence that the functionally well-defined areas such as the visual motion or the motor cortex can vary across subjects in terms of size (Watson et al., 1993) or mapped anatomical location (Tootell et al., 1995). However, labeling activations based on rather highly related functional, anatomical and cytoarchitectonic labels is not as controversial as labeling regions of hyper and hypo activations in complex tasks such as working memory or when making inferences for a large population separated as groups of multiple subjects based on their state of mental health (*i.e.* , controls or patients).

A relatively recent work by Sabuncu et al. (2009) provides an array of examples where structural anatomical landmarks on the cortex were offset or inconsistent with estimated locations of corresponding functional activity. Their method utilized fMRI scans from task-1 (visual stimulus) to functionally re-align task-1 data and data from another visual task (task-2), both performed by the same group of subjects. The warps derived using data corresponding to one half of task-1 generalized successfully to the other half and resulted in improved statistics and higher detection sensitivity. Interestingly, these warps also facilitated in increase of detection sensitivity when applied to task-2. . This study supports our preamble that functional domains of individual brains are as important as individual structural architectures, when trying to detect patterns of neural activity within a group of subjects.

In order to address the aforementioned problem, researchers have tried different types of approaches and seen improvements in context to specific requirements of their studies. Some of these include constructing templates for region-of-interest (ROI) analyses in a standard space (Hammers et al., 2002, Kubota et al., 2006), development of specially tailored transformation methods to serve specific anatomical landmarks (Grachev et al., 1999, Hammers et al., 2003), creating atlases based on cortical surface averaging (Argall et al., 2006, Fischl et al., 1999), utilizing localizer contrasts or functional ROIs prior to applying hypothesis tests for detecting activity across the cortex (Saxe et al., 2006), and developing templates to compensate for age and gender differences (Lee et al., 2005). Comprehensive surveys such as by Crivello et al. (2002), Robbins et al. (2004), and Ardekani et al. (2005), present an elaborate description of differences between some of the widely used spatial

normalization techniques. However, none of these approaches incorporate a methodology into the fMRI preprocessing pipeline. Amongst common drawbacks, most of these approaches lack the ability to compensate for group-level functional variability, that is, these methods are blind to effects of activation intensities modulating differently for different subjects in different regions for different complex tasks.

A more specialized approach is to use a 'study-specific template' (SST), which was initially proposed by Good et al. (2001b) for voxel-based morphometric (VBM) study of multiple subjects. The SST is generated in two steps: normalizing all individual T1-weighted images to the MNI T1-weighted template and then taking the average of all normalized images to create the SST. This method proved to be extremely useful in improving the results of the VBM analysis as initially shown in (Good et al., 2001b). More recently, Huang et al. (2010) proposed a new approach for deriving a SST using the EPI scans of the individual subjects belonging to the group being analyzed. The effects of the method were reported in two groups (young and old) each of which performed a different task. Significant differences were reported in both smoothed and unsmoothed raw data when comparing statistics from the MNI-template approach against the EPI-SST approach, with a large improvement in the latter in addition to achieving better sensitivity of local maxima. This study, in addition to previous experiments by Good et al. (2001a,b), can be seen as compelling evidence that anatomical variations within a group of subjects as well as differences in scanners used for acquisition can cause considerable spatial distortion when mapping the data to a common coordinate space. This causes the statistics to change significantly, and can lead to misinterpretation when studying spatial patterns of cognitive activity.

A possibly favorable alternative to collecting data from a battery of tasks as proposed by Mazziotta et al. (2001) and recently implemented by Sabuncu et al. (2009), is to robustly estimate functional landmarks using resting-state fMRI data and use these for functional re-alignment. Such an approach is expected to supersede SST-based techniques proposed with respect to locating accurate functional activation centers and yielding relatively more accurate modulation levels of activation voxels. It can potentially be implemented by incorporating locally defined functional information that not only aligns activation centers but also the boundaries of these areas and some aspects of

within-activation topography at a network level.

3.2 Rest and task: Co-existing Spatial Dynamics

Prior to generalizing some recent work that addresses functional co-registration of group fMRI data, we introduce here a few phrases and relevant definitions that can be useful in order to clearly follow the objectives, methods and results presented in this chapter.

Intrinsic Networks: Brain regions which exhibit temporally coherent fluctuations and are identified from an fMRI scan collected during rest or during a task (Calhoun et al., 2008, Smith et al., 2009).

Intrinsic Dynamics: Spontaneous temporal fluctuations exhibited by *Intrinsic Networks*.

Functional Domains/Systems: Spatial characteristics of intrinsic networks, essentially represented by a region or group of regions showing variable spatial patterns across individuals.

Functional Standard Space: N-dimensional space that consists of each individual's data co-registered for variation in N functional domains in order to bring functional normality to the group being analyzed.

Functional Normalization: Process of registering fMRI images to a standard functional space.

In the past decade, functional organization of the human brain has been increasingly studied using intrinsic networks (INs) alternatively known as the ***resting state networks***. Resting-state fMRI has been collected on a large scale (Allen et al., 2011, Biswal et al., 2010) since the seminal discovery of intrinsic networks in the resting brain by Biswal et al. (1995). Independent component analysis (ICA) has been a widely used tool to analyze resting state fMRI data and draw inferences regarding functional connectivity (Beckmann et al., 2005, Biswal et al., 2010, Calhoun and Adali, 2012, Calhoun et al., 2008, Damoiseaux et al., 2006, Harrison et al., 2008, Smith et al., 2009). Recent work by Mennes et al. (2010) shows that strong spatial associations, known as *transition zones*, exist between brain regions representing intrinsic dynamics and those active during a cognitive task. The abundance of resting data and increased interest in building the functional *connectome* (an

ultimate map of human brain connectivity) can play a key role in building novel methods. Thus, there exists a possibility of successfully utilizing functional information within rest-fMRI data to better inform the data collected for cognitive tasks (Arbabshirani et al., 2012, Calhoun et al., 2008) as later demonstrated in this chapter.

3.3 Functional Normalization: A New Framework

We propose a novel approach for co-registering a group of subjects by utilizing their intrinsic functional networks (resting-state fMRI) as an additional pre-processing step in contrast to the existing convention that only uses structure as a reference. The proposed method, hence forth referred to as ICA-based functional normalization or 'ICA-fNORM' delineates resting fMRI data into intrinsic networks using ICA and utilizes them as 'functional templates' (FT) to eventually derive normalization parameters. As shown by numerous studies (Calhoun et al., 2008, Ma et al., 2012, Smith et al., 2009), some of these networks co-exist independent of the cognitive state (e.g., at rest or while performing a task) and the health (e.g., control or patient) of the brain. Multiple networks exhibit temporal and spatial modulation during cognitive task versus rest which implies existence of common spatial excitation patterns between these identified networks (Calhoun et al., 2008). This congruence in neural activity raises two questions that are yet to be addressed definitively:

- *Is it possible to build normalization templates that re-align spatial boundaries of function rather than structure on a subject-to-subject basis?*
- *Can resting state networks be used to help improve group statistics for a cognitive task?*

The main contribution of the proposed ICA-fNORM framework is to attempt to answer these questions as completely as possible. We attempt to utilize the normalization parameters (set of non-linear basis functions) computed using a resting-state network (RSN) for re-aligning each subject's fMRI data corresponding to a cognitive task such as the auditory oddball design (AOD). For every subject, the new AOD data is normalized to the group according to variations in functional systems unique to that subject. This results in more robust co-registration of all subjects to a functionally standard space specific to that particular group. Our results indicate that the ICA-fNORM

approach applied in addition to the conventional MNI-based spatial normalization (Ashburner and Friston, 1999), improves the group statistics as compared to those obtained by applying the latter method alone.

The proposed functional normalization approach is divided in to four stages:

- **Stage 1:** Derive functional templates through group ICA(Section 3.3.1).
- **Stage 2:** Estimate the functional re-alignment parameters corresponding to each subject (Section 3.3.2).
- **Stage 3:** Apply the parameters from Stage 2 to the pre-processed task-fMRI data acquired for the same set of subjects (Section 3.3.3).
- **Stage 4:** Perform statistical analysis using ICA and GLM (separately) and compare group level statistical significance and detection sensitivity between the 'before' and 'after' ICA-fNORM data sets (Section 3.5). This stage is added only to test the performance of the proposed method as all fMRI studies have a common goal of deriving meaningful activity from the data.

To implement Stage 1, we propose two options. First, each functional template may contain a single resting-state network, for example, a default-mode network (DMN), a temporal lobe network, a visual network, all may exist as separate stand-alone templates and be used for functional normalization. This is essentially treating an intrinsic network output by ICA as a functional template by itself. In my opinion, the second method, using multiple functional networks as a single fusion template, is the more desired method, and we expand upon the proposed methodology in Chapter 4. The fusion method provides flexibility to tune a functional template for any task data set, given that a resting-state data set exists for the same group of subjects. We present details and discuss the benefits and limitations of the second approach separately in Chapter 4. Note that the fusion approach is still in its nascent stages and needs to be validated rigourously prior to widespread application. We present an initial contribution towards this large paradigm shift in fMRI preprocessing. The following sections are focused on elaborating on the functional normalization framework and discussing its benefits and limitations through detailed analysis of its

application on a two group data sets comprising healthy controls and schizophrenia patients.

3.3.1 Functional Templates from Resting-state fMRI

In order to derive the functional templates, fMRI data is decomposed into multiple spatial independent components (intrinsic networks) using group spatial ICA implemented within the GIFT toolbox (Calhoun et al., 2001b) available online (`http://icatb.sourceforge.net/`). ICA is data-driven method that only requires one parameter to be set prior to application - number of desired independent components. In our approach, we utilize a high model order of 50 components for extracting large number of intrinsic networks. A recent study by Abou Elseoud et al. (2010) explains the effects of increasing model order on independent component analysis of resting state fMRI data. A low model order used for resting state is expected to yield a rather less informative set of large-scale brain networks. Whereas, there is loss of repeatability if a very high model order (¿100) is used. They also presented evidence depicting spatially overlapping components separated as different signal sources as a result of using model order of 30 - 40. The motivation to use a high model order also comes from recent studies (Allen et al., 2011, Biswal et al., 2010) that show separation of artefactual networks from meaningful components. A previous study (Calhoun et al., 2008) that utilized the same resting and task data sets, also summarized in Section 2.4.2, set a much lower model order - 19 components. However, we use a higher order keeping in sight a goal to develop a multi-network functional template, that is, to combine multiple known resting state networks into a single functional template that may further be used to co-register data from any cognitive paradigm.

Default mode network and the temporal lobe network are two of several intrinsic networks repeatedly found to co-exist in resting-state scans and in a cognitive task. It is worth noting that spatial characteristics of these two specific networks, used as functional templates here (see Figure 3.2), did not show considerable variation but it may be useful to experiment with the model order to develop a stable functional template. We perform similar experiments for the multi-network case presented in Chapter 4. Thus, high model order for decomposing rest data is more feasible in order to separate the intrinsic networks with more subtle differences that have systematic

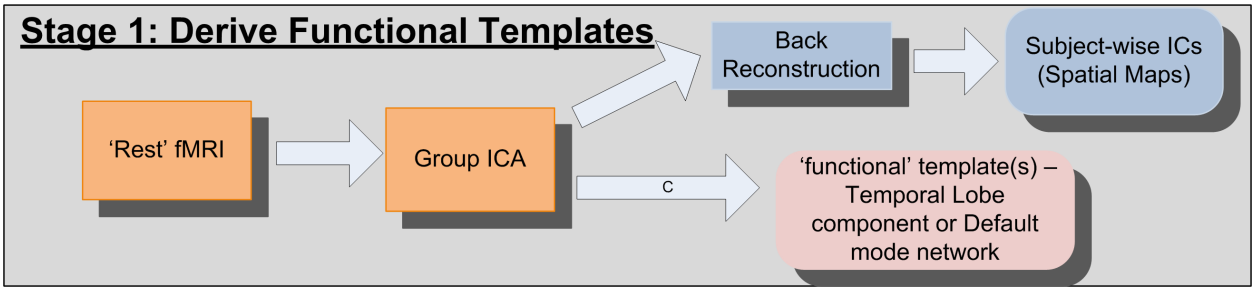

Figure 3.1: This is the first step of the ICA-fNORM technique. Here we derive group and subject-wise independent component maps using the group-ICA technique as explained in Calhoun et al. (2001b). For simplicity, we chose to proceed with two relevant components, TL_{rest} and DMN_{rest} .

significance in the context of resting-state patterns within the brain.

After estimating the group spatial component maps and corresponding time courses through group ICA, subject-specific components are estimated using that subject's fMRI data and the group independent time courses through a back-reconstruction step (Calhoun et al., 2001b, Erhardt et al., 2011). These subject-wise independent components are then used as target images to derive the subject-specific normalization parameters (explained in Section 3.3.2) by warping the subject's component map to the group mean component map.

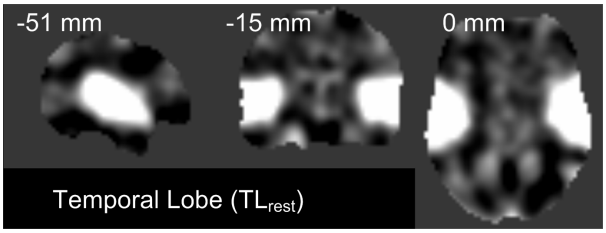

(a) TL_{rest}

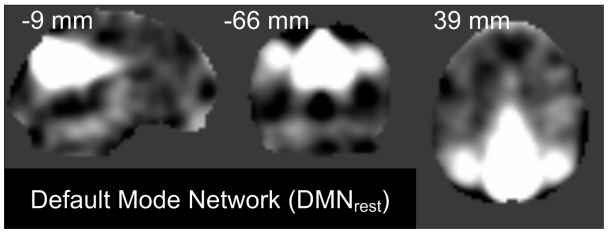

(b) DMN_{rest}

Figure 3.2: Orthogonal views of the intensity images (arbitrary values) derived using ICA: (a) temporal lobe (TL_{rest}), (b) default mode network (DMN_{rest}) component images treated as two different functional templates. The aggregate spatial components are presented here in the MNI co-ordinate space. As seen here, the activations are localized around known anatomical regions (temporal lobe and different regions of the default mode network). These spatial maps are similar to the those illustrated by Calhoun et al. (2008).

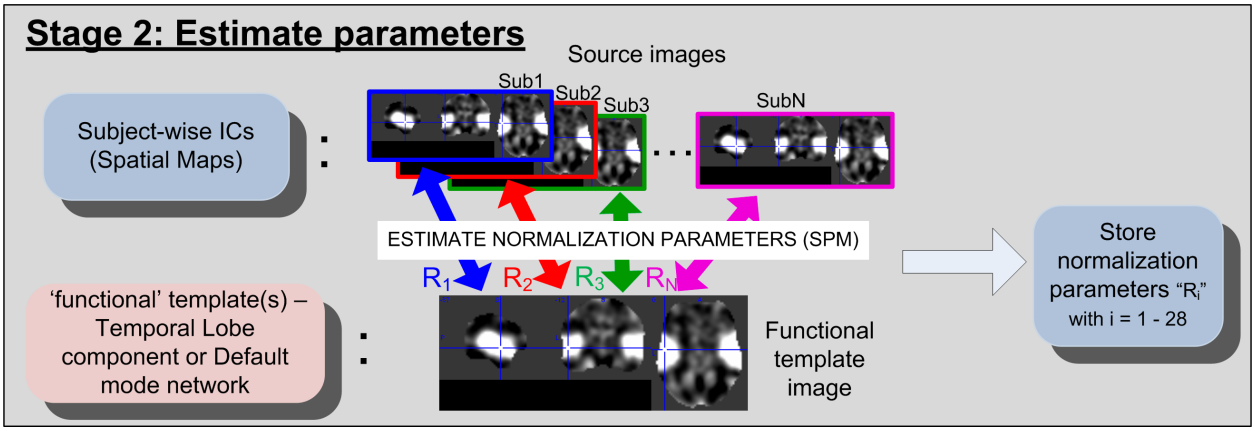

Figure 3.3: Normalization parameters (DCT coefficients) are estimated using the group mean component as a reference image and each subject's back-reconstructed component as the *target* image.

3.3.2 Estimating Normalization Parameters

Next, the normalization parameters for each subject were estimated using the study-specific TL_{rest} network (or DMN_{rest}) as the reference image and that subject's DMN_{rest} component as the source image, as illustrated in Figure 3.3. Note that, the resting state data set utilized for functional normalization has already been spatially aligned using a study-specific MNI template as described by Huang et al. (2010) (done using SPM5 *Normalize* routine). This step is purely to map the data in a known coordinate space such as the MNI and to present meaningful overlays of BOLD activity. The proposed functional normalization approach is applied on this MNI-normalized data set.

We utilized the non-linear spatial normalization algorithm (Ashburner and Friston, 1999) for computing a set of non-linear basis functions comprising of Discrete Cosine Transform (DCT) coefficients that account for global shape differences between the functional network's boundaries of each subject and that of the group level network. This process resulted in low-frequency DCT coefficients, a total of 392 parameters (787 warp matrix), to describe deformations between the two volumetric images. The basis functions were estimated using 3-D discrete cosine transform (DCT) and regularization was done using $\lambda = 0.01$. The non-linear registration was performed as 12 iterations, that is, until a linear least squares solution converged and the resulting normalization parameter matrix is stored. Warping parameters were computed for each subject and used for

registration of the task-related data corresponding to the same subject, as explained in the next section (see 3.5). The above process is repeated with the DMN_{rest} network used as the functional template and the data were stored for further analysis.

3.3.3 Functional Normalization of AOD Data

The normalization parameters derived above are representative of the difference between each subject's functional activity patterns and the group's average activity with respect to a particular functional system/network. Utilization of resting-state functional boundaries as a reference to re-align another independently acquired data set (AOD) facilitates transformation of all the data to a functionally standard space. In this paper we restrict to utilizing only two networks (one at a time), known to play a significant role in performance of this task and validate our proposed methodology. Hence, the functionally transformed AOD data was able to incorporate the template network's spatial variations that exist between multiple subjects within the same group. In this

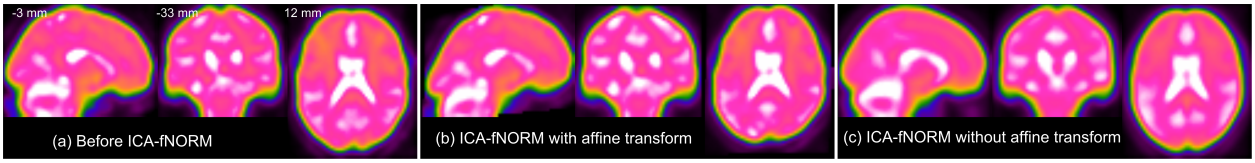

Figure 3.4: A comparison showing global shape distortion effects due to affine transformation applied along with the functional normalization step: (a) Original image, (b) ICA-fNORM with second affine transform, (c) ICA-fNORM without second affine transform. We use a non-conventional color-scheme to better highlight the shape distortion effects. Images in (a) - (c) are derived from the same MNI co-ordinates mentioned in (a).

experiment, we only applied the non-linear transformation (derived above) for re-aligning every subject's AOD data using SPM's 'normalize' routine. As mentioned before, AOD data was prepared for analysis using a conventional preprocessing pipeline that included spatial normalization to the MNI space using SPM (see Section 2.4). The spatial normalization step in preprocessing included a 12-parameter rigid-body transformation, thus eliminating the need for applying another affine transformation when performing the functional normalization step. The geometric differences (affine matrix) between the group-level network (reference) and each subject's network (object) are local in nature in the sense that they may not generalize well to the rest of the brain if applied as a

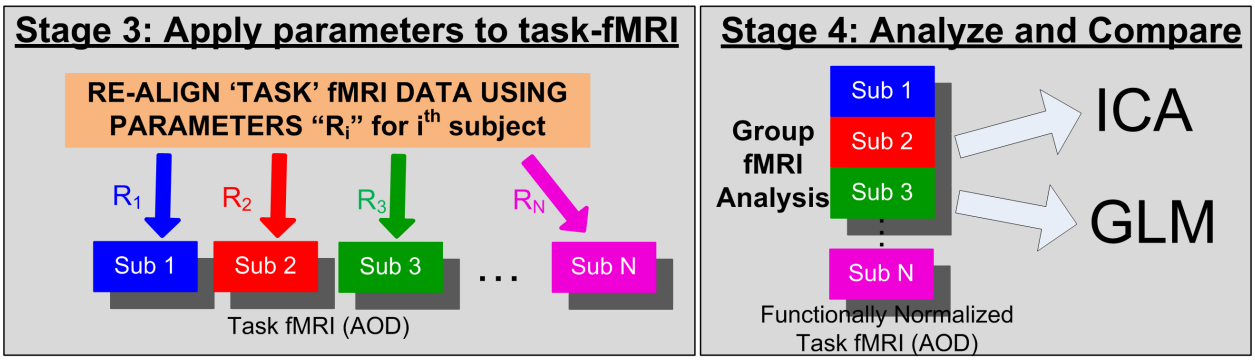

Figure 3.5: Each set of Normalization parameters is tied to a unique subject's global shape differences for a single intrinsic network. However, applying this on task data yields a new functionally normalized set of fMRI data which incorporates functional variabilities, especially relating to spatial interactions around a certain region (temporal lobe or the areas covered by the DMN). These functionally normalized data sets for multiple subjects can then further be analyzed using ICA and GLM and the results are presented in Section 3.4

set of affine parameters. Therefore, the affine matrix was set to an identity matrix in order to avoid distortions in the shape of the brain since the reference image for deriving this affine transform was an activation component with most positive values spatially distributed within a small region across the whole brain (such as the temporal lobe or the DMN regions). To corroborate the aforementioned observations, some of the adverse effects, of using a second affine transformation, such as shape distortion of the overall brain are highlighted here through Figure 3.4. only the non-linear transformation R_i for every i^{th} subject derived in the estimation step (see Fig. 1) was applied to each subject's AOD task data.

It is worth noting that the fNORM (functional normalization) parameters (non-linear transformations) that were derived from the resting state networks were highly dependent on the spatial characteristics of the reference and source images. The reference image, and in most cases the source image, mostly had positive values concentrated within or around the primary activation region as seen in Figure 3.2.

The functional dynamics across individuals within a group can be quantified in the form of intrinsic networks and thus inform us about the functional organization of each individual's brain. Therefore, these networks and in turn the normalization parameters act as a default basis set for that particular subject. The key to our hypothesis is that functional normalization using these

intrinsic networks compensates for absence of these functional systems in structural templates such as the MNI-EPI template or the T-1 weighted images used to register data to a stereotactic space through spatial normalization. The intrinsic networks were most likely able to provide us with a priori information about how each individual's brain is organized at a functional level. It is known from literature that the brain's functional organization is modulated in many ways when performing a task as compared to being at rest (Calhoun et al., 2008, Mennes et al., 2010, Smith et al., 2009) while the spatial organization of these networks remains similar on a global scale. Note that, the same set of functional normalization parameters for each subject were used to co-register each volume of the AOD fMRI data set for that subject.

3.4 Analysis Methods

This section briefly describes the methods used to compare the effects of functional normalization. In order to see the improvements at a group level, we applied two of the standard fMRI analysis methods on the functionally re-aligned AOD data: (a) group independent component analysis (GICA) (Calhoun et al., 2001b) and (b) general linear model (GLM) analysis (Friston et al., 1994) implemented within the **SPM5** toolbox. For comparisons, these analysis methods were also applied to the regularly pre-processed AOD data (spatial normalization with MNI-305 template) as presented here-after.

For the AOD task, data from each participant was entered in to the GLM group analysis framework using SPM5. Regressors were created by modeling the target, novel and standard stimuli as delta functions convolved with the default SPM5 canonical hemodynamic response function (HRF). This resulted in a set of activation maps (β-weight maps) associated with each of the parametric regressors. Scanner drift was modeled by a high pass filter with cutoff at 128 seconds. Contrasts between targets versus standard (hereafter referred to as target) were created for further analysis. This specific contrast was selected based on existing evidence (Halgren et al., 1998, Kiehl et al., 2005) showing robust detection of extensive and spatially distributed time-locked brain activity during processing of the target stimuli in an AOD task. The resultant statistics were

corrected for multiple comparisons with $p < 0.01$ using false discovery rate (FDR) (Genovese et al., 2002).

We utilized a group-ICA method first proposed by Calhoun et al. (2001b) for deriving maximally independent components representing distributed neural activity across the brain. In our experiment, the order was set to N= 20 components and ICA applied to regularly pre-processed (*before* ICA-fNORM) AOD data and the functionally re-aligned (*after* ICA-fNORM) AOD data separately. Two task-relevant components were chosen to investigate and verify the improvements introduced by ICA-fNORM: (a) temporal lobe component (TL_{AOD}), and (b) default mode network (DMN_{AOD}). These correspond to the same networks that were chosen as functional templates for normalizing AOD data before. All 20 components were estimated for each individual subject using a back reconstruction method known as GICA3 (Erhardt et al., 2011). The back-reconstruction method uses the mixing matrix output from group ICA and projected on to subject-specific fMRI data to obtain subject-specific independent components. The implementation details are covered in Calhoun et al. (2001b).

3.5 Results

In order to study and report the effects of functional normalization, we compared the statistics and spatial characteristics of two task-relevant components mentioned above. Each of these was estimated twice, that is, once before applying ICA-fNORM (that is, MNI-based normalization only), and once after applying ICA-fNORM (MNI-based normalization followed by functional re-alignment using ICA-fNORM) with each of the two templates. The first set of results highlight the spatial differences between activation regions corresponding to before and after ICA-fNORM followed by the comparisons based on difference ***threshograms***. Please note that the term *threshograms* is coined to avoid confusion with conventional histograms, even though they appear graphically similar. A threshogram is estimated by subtracting two different histograms corresponding to *before* and *after* ICA-fNORM. This comparison is similar to subtracting the reverse cumulative density

functions of the two methods where the x-axis corresponds to increasing t-thresholds. Threshogram-related results are presented later in Section 3.5.3. Also, Region-of-interest (ROI) analysis is later presented using multiple anatomical atlases. Each of the aforementioned comparison is presented using results from each of the analysis methods (GLM and ICA) for both functional templates (TL_{rest} and DMN_{rest}).

3.5.1 Morphological and Intensity Variations

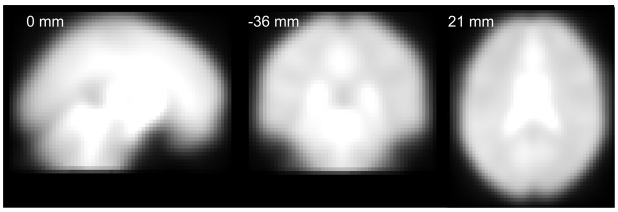

(a) average of *after* ICA-fNORM fMRI data from 28 subjects

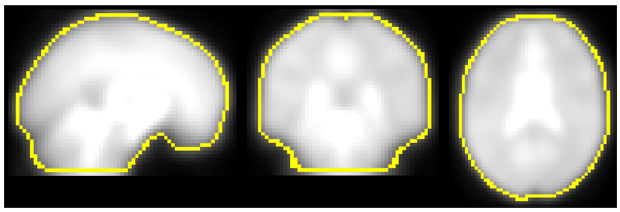

(b) Outline of (a) overlaid on average of *before* ICA-fNORM fMRI data

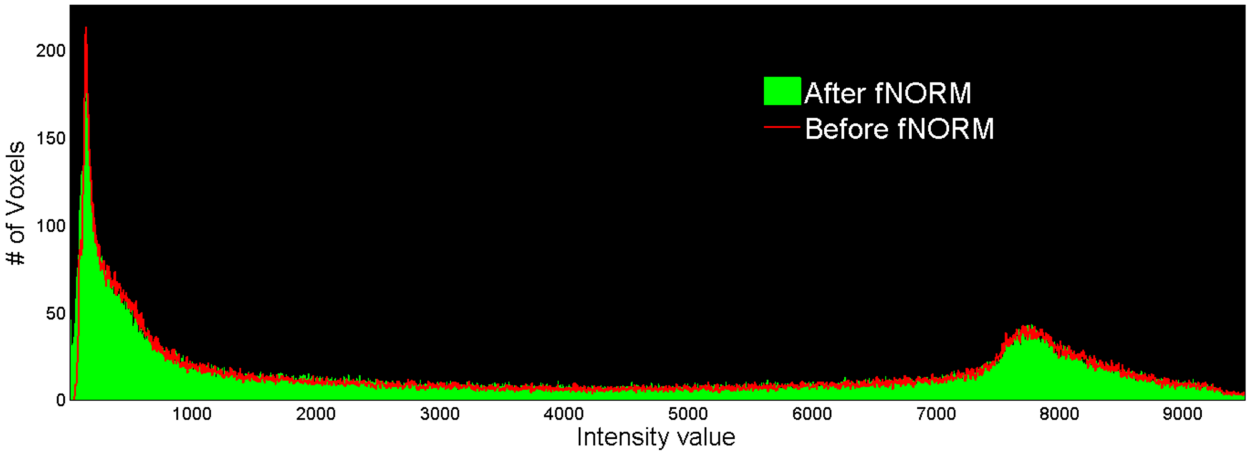

(c) Histograms of (a) and (b)

Figure 3.6: Averaged data from all 28 subjects in three orthogonal views corresponding to the two methods under comparison: (a) *After* ICA-fNORM, (b) *Before* ICA-fNORM with overlaid boundaries extracted from images in (a), (c) Intensity histograms corresponding to images presented in (a) and (b).

Prior to presenting the statistical improvements introduced by ICA-fNORM, the similarities in shape, size and contrast differences between the data obtained before and after application of ICA-fNORM are demonstrated. Global differences in shape and size introduced by ICA-fNORM

at an individual level are visible only in a few areas as seen from the mean images estimated by averaging all volumes from all subjects (Figure 3.6). Thus, there is minimal distortion in terms of shape, size and intensity values. The outline of the mean image of the preprocessed fMRI data (from 28 subjects) *after* ICA-fNORM is overlaid on the *before* ICA-fNORM mean image as shown in Figure 3.6b. The outline was computed using 80 percent of the mean intensity value from Figure 3.6a. The overall shape of the brain is preserved and only a few differences are seen near the areas that are sensitive to magnetic susceptibility artifacts. Also, there is little variation in intensities introduced by ICA-fNORM, mostly at very low intensity values as seen from the histograms in Figure 3.6c estimated using images from Figure 3.6a and (b).

3.5.2 Spatial Overlap and Differential analysis

Group activation patterns were extracted using a one-sample t-test on each subject's activation maps obtained after - (a) first level GLM analysis built into SPM5 and (b) group ICA, both applied to the functionally re-aligned (*after* ICA-fNORM) and regularly processed (*before* ICA-fNORM) AOD data separately. The two main advantages of the proposed approach that were observed irrespective of the analysis method (GLM or ICA) used, were higher t-statistics for the same voxel locations and more number of significant voxels that seemed to fill in possibly task-modulated regions that showed little significance before applying ICA-fNORM. We investigated the effects of applying ICA-fNORM using different templates - (a) TL_{rest} and (2) DMN_{rest} . These were compared against the results corresponding to regularly processed data, that is, when ICA-fNORM was not applied.

General Linear Model

Group activation t-maps (n = 28) obtained after the group GLM analysis of the two data sets (*before* and *after* ICA-fNORM) were overlaid for the target condition and presented in Figure 3.7. Each color on the map represents whether a voxel passed the significance threshold ($t > 6$) using either or both methods under comparison. Overlapping and differential areas seen in Figure 3.7a depict several differences introduced by mapping the data with ICA-fNORM and TL_{rest} intrinsic

network, with the following two as the most clearly observable. Firstly, some small clusters were found to be absent in either of the two approaches in addition to some new voxels that filled the gaps between neighboring active clusters, thus affecting detection sensitivity. Secondly, the number of significant voxels (thresholds range as $4 < t < 10$) obtained *after* ICA-fNORM were notably larger (maximum of 300 voxels) than those *before* ICA-fNORM for both the templates.

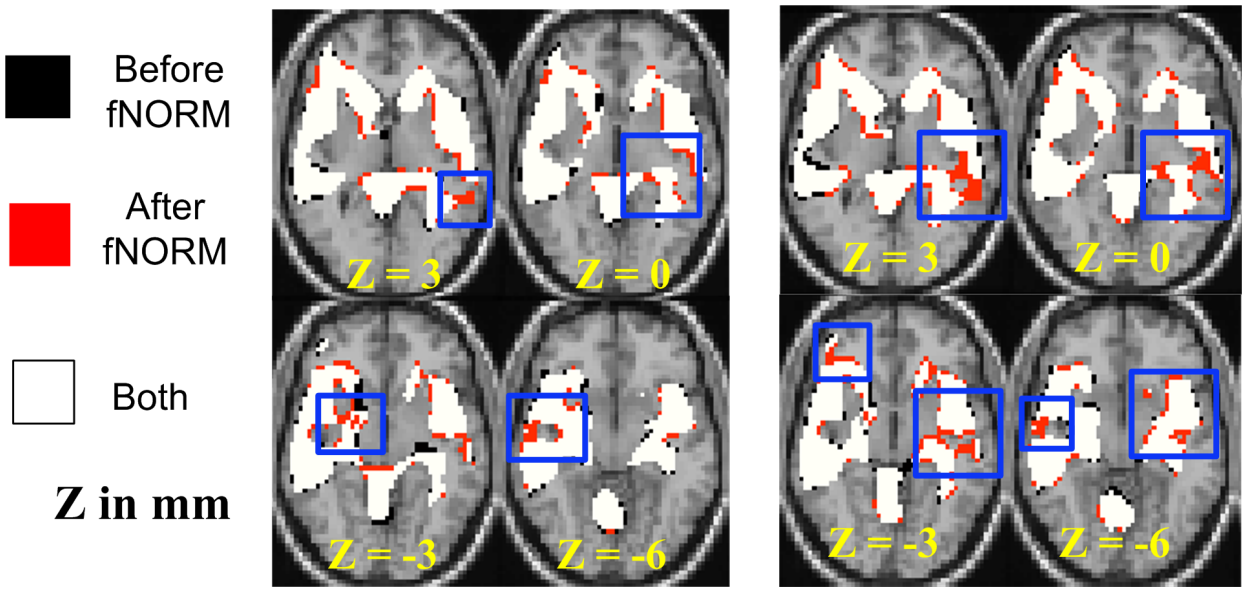

(a) TL_{rest} (b) DMN_{rest}

Figure 3.7: Thresholded activation maps ($t > 6$, $p < 0.0001$) for the target condition from the GLM analysis (n = 28) showing overlapping and differential regions obtained *before* and *after* ICA-fNORM of AOD data done using different templates: (a) TL_{rest} , (b) DMN_{rest} . Each method is indicated using different colors: (i) red - *after* ICA fNORM; (ii) black - *before* ICA-fNORM; and (iii) white - active in both (i) and (ii). The functional maps were overlaid on a re-sliced and co-registered anatomical template in SPM.

A similar comparison was done for the t-maps obtained by analyzing the AOD data *after* ICA-fNORM using the DMN_{rest} template. Overlapping and differential areas of activation for this particular case are presented in Figure 3.7b. Additional voxels (marked red) form contiguous connections between previously unconnected neighboring activations (see slice Z = 3 mm), which was also our first major observation from Figure 3.7a. Secondly, there were a few small clusters where either of the methods have little or no significant voxels present. Overall, the number of significantly active voxels is considerably greater in t-maps estimated after ICA-fNORM.

Independent Component Analysis (ICA)

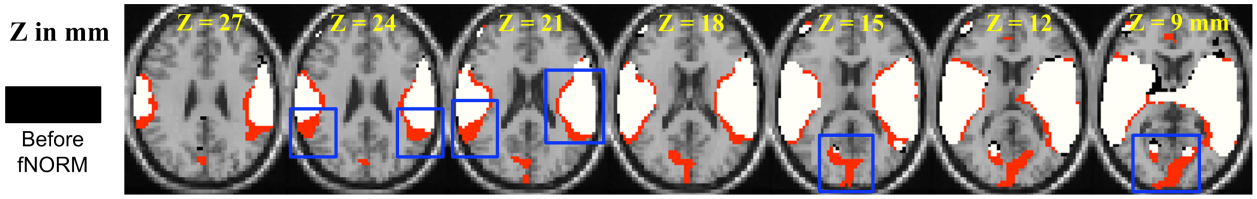

(a) TL_{rest}

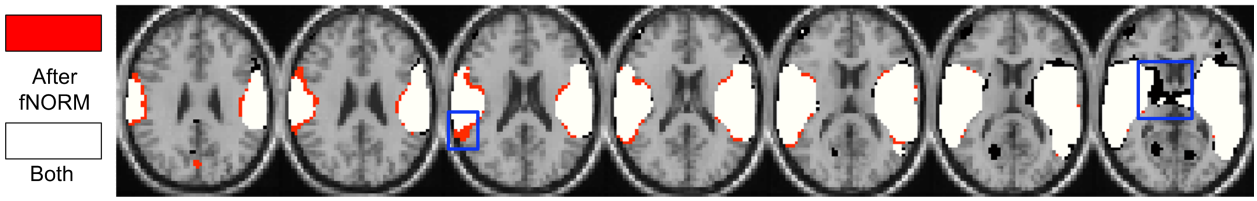

(b) DMN_{rest}

Figure 3.8: Thresholded activation maps ($t > 6$, $p < 0.0001$) for the TL_{AOD} component from ICA analysis (n = 28) showing overlapping and differential regions obtained *before* and *after* ICA-fNORM of AOD data done using different templates: (a) TL_{rest} , (b) DMN_{rest} . Each method is indicated using different colors: (i) red - *after* ICA fNORM; (ii) black - *before* ICA-fNORM; and (iii) white - voxels active in both (i) and (ii). The functional maps were overlaid on a re-sliced and co-registered anatomical template available within in SPM.

The second method used to analyze the effects of functional normalization on task data (AOD) is group independent component analysis (Calhoun, et al. 2001). Note that the same method was applied to the resting state fMRI data in order to derive the functional templates (TLrest and DMNrest) from the resulting independent components. Here, the order was set to N = 20 and the primary task-related component (termed TL_{AOD} hereafter) is selected for spatial overlap and region of interest analysis. The t-map for TL_{AOD} was extracted by performing a one-sample t-test on all 28 back-reconstructed subject-specific maps corresponding to this particular component. These t-maps correspond to ICA component maps estimated separately for the two data sets (before and after ICA-fNORM) as presented in Figure 3.8. The main observation from Figure 3.8 is appearance of new clusters of significant voxels (in red) that failed the threshold (t > 6) prior to functional normalization. Also some small and medium-sized clusters were found absent in either of the two approaches. Most new voxels appear along boundaries of activation regions already detected before applying ICA-fNORM (in white and black) as seen in Figure 3.8a. This was a direct result of

re-aligning subjects to a common functional space, in turn improving the detection sensitivity of the t-test performed on that group of subjects.

A reverse effect is observed in Figure 3.8b which corresponds to functional normalization performed using the DMN_{rest} template. Voxels around the boundaries belong to the *before* maps in most slices in Figure 3.8b, thus showing the inhibitive nature of the DMN towards positively task-modulated functional systems. Such modulating behavior along functional boundaries was recently illustrated in Mennes et al. (2010) where they utilized the resting state functional boundaries to predict BOLD fMRI task activity. Our experiment provides further evidence that the most cross-linked relationships between different networks exist along the boundaries of these systems and may be utilized favorably to improve the resultant statistics.

3.5.3 Difference *Threshogram* Analysis

Next, we compare the results obtained *before* and *after* ICA-fNORM by subtracting the t-maps (*after* - *before*) corresponding to multiple thresholds. The resulting graphic is called a difference threshogram as the information presented through it suggests. The process was repeated for results corresponding to each analysis method used (GLM and ICA) as well as each functional template utilized in ICA-fNORM. Voxels corresponding to the primary task-modulated region-of-interest, that is, the temporal lobe, were extracted using a mask constructed from the Wake Forest University Pick-atlas (WFU-Pick Atlas) (Lancaster et al., 2000). The masked t-maps for the *before* and *after* images were subtracted and thresholded using a range of thresholds.

The aforementioned steps were first applied on t-maps obtained through GLM analysis. Figure 3.9a and 3.9b show the difference threshograms under the target condition for the whole brain (left column) and the temporal lobe (right column) corresponding to the TL_{rest} and DMN_{rest} templates respectively. Application of ICA-fNORM clearly helps improve the statistics as seen from the large positive change in number of voxels over different thresholds.

An approach similar to the one used to estimate the threshograms in Figure 3.9, is followed for computing the difference threshograms for the ICA component (TL_{AOD}) t-maps . Threshograms corresponding to the whole brain and the task-relevant ROI, *i.e.* the temporal lobe, are presented

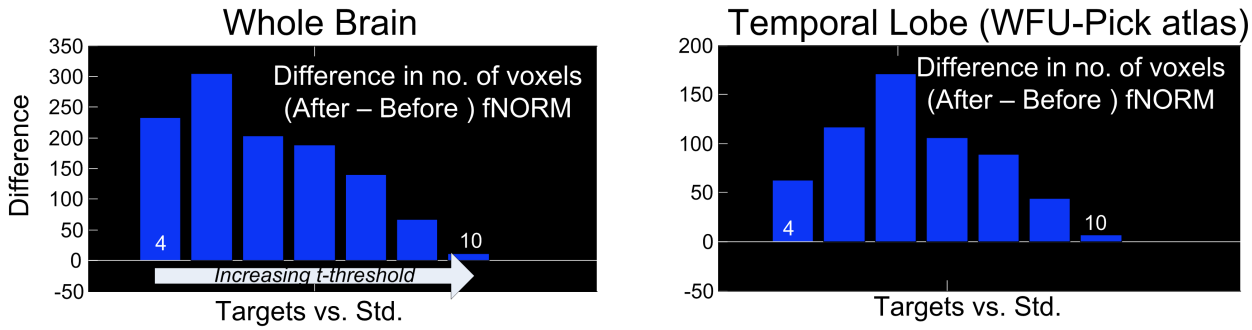

(a) TL_{rest}

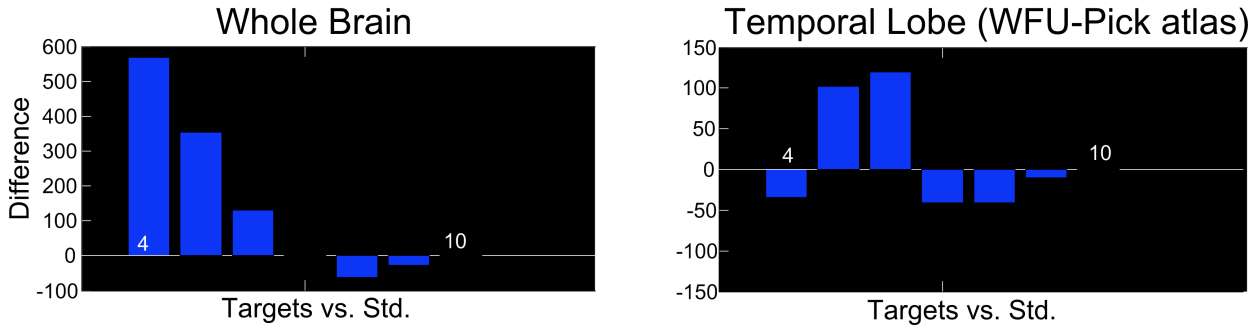

(b) DMN_{rest}

Figure 3.9: Difference threshograms derived by subtracting the *after* and *before* ICA-fNORM t-maps for the target condition estimated through GLM analysis. The bars correspond to number of voxels gained (*y-axis*) after ICA-fNORM for increasing t-threshold (*x-axis*). Differences are presented for **whole brain** (left) and **temporal lobe ROI** extracted using WFU Pick Atlas (right) for each template: (a) TL_{rest} and (b) DMN_{rest} .

separately in Figure 3.10. The maximum change is seen in case of TLrest at $t > 15$ (854 voxels for whole brain; 739 voxels within the temporal lobe) as seen from the threshograms in Figure 3.10a. The peaks were observed at a low t-threshold ($t > 6$), with gradual increase until attaining the maximum height at $t > 15$, eventually decaying to lowest height at the maximum t-threshold ($t > 30$). Such behavior was observed in both threshograms presented in Figure 3.10a. Thus, t-statistics improved consistently across the task-engaged region after application of ICA-fNORM with TL_{rest} .

In the case of the DMN_{rest} template, a bimodal type of pattern is observed from the difference threshograms as seen in Figure 3.10b. Initially, there is a large decrease in the number of voxels (after vs. before ICA-fNORM) over lower thresholds, but our method appears to gain more at

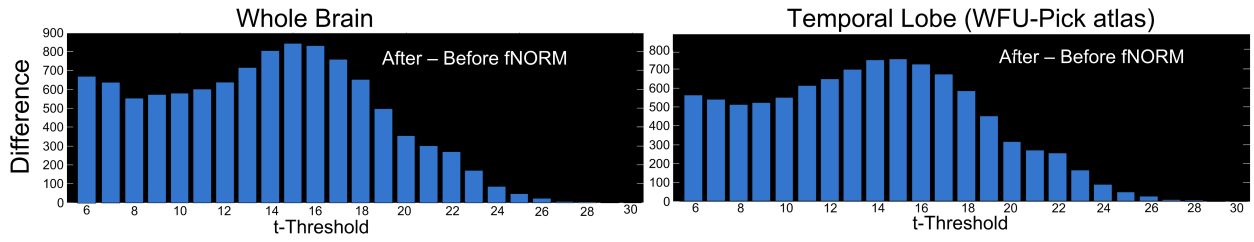

(a) TL_{rest}

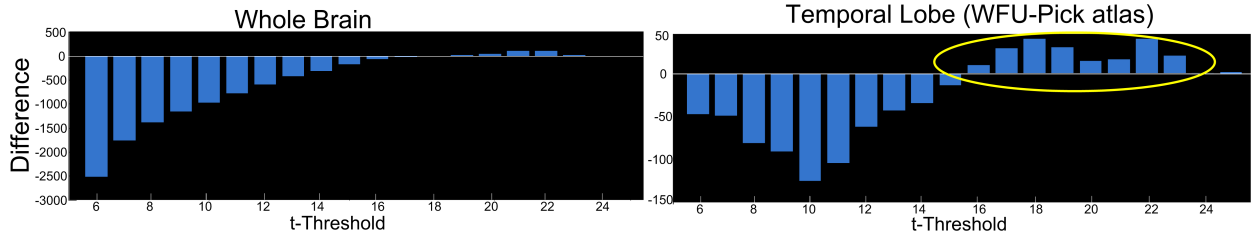

(b) DMN_{rest}

Figure 3.10: Difference threshograms derived by subtracting the *after* and *before* ICA-fNORM t-maps for the TL_{AOD} component estimated through ICA. The bars correspond to number of voxels gained (*y-axis*) after ICA-fNORM for increasing t-threshold (*x-axis*). Differences are presented for **whole brain** (left) and **temporal lobe ROI** extracted using WFU Pick Atlas (right) for each template: (a) TL_{rest} and (b) DMN_{rest} .

higher thresholds ($t > 15$) as seen from the ROI threshogram (right column) in Figure 3.10b. This can be attributed to the approximate shapes of the t-value distribution in an activation map (originally derived from an independent component).

3.5.4 Region-of-Interest Analysis

To provide further insight into the differences between *before* and *after* ICA-fNORM results, the activation maps were analyzed using the automatic anatomical labeling (AAL) atlas (Tzourio-Mazoyer et al., 2002) and ROI labels of most significant voxels. Prior to ROI analysis, the activation maps were corrected for multiple comparisons ($p < 0.01$) and eventually thresholded ($t > 6$). We estimated the location of maxima (x, y, z), mean t-value, maximum t-value , and number of significant voxels above the threshold, for all regions labeled within the thresholded t-maps for both methods. Spatial shifts in activation foci between the two approaches were computed as the Euclidean distance (ED) between the local maxima. As in Section 3.5.2 and 3.5.3, these calculations

were repeated on results corresponding to each functional template (TL_{rest} and DMN_{rest}) for the two analysis methods (GLM and ICA).

Note that we utilized two different types of masks to generate results in Figure 3.9b and Tables 3.1 and 3.2. The former was generated using a binary mask where the bilateral temporal lobe is labeled as the only ROI and voxels qualifying the t-threshold ($t > 6$) within that region are used to generate the difference threshograms in Figure 3.9b, whereas the values in Table 3.2 were estimated using AAL atlas that contains several different regions to parcellate the functional activation maps anatomically. The motivation for using separate masks was to present the overall improvements in t-values by covering the anatomical regions that were not specific to the AAL atlas.

General Linear Model (GLM)

The results of the ROI analysis done for the target condition's t-maps are presented in Table 3.1. The results are tabulated separately based on the template used for ICA-fNORM and compared against the GLM results of regular analysis.

GLM	Before ICA-fNORM						TL$_{rest}$ (After ICA-fNORM)									DMN$_{rest}$ (After ICA-fNORM)								
Targets	x	y	z	t_{max}	t_{mean}	*voxels (t>6)*	x	y	z	t_{max}	% *Gain*	t_{mean}	% Gain	*voxels (t>6)*	% Gain	ED (in mm)	x	y	z	t_{max}	% *Gain*	t_{mean}	% Gain	*voxels(t>6)*	% Gain	ED (in mm)
L Insula	-42	-3	6	10.85	7.54	206	-42	-3	6	11.37	**4.79**	7.68	**1.86**	229	**11.17**	0	-42	-3	6	10.65	-1.84	7.44	-1.28	214	**3.88**	0
L Inferior Parietal Lobule	-54	-33	48	7.24	6.48	67	-54	-33	36	7.23	-0.14	6.54	0.93	57	-14.93	**12**	-54	-36	36	7.29	0.69	6.39	-1.37	51	-23.88	**12.37**
L Supramarginal Gyrus	-60	-24	15	8.02	7.08	162	-60	-24	15	8.56	**6.73**	7.25	**2.4**	159	-1.85	0	-51	-39	27	8.19	**2.11**	7.14	**0.83**	151	-6.79	**21.21**
L Thalamus	-12	-30	9	8.15	6.98	117	-15	-18	15	8.56	**5.03**	7.22	**3.44**	149	**27.35**	**13.75**	-12	-30	9	9.07	**11.24**	7.1	**1.76**	138	**17.95**	0
L Superior Temporal Gyrus	-45	-3	0	9.17	7.05	256	-45	-3	0	9.69	**5.67**	7.21	**2.27**	283	**10.55**	0	-45	-3	0	9.26	**0.89**	7.07	**0.2**	252	-1.56	0
L Middle Temporal Gyrus	-60	-18	0	7.47	6.43	24	-60	-18	0	7.72	**3.35**	6.49	**0.93**	38	**58.33**	0	-60	-21	0	7.77	**4.06**	6.47	**0.67**	52	**116.67**	3
L Postcentral Gyrus	-54	-21	27	8.57	6.86	48	-60	-18	15	8.53	-0.47	6.88	0.29	48	0	**13.75**	-60	-18	15	7.56	-11.8	6.61	-3.67	34	-29.17	**13.75**
R insula	48	12	-9	8.97	7.12	167	48	12	-9	9.25	**3.12**	7.33	**2.95**	175	**4.79**	0	48	12	-9	8.4	-6.33	6.93	-2.66	154	-7.78	0
R Supramarginal Gyrus	51	-39	42	7.75	6.58	63	63	-36	24	7.01	-9.55	6.28	-4.56	90	**42.86**	**21.84**	57	-30	48	7.46	-3.74	6.49	-1.37	146	**131.75**	**12.37**
R Thalamus	6	-15	15	7.57	6.69	73	21	-24	12	8.84	**16.78**	6.94	**3.74**	100	**36.99**	**17.75**	18	-24	15	8.48	**12.06**	7.04	**5.11**	95	**30.14**	**15**
R Superior Temporal Gyrus	63	-36	15	7.17	6.43	64	63	-39	18	7.21	0.56	6.46	0.47	82	**28.13**	**4.24**	63	-39	18	7.12	-0.73	6.47	0.62	89	**39.06**	**4.24**
R Middle Temporal Gyrus	48	-21	-9	7.48	6.29	59	48	-21	-9	7.33	-2.01	6.32	0.48	83	**40.68**	0	48	-21	-9	7.25	-3.08	6.29	-0.03	57	-3.39	0
					Total = 1306								**Total = 1493**										**Total = 1433**			

Table 3.1: **GLM Analysis**:Results of the ROI analysis done on target condition group level t-map (corrected for $p < 0.01$). Regions of activation (from AAL atlas), MNI coordinates (x, y, z), t-values of local maxima, averaged t-values under each label, and the activation extent (voxels for $t > 6$) obtained with the two methods under comparison: (1) before ICA-fNORM (white + black voxels in Figure 3.7a); (2) after ICA-fNORM (white + red voxels in Figure 3.7). Percentage gains for each attribute ($\boldsymbol{t}_{max}$, $\boldsymbol{t}_{mean}$, and ***voxels***) depict the improvement in t-statistics or detection sensitivity achieved by the proposed method. The results for different templates - TL$_{rest}$ and DMN$_{rest}$ are presented under different set of columns that provides a clear comparison against the results obtained before ICA-fNORM.

In the case of TL_{rest} , we found five bilaterally active regions - insula, supramarginal gyrus, thalamus, superior temporal gyrus, middle temporal gyrus, and two regions that were significant in the left brain only - inferior parietal lobule and postcentral gyrus. Percentage gains were estimated for t_{max}, t_{mean}, and *voxels* (as listed in Table 3.1), and it was observed that several regions show positive gain percentages in favor of ICA-fNORM. Regions such as the left insula (4.79%), left supramarginal gyrus, left thalamus, left superior temporal gyrus, left middle temporal gyrus, right insula and right thalamus show highest gains in tmax among all regions (highlighted in Table 3.1). A similar pattern was also observed for the mean t-values where most regions had conforming trends for t_{max} and t_{mean}. A large fall in the t-values was observed for the right supramarginal gyrus although there was a considerable increase in this region's activation volume (42.86%) after ICA-fNORM. This result was an apt example of the ability of our proposed method to improve the detection sensitivity while assisting in determining a region's significance more accurately based on the functional organization of all subjects within that particular group. Considerable increase in activation volumes was recorded for nine out of twelve regions (in bold) presented in Table 3.1, highest being for the left middle temporal gyrus (58.33%).

The group t-maps corresponding to the DMN_{rest} were also analyzed using the ROI analysis and the most significant regions reported in Table 3.1 under the DMN_{rest} columns. This experiment helped reveal higher t_{max} values for left superior temporal gyrus, left middle temporal gyrus, and left supramarginal gyrus whereas lower t_{max} values for these regions were recorded in the right half of the brain. Almost similar patterns were observed for the t_{mean} with an exception of right supramarginal gyrus and left inferior parietal lobule. As observed in the case of TL_{rest} , the right supramarginal gyrus showed the maximum increase in volume of activation even though there was a minor drop observed in the t_{max} and t_{mean} values. Other task-engaged regions such as the left middle temporal gyrus (116.67%), thalamus (L: 17.95%; R: 30.14%), and right superior temporal gyrus (39.06%) show large increases in activation.

Irrespective of the template used, the activation foci of some regions shifted considerably after applying ICA-fNORM as seen from the Euclidean distance (ED) columns in Table 3.1. The regions that experienced maximum shift in local maximum include left postcentral gyrus, right

supramarginal gyrus, right thalamus, and right superior temporal gyrus. The increase in right-sided regions can be attributed to average dominance of handedness in our data set, that is, about 73% of the subjects were right-handed.

Independent Component Analysis (ICA)

The results of the ROI analysis done for the group-level t-maps corresponding to the temporal lobe component are presented in Table 3.2. The activation maps corresponding to the primary task-positive component from functionally re-aligned AOD data (TL_{AOD}) were analyzed and ROI labels of most significant voxels were derived. The results corresponding to different templates are summarized below.

In the case of TL_{rest} , we identified eight anatomical regions out of which six showed significant bilateral activity - precentral gyrus, supramarginal gyrus, thalamus, superior temporal gyrus, middle temporal gyrus, and postcentral gyrus. Two regions - insula and inferior parietal lobule, were significant in the left brain only as presented in Table 3.2. Two regions that recorded the maximum relative percentage gain in t_{max} were the superior temporal gyrus (L: 10.51%; R: 43.87%) and the middle temporal gyrus (L: 19.36%; R: 23.37%). These anatomical regions also showed similar patterns of improvement in t_{mean} with gains as high as $\approx$ 16% (right superior temporal gyrus). However, the volumetric gains for the aforementioned regions were minimal. The maximum improvement in terms of volume was observed for supramarginal gyrus (L: 35.5%; R: 65.87%) and precentral gyrus (L: 30.65%; R: 40.74%). As an outlier, the right thalamus experienced decrease in tmax and tmean and a slight improvement in volume (10.48%).

ICA	Before ICA-fNORM						TL$_{rest}$ (After ICA-fNORM)									DMN$_{rest}$ (After ICA-fNORM)								
TL$_{AOD}$	*x*	*y*	*z*	t_{max}	t_{mean}	*voxels (t>6)*	*x*	*y*	*z*	t_{max}	*% Gain*	t_{mean}	% Gain	*voxels (t>6)*	% Gain	ED (in mm)	*x*	*y*	*z*	t_{max}	*% Gain*	t_{mean}	% Gain	*voxels(t>6)*	% Gain	ED (in mm)
L Precentral Gyrus	-60	6	21	13.42	8.27	186	-60	6	21	14.87	10.8	8.25	-0.24	243	**30.65**	0	-60	6	21	13.87	3.35	8.59	3.87	139	**-25.27**	0
L Insula	-36	-9	9	**27.07**	13.99	334	-36	-12	6	24.04	-11.19	14.15	1.14	338	1.2	4.24	-39	-15	6	24.78	-8.46	13.88	-0.79	306	-8.38	7.35
L Inferior Parietal Lobule	-51	-36	54	8.74	7.14	35	-51	-36	54	9.06	3.66	6.98	-2.24	53	51.43	0	-51	-36	54	8.91	1.95	6.91	-3.22	33	**-5.71**	**0**
L Supramarginal Gyrus	-66	-21	15	16.27	9.56	200	-60	-24	15	19.02	**16.9**	10.41	**8.89**	271	**35.5**	**6.71**	-60	-24	15	18.12	**11.37**	9.85	**3.03**	223	**11.5**	**6.71**
L Thalamus	-6	-15	6	19.23	11.74	164	-12	-21	3	20.17	**4.89**	12.41	**5.71**	181	**10.37**	**9**	-9	-18	3	17.03	-11.44	10.8	-8.01	143	-12.8	5.2
L Superior Temporal Gyrus	-57	-9	6	24.36	15.67	559	-51	-18	0	26.92	**10.51**	18.06	**15.25**	559	0	**12.37**	-45	-21	3	25.39	**4.23**	15.59	**-0.51**	557	**-0.36**	**17.23**
L Middle Temporal Gyrus	-54	-18	0	23.04	11.59	879	-54	-18	-3	27.5	**19.36**	13.15	**13.46**	921	**4.78**	**3**	-48	-21	-3	24.12	4.69	11.24	-3.02	773	-12.06	**7.35**
L Postcentral Gyrus	-60	-12	15	18.79	9.36	519	-60	-12	15	20.61	**9.69**	10.17	**8.65**	577	**11.18**	0	-57	-15	15	18.95	0.85	9.94	6.2	482	-7.13	**4.24**
R Precentral Gyrus	60	3	18	9.06	7	54	60	3	18	10.5	**15.89**	7.37	**5.29**	76	**40.74**	0	60	3	18	11.24	**24.06**	7.49	**7**	82	**51.85**	0
R Supramarginal Gyrus	54	-24	18	19.97	9.2	126	57	-27	18	22.31	**11.72**	10.13	**10.11**	209	**65.87**	**4.24**	54	-24	18	19.55	**-2.1**	9.61	**4.46**	177	**40.48**	0
R Thalamus	6	-18	3	15.86	10.31	124	6	-18	3	14.69	-7.38	9.86	-4.36	137	10.48	0	9	-15	3	12.72	-19.8	8.64	-16.2	100	-19.35	4.24
R Superior Temporal Gyrus	63	-33	9	21.79	15.1	681	51	-15	-9	**31.35**	**43.87**	17.51	**15.96**	689	**1.17**	**28.14**	66	-27	0	**26.52**	**21.71**	15.39	**1.92**	684	**0.44**	**11.22**
R Middle Temporal Gyrus	63	-30	0	21.57	11.81	650	51	-12	-12	26.61	**23.37**	12.97	**9.82**	678	**4.31**	**24.74**	63	-30	0	26.11	**21.05**	11.41	**-3.39**	583	**-10.31**	0
R Postcentral Gyrus	63	-15	15	14.38	8.13	242	63	-15	15	16.83	**17.04**	8.92	**9.72**	210	-13.22	0	63	-15	15	16.89	**17.45**	8.78	**8**	209	-13.64	0
					Total = 4753								**Total = 5142**										**Total = 4491**			

Table 3.2: Activation labels within the t-map of the TL$_{AOD}$ component (correct $p < 0.01$) sorted in to anatomical labels (AAL) and the respective details: MNI coordinates (x, y, z), t-values of local maxima, averaged t-values , and activation extent (voxels for $t > 6$), estimated for each of the two methods under comparison: (1) before ICA-fNORM (white + black voxels in Figure 3.8); (2) after ICA-fNORM (white + red voxels in Figure 3.8). Percentage gains for each attribute ($\boldsymbol{t}_{max}$, $\boldsymbol{t}_{mean}$, and ***voxels***) depict the improvement in t-statistics or detection sensitivity achieved by the proposed method. The results for different templates - TL$_{rest}$ and DMN$_{rest}$ are presented under different set of columns that provides a clear comparison against the results obtained before ICA-fNORM.

Interestingly, the global maximum for regularly processed data was observed within the left insula. Whereas, the global maximum for functionally re-aligned data was found in a more highly task-engaged region, that is, the right superior temporal gyrus (highlighted in Table 3.2) alongside highest improvement in mean t-value . Euclidean distance measures (TL_{rest}) shown in Table 3.2 indicated maximum shift of the activation foci for two regions that also showed consistent improvement in rest of the statistics - right superior temporal gyrus ($28.14mm$) and the right middle temporal gyrus ($24.74mm$). A slightly different pattern was observed, in the case of DMN_{rest} template, where large shifts in activation foci were observed for the left superior ($17.23mm$) and middle temporal gyrus ($7.35mm$), right superior temporal gyrus ($11.22mm$) but no change for right middle temporal gyrus. In addition to the above regions, more than half other regions reported in Table 3.2 showed significant shifts in activation foci for of both the templates.

In case of the DMN_{rest} template, we used two different thresholds to perform the ROI analysis separately. The two thresholds used for this experiment were $t > 6$ (Table 3.2) and $t > 16$ (Table 3.3). The choice of higher threshold is attributed to the peak observed at $t > 16$ in threshograms. A reasonable explanation for performing a multi-threshold analysis can be justified through the bipolar nature observed in Figure 3.10b. An expected but interesting pattern was observed after analyzing the component t-maps using multiple thresholds.

Threshold - $t > 6$: Although minor, several regions showed negative gain (decreases) in t_{mean} values after ICA-fNORM with exceptions of precentral gyrus, postcentral gyrus, supramarginal gyrus and right superior temporal gyrus. Similar pattern was observed in volume calculations with exceptions of supramarginal gyrus (L: 11.5%; R: 40.58%) and right precentral gyrus (51.85%) indicating enlarged activation volume. However, large improvements in local maxima were observed for all regions other than the thalamus region as reported in Table 3.2.

Threshold - $t > 16$: Regions with significant differences at this threshold are presented in Table 3.3 separately. Considerable percent gain was observed in t_{mean} and volume for the primary task engaged regions reported here. The superior temporal gyrus (L: 1.54%, R: 16.67%), left middle temporal gyrus (22.54%) and supramarginal gyrus (L: 200%; R: 16.67%)

showed large gain in activation volume. Thus, at higher significance levels, the DMN_{rest} template has more impact on the functional boundaries of primary task-engaging regions. This section provided evidence showing how ICA-fNORM, using functional information from

ICA	Before ICA-fNORM					DMN_{rest} (After ICA-fNORM)							
TL_{AOD}	*x*	*y*	*z*	t_{mean}	*voxels (t>16)*	*x*	*y*	*z*	t_{mean}	% Gain	*voxels (t>16)*	% Gain	ED (in mm)
L Supramarginal Gyrus	-66	-21	15	16.24	2	-60	-24	15	17.3	**6.53**	6	**200**	**6.71**
L Superior Temporal Gyrus	-57	-9	6	19.13	260	-45	-21	3	19.8	**3.5**	264	**1.54**	**17.23**
L Middle Temporal Gyrus	-54	-18	0	18.15	71	-48	-21	-3	18.8	**3.58**	87	**22.54**	**7.35**
L Postcentral Gyrus	-60	-12	15	17.46	14	-57	-15	15	17.33	-0.74	21	**50**	**4.24**
R Supramarginal Gyrus	54	-24	18	17.77	6	54	-24	18	17.85	**0.45**	7	**16.67**	0
R Superior Temporal Gyrus	63	-33	9	18.49	295	66	-27	0	18.46	-0.16	325	**10.17**	**11.22**
R Middle Temporal Gyrus	63	-30	0	18.01	90	63	-30	0	18.91	**5**	83	-7.78	0
				Total = 738						**Total = 793**			

Table 3.3: Activation labels and other attributes estimated using a higher threshold ($t>$ 16) for t-maps corresponding to ICA-fNORM using DMN_{rest} template. We utilized multiple thresholds to depict the differences in regional activity and highlight the advantages of ICA-fNORM (using this particular template). Table 2 shows the results corresponding to t-maps thresholded at t ¿6 and this table shows the results for t-maps thresholded at t ¿16. Note that the tmax values do not depend on the threshold used, thus omitted from being reported here.

two intrinsic networks, can help improve various aspects of post-analysis results such as t-statistics and detection sensitivity and possibly help identify differences in region-wise activity that may not be noticed otherwise.

3.5.5 Transition Regions

In results presented so far, the most consistent post ICA-fNORM differences in spatial maps were observed around the edges of activation regions. These observations partially concur with recent work (Mennes et al., 2010) that presented evidence regarding strong spatial associations, known as transition zones, that exist between regions representing resting state dynamics and those active during a cognitive task. After doing a selective threshold

analysis (see Figure 3.11), we observed differences around regions that conformed the recent findings (Mennes et al., 2010) about interactions between various cognitive states. In Figure 3.11, some major regional differences occurring at various levels of significance are shown by utilizing the t-maps presented for TL_{AOD} (Figure 3.8a) and different intervals of t-thresholds to divide them into boundary-type representations at various levels of statistical significance. It was already clear from Figure 3.9 that more voxels appear to be significant ($t > 6$) after application of ICA-fNORM. Whereas Figure 3.11 is focused on the distribution of voxels around edges at various levels of significance (starting at $t > 4$), thus establishing favorable relationship between the intrinsic networks from resting state and functional systems involved in cognitive-task processing. Other than transitions occurring around edges, several small clusters of active voxels exist at high range thresholds indicating activity that went undetected prior to ICA-fNORM. The new regions were detected only after involving the intrinsic systems of each subject's brain and re-aligning them with respect to the functional properties of that group.

3.6 Discussion

In this chapter, we presented a new framework for functional normalization using resting state networks. We provided evidence suggesting that the proposed algorithm assists in improving the statistical results of activation patterns extracted from task-fMRI data. Temporally coherent intrinsic networks were treated as a basis set depicting functional boundaries of an individual's brain (rest-fMRI) and successfully utilized to re-align the same individual's data acquired while they performed a cognitive task. Thus, each individual's task data was brought to a standard space by warping it based on spatial variations in functional domains relative to the group. The improvement in statistics led to a more informed inference about the functional involvement of various regions as compared to what was known before application of ICA-fNORM.

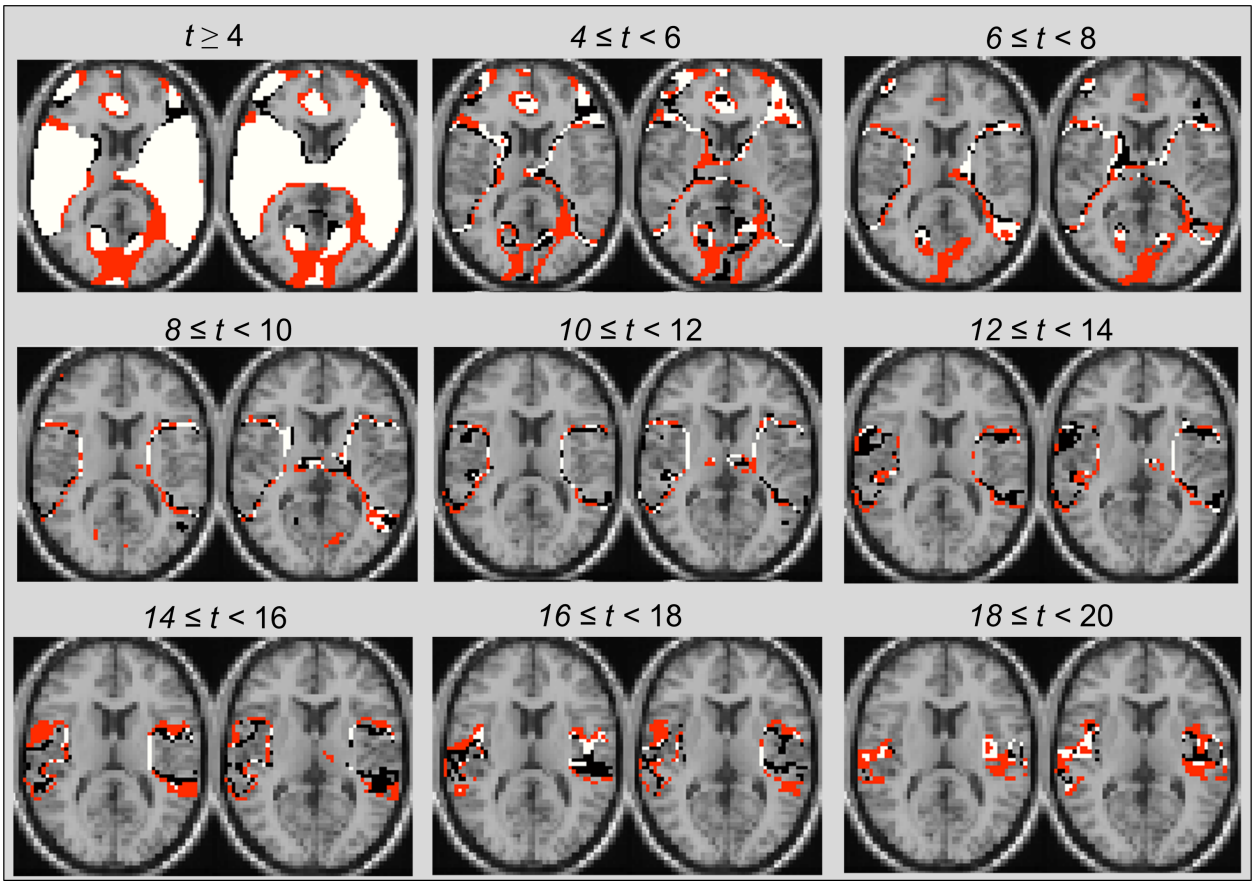

Figure 3.11: Illustration of *transition* zones using range-thresholding of the primary task-positive component t-map obtained through group-ICA. All voxels are labeled based on the method - (i) 'black': Before ICA-fNORM, (ii) 'red': After ICA-fNORM, and (iii) white - voxels active in both (i) and (ii). Most edge-based differences are seen at lower and middle-range thresholds whereas large cluster-based differences are seen at high thresholds.

The different fMRI images obtained from the two approaches (*before* and *after* ICA-fNORM) were first seen to be different through minor changes observed in the histograms presented in Figure 3.6. There was minimal morphological distortion and minor changes in the shape of the brain after proper application of functional normalization (see Section 3.5.1 for a discussion of the need to reset the affine transformation to an identity matrix). Therefore, the proposed algorithm re-aligns the task fMRI data without introducing large morphological or intensity variations in the resulting images.

3.6.1 Enhanced Detection Sensitivity

Analysis of the functionally re-aligned AOD data showed larger activation volumes. This result was further supported by metrics computed using t-maps from the two analysis methods (ICA and GLM). In order to compare the results on a global scale, difference threshograms were presented for each template in Figure 3.9 (GLM) and Figure 3.10 (ICA).

Comparisons based on GLM analysis revealed substantial differences in spatial properties of activation. Spatial analysis of t-maps demonstrated large overlapping and differential areas of activation for either or both methods (Figure 3.7). Application of ICA-fNORM resulted in considerably greater number of voxels being active at high levels of significance. These voxels mostly existed as small clusters or edges around regions active prior to ICA-fNORM, especially around the supramarginal gyrus, superior and middle temporal regions, and the thalamus. Such spatial behavior was observed irrespective of the functional template (TL_{rest} or DMN_{rest}) used for normalization. More prominent shape of the temporal lobe was observed in case of activation components derived using ICA as compared to the t-maps derived using GLM. However, the two methods share the primary spatial characteristics of activation patterns observed, that is, the differences introduced after ICA-fNORM mostly exist around edges and in the form of small overlapping clusters as seen from Figures 3.7 and 3.8. For the ICA results, the t-statistics improved consistently across the task-engaged region after application of ICA-fNORM for the TL_{rest} template. However, a different behavior was observed in case of DMN_{rest} which exhibited decreasing differences until a certain threshold ($t > 15$), followed by a positive gain at higher t-values . The transitions from negative to positive gain occur at $t = 15$ which is also the peak threshold in case of TL_{rest} . To further support these findings, a brief discussion on transition zones alongside thresholded representations of ICA component map was provided in Section 3.5.5 where we demonstrated that there were an increasing number of voxels showing differences at high threshold levels.

It is possible that changes in activation extent (Figure 3.9 and 3.10) in group analysis can be a result of complicated interactions between individual subject's activation boundaries

during the functional normalization performed using SPM's spatial normalization routine (low dimensional non-linear basis functions). However, significant improvements in statistics were observed even in regions that were spatially distant from the region(s) used for functional normalization, for *e.g.* , ICA-fNORM with DMN_{rest} improved statistics for regions active within the temporal lobe. This provides initial evidence to suggest that there are undiscovered relationships between the intrinsic functional organization of an individual's brain and the manner it deploys resources to process a cognitive task.

3.6.2 Default Mode Network and ICA-fNORM

Several studies in the past have shown the deactivation patterns in the DMN to be associated with regions routinely exhibiting positively task-modulated patterns (Fox et al., 2005, Raichle et al., 2001). Even though DMN is known to be negatively modulated during a task, we hypothesized that the spatial boundaries of an individual's DMN during rest can be used to re-align the functional boundaries corresponding to the same brain while it performs a cognitive task.

We bolstered our argument relating intrinsic functional boundaries and task related statistics by presenting results obtained after applying ICA-fNORM using an intrinsic network (DMN_{rest}) that is known to be deactivated during a task (see Sections 3.5.2 - 3.5.4). In addition to being negatively task-modulated, the DMN_{rest} template does not spatially correlate with the positively task-modulated region (temporal lobe) and yet we observe large improvements in a statistical sense (Tables 3.1 and 3.2) and in detection sensitivity (Figures 3.7- 3.10). The improvements in detection sensitivity were rather obvious from the results corresponding to the GLM analysis (Figures 3.7 and 3.9). However, a relatively contrasting result in ICA analysis was observed for the case when the DMNrest template was utilized for re-alignment. The number of significantly active voxels demonstrated negative gain for relatively lower ($6 < t < 15$) and positive gain for higher ($t > 16$) thresholds

(see Figure 3.9, and Tables 3.2-3.3). We hypothesize that re-alignment with warp parameters based on DMN_{rest} leads to complimentary interactions with the task-engaged region (temporal lobe) at a global level. This led to improvement in statistics especially at higher t-values . Such a behavior can reveal initial information regarding the DMN's boundaries being more interactive with voxels that were of high significance in the majority of subjects, and thus being highly significant at a group level. By individually warping each subject's DMN_{rest} network to the group mean, our method was able to compensate for the inter-subject variability in activation boundaries for this particular network. As a result, the statistics and detection sensitivity increased considerably at a group level, irrespective of the type of template used for normalization.

3.6.3 Intra-group regional dependencies revealed by ICA-fNORM

The spatial analysis done using histograms and overlapping t-maps did not reveal information about anatomical regions that experienced change, large or small, after functional normalization. In order to specifically label the anatomical regions that comprise the activation patterns obtained after different methods of normalization, we applied an ROI analysis on activation t-maps from GLM and ICA as presented in Sections 3.5.4 and 3.5.4. This revealed further details about the specific improvements in certain statistical features that were helpful in supporting the utility of our proposed method. Using this ROI analysis, it was discovered that certain regions such as the thalamus, superior and middle temporal gyrus, supramarginal gyrus, and precentral gyrus demonstrated consistent improvements in number of significant voxels, mean t-values and local maximum, across both analysis methods (GLM and ICA). In case of task-positive template (TL_{rest}), most identified regions show consistent percentage gain in t_{max} and t_{mean} values irrespective of the analysis method used as seen in Tables 3.1-3.3. However, in the case of DMNrest template, the two regions also identified as the primary task-engaged regions - (1) superior temporal gyrus, and (2) middle temporal gyrus, stood out in terms of improvement in local maxima and mean t-values

irrespective of the method used. Another striking change observed as a result of applying ICA-fNORM was the shift in the location of the global maximum (tmax) of the TLAOD component from the insula to the superior temporal gyrus. The latter region, in addition to the middle temporal gyrus, is known to be relatively more engaged in processing the auditory stimulus (targets) presented randomly during the AOD task (Kiehl et al., 2005). Thus, the new location of the global maximum is more intuitive and anatomically relevant to the task at hand as compared to the results observed before (see Table 3.2). These changes suggest that intrinsic functional systems within the brain are capable of compensating for the inter-subject variation in functional properties. Thus, the above observations further strengthen the undiscovered, but statistically favorable relationships between the boundaries of intrinsically and variably modulated functional systems with task-modulated regions of highest significance within each individual. Hence, the results (Tables 3.1-3.3) suggest our method may provide relatively more accurate information regarding the location of activation maxima, voxels and boundaries involved in processing the task stimuli.

3.6.4 Inter-group differences: Controls vs. Patients

One of the primary motivation for studying the human brain is to discover disease-specific bio-markers that are consistent and distinguishable from other signs of abnormalities in the brain. The specificity of such activations sites is the key to diagnosis and appropriate targeted drug treatment. To advance the above goal, we present supporting evidence with respect to use of the proposed ICA-fNORM technique to better identify differences between a group of healthy controls (HC), also used above, and schizophrenia subjects (SZ).

To start with, resting state networks are derived by applying group ICA on a total of 55 subjects (28 HC, and 27 SZ). The temporal lobe component (TL_{rest}) is selected manually followed by estimation of normalization parameters for each subject using their respective back-reconstructed subject-specific temporal lobe component maps. A 2 sample t-test is conducted on the temporal lobe component and corrected for multiple comparisons. The

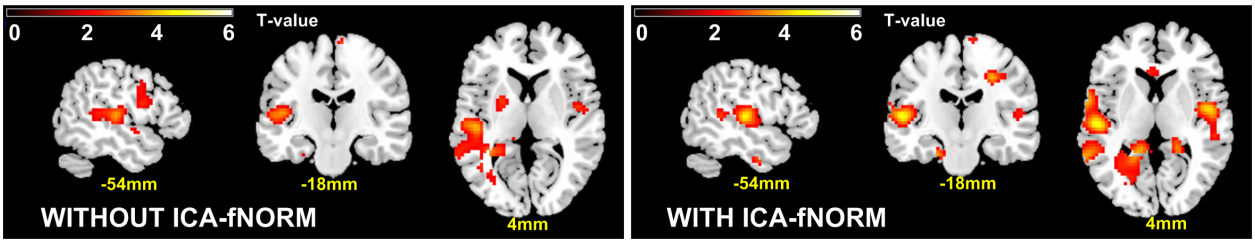

(a) HC>SZ

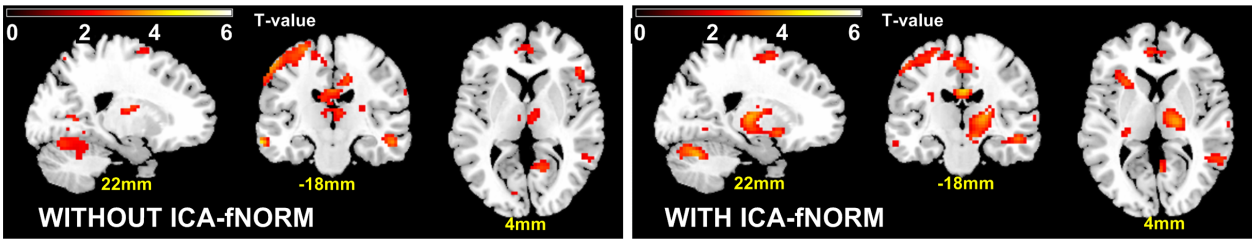

(b) SZ>HC

Figure 3.12: A multi-group comparison shows significant differences between patients and controls within the temporal lobe component (TL_{AOD}) derived through group-ICA done with and without functional normalization. The results reveal positive differences for (a) **HC>SZ** and (b) **SZ>HC**.

thresholded map indicating significant regions is presented in Figure 3.12 for two different conditions - HC > SZ and SZ > HC. A cluster-based FDR correction was performed with $p - value < 0.001$ and the voxels seen active in Figure 3.12 are within the range $[2, 6]$, although they are scaled between $[0, 6]$ for absolute comparison.

It is evident from the comparison in Figure 3.12 that ICA-fNORM reveals significant differences between the two groups. There are certainly a greater number of voxels that appear to be active in healthy controls vs. Schizophrenia subjects. These findings are in agreement with those observed by Calhoun et al. (2008), Kiehl et al. (2005). The patients show reduced activation around the temporal lobe. This can be credited to better alignment of the AOD data with the help of warps representing the functional organizations of different brains, in this case, controls and patients.

3.6.5 Other Experiments with ICA-fNORM

We believe that applying ICA-fNORM to the rest-fMRI data using the resting state networks that are derived from the same data set might assist in making better decisions about functional network connectivity and also reveal new regions that have significant connections that were previously averaged out due to inter-subject functional variability. Three substantial reasons for why we used AOD-fMRI were, 1) to validate the approach on an independently acquired data set, 2) to show that the intrinsic networks at rest can be used to spatially normalize the intrinsic networks at work, and 3) to use both GLM and ICA to validate the framework on task data that has a specific temporal pattern associated with it in contrast to the low-frequency fluctuations within resting state networks. On the other hand, the notion of using activation networks from the task data set to re-align the same data may theoretically be considered a valid approach but it is more susceptible to circular analysis (double-dipping) type of concerns that may in turn bias the final results. However, the work by Sabuncu et al. (2009) has revealed that using two different tasks, known to engage similar brain regions, for functional re-alignment can convincingly improve the statistical significance of the regions involved in performing the task. This work provided initial evidence that cross-utilization of information from multiple data sets could be used in order to make more informed inference about the patterns of neural activity.

3.7 Methodological Limitations & Future Work

3.7.1 Subject-level Improvements: A Pragmatic Explanation

When studying a group of subjects, it is a known fact that structure and function are not always tightly coupled. Perfect registration of structure does not imply the same for regions that perform similar functions in different individuals. In this paper we introduced a novel framework that utilized resting state networks to derive a functionally standard space specific for a group of subjects. This process revealed interesting positive and negative relationships

between various intrinsic resting networks and regions involved in performing a task. In this section we discuss a few methodological limitations and present possible reasoning and arguments.

A noteworthy issue with the current model used to derive the non-linear warps is its property of being non-invertible, thus making it difficult to transfer the results from template space to subjects' individual co-ordinates. An alternative to compute inverse deformation fields that exists within SPM5 uses symmetric priors and group-specific averages to compute mappings efficiently (Ashburner and Friston, 2000). We plan to experiment with inverse deformations and other algorithms that generate invertible mappings as part of our future work. Another possible problem that may arise as a result of non-linear warping is unnecessary spatial expansion of certain regions, especially the ones corresponding to high loading values in the resting-state ICA templates used for registration. To further explore this issue, subject-specific activation maps obtained after ICA (temporal lobe component) of AOD data are overlaid and compared in Figure 3.13. Different colors in Figure 3.13 represent the number of subjects with that particular voxel active. Regions with the most striking differences between before and after ICA-fNORM results exist near the center of activation regions where most subjects have significantly active ($\mathbf{Z} > 3$) voxels. This finding is further illustrated in Figure 3.13b where voxels that are significant ($\mathbf{Z} > 3$) in all 28 subjects are shown separately using an axial rendering. These differences help establish the fact that there is certain improvement in functional significance of centrally located voxels across all subjects without introducing a large number of false positives (expected due to non-linear registration) within the activation region (see Fig. 10 (a)). At this stage, it is appropriate to re-iterate that we chose two specific networks as templates in order to illustrate a proof-of-concept explaining the possibility of doing re-alignment of task fMRI using resting-state fMRI data. This research work, at no point, claims to suggest that these networks are the best suited functional templates for normalization of AOD data. It is evident from existing literature that performing an auditory oddball task excites a network of regions in the

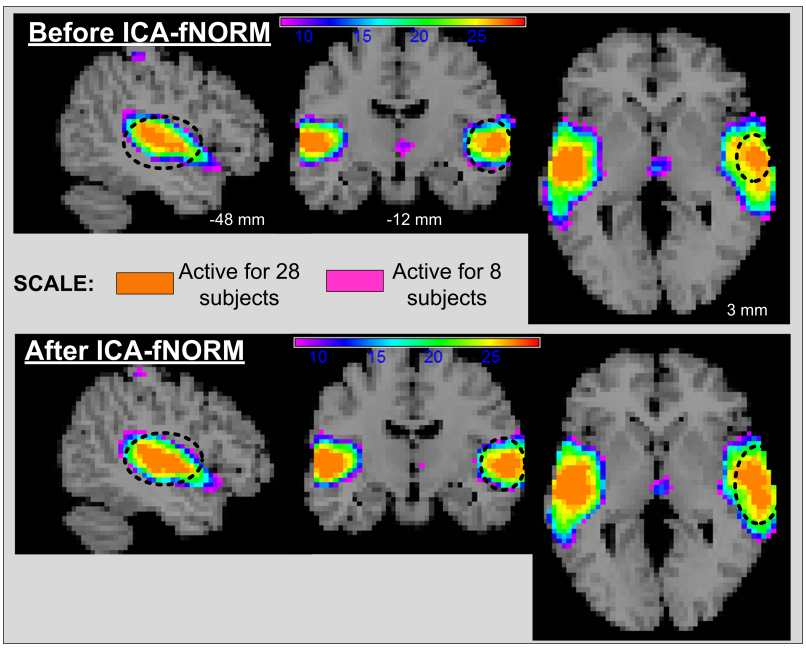

(a) Overlap Comparison (Incidence Maps) from subject-specific results

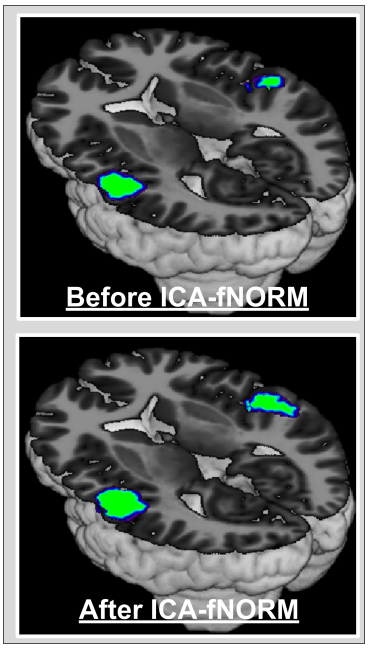

(b) Voxels active in all 28 subjects (Orange region from (a))

Figure 3.13: Subject-specific results from all 28 subjects presented using incidence maps from the temporal lobe IC derived from before and after ICA-fNORM data sets. (a) Incidence maps with voxels that overlap in at least 8 subjects (pink) to all 28 subjects (orange). Significant differences near the center of activation clusters are highlighted to illustrate higher functional significance of neighboring voxels after ICA-fNORM is applied. (b) Rendering of voxels from all 28 subjects to highlight the improvement in functional localization at a subject-specific level. More common voxels across subjects are found to be significant after applying ICA-fNORM.

temporal, parietal, frontal cortices and insula. Thus, it is highly likely that these intrinsic networks may prove to be more or as much useful for functional re-alignment. We propose to investigate effects of using combination of multiple components in coherence with a more sophisticated registration scheme as a part of related future work.

3.7.2 Multi-Network Templates: extending the proof of concept

After illustrating the advantages of single-network functional templates and functional normalization, the next foray for exploring and extending the ICA-fNORM is to develop an image fusion framework for forming a functional template that is comprised of any number

of relevant templates. As stressed in earlier chapters about the likelihood that development of a template consisting multiple intrinsic networks can be highly beneficial for extraction of normalization parameters from resting state group fMRI data. The next chapter is an introduction to the concept of multi-network functional templates that does not exist or being actively explored by fMRI researchers.

3.8 Summary

This chapter lays a foundation for utilizing several known resting (intrinsic) networks as multiple basis functions to derive a functionally standard space. Our proposed framework, termed as ICA-fNORM utilizes the inter-subject variation in functional boundaries across a group to better align the functional domains within task-fMRI data recorded for the same group. A comprehensive set of results presented in this paper show significant improvements in detection sensitivity, localization of activity and above all statistical significance of most regions known to be involved in performing an auditory oddball task. Using a task-positive (TL_{rest}) and a task-negative (DMN_{rest}) intrinsic network as separate functional templates not only helps achieve gains in the statistical significance of the derived results, but also reveal interesting relationships about variability in interactions at multiple levels of significance (transition zones). Our results suggest that combining multiple intrinsic networks into a single functional template, based on the nature of task (auditory, visual or attention), may help uncover higher levels of interactions associated with intrinsic dynamics and task-performance. We believe that the proposed method has a lot of potential and can be considered user-ready in its current form for experimentation under various pre-processing scenarios. It is possible that a high dimensional warping scheme may benefit this particular framework as compared to the current low-dimensional scheme (from SPM) utilized in our approach.

Chapter 4: Towards Functional Templates for Normalization

Making inferences about the relationships between functional organization (activation maps) and known neuro-anatomical markers requires methods for relating the inter-subject variability in functional anatomy to the population variability. A new preprocessing approach, ICA-fNORM, was presented in the previous chapter. This framework attempts to achieve the above mentioned goal by performing spatial normalization using resting-state networks as templates. In order to illustrate the benefits of using such a method in addition to the existing spatial normalization method, one intrinsic network, considered relevant based on certain assumptions, was utilized in place of a standard structural or an EPI template (Collins et al., 1994, Mazziotta et al., 2001).

In this chapter, we present a nascent perspective on the next possible direction for taking forward the functional normalization framework. Resting state networks and intrinsic brain connectivity is arguably the most proliferating topic associated with fMRI and brain imaging research. These maps of coherent brain activity are rapidly being considered one of the most informative non-invasive ways to quantify and identify the hierarchy of brain function. Today, an increasing number of researchers couple their studies involving a cognitive task with acquisition of resting-state fMRI. The benefit of possessing more data from a resting brain against the cost of using the MRI scanner for an additional 5-10 minutes. The extra data is invaluable to those researchers trying to understand intrinsic brain function and answer questions related to the human conscious under various environments. A resting-brain is arguable considered the source of baseline functional patterns, that is when the mind is allowed to wander into random thinking and mimic its baseline associations in the real world (outside the scanner) as much as possible.

4.1 Preprocessing through Co-design

Independent component analysis (ICA) is commonly applied to separate or parcellate the resting state brain in to multiple intrinsic networks of brain function. This is done using a mathematical framework to separate multiple regions of the brain showing temporal coherence under certain established models. Conventionally, these networks have only been analyzed for functional correlation, commonly referred to as *functional connectivity*. Over the past few years, a number of studies citing the use of intrinsic activity maps for estimating connections within and across neural pathways have piqued interest (Allen et al., 2011, Biswal et al., 2010, Bullmore and Sporns, 2009, Calhoun et al., 2011, Filippi et al., 2012). This particular application of resting-state data has been explored very widely whereas some of the other possible uses are still unexplored. Despite some interesting findings showing co-existing networks induced during rest and task (Calhoun et al., 2008, Smith et al., 2009), there has been little research in using these two data sets together. Only recently, Mennes et al. (2010) demonstrated the possibility of predicting task-induced BOLD activity using inter-individual differences from resting-state networks.

For advancing applications of these well-established and tested intrinsic networks, we proposed the ICA-fNORM framework and presented arguments for its application and position in the fMRI preprocessing pipeline by illustrating the benefits as well some methodological limitations for group-fMRI analysis. The increasing interest in new fMRI analysis methods developed using data-driven techniques such as ICA and multi-modal fusion asks for re-defining fundamental questions posed prior to designing an fMRI study. Well-targetted and adaptive fMRI processing methods can help reveal hidden relationships across different networks of the brain. That being said, it will require a significant level of conviction amongst researchers and clinicians to bolster the place of data driven approaches alongside some of the well-established theoretical concepts such as graph theory Sporns (2011), Sporns et al. (2004) and causality Stephan and Roebroeck (2012), for advancing tools for fMRI research.

4.2 Selection of Relevant Intrinsic Networks

Resting state fMRI data is usually analyzed using a data-driven method such as ICA since there is no known temporal paradigm associated with it as is the case with task-based data sets. The first study showing connectivity patterns across closely linked voxels (motor-cortex in this case) within resting-fMRI data was first demonstrated by Biswal et al. (1995).

However, the first few papers (Greicius et al., 2003, Kiviniemi et al., 2003) that demonstrated the existence of low-frequency BOLD patterns around the whole brain came several years after the seminal finding by Biswal et al. (1995). Since then, independent component analysis (ICA) has successfully and repeatedly been applied as the primary tool to estimate these resting-state networks and they typically exhibit BOLD signals fluctuating at low frequencies. These findings have been thoroughly verified by several researchers and cross-validated against Alpha rhythms (neural oscillations in the frequency range of 812 Hz arising from synchronous and coherent electrical activity, mostly arising from the occipital lobe.) from EEG data (Goldman et al., 2002). Interestingly, increased alpha power was found to be consistently correlated with decrease in BOLD signal across multiple regions in the brain. An important benefit of data-driven techniques such as ICA, over the hypothesis-based techniques (such as GLM) is the ability to identify and separate spatially and temporally distinct signal fluctuations across the whole brain without the need to specify an explicit temporal model. Since the above discovered relationships, the consistency of the existence of these networks has been well established through a group-ICA study of healthy subjects (Damoiseaux et al., 2006) followed by continuous experiments involving associations of these networks with covariates such as age, gender, and ethnicity (Allen et al., 2011).

For application to functional normalization, we depend upon the findings by the numerous studies mentioned here, that is, selection of relevant intrinsic networks is done based on two criteria:

1. Known networks that are essential to brain function and comprise a robust array of

components from previous studies such as occipital, sensory motor, parietal, inferior frontal, cingulate cortex and temporal regions.

2. The primary task-relevant region known from a data-set of interest, for *e.g.* , temporal lobe and somatosensory motor in case of an auditory oddball task (AOD).

These two assumptions play a crucial role in the final outcome of fMRI analysis involving functional normalization as one of the preprocessing approaches. Most fMRI activation maps represent BOLD activity in blood vessels surrounding the neurons that are active. As seen from results presented in previous chapter, the active voxels are spread over multiple large contiguous regions within known anatomical areas. In Figure 4.1, a few relevant networks are presented as an example and will also be used in the following sections to demonstrate the methodology for formation of multi-network functional templates (**mnFT**).

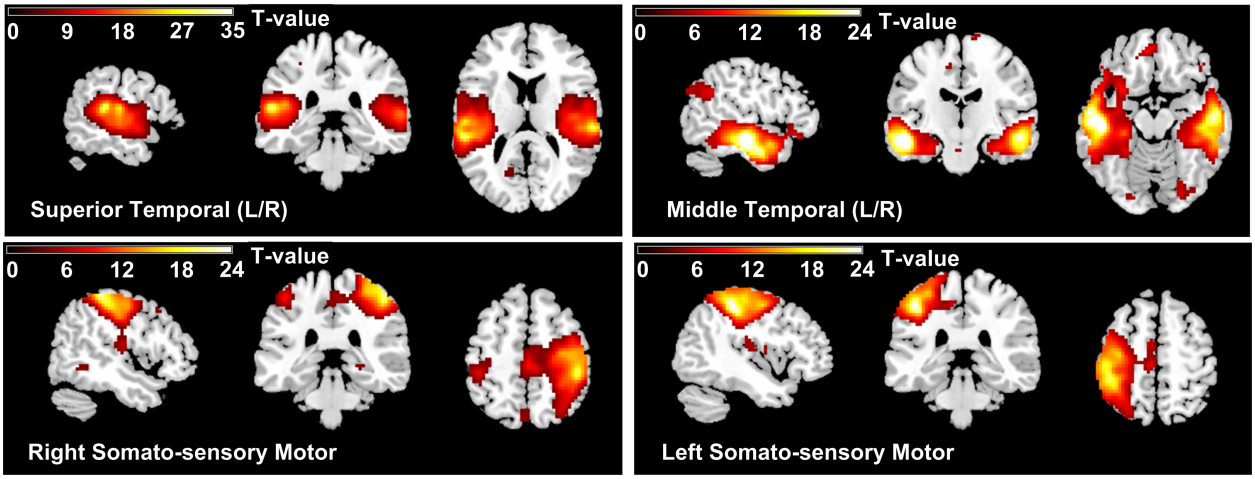

Figure 4.1: Some of the intrinsic networks shown here that may be utilized to form the multi-network template. The 3 geometries for different networks - occipital, visual, anterior cingulate, default mode network etc. The chosen planes correspond to the maximum values within these components as obtained after applying ICA to a resting-state fMRI data set.

In the next section, we present application of an image-fusion technique proposed by De and Chanda (2006) for merging two images of the same scene captured at two distinct focal planes as illustrated in Figure 4.2.

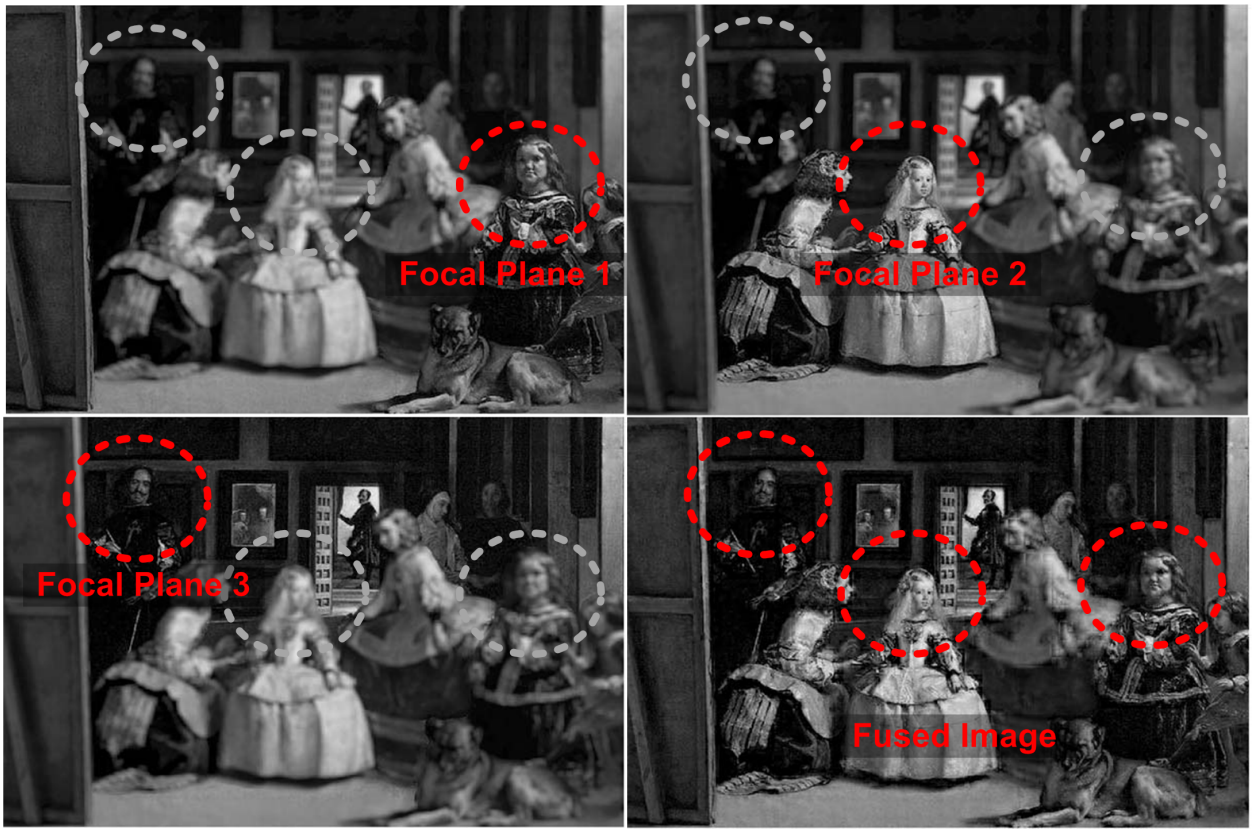

Figure 4.2: Taken from De and Chanda (2006). Images captured at multiple focal lengths with objects at different depth along side the merged image with all corresponding features in focus. This process is known as *multi-focus image fusion*.

4.3 Multi-Network Fusion Framework

Image fusion is an important and widely researched sub-area in the diverse field of image processing. In optics, imaging sensors can focus on certain objects in a single shot, this is controlled by the focal length of the lens used. Thus, to capture a focused representation of objects placed at different depths requires multiple images of the scene at various focal lengths followed by computational aggregation. This image set is commonly known as the *focal stack*. This is aggregation process is achieved by different types of algorithms proposed in the literature, referred to as *multi-focus image fusion*. The advantages of using multi-focus data aggregated in to a single image are manifold. The redundant information alongside complimentary features from various constituent images are much improved in a fused image.

Secondly, this provides a better view for human as well as machine perception. Other advantages are based on the position of image fusion in the image processing hierarchy, that is, several derivative applications like feature extraction, segmentation, compression take advantage of a good image fusion algorithm. A common example is image demosaicing where information from red, green, and blue sub-pixels is merged in to a single multi-color RGB image (Li et al., 2008).

In context to fMRI, we may view the different intrinsic networks as raw channels of an RGB image. The various networks derived from ICA have minimal spatial overlap, thus indicating towards a possibility of a merging approach almost mimicking the ***demosacing*** method for RGB images. ICA serves as a pivotal tool to achieve this task. Resting-state data is decomposed in to multiple components, thus providing enough flexibility to choose the appropriate networks that may correspond closely to a cognitive task that we are interested in studying. The functional template is then used in conjunction with the conventional spatial normalization process to adjust for inter-subject functional variability within the fMRI data associated with that cognitive-task. In Chapter 3, we demonstrated the implementation of the functional normalization framework whereas in this section we focus on formation of multi-network functional templates.

The motivation for merging multiple intrinsic networks comes from the realization of co-design presented in the previous section. Using resting-state networks as disjoint but aggregated representations of the functional organization of the brain. In order to better understand functional variability across individuals within a group or population, there is a need to account for the spatial characteristics of these functional networks. Thus, we propose a fusion methodology to merge multiple networks of functional organization into a single MNI-type functional template. An illustration of our proposed idea is presented in Figure 4.3.

Due to the complex nature of information embedded in these networks, merging them in to a single volumetric image is more challenging than just simple aggregation. As is the case

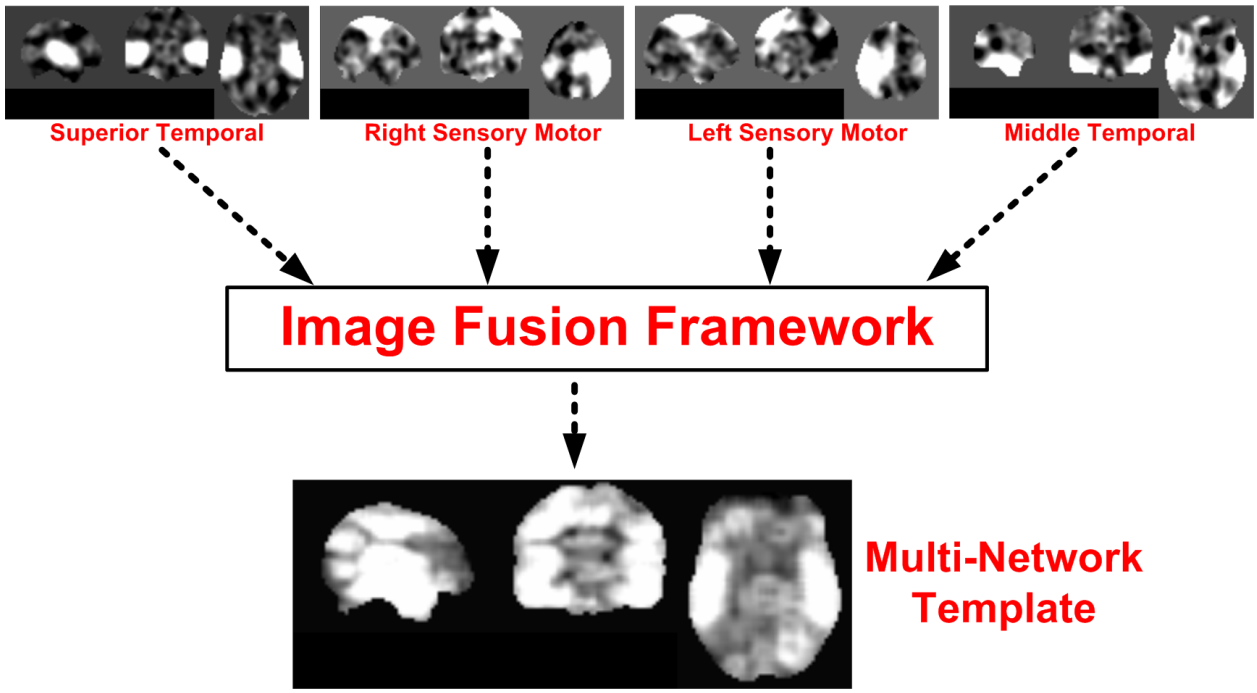

Figure 4.3: An illustration of the proposed template formation framework from resting-state intrinsic networks. The main function of the image fusion block is to find an ideal combination of multiple networks, and provide priority values for a *fused* value for each voxel in the brain from multiple input networks.

with many template-based normalization algorithms, it is important to note that the method used to form the multi-network template may also depend on the registration methodology used.

4.3.1 General Background

There are a number of techniques for merging two or more images in to a single aggregated image. Simple techniques involving basic operations such as weighted averaging can have serious side-effects on the contrast of the fused image. Probabilistic techniques come with a large overhead of computational complexity and reduced efficiency (De and Chanda, 2006). Some of the commonly used approaches include - probabilistic fusion (Bloch, 1996), image gradient with majority filtering (Eltoukhy and Kavusi, 2003), and more recently developed multi-scale (Mukhopadhyay and Chanda, 2001) and multi-resolution approaches (Piella, 2003). A comprehensive survey of techniques covering some of the aforementioned techniques in addition to some techniques in multi-sensor fusion for remote sensing applications can be found in Blum and Liu (2005).

4.3.2 Wavelets and Image Fusion

The most favored and established theory for image fusion, be it single or multi-sensor, is wavelet transforms. Wavelets have been used for fusion of several types of images such as remote sensing, medical imaging, microscopy, IR and visible imagery as first shown by Li et al. (1995), and later surveyed by Pajares and de la Cruz (2004). Results have shown consistent performance enhancements based on metrics for information retention as well as image quality. The multi-resolution and sub-band based wavelet framework provides adaptability for successfully combining a wide range of features belonging to different scales and spatial frequencies. The majority of wavelet-based approaches utilize the discrete wavelet transform (DWT) where the wavelet coefficients of the source images are merged and the fused image reconstructed back to the original space using an inverse transform. However,

the main limitation of this approach is that wavelets like Haar or Daubechies are unable to preserve the dynamic range of original data in the wavelet domain. This poses as a problem when dealing with fMRI networks which acquire arbitrary values as independent components. The second and more serious limitation in context to our application to fMRI is that the inverse transform is an approximation and may result in reconstruction errors. Such reconstruction errors are minimal when there is a single source image, and the application utilizes all the coefficients as is the case with image denoising. However, it is desirable to avoid reconstruction errors when multiple source images are combined based on a weighted coefficients or metric as generally practiced for image fusion.

Non-linear extensions of the DWT have been proposed through various schemes such as *lifting* (Sweldens, 1996) and *morphological pyramids* (Goutsias and Heijmans, 2000, Heijmans and Goutsias, 2000). The advantage of using non-linear extensions of the DWT for image fusion is manifold. It possesses many types of invariance properties: 1) Shift invariance (as in the case of SWT) is achieved through the formulation of analysis (decomposition) and synthesis (reconstruction) operators, and 2) grey-value shift invariance provides a great advantage where grey values (activation intensities from different networks) are preserved in the fused image. That is, adding or multiplying a certain value throughout the volumetric image is equivalent to adding or multiplying by the same value during any step in the analysis (decomposition). The direct effect of this property is do with minimal or no change around the detail regions (edges, corners etc.).

For the purpose of demonstrating the possibility of using multi-network functional templates with our proposed ICA-fNORM framework, we extend the multi-focal image fusion scheme presented by De and Chanda (2006) to fMRI analysis. This is a new area of research for fMRI analysis, and there exists little literature that has attempted data fusion at the preprocessing stage as we do here. Most algorithms used for preprocessing fMRI are well-defined and have been repeatedly validated under various conditions. It is important to note that the propsed multi-network templates and ICA-fNORM framework are in no way

a replacement for the existing spatial normalization and registration schemes. Undermining the existing normalization approaches is not the goal of this work. The functional-template based normalization requires comprehensive validation on real fMRI data sets. However, the integration of various established approaches applied together in a single framework as ICA-fNORM provide sufficient ground for experimenting with multi-network templates. The work presented in this chapter will set a foundation for future studies that may apply ICA-fNORM on a diverse variety of data sets and help validate it further. This type of progressive testing will eventually help bolster the position of such hybrid approaches that can possibly advance the field of fMRI analysis.

4.3.3 Image Fusion: Theory and Examples

The theory, implementation and application of the *morphological* wavelet transform was first explained by Goutsias and Heijmans (2000), Heijmans and Goutsias (2000). They utilized the commonly used morphological operations: dilation and erosion for decomposition and reconstruction. For the multi-dimensional case, a non-separable and uncoupled case has been explored for multi-focus image fusion in De and Chanda (2006). We utilize the same scheme for the multi-network image fusion framework. There are two main reasons for choosing this particular methodology to achieve multi-network fusion: (1) This is a proof of concept strategy to demonstrate the feasibility of multi-network normalization, thus a simple to implement approach is adopted here. (2) This approach is capable of handling any number of intrinsic networks as input to the fusion routine. In the following section, we re-write the theory explained in De and Chanda (2006) with examples specific to fMRI analysis. The algorithm is divided in to three stages: (1) Analysis, (2) Fusion, and (3) Synthesis.

ANALYSIS

Unique analysis operators (forward wavelet transform) - $(\psi^{\uparrow}, \omega^{\uparrow})$ and synthesis operators (reconstruction) - $(\psi^{\downarrow}, \omega^{\downarrow})$ are used for a single level decomposition scheme. Due to the low

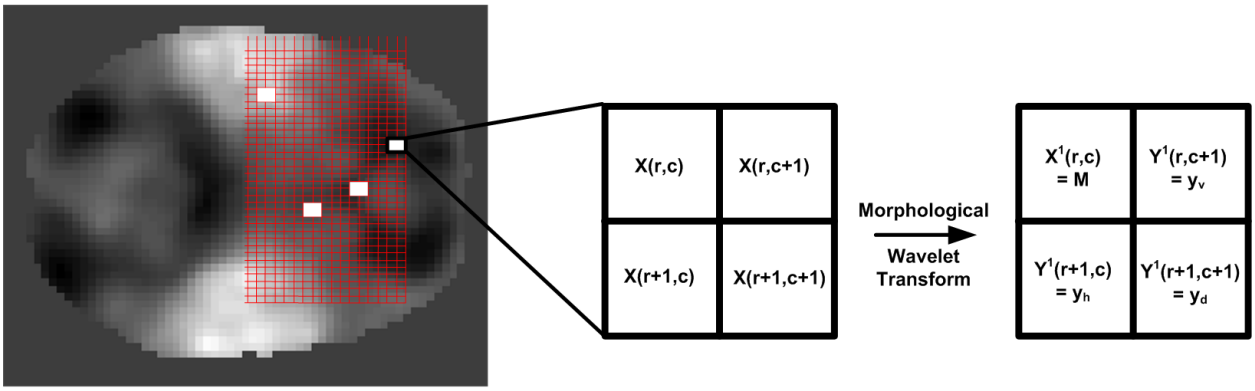

Figure 4.4: An illustration of the subdivision of images in MN/4 matrices alongside decomposition of a 2×2 sub-matrix in to approximation and detail bands.

resolution of the fMRI data, we restricted to a dual-resolution fusion scheme, that is only one level of decomposition for fusion. Further experimentation with a multi-resolution may prove to be useful in analyzing performance. Let X be an image in a signal space V_0 which can further be decomposed in to subspaces V_1 (approximation) and W_1(detail) at level 1 in the wavelet domain. Let $X \in V_0$ is a set of gray values in a 2-D space of size $M \times N$ such that M and N are both even. Thus, X can be subdivided in several disjoint 2×2 sub-images or blocks resulting in a total of $MN/4$ matrices as shown in Figure 4.4. Through quadrature down sampling (see Figure 2.4), the analysis and synthesis operators $\psi^{\uparrow} : V_0 \rightarrow V_1$ and $\omega^{\uparrow} : V_0 \rightarrow W_1$ are defined analytically in Eqns. 4.1 and 4.2.

$$\psi^{\uparrow}(X)(B) = M = max\{X(r,c), X(r,c+1), X(r+1,c), X(r+1,c+1)\}, \tag{4.1}$$

$$\omega^{\uparrow}(X)(B) = (y_v, y_h, y_d). \tag{4.2}$$

where y_v, y_h, y_d represent the *vertical, horizontal* and *diagonal* detail signals respectively and are defined as:

$$y_v = \begin{cases} M - X(r,c+1) & \text{if} M - X(r,c+1) > 0, \\ X(r,c+1) - M & \text{otherwise}, \end{cases} \tag{4.3}$$

$$y_h = \begin{cases} M - X(r+1,c) & \text{if} M - X(r+1,c) > 0, \\ X(r+1,c) - M & \text{otherwise,} \end{cases} \tag{4.4}$$

$$y_d = \begin{cases} M - X(r+1,c+1) & \text{if} M - X(r+1,c+1) > 0, \\ X(r+1,c+1) - M & \text{otherwise,} \end{cases} \tag{4.5}$$

The scaled approximation (M in Eqn. 4.1) and detail (Eqns. 4.3- 4.5) values obtained above are at level-1, that is, approximation X^1 and details Y^1, respectively. Thus, these 4 values can be stored in a 2×2 matrix as shown in Figure 4.4. The above step is repeated for n different intrinsic networks (chosen by the user) that are given by $X_1, X_2, X_2, ..., X_n$, thus resulting in a pair of coefficient matrices for each network - $\mathbf{X} = X_i, Y_i$. An example illustrating the above wavelet synthesis on an axial slice from the target resting-state networks used for fusion are shown in Figure 4.5 (see second column). For clarity, we select 3 different axial slices (at -3,-12 and $+42$ mm in MNI coordinate space), each corresponding to the maximum value in at least one network. This illustrates the intensity distribution across various networks that exist as a volumetric image.

An important point to note in Figure 4.5 is the range of transformed images. If all values of the image $\mathbf{X}$ belong to the range $[0, R]$, then the transformed approximation signal X belongs to range [0,R] whereas the detail signal Y belongs to the range [-R,R]. Larger values in any image X_i corresponds to a brighter pixel whereas a large value in Y_i corresponds to a possible edge, corner or other high-spatial frequency features.

FUSION

After the completion of analysis operation, 2 sets of n *approximation* (X_i^1) and *detail* (Y_i^1) signals are obtained at level-1. Based on the range of these images as discussed above, a priority condition is required to choose the network that may contribute to the pixel value

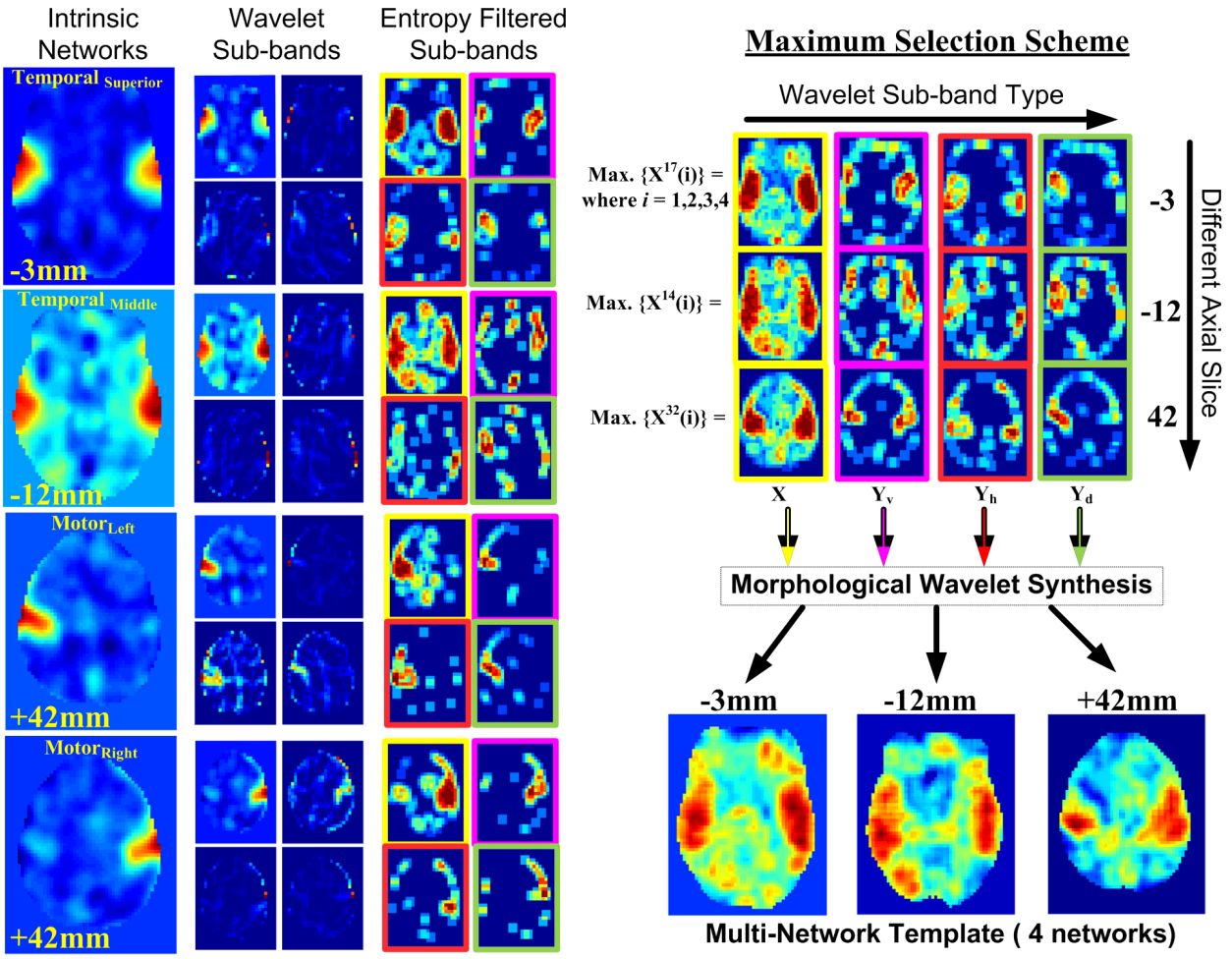

Figure 4.5: **MWT Example using Intrinsic Networks**: An example showing step-by-step illustration of different stages of the proposed entropy-filtering based wavelet fusion scheme. The final image is obtained through the stacked-image maximum selection scheme in the wavelet domain followed by morphological reconstruction. An orthogonal view (arbitrarily chosen) of the resulting template is illustrated depicting active regions present in the four input templates.

at each location (r, c). In other words, the priority condition is basically the fundamental fusion criterion to merge multiple target images, intrinsic networks in this case. There are several fusion criteria proposed in the literature as listed below:

Maximum Selection (MS) scheme: this scheme simply picks the coefficient from each sub-band which has the largest magnitude across multiple images.

Weighted Average (WA) scheme: This technique was introduced by Burt and Kolczynski (1993) utilizes a neighborhood based normalized correlation among target images' sub-bands. The final fused coefficient is estimated through a weighted average of the two images' coefficients. The disadvantage of this method is that it can not work with more than two images due to the application of the correlation operator.

Window-based verification (WBV) scheme: This scheme is probably the most sophisticated amongst all and has been used for several applications in combination with some other techniques (Li et al., 1995). It performs a fusion by means of a binary decision map estimated over a local neighborhood for two or more coefficients from the target images. The binary decision map decides what target image contributes to a pixel (r, c) in the final fused image.

For our implementation, we utilize the MS scheme that is also utilized by De and Chanda (2006) for fusion of multi-focus images. A minor, but substantial novel contribution to the MS scheme for fusion is proposed here. A pre-processing step to obtain a crude segmentation of meaningful voxels within the sub-bands is performed using an *entropy filtering* approach. Each voxel value is replaced by its entropy value (a statistical measure of reandomness) in the neighboring 3×3 neighborhood. It is computed as : $H(\mathbf{x}) = \sum_{\mathbf{N}} P_N(x) log_2(P_N(x))$, where (x) is the center pixel and $P_N(x)$ is the probability distribution (histogram) in neighborhood N. As noticed from Figure 4.5, the difference between the regularly processed sub-bands and the entropy-filtered bands is quite significant. The regions with higher activation values are now more prevalent in the filtered images (third column). Some of the voxels with low local entropy are removed whereas the activation specific voxels are scaled based on their

local entropy. This assists in image fusion where the activation across different networks is spread over a number of voxels in different planes (axial slices here) across the brain. This also serves as the primary reason for demonstrating the fusion process with the help of three different slices extracted from four different intrinsic networks - $-3mm$ for Superior Temporal, $-12mm$ for Middle Temporal, and $+42mm$.

An alternate approach that may utilize some type of functional connectivity metric to realize the weights of each component may be worthwhile to pursue. Here, we presented a proof of concept for functional template formation. Experimenting with fusion methods is outside the scope of this thesis but considered to be a substantially important part of future work.

The MS fusion scheme compares multiple intrinsic networks $\{X_i,\ i = 1, 2, ...n\}$ and combines them into $\mathbf{X} = \{X_f^1, Y_f^1\}$, where X_f^1 and Y_f^1 are given by $X_f^1(r,c) = max\{|X_1(r,c)|, |X_2(r,c)|, ...|X_n($ and $Y_f^1(r,c) = max\{|Y_1(r,c)|, |Y_2(r,c)|, ...|Y_n(r,c)|\}$, respectively. This operation results in 4 fused images (1 approximation, and 3 details) consisting of features from all the networks. These results are presented in Figure 4.5 that show initial images and the fused result using 4 different networks for different slices and sub-bands.

SYNTHESIS

The last and final step in template formation is the synthesis or reconstruction back from wavelet domain V_1 to the signal domain V_0. The fused image $X \in V_0$ is reconstructed by applying the synthesis operators $\psi^{\downarrow}$ and $\omega^{\downarrow}$ on the transformed and fused set $\mathbf{X} = \{X_f^1, Y_f^1\}$. The reconstruction to obtain the synthesized (fused) signal is done through the following equations:

$$\hat{X}(r,c) = \hat{X}(r,c+1) = \hat{X}(r+1,c) = \hat{X}(r+1,c+1) = M. \tag{4.6}$$

$$\begin{aligned} \hat{Y}(r,c) &= \min(y_v, y_h, y_d, 0), \\ \hat{Y}(r,c+1) &= \min(-y_v, 0), \\ \hat{Y}(r+1,c) &= \min(-y_h, 0), \\ \hat{Y}(r+1,c+1) &= \min(-y_d, 0). \end{aligned} \tag{4.7}$$

The reconstructed signal X' at any point $(u,v) \in \{(r,c),(r,c+1),(r+1,c),(r+1,c+1)\}$ is given by Eqn 4.8 and illustrated in Figure 4.6 through various slices.

$$X'(u,v) = \hat{X}(u,v) + \hat{Y}(u,v). \tag{4.8}$$

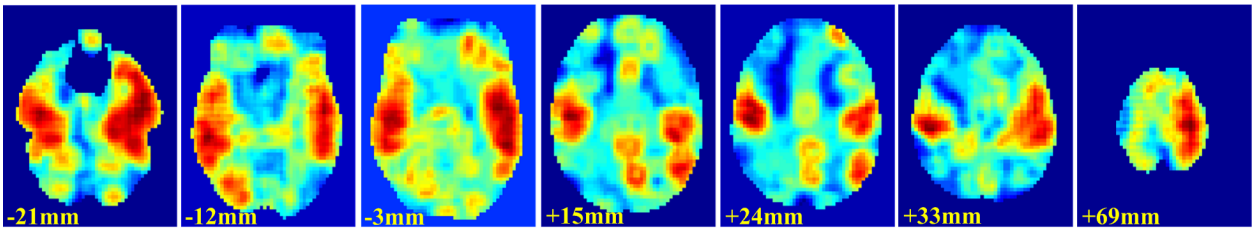

Figure 4.6: Illustration of the the multi-network functional template through a few selected slices spread throughout the brain. This image highlights the merging of features from various networks, also shown in 4.5.

In regard to the importance given to performance analysis for fMRI preprocessing algorithms, we present the results of the fusion algorithm proposed above. The final fused image is taken as the functional-template and used in conjunction with the ICA-fNORM framework presented in the previous chapter. The results are presented using the two-sample t-test from comparing AOD data from 28 healthy controls and 27 schizophrenia subjects.

4.4 Results

The multi-network functional template is developed using manually selected intrinsic networks that are known to be positively modulated by the cognitive task - (1) Superior Temporal and (2) Middle Temporal, (L/R), (3) Left Sensorimotor, and (4) Right Sensorimotor (illustrated in Figure 4.1). All four networks are actively modulated due to their known involvement (from other low-level experiments) with performing the task correctly. For example, the temporal lobe is the auditory region, and sensori-motor is responsible for motor-functions such as tapping a finger when the *target* tone is heard.

4.5 HC vs. SZ: Two-sample *t*-test

In order to obtain an initial estimate of the advantages of a multi-network functional normalization approach, we compare the component maps obtained *before* and *after* fNORM. The AOD group data containing 28 healthy controls and 27 schizophrenia subjects is normalized using the resting-data available for each subject and analyzed. The comparison maps are obtained through regular preprocessing followed by group ICA and 2 sample t-test.

The FDR corrected t-maps are presented for two conditions - Figure 4.7a where HC > SZ; and Figure 4.7b where SZ > HC. For the purpose of finding differences between these two groups through the AOD task, researchers are primarily interested in analyzing the temporal lobe component (Calhoun et al., 2008, Kiehl et al., 2005) as these are strongly modulated by the cognitive task.

HC > SZ: As noticed here, there are significant differences in regions near the intersection of the superior and middle temporal regions after functional normalization indicating higher activity in these regions in case of healthy controls. However, in case of regularly processed data (without ICA-fNORM), these differences are slightly translated ($9 - 12$ mm or $3 - 4$ voxels) towards the middle temporal region. Also, the t-value is much higher after normalization indicating the reduced effect of inter-subject variability during normal analysis. It

is highly likely that the increase in significance is a direct result of functional normalization using some of the positively task modulated networks. The false-discovery rate (FDR) correction on the two-sample t-test maps is done using the recently introduced cluster-based computation (Chumbley and Friston, 2009) with $p - value < 0.001$.

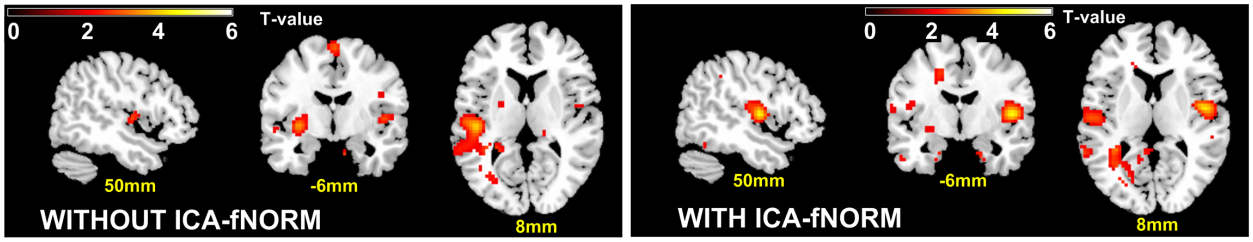

(a) HC>SZ

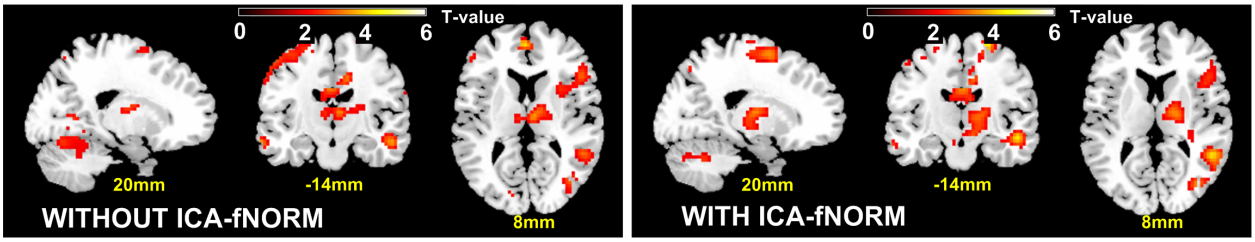

(b) SZ>HC

Figure 4.7: A multi-group comparison shows significant differences between patients and controls within the temporal lobe component (TL_{AOD}) derived through group-ICA done with(left) and without(right) functional normalization. The results reveal positive differences for (a) **HC>SZ** and (b) **SZ>HC**.

SZ > HC: Activation topography withing the temporal lobe network has repeatedly been used as a basis of classification in healthy controls and schizophrenia patients showing high accuracy and robust activation patterns (Calhoun et al., 2004). In this section we show the differences in regions that show higher BOLD activation in patients than in controls. As evident from Figure 4.7b, the superior and inferior temporal regions, in addition to some regions of the limbic system and the thalamus show increased activation patterns *after* ICA-fNORM. A reasonable number of new activation clusters qualify the significance after the fusion template is applied in the preprocessing stage. Another interesting feature is that spatially non-overlapping regions within the large temporal lobe (axial slice - 8 mm), show activity for HC > SZ and SZ > HC. Another interesting site of activation that appears *after*

ICA-fNORM is near the thalamus, which happens to be the *communication hub* of the brain where many networks converge. A higher acitivity in this region in patients may indicate hyperactivity patterns that may be closely connected with the activity in the temporal lobe region.

Coexistence of thalamus and temporal lobe differences within the same component clearly indicate the advantages of using our proposed functional normalization framework. The use of functional information relating to resting-state data in patients seems to play a larger role in uncovering hidden interactions within important regions of interest for a simple task as the AOD.

4.6 Limitations, Future Work and Summary

As mentioned repeatedly, the application of functional templates is a relatively new area of research. As per our knowledge, it has not been proposed or used previously in fMRI analysis studies. As with every new method, there come attached certain limitations especially when the system of application is as complex as the human brain.

The combination of multiple intrinsic networks has implications for how one interprets each of these temporally coherent networks on their own. That is, subtle effects of each network on the normalization methodology are difficult to separate and identify. The method using single network as a template was presented in the previous chapter as a foundational basis to understand this effect. Having said that, resting state networks are known to have complex interactions across the brain and it is important to carefully choose the robust and task-relevant networks for template fusion and functional normalization. Another point to note is that since the data collected during AOD contains task-related variance, it is difficult to know if the physiologic mechanism behind the patient versus control changes is the same for both paradigms (rest and task). It may be possible that AOD changes are the mixture of the two effects (rest and task), and are only enhanced when resting-state networks are used to normalize the group data.

The future directions are twofold. Firstly, further validation and analysis of the proposed morphological wavelet-based methodology is required to understand the implications of using such a *pick the best voxel* type of approach as compared to using a model-driven approaches in the literature such as deriving mixture of probability distributions or so on. The analysis or comparison of other fusion methodlogies is outside the scope of this thesis, but shall be an important part of the future work. Secondly, an exciting future direction is to be generate templates adaptively based on a chosen task. A large database of aggregated resting-state networks similar to the one presented by Allen et al. (2011) may play a large role in understanding the formulation of multi-network templates. A database where any researchers may choose relevant anatomical regions for their study and the system or algorithm presents with multiple templates formed using different combinations of resting state networks that correspond to function in the regions mentioned by the researcher. This may well become a crowd-sourced testing methodology for this method, as it is best to validate the method using large number of applied studies due to the different types variability (demongraphic, health, task etc.)associated with fMRI data sets collected and analyzed across the functional brain imaging community.

In summary, we presented a foundational methodology for forming multi-network functional templates that may be used for functional normalization or realignment (as presented in the previous chapter). These two chapters present the initial exploratory effort in a new and upcoming area of research in the fMRI community. This paradigm shift has been inspired by the availability of large amounts of data as well as increasing interest in the resting-state function of the brain and its interaction with task-modulated networks. I hope that this work contributes to inspiring new data-driven methods and bolstering the confidence of researchers and clinicians in data-driven approaches for fMRI preprocessing.

Chapter 5: Wavelet-based Denoising and Signal Separation

Denoising is defined as a process to remove the noisy component from a mixture of signal (known or sometimes expected) and noise (unknown or sometimes pre-defined). This process, also referred to as *smoothing*, usually involves a convolution operation such as averaging, filtering, or sometimes even subtraction, being applied locally on a subset of data points or globally on the whole array (or vector), to reduce the noise. Specifically for images, denoising presents the user with a trade-off between degree of noise suppression and preserving actual image discontinuities. An important feature to have for a successful image denoising algorithm is its *spatial adaptivity*, that is, a capability to preserve important spatial details while removing noise. Using the wavelet representation, a single pixel can be represented as part of multiple bands of frequencies. This property of providing sparsity to the data in a uniform space-frequency grid, in addition to clearly separating directional information (edges), intrinsically facilitate spatially adaptive denoising.

5.1 fMRI Denoising Methods

The interest in uncovering functional connections in the brain has grown rapidly with advancements being made in fMRI analysis methodologies, consequently necessitating the exploration of approaches to enhance the preprocessing methods. Researchers in the field of functional neuroimaging have faced a long standing problem in preprocessing fMRI data. Denoising is a common pre-processing step that is applied before analyzing the fMRI data. The most commonly utilized method for this task is to smooth the fMRI image with volumetric

Gaussian kernels (Poline et al., 1997). This method is widely applied as it suppresses high-frequency noise, is simple to implement and most importantly increases the overall signal-to-noise ratio (SNR). The drawbacks of Gaussian smoothing include considerable change in true intensity values (as a function of the size of the smoothing kernel), and secondly the noise is averaged along with the signal. These effects make it more difficult to accurately separate signal and noise during the later stages of analysis. In addition to the above, the Gaussian smoothing approach suppresses the edge details and other medium-frequency information present in the original image.

Previously, researchers have attempted to apply denoising schemes other than Gaussian smoothing or wavelet-based denoising to fMRI data. Some of the alternate methods include spectral subtraction (Kadah, 2004), spatially adaptive Gaussian smoothing (Tabelow et al., 2006), a novel non-local maximum likelihood estimation approach by He and Greenshields (2009), and a more recently proposed anisotropic spatial averaging technique (Monir and Siyal, 2009). All of the above methodologies emphasize denoising fMRI data for further analysis in the spatial domain. There has been little work done in the past involving combinations of 3-D denoising, wavelet transforms and ICA applied in the transform domain for analysis of fMRI data.

5.2 Noise and Estimators

In this section, we briefly discuss the notations used hereafter in addition to some basic principles associated with the concept of modeling signal and noise.

5.2.1 Noise Model and Notation

In general terms, an image can be easily represented as a vector $\mathbf{f} = [f_1, \ldots, f_n]$ with each element corresponding to a spatial location n. The additive model is most widely used to

describe a signal-noise mixture as in Eqn. 5.1.

$$\mathbf{v} = \mathbf{f} + \eta \tag{5.1}$$

where vector $\mathbf{v}$ is the measured image quantity. The noise term η is considered as a vector of random variables, whereas $\mathbf{f}$ can either be a deterministic signal or in some cases, a specific realization of a random vector. In classical terms, noise is considered to have zero mean ($E(\eta) = 0$) and a covariance matrix denoted as $C = E[\eta\eta^T]$ where the diagonal elements are populated by the variances, $\sigma_l^2 = E(\eta_l^2)$. The noise is classified to be uncorrelated or *white* if $E(\eta_l, \eta_k) = 0$ for $l \neq k$.

For *identically distributed* random variables contained in η, the variance is constant, that is, $\sigma_l^2 = \sigma^2$ for $l = 1, \ldots, n$. In image processing, the most common type of observed noise distribution is additive white Gaussian noise or AWGN. The Gaussian probability density function for a random variable vector η and covariance matrix C is represented in Eqn. 5.2. It is noteworthy to know that if Gaussian noise variables are uncorrelated, they are also statistically independent - in notation terms, $p_\eta(\eta) = \Pi_l p_{\eta_l}(\eta_l)$.

$$p_\eta(\eta) = \frac{1}{(2\pi)^{(n/2)}\sqrt{det(C)}} e^{-\frac{1}{2}(\eta^T Q^{-1}\eta)} \tag{5.2}$$

5.2.2 Noise in Wavelet Domain

An attractive feature of the noise in the wavelet domain is that it is spread over all coefficients, whereas the most informative details in the image such as edges, corners, peaks, etc. are encoded in to a few large-valued coefficients spread across various sub-bands. The noisy coefficients, at typical noise levels, can be easily recognized through statistical measurements estimated globally or locally. The noise model presented in Eqn. 5.1 remains unchanged in the wavelet domain due to linearity of the transform, and the transformation with W_d wavelet transform operator can be written as: $W_d\mathbf{v} = W_d\mathbf{f} + W_d\eta$, which yields the same model in

the wavelet domain:

$$\mathbf{w} = \mathbf{y} + \mathbf{n} \tag{5.3}$$

where $\mathbf{w}$, $\mathbf{y}$ and $\mathbf{n}$ are the wavelet domain representations of the observed signal, noise free data, and additive noise respectively. An *orthogonal* wavelet transform, as the name suggests, maps uncorrelated noise (white) in input image to white noise in wavelet domain. Thus, the noise variance σ^2 remains unchanged between the image and wavelet domain. However, for *bi-orthogonal* and *non-decimated* transforms, the noise variance becomes a function of the resolution (scale) and the sub-band orientation (horizontal, vertical or diagonal) (Pizurica et al., 2006), that is, each detail image denoted as $\mathbf{w}_j^d$ has a constant variance $(\sigma_{n,j}^d)^2$, where j and d are the resolution level and sub-band orientation respectively. This variance is expressed as S_j^d, a function of coefficients of the wavelet filters h_0 and h_1 (see Section 2.3.3).

$$(\sigma_{\eta,j}^d)^2 = S_j^d \, \sigma^2 \tag{5.4}$$

As seen from Fig. 2.4, the detail sub-bands $\mathbf{w}_j^{LH}$ and $\mathbf{w}_j^{HL}$ can be produced by applying the lowpass filter h_0 to the data a total of $2j-1$ times, whereas the highpass filter h_1 is applied only once (either horizontally or vertically). The third detail sub-band at level j, $\mathbf{w}_j^{HH}$, is obtained after applying filters h_0 and h_1 exactly $2(j-1)$ times and twice, respectively. An analytical derivation based on separate terms describing the second order derivative of the second moment of wavelet coefficients $\mathbf{w}_j^{HL}$, $\mathbf{w}_j^{LH}$ and $\mathbf{w}_j^{HH}$ can be found in (Foucher et al., 2001). We utilize the final term as an estimate for the resolution function S_j^d from 5.4 as given below:

$$S_j^{LH,HL} = (\sum_k h_{1k}^2)\,(\sum_l h_{0l}^2)^{(2j-1)} \qquad S_j^{HH} = (\sum_k h_{1k}^2)^2\,(\sum_l h_{0l}^2)^{2(j-1)} \tag{5.5}$$

By substituting Eqn. 5.5 in Eqn. 5.4, the noise variance of all subbands $(\sigma_{\eta,j}^d)^2$ can be estimated, given that the noise variance (σ^2) of the input image is known.

5.2.3 Input Noise Variance

After a discrete image has been synthesized through sampling continuous signal sources, the noise model is generated by using knowns associated with the system of acquisition (optics, shot noise, photon noise, ...). This assists in estimating a well-fitted model for noise and the input noise variance σ^2. The frequency distribution of noise present in 2-D images is usually noticed to be in a high frequency range.

In the wavelet domain, a purely high frequency sub-band (${w_j}^{HH}$) is commonly used to classify noise distribution in addition to its spatial representation. A possible drawback of this method is that high amplitude changes (high intensity edges and corners etc.) in the input data contribute to a substantial part of the total energy in the HH subband. A robust solution based on the median operator, which is highly insensitive to such outliers with high amplitudes, was proposed by Donoho (1995). If a set $\{I_n\}$ is comprised of N independent Gaussian random variables of zero mean and variance σ^2, then $E\big(\text{Median}(|I_n|)_{0\leq n\leq N}\big) \approx 0.6745\sigma$. Based on this theory, the noise variance estimate can be expressed as:

$$\hat{\sigma} = \text{Median}(\frac{|{w_1}^{HH}|}{0.6745}) \tag{5.6}$$

The term $Median(|\mathbf{w}|)$ is often known as the *Median Absolute Deviation* or MAD, is commonly used in image denoising algorithms (Donoho, 1995, Pizurica et al., 2003, Wink and Roerdink, 2004). We also utilize the MAD estimate in this thesis with $3-D$ wavelet subbands at multiple levels, explained in later sections.

5.2.4 Shrinkage and Attenuation Estimator

The most natural strategy adopted by researchers for solving the image denoising problem is joint estimation of signal and noise distributions. However, for efficiency reasons, the wavelet coefficients are modeled as independent or conditionally random variables. This deals with

calculating an estimate of the signal $\mathbf{y}$ (Eqn. 5.3) in the wavelet domain, given by

$$\hat{y} = \theta(y)w. \tag{5.7}$$

where y is the input data and w is the noisy wavelet coefficient. The estimator $\theta(y)$ ideally minimizes the mean squared error for Eqn. 5.7 and is given by,

$$E\{(y - \theta(y)w)^2\} = y^2(1 - \theta(y))^2 + \sigma_n^2\theta(y)^2 \tag{5.8}$$

$$\text{simplifying above: } \theta_{ideal}(y) = \frac{y^2}{y^2 + \sigma_n^2} = \frac{1}{1 + \frac{\sigma_n^2}{y^2}}, \tag{5.9}$$

given the noise is AWGN in nature with variance σ_n^2. In Eqn. 5.9, the estimator clearly takes the form factor of a Weiner filter with an inverse of signal-to-noise ratio (SNR) appearing in the denominator. However, it is different from a Weiner filter since σ_n^2 is a variance of a random variable (noise) and is different for every wavelet coefficient. The estimator θ can further be simplified in to a coefficient selector as shown to be useful for denoising by Pizurica et al. (2003), similar to a binary mask, as follows:

$$\theta_{mask} = \begin{cases} 1, \text{if } |y| > \sigma_n \\ 0, \text{if } |y| \leq \sigma_n \end{cases} \tag{5.10}$$

Since we do not know the noise free values of y, this estimator provides a fair estimate to begin the denoising procedure at a finer scale. The generalized terms introduced in Eqns. 5.10 will be utilized to estimate the signal and noise in various subbands.

5.3 3-D Wavelet Denoising

Wavelets have been previously applied for de-noising in many medical imaging applications (Bao and Zhang, 2003, Bullmore et al., 2001, Hilton et al., 1996, Unser and Aldroubi, 1996, Xu et al., 1994). The most general procedure is: (i) compute the discrete wavelet transform (DWT) (Mallat, 1999); (ii) utilize an appropriate method to remove or shrink the noisy wavelet coefficients; (iii) reconstruct the image by using an inverse wavelet transform from the de-noised wavelet coefficients. This procedure is usually applied on all the high-frequency wavelet sub-bands obtained post-DWT. A commonly used methodology for denoising wavelet coefficients as mentioned in (ii) is known as soft thresholding, originally proposed by Donoho (1995), Donoho and Johnstone (1994). The results in Donoho and Johnstone (1994) show that methods which introduce a high degree of smoothing also tend to produce more false positives, whereas, most wavelet-based methods with lower smoothing properties preserve the shape but may result in a higher number of false negatives. Another comprehensively comparative study (Wink and Roerdink, 2004) highlighted the differences between various threshold-selection schemes implemented in the WaveLab package (Buckheit et al., 1995) and the commonly used Gaussian smoothing.

The most popular approach for image denoising in the wavelet domain is coefficient thresholding in the orthogonal wavelet domain. First detailed by Donoho and Johnstone (1994) in the form of a systematic theory applied to one-dimensional curve estimation where various thresholding schemes for denoising were tested in simulated conditions. An extensive review of wavelet domain thresholding in image processing can be found in Jansen (2001).

In a wavelet decomposition, most coefficients contain the signal of interest. However, in numerous coefficients the signal component appears with insignificant energy. Thresholding helps identify these coefficients efficiently through the following hypothesis:

$$\begin{aligned} H_l^0 &: \text{"`signal of interest is absent."'} \Leftrightarrow |y_l| < T \\ H_l^1 &: \text{"`signal of interest is present."'} \Leftrightarrow |y_l| \geq T \end{aligned} \tag{5.11}$$

where T is a threshold that defines a criterion for signal of interest. Prior to describing our method for empirical thresholding 5.3, we summarize the limitations and advantages of the most common method of thresholding used in denoising applications.

5.3.1 Hard and Soft Thresholding

The two standard thresholding methods schemes are known as: *hard-thresholding* (*keep or kill*), and *soft thresholding* (*shrink or kill*). In both cases, the wavelet coefficients not qualifying a certain threshold are set to zero. In hard thresholding, there is no change in coefficient values that pass the threshold test:

$$T^{hard}(w) = \begin{array}{r} 0, \text{ if } |w| \leq T, \\ w, \text{ if } |w| > T. \end{array} \tag{5.12}$$

However, a disadvantage of the hard thesholding method is its abrupt discontinuity, that is, the denoised coefficients end up having a large variance and are highly sensitive to small changes in the data. As a result, this yields abrupt artifacts in the reconstructed signal when input signal noise is high (low SNR). Soft-thresholding is a favorable alternative that was proposed to mitigate the effect of above mentioned limitation. The magnitudes of the coefficients above the threshold are reduced by an mount equal to the value of the threshold, described as:

$$T^{soft}(w) = \begin{array}{r} 0, \text{ if } |w| \leq T, \\ sgn(w)(|w| - T), \text{ if } |w| > T. \end{array} \tag{5.13}$$

In soft thresholding, the reduced magnitude of resulting estimates result in an over-smoothed reconstructed image. In image processing applications, this is a fair trade-off to avoid having abrupt discontinuities in the signal as introduced by hard thresholding.

5.3.2 Likelihood Ratio of Signal Presence

The coefficients in each wavelet sub-band that correspond to signal of interest are assumed to be *independently identically distributed* (i.i.d.) random variables. An i.i.d. random variable's probability density function (pdf) is also commonly known as a conditional probability distribution if there is a certain condition that is assumed to be true for the distribution to hold. In other words, the wavelet coefficients either correspond to the presence of signal(H^1) or absence of signal (H^0) resulting in probability distribution functions - $p(w_l|H_l^1)$ and $p(w_l|H_l^0)$ respectively. Accordingly, the MMSE estimate of our denoised signal can be expressed as $\hat{y}_l$ (estimate of y_l), where sum of conditional means of signal and noise separately:

$$\hat{y}_l = E(y_l|w_l) = E(y_l|w_l, H_l^1)P(H_l^1|w_l) + E(y_l|w_l, H_l^0)P(H_l^0|w_l) \tag{5.14}$$

Simplifying Eqn. 5.14, the second term is assumed to be zero, since H_l^0 refers to absence of signal leaving only one term on the right-hand side of the equation. Note that, the solution we are going to present here, is similar to the model derived in Eqns. 5.7 - 5.9. For practical purposes, the mean of signal if the hypothesis H_l^1 is true can be assumed to take the value of the wavelet coefficient itself, *i.e.* , $E(y_l|w_l, H_l^1) = w_l$. The last component in Eqn. 5.14 - $P(H_l^1|w_l)$ can be formulated by applying the Bayes rule. These assumptions and substitutions help obtain the estimate $\hat{y}_l$ using the model derived in Eqn. 5.9:

$$\begin{aligned} &\hat{y}_l = \tfrac{\Lambda_l}{1+\Lambda_l} w_l, \qquad \text{with likelihood ratio} \quad \Lambda_l = \mu_l \tfrac{p(w_l|H_l^1)}{p(w_l|H_l^1)} \\ &\text{where, } \mu_l = P(H_l^1)P(H_l^0). \end{aligned} \tag{5.15}$$

Most wavelet domain estimators use the above model. However, what is essentially different in our approach is the application of a 3-D local spatial activity indicator to estimate the shrinkage factors (the coefficient of w_l in Eqn. 5.15) for each subband.

5.3.3 Spatial Adaptation

The most important question is how do we estimate the probability of signal presence in a given wavelet coefficient w_l at a location l (w is the signal in wavelet domain; see Eqn. 5.3). We propose an original approach in this respect, using 3-D wavelet transforms and a local spatial activity indicator.

The characteristics of various types of noise and estimators discussed in Section 5.2 deal with Gaussian noise. In fMRI data, it is better to model the noise adaptively in order to achieve efficient denoising and improved SNR. For noise types other than Gaussian, it is difficult to model the distribution of the noise free coefficients from their noisy histogram (Pizurica et al., 2003). For clarity,we redraw the framework from (Pizurica et al., 2003) in Figure 5.1 after merging the contributions of this thesis, that is, 3-D SWT, 3-D local spatial acitivity indicator and ban-specific estimation of noise variance as detailed below. Thus, a better approach is one that is built upon empirical parameters that are estimated using the data itself.

The empirical estimation of probabilities and the conditional probability density functions begin with derivation of masks that indicate the positions of significant wavelet coefficients in a given detail sub-band image. The hypothesis H_l^0 and H_l^1 presented earlier in Eqn. 5.11 can be represented as two events $X_l = 1$ and $X_l = 0$, respectively, where X_l is a binary random variable derived from the sub-band image using a set threshold T. Note that, the previous notation of prior probabilities change from $P(H_l^1)$ and $P(H_l^0)$ to $P(X_l = 1)$ and $P(X_l = 0)$ respectively, whereas $p_W(w|H^1)$ and $p_W(w|H^0)$ change to $p_{W_l|X_l}(w_l|1)$ and $p_{W_l|X_l}(w_l|0)$ for signal and noise distributions respectively. The estimated value of the signal-of-interest is given by:

$$\hat{y}_l = \frac{\xi_l \eta_l}{1 + \xi_l \eta_l} w_l, \tag{5.16}$$

$$\xi_l = \frac{p_{W_l|X_l}(w_l|1)}{p_{W_l|X_l}(w_l|0)}, \;\; \eta_l = \frac{P(X_l = 1|\Phi)}{P(X_l = 0|\Phi)} \tag{5.17}$$

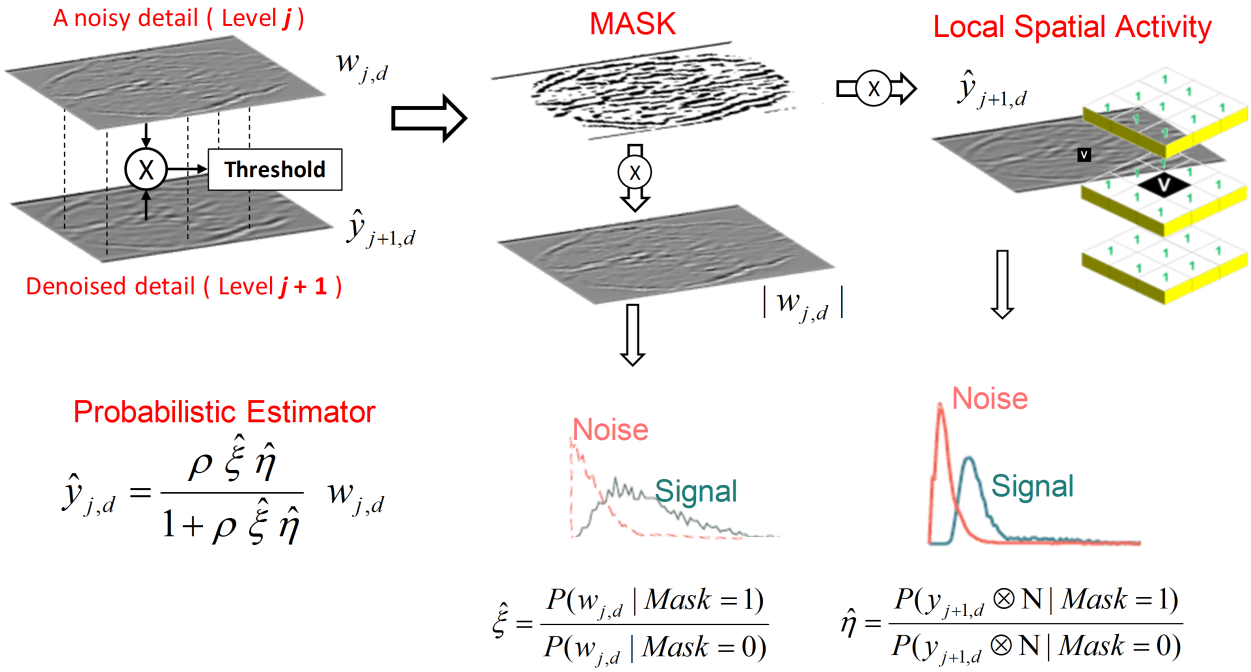

Figure 5.1: A step-by-step illustration of the proposed 3-D fMRI denoising scheme based on the approach proposed in (Pizurica et al., 2003)

where Φ represents abstract prior knowledge involved in estimating the probability of $H_l^{0,1}$.

In fMRI data, each voxel contains information relating to the BOLD signal and is associated with its neighboring voxels temporally and spatially. The ability to remove noise based on such spatial relationships is more beneficial compared to using a common filter, such as Gaussian or others, for all time points across all voxels.

If the probability of signal being present is known to be *local*, *i.e.* based on voxel location l, then this probability has to be a function of the wavelet coefficient w_l and its neighboring coefficients in a 3-D subspace. To simplify further, we will replace Φ with a i.i.d. random variable z_l in equation 5.17. Thus, an estimate of η_l can be simplified to Eqn. 5.18 by applying Bayes theorem:

$$\eta_l = \rho \frac{p_{Z_l|X_l}(z_l|X_l = 1)}{p_{Z_l|X_l}(z_l|X_l = 0)}, \qquad \rho = \frac{P(X_l = 1)}{P(X_l = 0)} \tag{5.18}$$

The variable z_l is modeled as the root-mean-squared (RMS) value within an isotropic 3-D

neighborhood δl of size $K \times K \times K$, that represents 26-connected voxels ($K = 3$) around any given voxel l and given by Eqn. 5.19.

$$z_l = \sqrt{\frac{1}{N} \sum_{k \in \delta l} |w_k|^2}. \tag{5.19}$$

where absolute value of w_k is utilized since the wavelet coefficients are symmetric around zero.

To estimate the unknowns in Eqn. 5.18 empirically from a 3-D detail sub-band, an estimate of the binary random variable, that is realized as a binary volume - $\hat{x}$ is required. A *coarse-to-fine* thresholding procedure proposed by Pizurica et al. (2003) is extended for each sub-band obtained through a separable 3-D stationary wavelet transform. The noise variance derivation for 3-D wavelet sub-bands can be considered as an extension of the discussion in Section 5.2.2. The sub-bands $w_j^{LLH,LHL,HLL}$ are computed for j by applying the low pass filter h_0 $3j-1$ times, whereas the high-pass filter is applied only once. Thus, the resolution function S_j^d introduced in Eqn. 5.5 is expressed for 3-D sub-bands as:

$$\begin{aligned} S_j^{LLH,LHL,HLL} &= (\sum kh_{1k}^2)\,(\sum lh_{0l}^2)^{(3j-1)}, \\ S_j^{LHH,HLH,HHL} &= (\sum kh_{1k}^2)^2\,(\sum lh_{0l}^2)^{(3j-2)}, \\ S_j^{HHH} &= (\sum kh_{1k}^2)^3\,(\sum lh_{0l}^2)^{3(j-1)}. \end{aligned} \tag{5.20}$$

The noise variance of each 3-D sub-band, $\hat{sigma}_{n,j}^2$ can be estimated by substituting Eqns. 5.6 and 5.20 in Eqn. 5.4, and is given by $\hat{sigma}_{n,j}^2 = \sigma_n^2 S_j^d$ for each detail sub-band d. In this respect, the coarse-to-fine procedure is applied to estimate the binary random variable $x_{l,j}$, at level j, using the estimate from a coarser level, $y_{l,j+1}$ with the coefficients of a finer level $w_{l,j}$ for every detail sub-band as given below (also see block diagram in Figure 5.2):

$$\hat{x}_{l,j} = \begin{cases} 1, & |w_{l,j}||\hat{y}_{l,j+1}| < (K\hat{\sigma}_{n,j})^2, \\ 0 & |w_{l,j}||\hat{y}_{l,j+1}| \geq (K\hat{\sigma}_{n,j})^2 \end{cases} \tag{5.21}$$

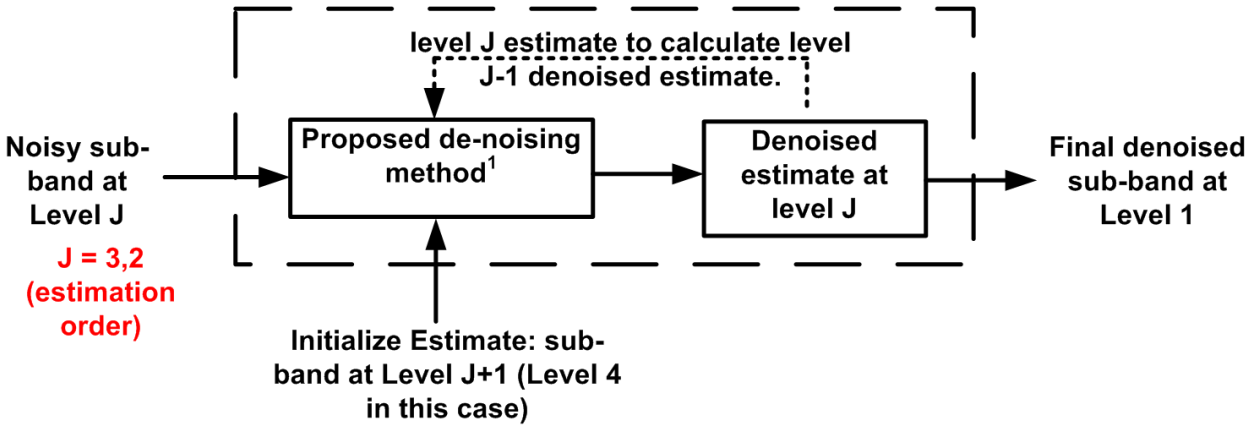

Figure 5.2: The hierarchical estimation scheme depicting the multi-level approach to calculate the denoised estimate of input fMRI data.

where K is a controlling parameter for the threshold that is set for determination of *signal of interest*. For fMRI denoising, we adopt $K = 2$ for empirical reasons also observed in (Pizurica et al., 2003). The already denoised coarser detail coefficients $\hat{y}_{l,j+1}$ at scale 2^{j+1} assist in detection of coefficients that most likely correspond to the *signal of interest* ($w_{l,j}$) at level j.

Finally, the binary mask $\hat{x}_l$ is utilized to calculate the empirical probability distributions - $p_{W_l|X_l}(w_l|1)$, $p_{W_l|X_l}(w_l|0)$, $p_{Z_l|X_l}(z_l|X_l = 1)$, and $p_{Z_l|X_l}(z_l|X_l = 0)$.

The former two *pdf's* are computed as normalized histograms of $\{w_l : l \in Q_0\}$ and $\{w_l : l \in Q_1\}$, where $Q_0 = \{l : \hat{x}_l = 0\}$, and $Q_1 = \{l : \hat{x}_l = 1\}$. Similarly, the *pdf's* for z_l can be estimated from the histograms of $\{z_l : l \in Q_0\}$ and $\{z_l : l \in Q_1\}$.

After obtaining the empirical estimates for all the probability distributions, we substitute the values in 5.16 where the estimates ξ_l and η_l first presented in Eqn. 5.17 can now be re-written as:

$$\xi_l = \frac{p_{W_l|X_l}(w_l|1)}{p_{W_l|X_l}(w_l|0)}, \quad \eta_l = \frac{p_{Z_l|X_l}(z_l|X_l = 1)}{p_{Z_l|X_l}(z_l|X_l = 0)} \tag{5.22}$$

The simplified terms in Eqn. 5.22 can now be substituted in Eqn. 5.16 to get the desired denoised value y_l. The final estimated value of y_l at level j=J, is utilized for initialization in order to compute $\hat{x}^l$ for the next coarser level $j - 1$ and so on. Finally, the aforementioned

procedure yields denoised estimates at the coarsest level ($j = 1$) which are then reconstructed back to the spatial domain and utilized for detection of brain activity using fMRI analysis tools such as ICA (Figure 5.2).

5.4 Wavelet Reconstruction of Denoised Data

In the next section, we present a combination of the wavelet-based denoising method and independent component analysis (ICA) for fMRI analysis. Since denoising is the last step in preprocessing pipeline, it can conveniently be combined with ICA that happens to be the first step in fMRI signal separation analysis. When performing multi-group studies especially those involving patients suffering from disorders such as schizophrenia or bipolar disorder, one needs to take the pre-processing effects on the data into account. The group difference statistics are undoubtedly affected by fMRI spatial pre-processing steps that include smoothing and normalization. As a solution to the denoising problem, we presented an alternative smoothing scheme in this section that utilized wavelets for denoising the fMRI volumes which can now be combined with ICA on wavelet-transformed (and denoised) data instead in the spatial domain as demonstrated in Figure 5.3. The ICA components are then reconstructed using inverse transform to obtain the activation maps in the spatial domain. The reason behind performing ICA in the wavelet domain is coherent with the fact that wavelet coefficients are decorrelated with respect to different spatial frequency bands. This serves as an added benefit for the ICA algorithm who's primary function is to separate the data into maximally independent components. The representation of data in the wavelet space helps in determining better edge-details and accurate contours for the resulting activation regions.

5.5 Wavelets and fMRI Signal Separation Methods

The ultimate goal of fMRI data analysis is to separate signal components due to true activations from components due to physiological fluctuations, instrumental artifacts and random

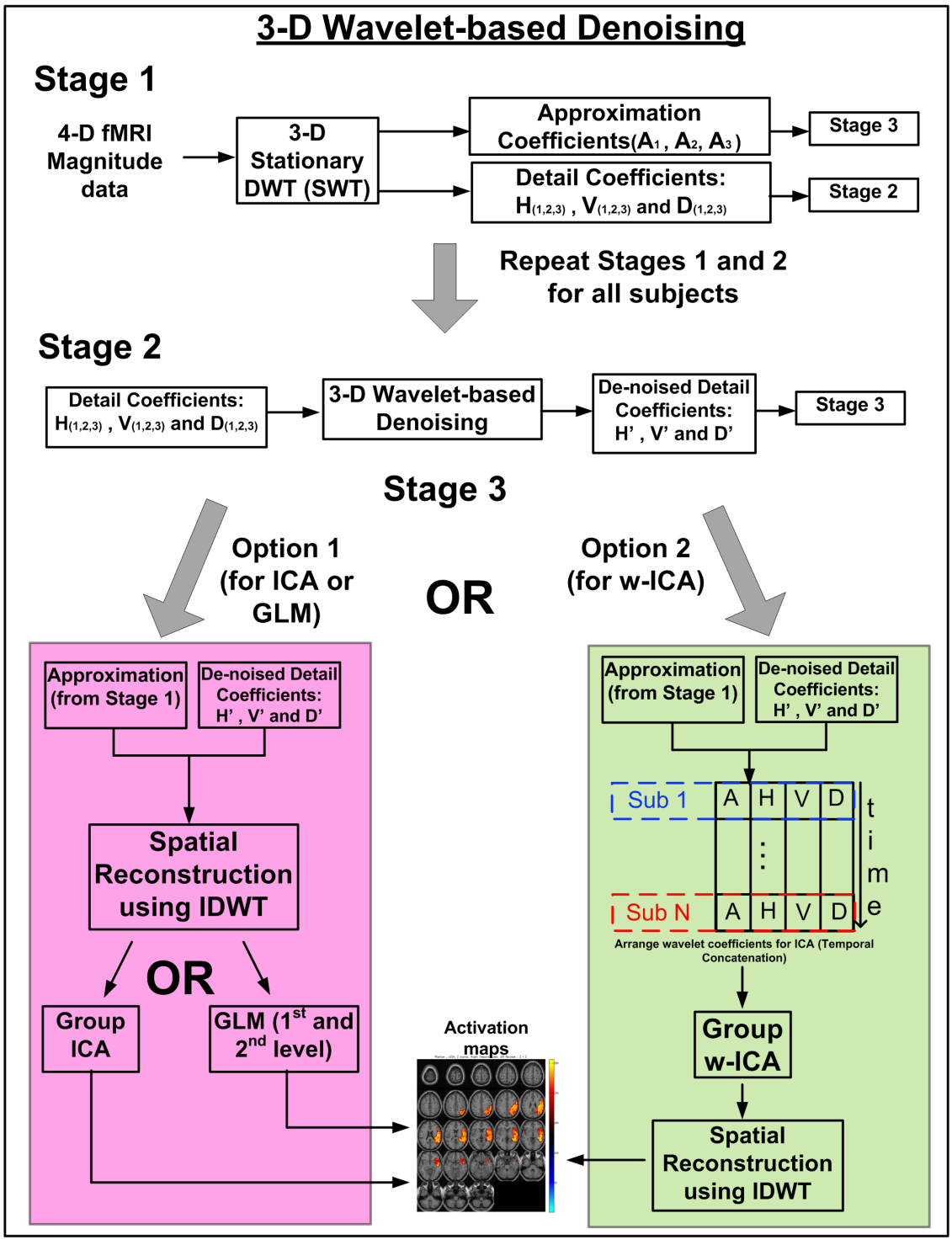

Figure 5.3: Block diagram illustrating the three major stages involved in the proposed wavelet-based fMRI processing framework. Stages 1 and 2 are repeated for all subjects followed by signal separation using group ICA in stage 3. The difference between the two presented options for stage 3 is based on the characteristic of the input data for ICA, spatial domain or wavelet domain. Option-1 was discussed in this section. whereas Option-2 is discussed in Section 5.5.

noise. To achieve this objective, suitable statistical methods are applied to these denoised volumes. As explained before SPM (Frackowiak, 2004, Friston et al., 1994) uses a linear model to derive a parameter map from Gaussian smoothed fMRI data (Poline et al., 1997). A relatively new framework that integrates wavelet-based processing with statistical testing (SPM), known as the Wavelet-SPM or WSPM was introduced by Van De Ville et al. (2006, 2007). This method uses the favorable properties of wavelets, such as de-correlated wavelet coefficients, to adaptively denoise the parameter map (Van De Ville et al., 2006) and perform statistical testing in the spatial domain after reconstruction (Van De Ville et al., 2007). The final detected parameter map in (Van De Ville et al., 2007) is observed to be more closely related to the measured data and has reduced spatial bias as compared to the Gaussian smoothing approach implemented in SPM.

Apart from highly successful parametric methods stated above, wavelet processing has been utilized alongside non-parametric processing techniques. Long et al. (2004) directly derive well-defined activation maps using a spatially constrained maximum-likelihood criterion on multi-scale representations of the data. Another technique proposed by Breakspear et al. (2004) utilized bootstrapping methods in the spatial and spatio-temporal domain. They applied non-parametric null-hypothesis testing on spatiotemporally re-sampled data in the wavelet domain. This helped preserve spatial and temporal correlations between slices and also maintained the irregular geometry of intracranial images. A more recent extension of this method (Sendur et al., 2007) utilizes a similar re-sampling method to estimate multi-level noise variance and thresholds for significance testing.

Independent component analysis (ICA) is a data-driven approach based upon signal source separation. It is widely used for both task and resting-state data and combined with the basic pre-processing steps such as PCA and whitening (Calhoun09b; McKeown98). This approach identifies components which are maximally independent and linearly mixed; hence each component reflects brain regions which exhibit temporal coherence (functional

connectivity). The foremost advantage of ICA is its applicability to detect cognitive patterns for which an a priori temporal model is unavailable. ICA has proven to help reveal inter-subject and inter-event differences in temporal dynamics as well as detect changes with respect to spatially distributed brain networks (Calhoun et al., 2009a). By far the most common application of ICA is extraction of spatially independent brain regions (spatial ICA) although temporal ICA is also possible (Calhoun et al., 2001b).

The advantages of wavelet-based processing combined with a source separation technique such as ICA remain unexplored and have not yet been reported with sufficiently supportive and convincing results. Previously, there have been a few attempts to combine the power of wavelet processing (in order to de-correlate data), with a widely applied fMRI analysis technique such as ICA (Azzerboni et al., 2004, 2005, Johnson et al., 2007). A more recent technique that utilizes a combination of wavelet-domain ICA with Wiener filtering of wavelet coefficients is introduced in (Boroomand et al., 2007). They utilize a hybrid approach in order to remove undesirable effects due to noise on accurate source separation using ICA. Comparison between different ICA algorithms is performed for data sets with SNR ranging up to $70dB$. At realistic SNR levels ($\approx 15 - 35dB$), the algorithm performs with a low percent sensitivity (true positive rate) of about 70% with little emphasis on preservation of shape of the activation regions. The application of the Wiener filter in the wavelet domain improves the performance of time-domain Wiener filtering, introducing the least amount of temporal smoothing, eventually resulting in a good estimate of noise in a least squares sense.

5.5.1 Proposed Wavelet-ICA (w-ICA) Approach

When performing multi-group studies especially those involving patients suffering from disorders such as schizophrenia or bipolar disorder, one needs to take the pre-processing effects on the data into account. The group difference statistics are undoubtedly affected by fMRI spatial pre-processing steps that include smoothing and normalization. As a solution to the denoising problem, we presented an alternative smoothing scheme in Section 5.3 that

utilized wavelets for denoising the fMRI volumes. In addition to denoising in wavelet space, we explored the option of applying ICA on wavelet-transformed data instead in the spatial domain (Khullar et al., 2011c). The primary reason for applying ICA on transform domain data is based on the fact that wavelet sub-bands are highly uncorrelated in terms of spatial distribution.

The sparsely distributed data in the wavelet domain is obtained by applying symlets filters in all three directions sequentially, eventually resulting in seven detail sub-bands at every level. Each of these sub-bands emphasize upon different sets of spatial frequencies comprising a volumetric image at any given time point in the fMRI data set. This data is then smoothed using the proposed denoising scheme (Section 5.3). After applying the proposed denoising scheme to these detail sub-bands, the wavelet coefficients are reconstructed along the z-dimension as shown in Fig. 5.4 to avoid any possible redundancies in the data set in addition to increasing computational efficiency followed by application ICA (see Eqn. 2.14). This reconstruction also reduces data redundancy while maintaining de-correlated state of the input data. The ICA components are then transformed back to the spatial domain using an inverse discrete wavelet transform. A more detailed description of aforementioned approach can be found in Khullar et al. (2011b,c).

The sparsely distributed data in the wavelet domain is obtained by applying *symlets* filters in all three directions sequentially, eventually resulting in seven detail sub-bands at every level. Each of these sub-bands emphasize upon different sets of spatial frequencies comprising a volumetric image at any given time point in the fMRI data set. After applying the proposed denoising scheme to these detail sub-bands, the wavelet coefficients are reconstructed along the axial dimension (see Figure 5.4) to avoid any possible redundancies in the data set in addition to increasing computational efficiency.

Each denoised sub-band was lexicographically ordered along the temporal dimension and concatenated into a $(4 * L) \times T$ mixed signal matrix known as $M(x, t)$ (see Figure 5.5), where L is the total number of voxels in a single sub-band and T is the temporal extent for any

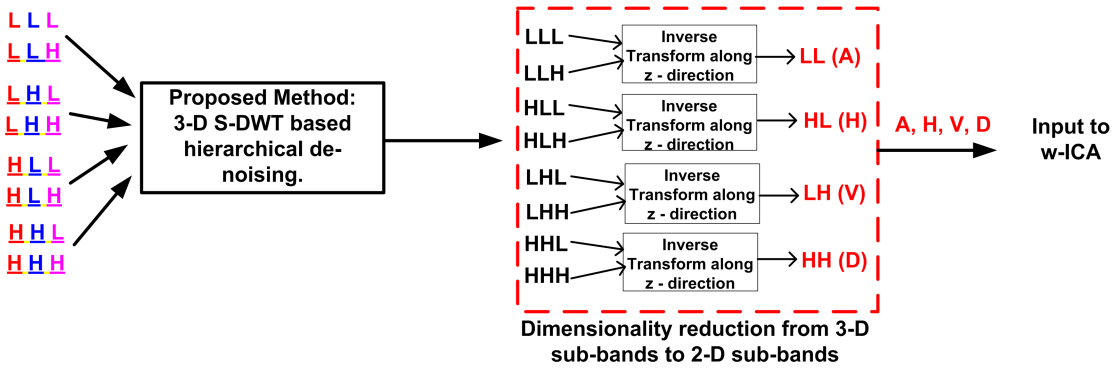

Figure 5.4: Partial reconstruction of wavelet coefficients for applying ICA in the wavelet domain: **Partial reconstruction of wavelet coefficients for applying ICA in the wavelet domain:** The denoising module works with 3-D wavelet coefficients whereas the input to the ICA module is prepared by reconstructing along the z-direction to improve computational complexity. The reconstruction also reduces data redundancy while maintaining de-correlated state of the input data.

arbitrary voxel ($T = 150$). Each row in $M(x,t)$ represents the temporal signal associated with each voxel. Spatial ICA decomposes $M(x,t)$ into numerous components, each comprising a spatial map and a corresponding time course (Calhoun et al., 2003, McKeown et al., 1998), which may be written as Eqn. 5.23 below.

$$M(x,t) = \sum_{k=1}^{K} S_k(x) A_k(t) \tag{5.23}$$

where K is the number of spatially independent components, which was set to 20 for the simulated data. The number of optimal number of components (≈ 20) for our experiment was obtained using the MDL criterion (Tenmoto et al., 1998). A_k is the time course of component k whereas S_k represents the spatial data in the transform domain. For final analysis, S_k is transformed back to the spatial domain by utilizing the wavelet reconstruction filters.

The primary reason behind performing ICA in the wavelet domain is coherent with the fact that wavelet coefficients are decorrelated with respect to different spatial frequency bands. This serves as an added benefit for the ICA algorithm who's primary function is to separate the data into maximally independent components. The representation of data

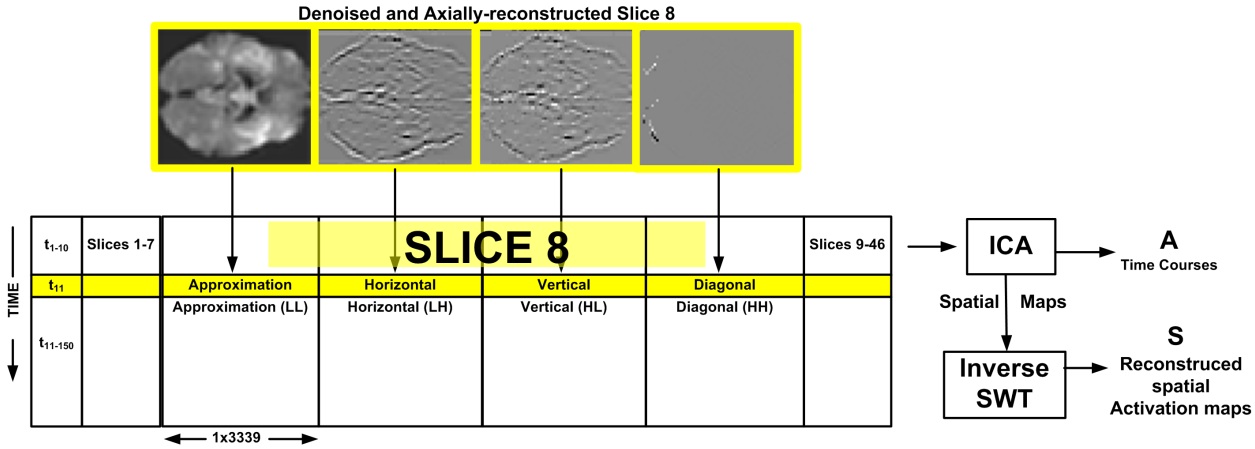

Figure 5.5: **Illustration of wavelet-domain ICA:** Note how each wavelet sub-band is arranged slice-by-slice after reconstructing the 3-D denoised sub-bands along the axial dimension.

in the wavelet space helps in determining better edge-details and accurate contours for the resulting activation regions.

5.6 Results

In what follows, we illustrate the results from our denoising framework through illustrative, qualitative and quantitative comparisons against the well-established and commonly applied Gaussian kernel smoothing approach. At the end of this approach, the reader will be able to quantify and compare the advantages of the wavelet denoising method on its own and in combination with ICA (w-ICA) over the conventionally used denoising and signal separation methods for fMRI data.

5.6.1 Simulated fMRI Data

For clearly demonstrating the advantages of denoising, a set of ground truth activation maps were chosen and simulated data was generated accordingly. For this study, the artificial data was generated using a real resting state fMRI data set as the baseline signal and by adding activations of varying percent signal change. The data was primarily divided on the basis of known anatomical regions of the brain. The spatial maps corresponding to the regions of

interest (ROI) were created by utilizing the software package WFU Pick Atlas (Lancaster et al., 2000) . The left temporal lobe and the left occipital lobe regions were selected as the two main ROIs on the basis of number of voxels and their complex shape.

In our simulations, there are three main aspects associated with the generation of the fMRI data set: (1) baseline signal (no task-related activation); (2) signal level of activation voxels; (3) noise level in data set. For the activation signal, a simple block design type signal was used (six blocks of ten-second off time, fifteen second on time) lasting 150 seconds. 4-D binary masks corresponding to each region of interest (temporal lobe, occipital lobe) were multiplied by this activation signal in order to simulate a data set closely corresponding to BOLD related activity. The question here to be asked is how much intensity change is a fair representative of the change in BOLD signal when a task-related activity occurs in the brain. For our simulations, we generate data sets for two signal levels, 1% and 3%, of the maximum numerical value in resting state fMRI data used as the baseline signal. These values were chosen based on the fact that task-related BOLD signal change is very small compared to the total spatial and temporal variability across images (Huettel et al., 2004). The block diagram shown in Figure 5.6 depicts the process applied for the generation of a software phantom.

As additional noise, Rician distributed noise is introduced into the data set after the superposition of the 4-D activation mask as explained above. Eqns. (1) and (2) summarize the data generation process below:

$$\begin{aligned} &Y = S_0 + LS_P, \qquad \text{where} \quad L = PS_0^{max} \text{with} P \in 1\%, 3\% \\ &Y_{noisy} = \sqrt{(Y+\alpha)^2 + \beta^2} \end{aligned} \tag{5.24}$$

where S_0 is the baseline resting state fMRI magnitude data, S_P is the 4-D ROI activation mask, L is the artificial signal level and Y is the clean magnitude data phantom (no external noise added). Y_{noisy} is obtained by utilizing a Rician distribution model (Gudbjartsson and Patz, 1995) where α and β are randomly generated Gaussian noise frames given by $N(0, \sigma)$

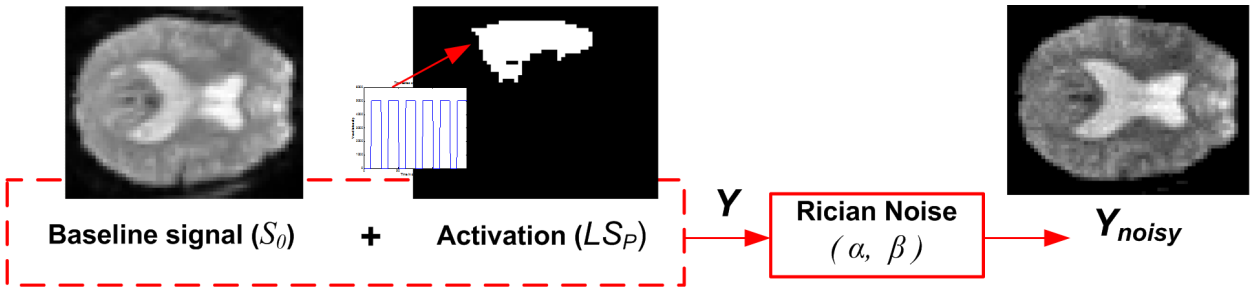

(a) Simulated data generation

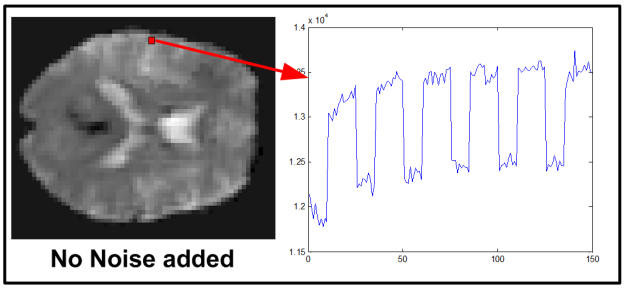

(b) no added noise

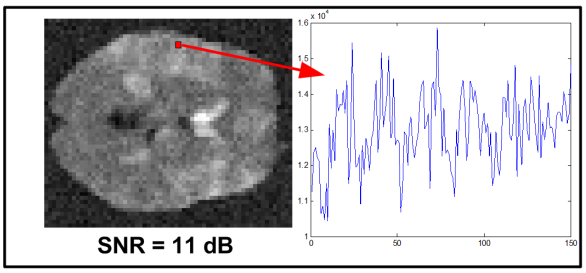

(c) 12% added noise

Figure 5.6: **Software phantom data generation:** (a) Illustration of phantom data generation: a single slice depicting baseline intensity values along with the block design type task related time course and the ROI mask (temporal lobe). These are added together and input to the Rician noise model to obtain the noisy slice (Y_{noisy}); the bottom two figures depict the time course and intensity representations when (b) no noise is added, and when (c) there is added Rician noise.

and where σ is different noise levels ranging from $6\% - 12\%$ of the mean value of the baseline signal (μ_{S_0}).

The process described above was repeated to generate data for all combinations of signal levels (1% and 3%), noise levels (6%, 8%, 10%, and 12%), and the selected ROIs (temporal lobe and occipital lobe) providing 16 different simulated 4-D fMRI data sets. These simulated data sets are referred to as 'software phantoms' in the remaining portion of this chapter. An important fact associated with the above simulation process is that the baseline resting state fMRI signal is slice time corrected, re-aligned and spatially normalized, but no denoising/smoothing scheme is applied. Effectively, the baseline data is already noisy due to the intrinsic noise in raw data in addition to the externally simulated Rician noise as explained above.

An example depicting both spatial and temporal representations of an activation component is presented in Figure 5.7.

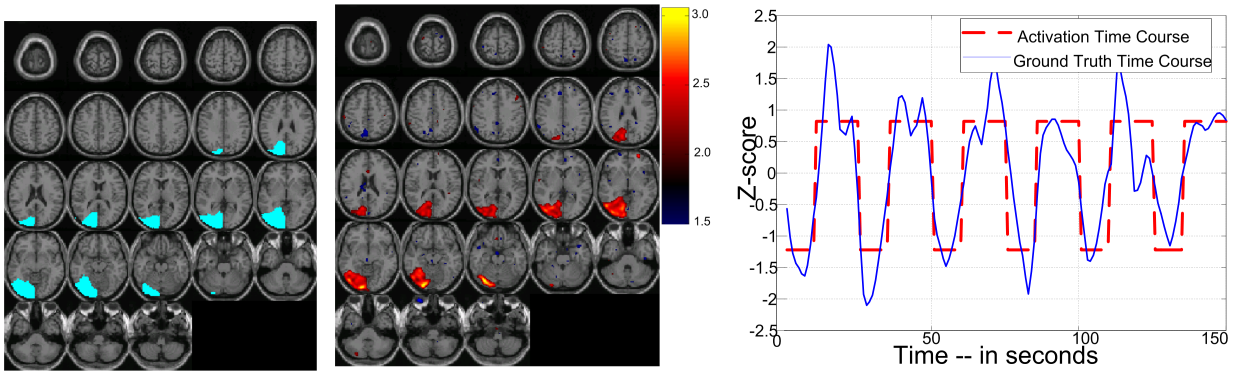

(a) Ground Truth (b) Activation Component (c) Time Course

Figure 5.7: An example of the activation component obtained using the proposed method: (a) ground truth voxels represented as a different color (not Z-scores); (b) spatial Z-score map ($Z \geq 3$) representing the activation regions as extracted through ICA in the wavelet domain; (c) corresponding time course of the component shown in (b) along with the waveform of the ground truth introduced as activation.

5.6.2 w-ICA vs. s-ICA

The results from the proposed denoising/w-ICA framework were benchmarked against those obtained through the conventionally used FWHM Gaussian smoothing/s-ICA methodology. In order to furnish a fair indication of the overall performance of our proposed w-ICA framework, ROC curves were estimated for sixteen data sets artificially generated through all possible combinations of ROIs (Temporal and Occipital Lobe), signal (1% and 3%) and noise levels (6%, 8%,10%, and 12%) as explained previously in Section 5.6.1. Each of these data sets is comprised of 46 slices per volume and 150 time points, thus resulting in a single spatio-temporal image of size $53 \times 63 \times 46 \times 150$. In addition, to understand and quantify the effect of the random distribution of noise in the data sets, we generated 10 spatio-temporal images for every unique combination of the above parameters (signal + noise (n)) where noise (n) corresponds to a random noise frame. Effectively, the complete software phantoms data set is comprised of a total of 160 spatio-temporal volumetric images (16 unique combinations $\times$ 10 noise frames per combination). This experiment allowed us to determine an unbiased estimate representing the performance of each algorithm, as discussed in this section.

For the purpose of obtaining the comparative de-noised data corresponding to the widely used Gaussian-based method, we applied an $8 \times 8 \times 8$ mm^3 FWHM Gaussian kernel built in the SPM package (Friston et al., 1994). This was followed by estimation of the activation components using the GIFT toolbox (Rachakonda et al., 2007), and the final Z-score maps for each smoothed data set.

ROC Analysis: Occipital Lobe (or Visuo-motor)

This ROI was selected based on its complex shape in terms of contours and edges in addition to its correspondence with visual tasks that stimulate the Visuo-motor in case of real fMRI experiments.

ROC curves were estimated by utilizing the activation component Z-maps for all data and the results are presented in Table 5.1a. For better understanding, the ROC curves

Signal Level = 1%					
Method	ROC	6% Noise	8% Noise	10% Noise	12% Noise
w-ICA	TPR %	89.3 ± 0.3	88.4 ± 0.4	88.3 ± 0.6	87.5 ± 0.4
	FPR %	0.3 ± 0.03	0.31 ± 0.04	0.37 ± 0.07	0.41 ± 0.09
s-ICA	TPR %	86.7 ± 0.2	86.51 ± 0.2	86.3 ± 0.2	86.1 ± 0.37
	FPR %	1.06± 0.07	1.21 ± 0.03	1.22 ± 0.08	1.39 ± 0.04

Signal Level = 3%					
Method	ROC	6% Noise	8% Noise	10% Noise	12% Noise
w-ICA	TPR %	90.91 ± 0.08	90.86 ± 0.11	90.78 ± 0.13	90.51 ± 0.18
	FPR %	0.41 ± 0.02	0.39 ± 0.02	0.39 ± 0.02	0.29 ± 0.02
s-ICA	TPR %	87.29 ± 0.17	87.15 ± 0.11	87.14 ± 0.07	87.09 ± 0.1
	FPR %	1.3 ± 0.03	1.3 ± 0.02	1.29 ± 0.02	1.3 ± 0.01

Table 5.1: **ROC statistics (Occipital Lobe):**Depicting the mean and std. deviations for 10 random noise frames generated for each combination of signal and noise: (a) Signal level = 1%: an improvement of about 2 - 3% for the TPR and 0.7 - 1% for FPR is observed for w-ICA; (b) Signal level = 3%: The TPR and FPR values remain almost constant for varying noise levels with w-ICA outperforming s-ICA in every case above.

corresponding to the lowest and highest noise levels (6% and 12%) are shown in Figure 5.8. These curves were generated using Z-values in steps of 0.1 within the threshold interval (1.5, 3.0). In order to fairly represent the TPR and FPR values, an empirical Z-threshold value was obtained using the data set with highest noise content (1% signal, 12% noise). There is not an imperative requirement for an empirical threshold, as seen in Figure 5.8, but in order to numerically present the performance difference between the two methods (see Table 5.1a), we carefully choose an empirical threshold which helps capture a good estimate of this difference. This empirical threshold was set to $Z_{empirical} = 2.0$ and used across all occipital lobe data sets for estimation of the TPR and FPR values (reported in Table 1). Further, the thresholded binary map is utilized as input to estimate the values of the proposed shape metrics.

Note that, a single data point on any curve in Figure 5.8 corresponds to the mean of true positive rate (TPR) or false positive rate (FPR) value across 10 noise frames at a threshold in the interval (1.5, 3.0). These mean and standard deviation values are reported in Table 5.1.

It is evident from Figure 5.8 and Table 5.1a that the proposed w-ICA framework performs better in terms of classifying activation voxels as compared to the existing framework (s-ICA) for this ROI. These improvements are a direct result of applying and utilizing the selective smoothing abilities of wavelets (preserving edges) and the novel multi-directional denoising technique adopted in this paper.

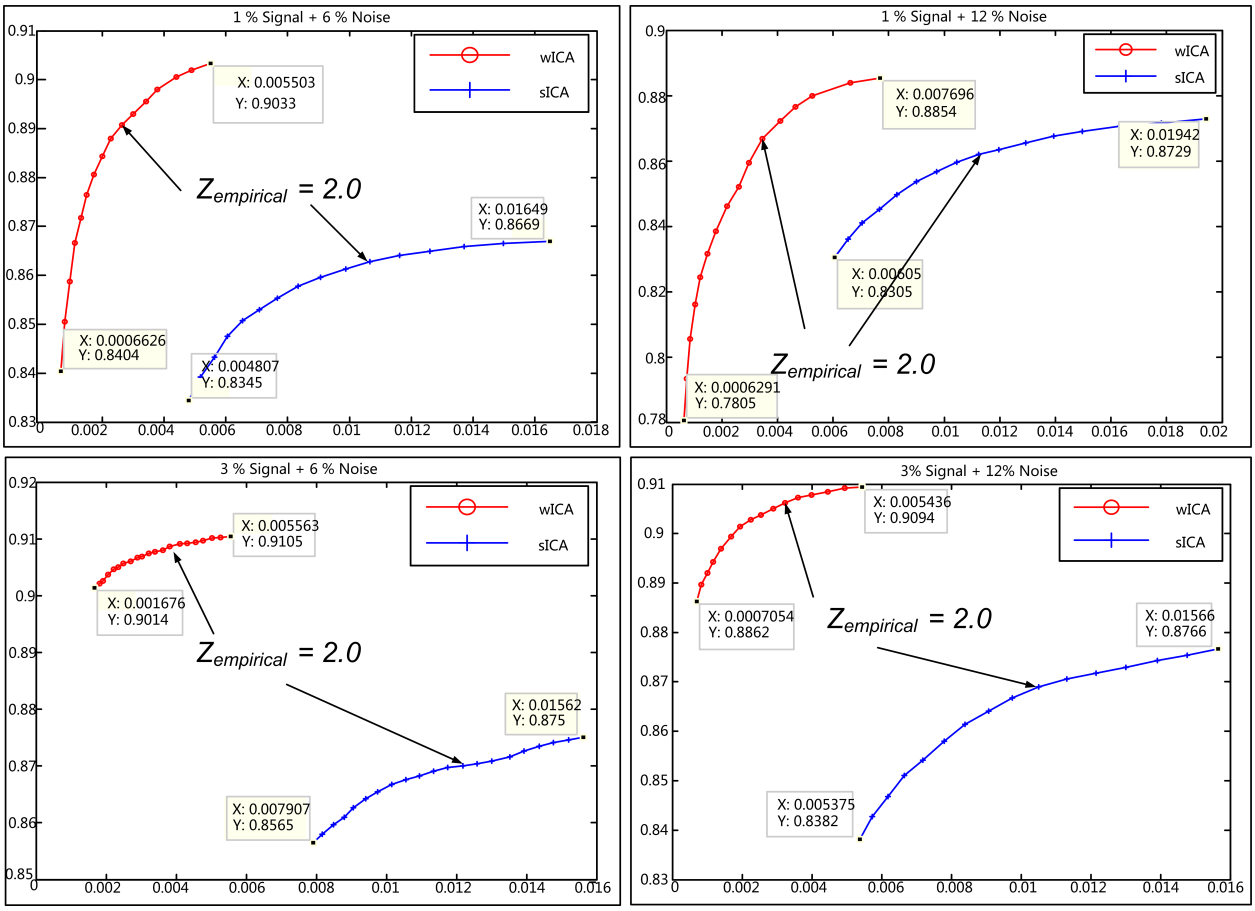

Figure 5.8: **ROC Curves (Occipital Lobe):** with indication of empirical threshold for two signal levels (1%: top row, 3%: bottom row) and two selected noise levels (6%: left column, 12%: right column) used. Curves for w-ICA show consistently lower FPR for any signal/noise combination (see discussion).

The TPR and FPR vary with varying noise levels. As the amount of noise increases, the TPR is expected to decrease, but more importantly the FPR is expected to significantly increase due to a greater number of voxels being misclassified. In the case where the diagnostic criteria between two groups of subjects are the spatial extent of an activation region or the accuracy of its shape, the ability to achieve a low number of false positive voxels is an imperative requirement. The proposed framework is able to achieve this with ease and facilitates avoiding high FPR even when applied to data with SNR as low as 11 dB (1% signal, 12% noise). As the noise is increased for signal level $\approx 1\%$, the TPR for w-ICA reduced by less than 2% whereas the FPR only increased from 0.3% to about 0.4% (an increase of about 40 voxels).

The results for the s-ICA framework are close to the theoretical expectation, where the TPR and the FPR do not vary significantly with increasing noise levels due to the high spatial smoothing property of FWHM kernels. An essential requirement of any denoising/classification algorithm is to produce the least number of false positives while being able to produce a greater number of true positives. To this effect, s-ICA was outperformed consistently by the proposed w-ICA technique with it yielding about 200 to 400 less false positives on an average for all combinations of signal levels (1%, and 3%) and noise (6%, 8%, 10%, and 12%).

Another interesting characteristic of results is observed with regard to the maintenance of intensity integrity in the spatial component maps across most voxels associated with the activation regions obtained through the w-ICA framework. Whereas in results obtained through the s-ICA framework, the activation regions consist of high valued voxels towards the center (see Figure 5.9b). This is a direct result of crude spatial smoothing using FWHM Gaussian kernels where the nearby voxels which do not represent the ROI are taken into account while smoothing, thus resulting in higher values and more false positives (as depicted in Figure 5.9b).

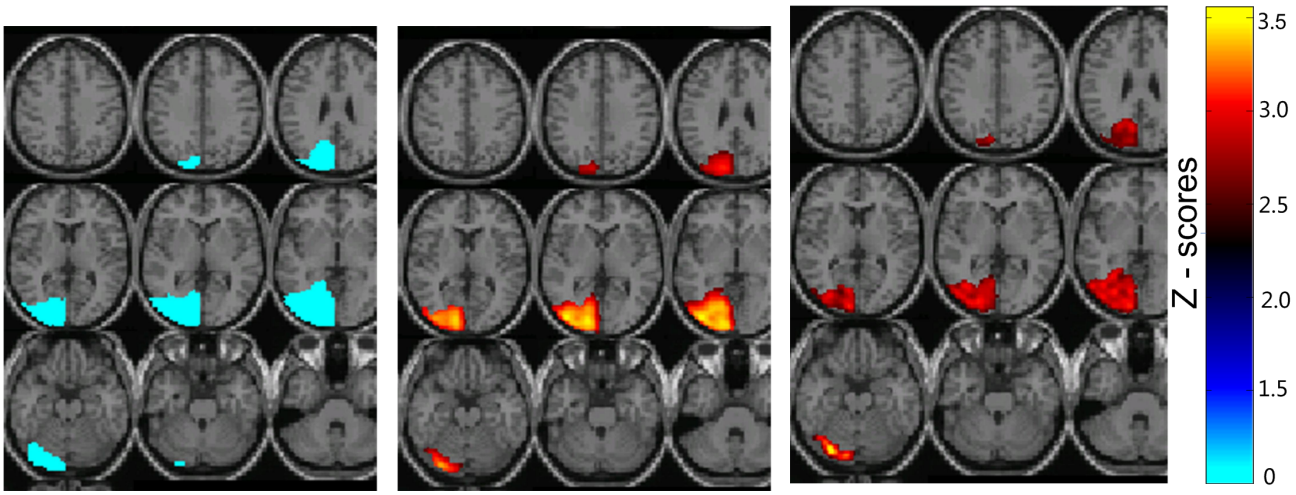

(a) Ground Truth (b) s-ICA (c) w-ICA

Figure 5.9: **Intensities across the activation region:** The image for s-ICA shows centrally bright areas due to its high spatial smoothing properties. The image for w-ICA has more uniform values throughout the activation region (5.9c) as originally introduced in form of the ground truth (5.9a). The ROI highlighted in ground truth is label map in contrast to the Z-score maps presented for s-ICA and w-ICA.

This added advantage of w-ICA may play a useful role when analyzing functional connectivity of default mode networks through spatial correlations and overlap. A great deal of research has been done to understand spatial patterns of inter-correlation between underlying cognitive networks in absence of task-evoked activity (Calhoun et al., 2009a,b, Smith et al., 2009). For example, an arbitrary voxel with high Z-score value (or any other statistic) within an activation region is utilized in connectivity analysis for establishing functional relationships. Spatial correlation analysis may incidentally indicate strong connectivity due to the high Z-score associated with this voxel but ground truth may indicate otherwise. Effectively, this may lead to a large bias and sometimes even false connections when performing a study on a group of subjects. However, the proposed w-ICA framework combined with our 3-D wavelet denoising approach is expected to perform better by facilitating the elimination of such a bias.

ROC - Signal Level = 1%					
Method	ROC	6% Noise	8% Noise	10% Noise	12% Noise
w-ICA	TPR %	91.89 ± 0.65	90.83 ± 0.73	89.3 ± 0.7	86.67 ± 0.8
	FPR %	0.602 ± 0.02	0.57 ± 0.03	0.59 ± 0.03	0.58 ± 0.04
s-ICA	TPR %	92.43 ± 0.35	92.09 ± 0.65	91.15 ± 0.43	91.1 ± 0.63
	FPR %	1.05 ± 0.02	1.05 ± 0.05	1.25 ± 0.03	1.26 ± 0.39

ROC - Signal Level = 3%					
Method	ROC	6% Noise	8% Noise	10% Noise	12% Noise
w-ICA	TPR %	96.1 ± 0.12	96 ± 0.18	95.9 ± 0.18	95.77 ± 0.34
	FPR %	0.62 ± 0.02	0.61 ± 0.03	0.6 ± 0.02	0.61 ± 0.03
s-ICA	TPR %	93.54 ± 0.16	93.49 ± 0.16	93.47 ± 0.16	93.44 ± 0.12
	FPR %	1.2 ± 0.02	1.21 ± 0.02	1.21 ± 0.02	1.21 ± 0.02

Table 5.2: **ROC statistics (Temporal Lobe):** Depicting the mean and std. deviations for 10 random noise frames generated for each combination of signal and noise: (a) Signal level = 1%, (b) Signal level = 3%. Clearly, w-ICA shows superior statistics for all combinations except lower TPR for 1% signal and higher levels of noise.

ROC Analysis: Temporal Lobe

This particular ROI was selected based upon the fact that the temporal lobe contains large number of voxels. Large spatial smoothing kernels introduce a significant amount of smoothing which may be harmless or sometimes even beneficial when the size of ROI is large as their shapes tend to vary gradually leading to lower variability after smoothing. The ROC statistics presented in this section corroborate the above statement reasonably well. The s-ICA framework performs competitively well against the w-ICA framework as noticed from larger number of true positives (see 5.2). Although, when the shape of an ROI varies rapidly, which is the case for some of the slices in the temporal lobe, then smoothing with a spherical Gaussian would not be a robust choice and would tend to destroy the edges. Thus, s-ICA fails to preserve the overall shape of an activation region in addition to creating a large number of misclassified voxels.

The ROC curves for two extreme noise levels ($Z_{empirical} = 2.0$) presented in Figure 5.10 clearly show that w-ICA assists in establishing a highly desirable requirement of low number of false positives for various neuroimaging applications. The ROC curves for the w-ICA method yielded higher TPRs and lower FPRs, given a higher percentage of simulated BOLD signal ($\approx 3\%$), whereas w-ICA performed competitively well against s-ICA when compared for 1% BOLD signal change. The TPR values of w-ICA differ by a small percentage whereas a significant improvement is evident from the FPR values, as compared to s-ICA at every

given noise level (also seen from Table 5.2).

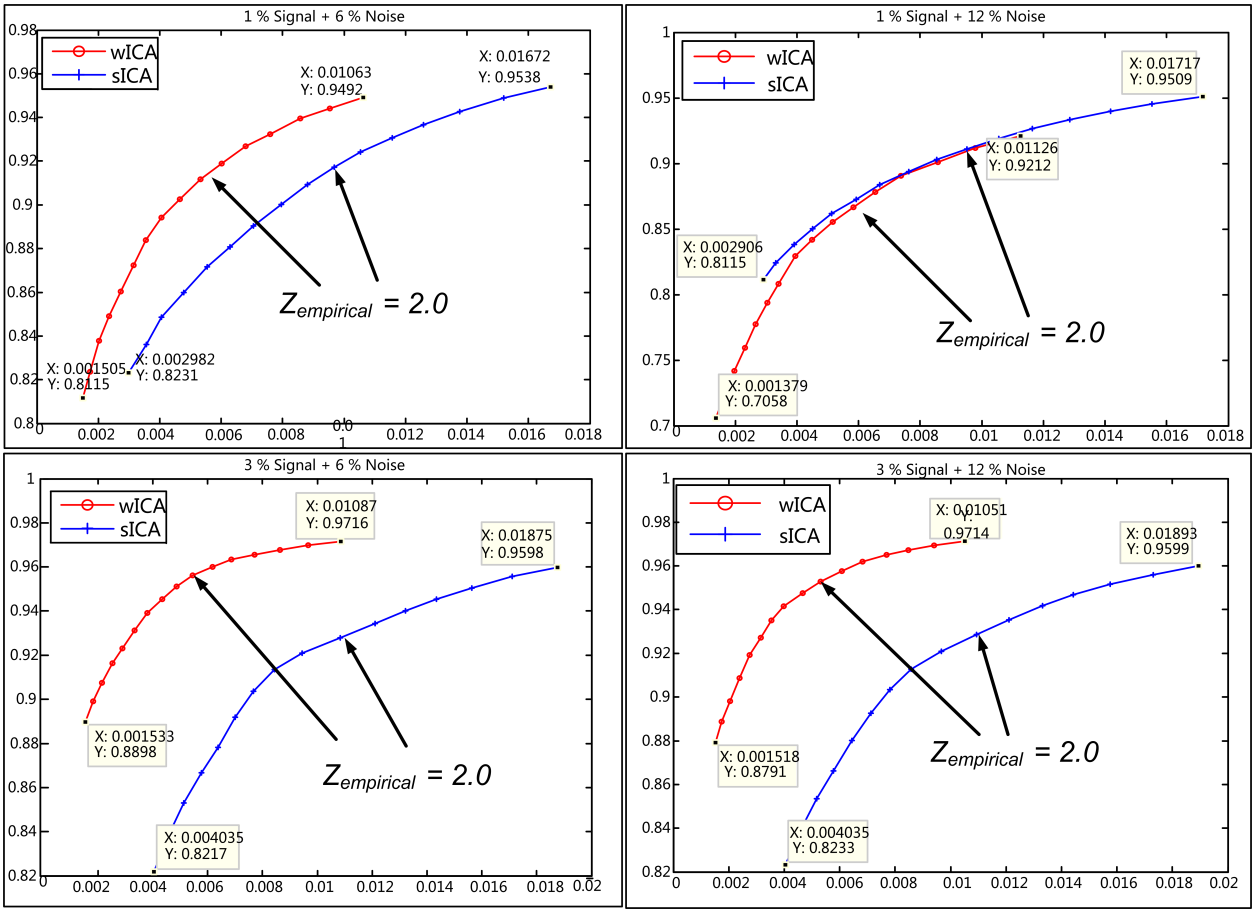

Figure 5.10: **ROC Curves (Temporal Lobe)**: with indication of empirical threshold for two signal levels (1%: top row, 3%: bottom row) and two selected noise levels (6%: left column, 12%: right column) used. In all cases above and as presented in Table 5.2 also, the number of false positives always remains lower for w-ICA as compared to s-ICA. The TPR is competitive for 1% signal and higher for 3% for w-ICA against s-ICA.

The effect of increasing noise levels on ROC statistics is markedly visible from the values in Table 5.2a. The TPR values for w-ICA show a significantly decreasing trend (4% reduction for signal level = 1%) as noise increases, in comparison to s-ICA. The advantage of w-ICA lies in restricting the false positives, in this case, below 1% for any given signal and noise combination. On an average, an improvement of about 150-200 voxels (equivalent to ΔFPR $\approx$ 0.5 - 0.7%) is observed for w-ICA results. This difference is expected to be significantly high when the data is acquired at a finer resolution in comparison to the current simulated

3×3×3mm sampled resting state fMRI data set. In the case where the signal level is high (3%), the w-ICA technique is able to achieve TPR and FPR values much greater than those obtained using the s-ICA method (see Figure 5.10 (bottom row), and Table 5.2b).

Multi-directional Perimeter Analysis

The second evaluation metric for simulated data analysis, multi-directional perimeter, is based on the underlying fact that activation components have closed surface ROIs. The primary advantage of this metric lies in its ability to quantify the shape of a 3-D polygon using three different estimates computed using perimeters of slices extracted along the axial, coronal and sagittal viewing geometries. This results in a more robust measure of shape congruence as compared to measures estimated using only a single viewing geometry.

An ROI extends in all three dimensions forming a non-rigid shape that represents the activation voxels. The Z-score volumetric image (Z) is thresholded using an empirical threshold value (Z-value ≥ 2.0) to obtain the binary map of ROI (as seen in Figure 5.11 for each observation. The Z-threshold of 2.0 was arbitrarily selected based on commonly used Z-thresholds in fMRI analysis. A Z-threshold of 2 or higher yields meaningful results in terms of significance and filters voxels that are too close to the mean. This binary map is known as Z^B. The perimeter of a non-rigid shape is defined as the sum of Euclidean distance between all pairs of adjacent voxels. Let $Z^{B,Edge}$ be the binary edge map of the largest contiguous region which is utilized for estimation of the perimeter values as shown in Figure 5.11. Three different sets of perimeter values corresponding to three orthogonal viewing angles - (1) Axial, (2) Sagittal, and (3) Coronal, were estimated in a slice-by-slice manner. This resulted in three variable length vectors ($1 \times L_i$) populated by the perimeter values, known as P_i^{wICA} (index i corresponds to the aforementioned viewing angles). Note that, L is of variable length as the extent of spread of non-zero voxels ($Z^B = 1$) across slices is not necessarily equal for different viewing angles.

The aforementioned process was repeated on the Z-score maps estimated through s-ICA

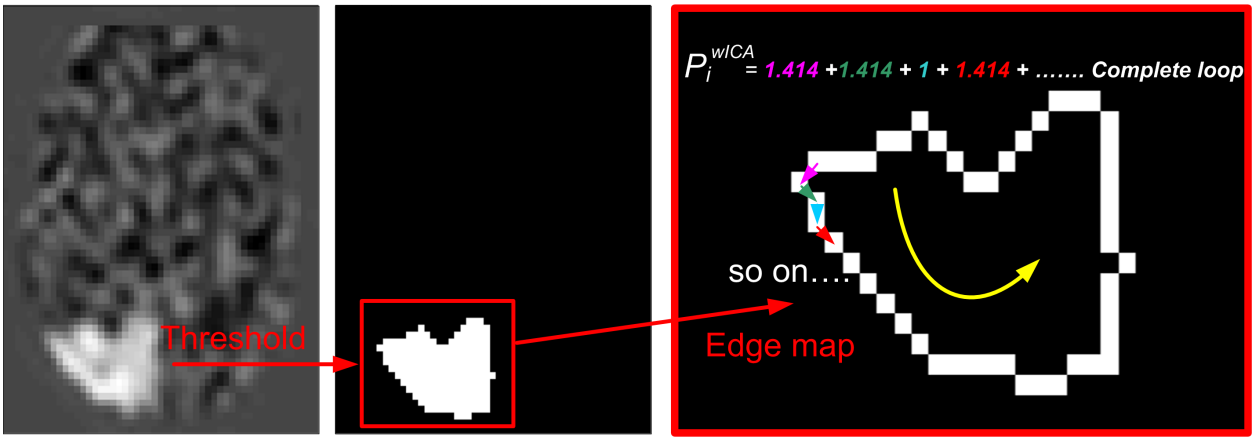

Figure 5.11: **Generation of a binary edge map and illustration of the proposed perimeter metric:** Slice no. 12 of Z_k and the corresponding Z^B image alongside the Enlarged edge map $Z^{B,Edge}$ and perimeter estimation. All pixel pairs oriented at an angle of 45°, 135°, 225° or 315° has perimeter $= \sqrt{2} = 1.414$, whereas all other pixel pairs have a perimeter = 1.

and the available ground truths, resulting in two additional sets of perimeter vectors - P_i^{sICA} and P_i^{Truth} respectively. For comparison purposes, P_i^{Truth} was utilized as the reference set, whereas P_i^{wICA} and P_i^{sICA} were considered as the test sets. Further, the MSE value for each comparison pair ($MSE_i^{wICA-Truth}$ and $MSE_i^{sICA-Truth}$) was calculated for each of the three viewing geometries mentioned previously. The generalized MSE equation can be expressed as:

$$MSE_i^{Method-Truth} = \frac{1}{L_i}\sum_{s=1}^{L_i}[P_i^{Method}(s) - P_i^{Truth}(s)]^2 \quad \text{where} \quad G \in \{wICA, sICA\} \tag{5.25}$$

It can be inferred from the above discussion that the $MSE_i^{Method-Truth}$ metric has a low value when perimeters of most slices in group G (w-ICA or s-ICA) are almost equal to those of the ground truth.

Figure 5.12 depicts the perimeter distributions along the set of slices associated with three viewing angles for an example data set based on the Visuo-motor(VM) mask. Notice the high correlation between the *w-ICA* (cyan) and the *ground truth* (orange) perimeter values. This observation corroborates our previous statement about preservation of shape. That

is, directional and spatial relationships between adjacent pixels are quite intact even after denoising using wavelets in addition to performing ICA in the transform domain. Whereas, there are large differences between perimeters of *s-ICA* maps and ground truth for every viewing angle, eventually leading to higher values of $MSE_i^{sICA-Truth}$.

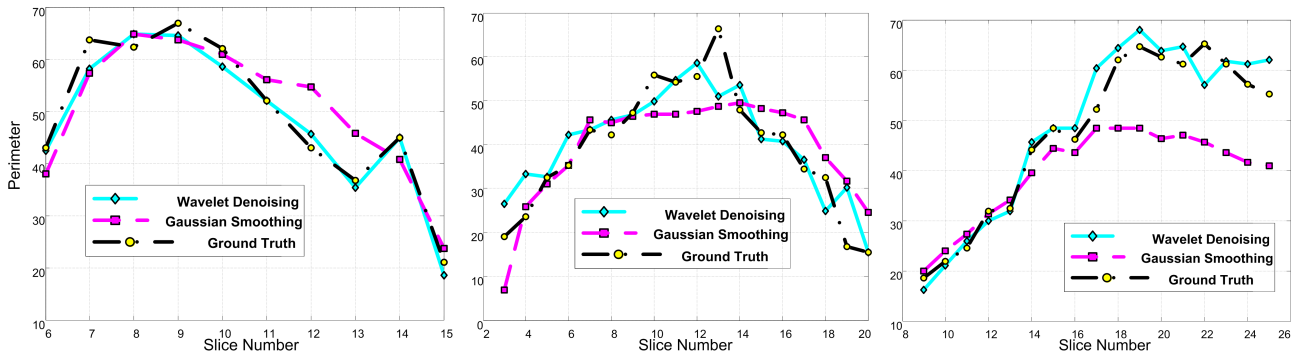

(a) Axial (b) Coronal (c) Sagital

Figure 5.12: **Plots depicting perimeter variation between w-ICA and s-ICA for different viewing angles:** High correlation is seen between the curves for ground truth and the w-ICA scheme as compared to the s-ICA framework. This preliminary analysis establishes the significance of slice by slice comparison of perimeters in various viewing geometries. Coronal MSE values for this ROI show the most deviation from ground truth with reasons discussed in the text

Occipital Lobe: MSE

The multi-view perimeter metric (MPSM) values were estimated across 10 noise frames and the results are reported here as their mean and standard deviations. The large number of discontinuous contours in some of the coronal slices and relatively lower smoothing properties of w-ICA (as compared to s-ICA) resulted in large standard error as seen in Figure 5.13. An interesting observation regarding the measurements for coronal geometry was that there were multiple instances with more than one closed contour in a single slice for the ground truth. Binary maps each obtained from w-ICA and s-ICA result in a more dilated version of the closed contours due to the smoothing process, sometimes resulting in only one closed region instead of multiple regions as originally present in the ground truth. The s-ICA method is more susceptible to this error (as seen from the tall blue bars in Figure 5.13), but has

low variance due to its significant smoothing properties. In most cases, w-ICA was able to maintain the isolation between multiple regions within a slice (if present) resulting in lower mean MPSM values.

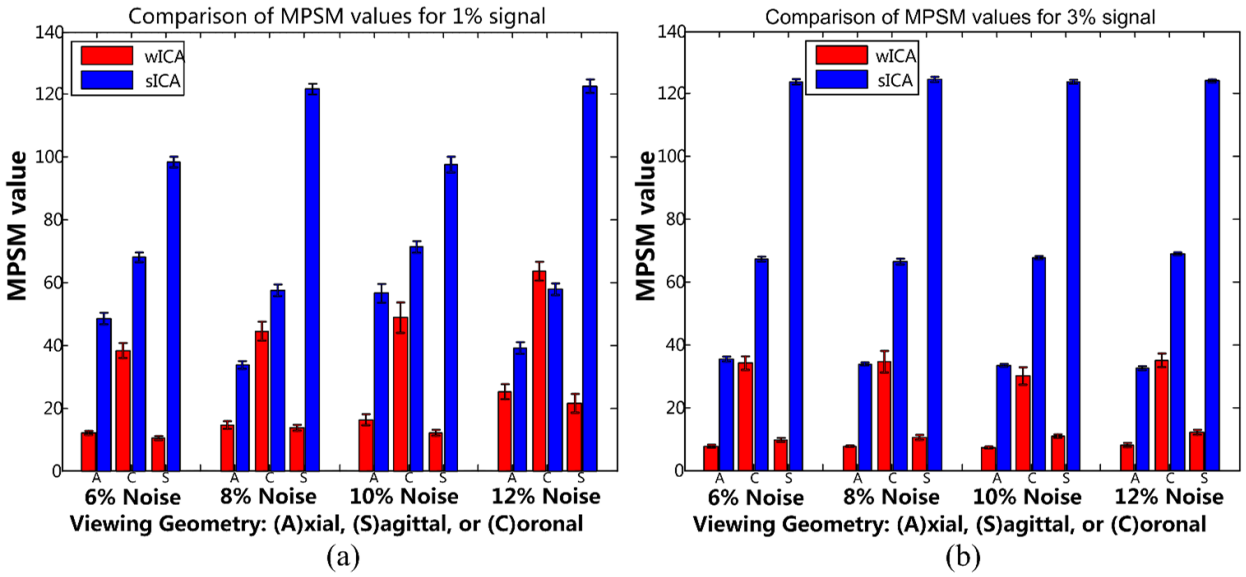

Figure 5.13: **Occipital lobe: MPSM statistics:** The bars are grouped based on different levels of noise and three different viewing geometries (A: Axial, C: Coronal, S: Sagittal). The mean and standard deviation values were computed using MSE values across 10 noise frames for every possible signal/noise combination: (a) signal = 1%; (b) signal = 3%. Note that the level of shape congruence is inversely proportional to the metric values. The metric acquires low values if the shape is more similar to the ground truth and vice versa. Each bar represents the mean MPSM value and the error bars correspond to the 'standard error' computed using the standard deviation values across $n = 10$ noise frames.

Temporal Lobe: MSE

In this section, we highlight the perimeter results obtained from simulated data sets for the second ROI (Temporal lobe) used to generate the simulated fMRI data sets. As expected, the s-ICA framework introduces large number of false positives around the activation region. This directly causes a large amount of shape distortion and is demonstrated here. Evidence related to shape distortion caused by smoothing is presented in the form of thresholded Z-score maps of the activation component. Figure 5.14 depicts the shape of the resulting Z-score maps for two different axial slices obtained after the application of the s-ICA and

the w-ICA frameworks alongside the ground truth activation. It is visible that the cusps and sharp boundaries are preserved in the case of the w-ICA result (see Figure 5.14c). Whereas, the shapes change considerably as a result of Gaussian smoothing incorporated in s-ICA (see Figure 5.14b).

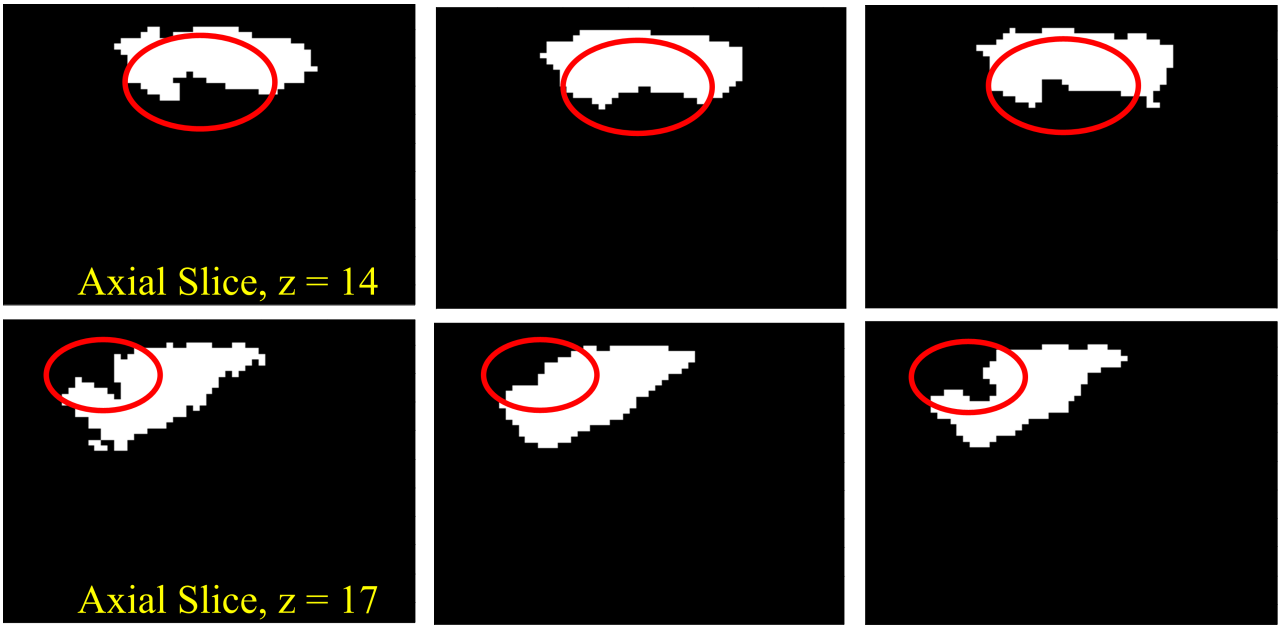

(a) Ground Truth (b) s-ICA (c) w-ICA

Figure 5.14: **Illustration of variation in shape of the activation region for temporal lobe ROI.** Slice 15 (top row) and slice 17 (bottom row): (a) Ground truth; (b) s-ICA; (c) w-ICA. The areas highlighted above are the most significance regions in context to shape preservation as achieved by w-ICA over s-ICA. Notice that the cusp in slice 17 is smoothed out as a result of s-ICA and preserved by the w-ICA framework. These shape distortions are expected to be even higher when comparing the un-thresholded Z-score maps.

In addition, the low MPSM for w-ICA indicate higher shape congruence for this ROI which is similar to the trend observed in the other ROI (see Figure 5.13). The high sagittal MSE values seen in Figure 5.15 are due to the rapidly varying shape of the temporal lobe ROI for this viewing geometry. Also, these large variations may be accounted by multiple instances of more than one closed contour being present in a single sagittal slice for ground truth. These multiple closed regions, when in close proximity, undergo dilation due to smoothing and thus yield high MSE values when compared with the ground truth. The

distribution of MPSM values also seem to vary more with increasing noise as inferred from high values of standard errors in Figure 5.15. In a broader sense, MPSM is capable of yielding a fair estimate of the amount of shape congruence for all three viewing geometries and provides enough information to make a decision about the quality of performance of the two frameworks.

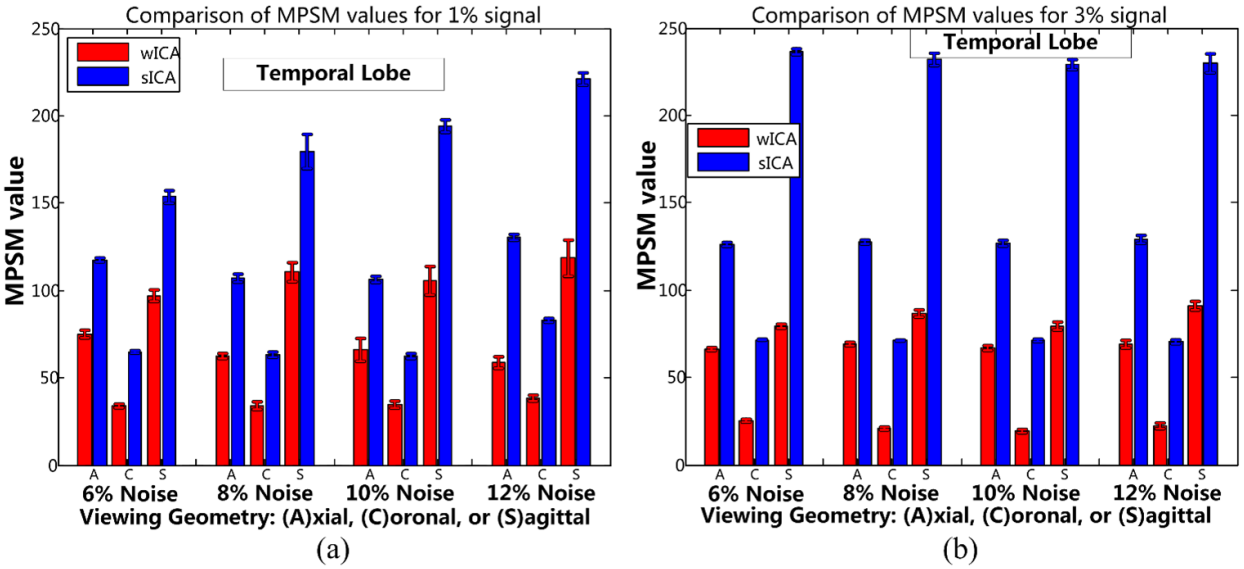

Figure 5.15: **Temporal lobe: MPSM statistics:** The bars are grouped based on different levels of noise and three different viewing geometries (A: Axial, C: Coronal, S: Sagittal). The mean and standard deviation values were computed using MSE values across 10 noise frames for every possible signal/noise combination: (a) signal = 1%; (b) signal = 3%. The bars are grouped based on different levels of noise (6% to 12%). Note that the level of shape congruence is inversely proportional to the metric values, that is, the metric acquires low values if the shape is more similar to the ground truth and vice versa. The w-ICA consistently performs better than s-ICA framework and is able to preserve the shape of the activation region while having little effect due to increasing amount of noise and low standard error across various signal/noise combinations.

Simulated Data: Summary

Overall, the proposed methodology performed significantly better in terms of shape preservation, whereas it yielded competitive results in terms of classified (TPR) and misclassified voxels (FPR) depending upon the size of the ROI under consideration. The ROC statistics for the two methods in case of larger ROIs, such as the temporal lobe (2900 voxels) were

observed to be closely competitive, whereas the proposed framework dominated for smaller ROIs such as the occipital lobe (1600 voxels). The reason behind the aforementioned observation can be associated with the size of the FWHM kernel utilized in s-ICA. As the size of this kernel is comparable to the size of the ROI in some of its slices, more false positives are introduced eventually resulting in poorer ROC statistics. This is not the case for larger ROIs such as the temporal lobe, where the additional false positives in s-ICA appear due to high spatial smoothing around the edges. The proposed framework was able to overcome the aforementioned problem, and thus resulted in lower FPR values for any combination of signal and noise.

More results using the simulated data sets are presented in the next chapter that introduces a new simple shape metric for quantifying fMRI activation regions spatially.

5.6.3 Group fMRI Motor-tapping study

For this experiment, 20 healthy subjects participated in a motor tapping experiment, 17 subjects were right-handed, and 3 subjects were left-handed and in the age group between 18 and 62 years, with 12 male subjects and 8 female subjects. The details of the stimulus protocol were briefly described in Section 2.4.1.

Qualitative comparisons between the proposed algorithm and other commonly used methods are done based on two attributes: (1) Peak signal-to-noise ratio (PSNR) for smooth and noisy images, and (2) additional results depicting shape differences are presented in Chapter 6.

Intensity Differences

Prior to presenting differences in activations, it is important to compare the smoothing effects of different algorithms. Figure 5.16 illustrates some of the key advantages of wavelet-based denoising over Gaussian smoothing, such as preservation of edges, minimal variation in gray levels etc.. An orthogonal view of a slice extracted from a subject's brain is presented here.

The amount of smoothing introduced by the proposed method when different number of decomposition levels are used, is clearly perceivable from Figure 5.16c and 5.16d. There is some increase in the degree of smoothing when applying denoising with 3 levels of decomposition as compared to 2 levels. Overall, the level of details such as edges, intensity variations, and contours of other anatomical structures such as the ventricles and the temporal gyrus still remain relatively intact as compared to the Gaussian smoothed image. These advantages enable detection of activation patterns that are spatially more accurate and are less impacted by smoothing artifacts.

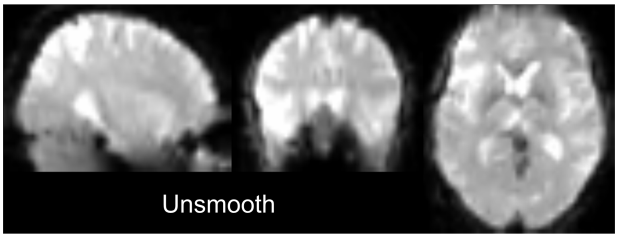

(a) Unsmooth

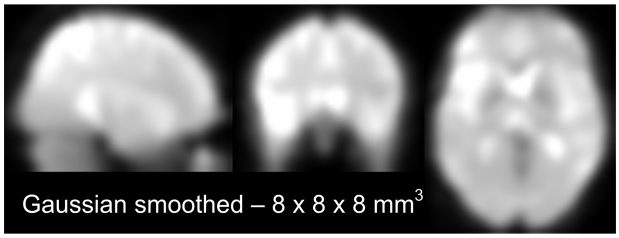

(b) Gaussian Smoothing

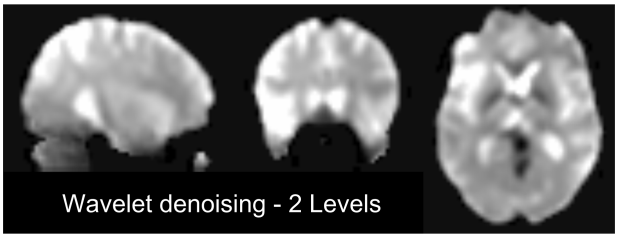

(c) Wavelet Denoising - 2 levels

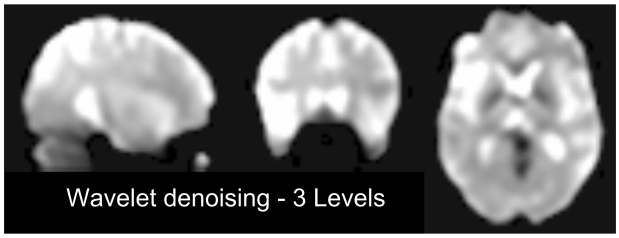

(d) Wavelet Denoising - 3 levels

Figure 5.16: An illustrative comparison of the effects of smoothing relating to preservation of details: each image shown here represents the orthogonal views (coronal, sagital, and axial - in that order) for a single slice from subject 1's first scan under different image smoothing conditions. (a) Unsmoothed raw image; (b) Gaussian smoothing applied on image in (a); and Wavelet denoising applied with (c) 2 decomposition levels; (d) 3 levels. Note the similarities between (c), (d) and (a) where most details in the image such as edges, intensity values and contours are almost preserved in their original spatial form.

Two of the most common metrics for quantifying image distortion is the peak signal-to-noise ratio (PSNR) computed using the maximum value in an image and the mean squared error (MSE). To estimate MSE, it is required to have a reference and an observation image

available which are further utilized as:

$$PSNR = 10log_{10}\left(\frac{[MAX(I)]^2}{MSE}\right) \quad \text{where} \quad MSE = \frac{1}{N}\sum_{n=1}^{N}[I(n) - K(n)]^2 \tag{5.26}$$

where N is the total number of voxels in a volume. The image $I(n)$ corresponds to either of the two methods under comparison - Gaussian smoothing (GS) and wavelet denoising-3 levels (WD3), whereas the image $K(n)$ corresponds to unsmoothed data with n representing the voxel index within the volume.

The PSNR values for each of the aforementioned methods are computed relative to the unsmooth fMRI images (e.g. shown in Figure 5.16). The mean and standard deviation for PSNR corresponding to fMRI images from 20 subjects are computed to be 22.93 ± 1.65 for the Gaussian smoothing method. The wavelet denoising using 3 levels has a perceptually more favorable value of 31.40 ± 2.1 indicating a superior performance in preserving the true intensity levels as compared to the conventional Gaussian smoothing method.

Next, we present some strong comparisons between task-positive component maps (somatosensory motor) obtained by applying ICA on two sets of the same fMRI data that were smoothed using different techniques, namely - (1) Gaussian smoothing; and (2) Wavelet denoising with 3 levels. The t-maps were estimated for the task-positive component (somatosensory motor) by applying a 1-sample t-test on the back-reconstructed task-positive components corresponding to each subject (Calhoun et al., 2001b). Since the ground truth for spatial activations is unavailable, it is difficult to compute the exact number of false positives introduced as a result of different smoothing schemes. In order to partially overcome this problem and illustrate the advantages of our method, we extracted independent components from unsmoothed fMRI data. This facilitates comparisons with the spatial extent of neural activity that is at least free from smoothing artifacts but still cannot be considered as the absolute ground truth. Fig. 3 presents the aforementioned comparisons using group-wise t-maps corresponding to various smoothing methods. The overlay images were derived using

a threshold of $t \geq 4$ ($p \geq 0.0008$; DoF $= 19$).

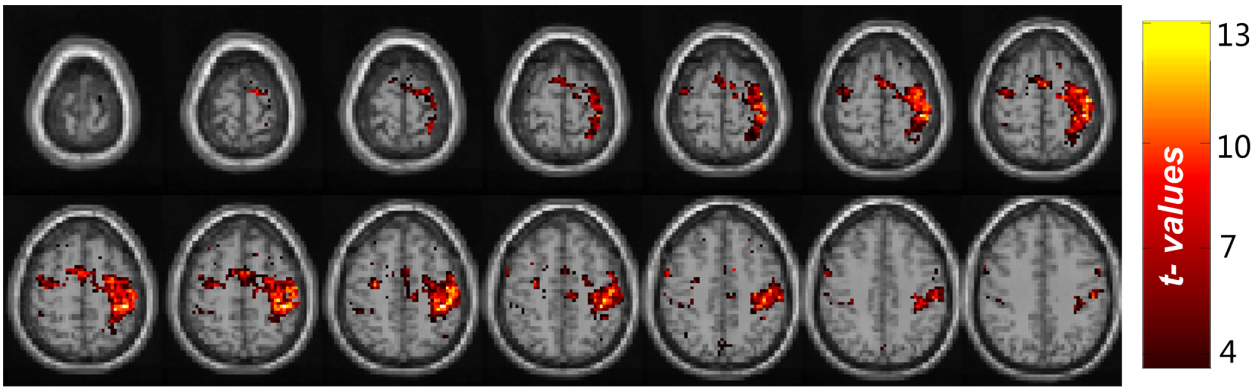

(a) Unsmoothed

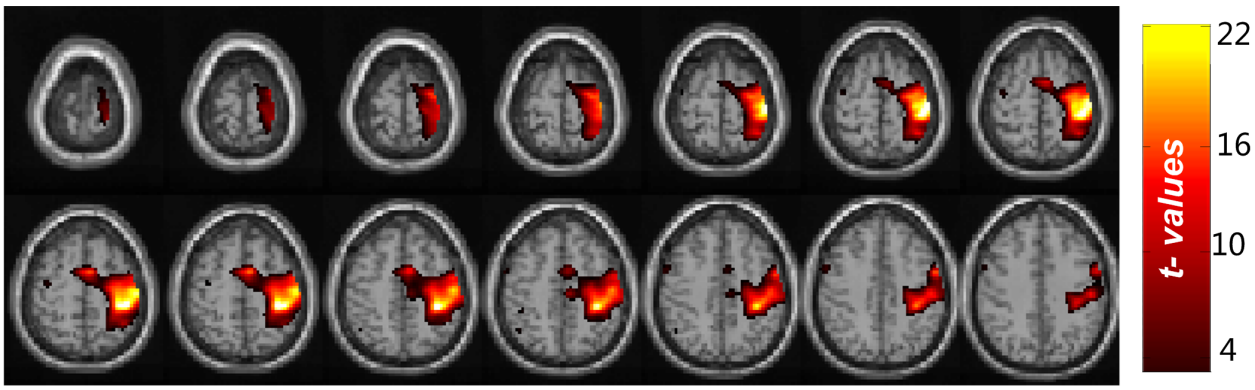

(b) Gaussian Smoothing

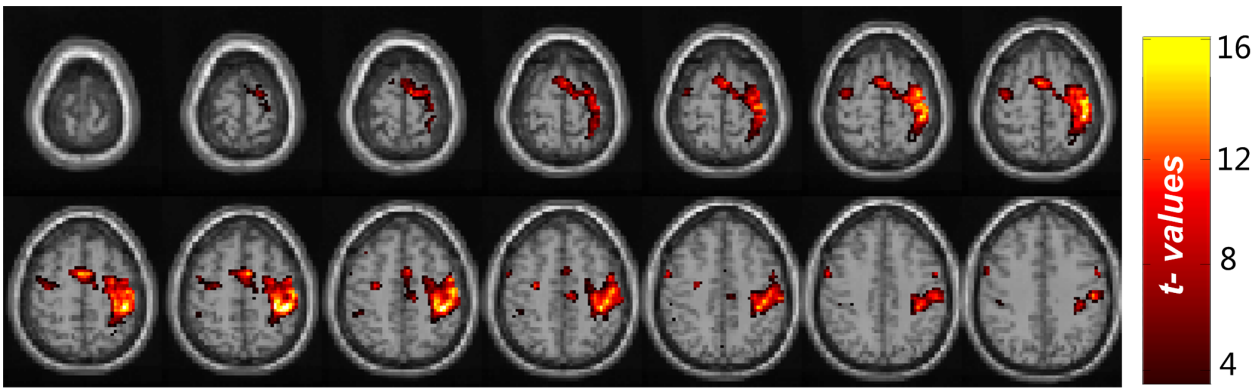

(c) Wavelet Denoising - 2 levels

Figure 5.17: Thresholded t-maps (slices 31 - 44) corresponding to the task-positive motor cortex component resulting from different smoothing schemes - (a) No smoothing, that is, ICA applied on noisy data; (b) Gaussian smoothing; (c) Wavelet denoising- 3 levels. Notice the similarities in shape between (a) and (c) indicating preservation of shapes even after denoising. Whereas, in (b) the activations have a significantly different shape and a larger spatial spread indicating presence of more false positives.

Differences between the proposed methodology (WD3) and the Gaussian smoothing (GS) are clearly evident from Figure 5.17 where the spatial extent of GS based activation indicates the presence of several false positives when compared to the unsmoothed data's activations (see Figure 5.17a). More voxels seem to have high t-values (see scale on right) which may be a result of crude spatial smoothing of raw data causing neighboring intensities (activation-related) to bleed into these voxels resulting in their classification as significantly active voxels. Lastly, the shapes, in addition to edges and contours of the activation clusters seen in Figure 5.17a are mostly well preserved in the case of WD3 activations (5.17a). This important feature serves as a major benefit when comparing multiple groups for specific patterns of activity and connectivity across different regions.

The most common form of studying brain activity using fMRI images is through analysis of t-maps. It is thus imperative to have the t-maps that represent significantly activated voxels and are free from preprocessing artifacts. The significance of neural activity can vary based on its location within the region of interest (somatosensory motor in this case). Centrally located voxels in the t-map corresponding to GS (see Figure 5.17b) have high t-values clearly indicating artifacts due to smoothing. Also the neighboring voxels lose their original significance since the data was highly smoothed in the first place. To further illustrate this effect, we divide a 2-D slice (slice 37) of the activation region into differently leveled contours based on increasing t-value. Figure 5.18 consists of contour-based representations corresponding to data that is (a) unsmoothed; (b) Gaussian smoothed; and (c) smoothed using the proposed wavelet denoising. Each colored layer in Figure 5.18 represents a group of voxels with their approximate mean t-value indicated on the z-axis. Clearly, there are fewer layers in Figure 5.18b when compared to Figure 5.18a and 5.18c due to loss of detail after crude averaging of the Gaussian smoothing kernels. On the other hand, wavelets facilitate in preserving the significance of active voxels in addition to avoiding falsely elevated t-values of neighboring voxels. Other featured differences highlighted in Figure 5.18 include preservation of shape after smoothing. From the aforestated summary, it may be inferred that wavelet

denoising does a good job of preserving the shape of activation while removing noise and increasing the SNR without falsely elevating the measured t-values.

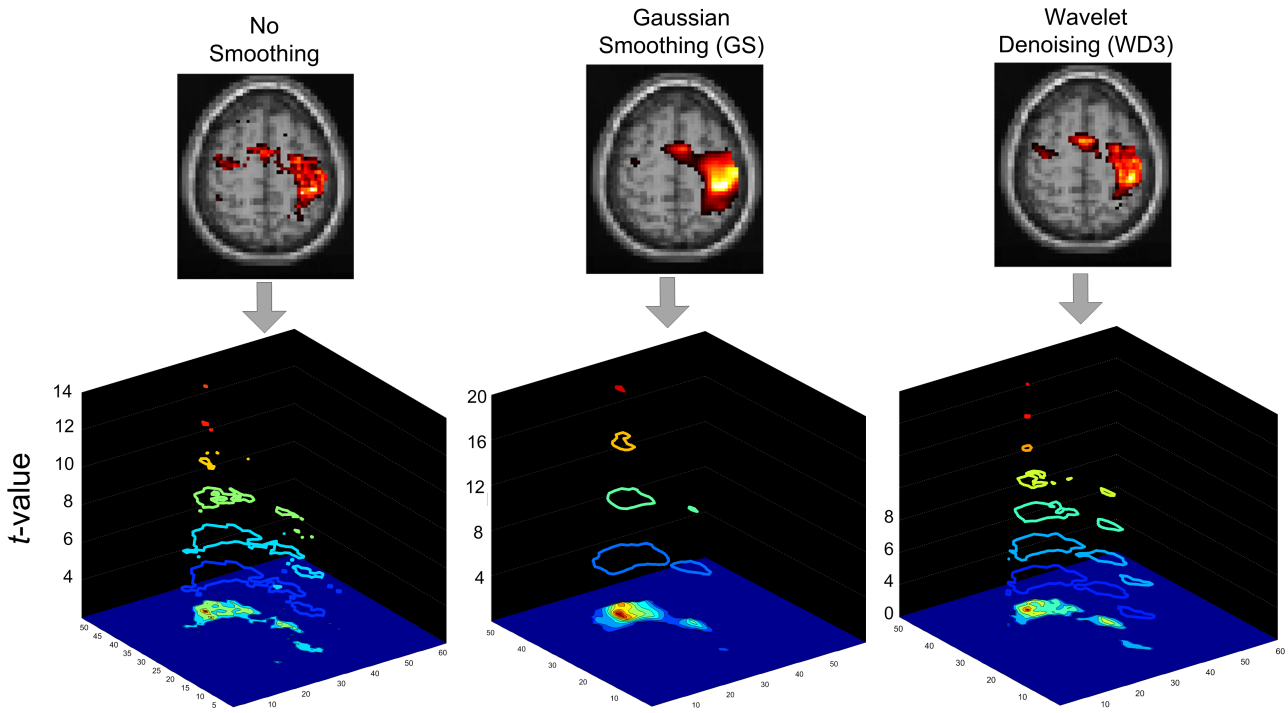

Figure 5.18: **Activity Intensity Distribution:** A comparative illustration of different methods having an effect on the significance level (t-values) of a voxel (or a group of voxels). Images on top are single slice t-maps (slice 37; also seen in Figure 5.17) projected as contour maps below showing the shape comprised by a group of voxels (colored contours along z-axis) that are clustered based on their mean t-value (z-axis) for different methods: (a) No smoothing: more noisy; (b) Gaussian smoothing: less number of contours due to heavy averaging of activation intensities in adjacent voxels (raw data) resulting in distortion/elevation of t-values; (c) Wavelet denoising: Smooth activation contours in addition to preservation of shape and significance.

5.6.4 Inter-Group Study: Controls vs. Patients

In this section, results from application of the 3-D denoising scheme on the AOD data set 2.4.2 are observed. The data set is divided as 5 healthy controls and 5 schizophrenia patients. When performing multi-group studies especially those involving patients suffering from disorders such as schizophrenia or bipolar disorder, one needs to take the pre-processing effects on the data into account. The group difference statistics are affected by fMRI spatial

pre-processing steps that include smoothing and normalization. As discussed in the previous section, it is difficult to estimate the 'ground truth' activation maps for fMRI data. In order to highlight the improvements served by our proposed framework, we present two types of comparisons with the conventional framework (Gaussian smoothing followed by spatial ICA): (1) Empirical specificity (as there is no ground truth) with focus on contours/edges of the activation regions; and (2) a quantitative comparison using the shape metrics presented in the next chapter.

The first point of comparison is presented in Figure 5.19 in form of Z-scores computed for the mean activation maps for the task-positive component showing dominant temporal lobe activity during the Auditory Oddball task. Five specific regions of interest (ROI) are highlighted in the HC maps presented for the two methods in Figure 5.19a. The differences can be classified as those in size (ROIs 1 and 2) and shape (ROIs 3, 4 and 5). Similarly, there are six ROIs in the SZ maps (see Figure 5.19b) which highlight differences in size (ROIs 1, 2 and 6) and shape (ROIs 3, 4 and 5) of the activation regions obtained through the two different methods.

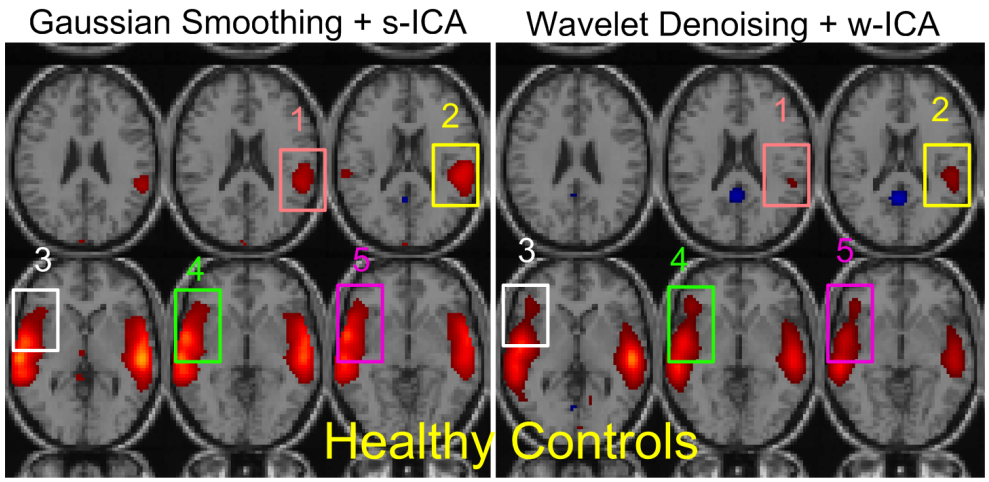

(a) Healthy Controls

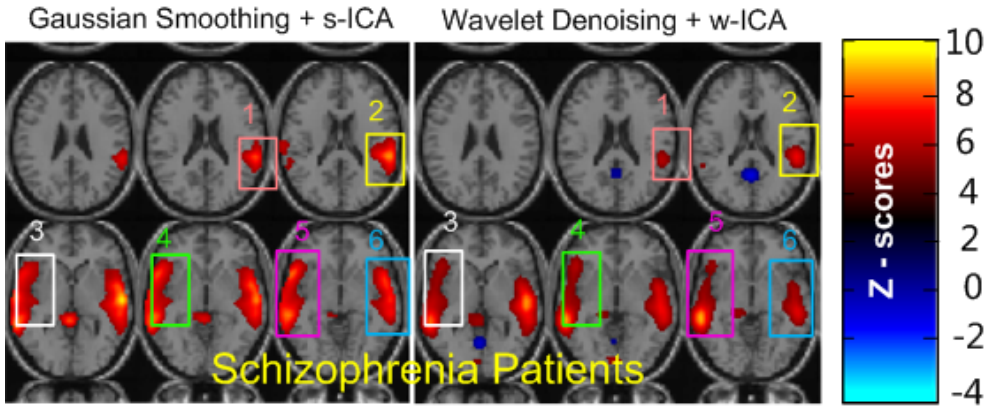

(b) Schizophrenia Patients

Figure 5.19: **HC vs SZ:** Task-positive (auditory) component activation maps (scaled to Z-scores) obtained through a group-ICA of 10 HC and SZ (rows) subjects using the two different frameworks (along columns). The regions of interest (ROIs) are highlighted for emphasis on the difference in shapes and sizes of the activation regions obtained through different methods for (a) 5 Healthy Controls and (b) Schizophrenia Patients.

It is clear from Figure 5.19 that the proposed denoising framework is able to obtain more specificity where the activations have sharper edges and contours in contrast to circular and smooth edges. In lieu of assuming a ground truth, we utilized activation maps obtained through group ICA on unsmoothed fMRI data to obtain a fair idea of actual activation regions. The conventional framework clearly seems to lose specificity because of Gaussian smoothing whereas the proposed framework shows higher specificity in addition to preservation of shape, especially cusp-type edges and sharper contours indication minimal loss of detail.

A critical observation related to comparisons involving controls and patients is accounting for behavioral differences between these two groups. This additional feature can sometimes help reveal certain outliers within a group data set. This observation will be revisited in the next chapter when discussing shape differences between activation maps from this data set.

Lastly, it would be interesting to study resting-state networks using the proposed framework in order to obtain more accurate shapes and sizes of the regions functioning as coherent networks in the brain. This might be an initial step towards improving the statistical power in spatial functional connectivity analysis within large groups of subjects.

The cognitive tasks (MOTOR and AOD) used to record the corresponding BOLD activity were chosen based on robustness and simplicity. Thus, the activations recorded in both these experiments are less likely to vary significantly (approximately centered around the same region) spatially across multiple subjects. This is one of the primary reasons for obtaining meaningful activation maps even though there was no smoothing applied prior to ICA (Figure 5.17). This advantage also enables us to highlight the effects of smoothing while presenting the advantages of using wavelet denoising. Therefore, in case of high level cognitive tasks that demand more attention, our proposed denoising method is expected to bring out small but important variations in spatial activity in different subjects in a group or even between multiple groups.

5.7 Summary

We presented a new efficient 3-D wavelet based denoising methodology which utilizes an isotropic neighborhood based indicator in combination with prior probabilistic information to achieve a robust estimate of denoised signal. Results indicate a clear advantage of wavelet based methods in terms of achieving shape accuracy in addition to higher specificity and ability to suppress noise. We presented results using simulated data as well as real fMRI data sets acquired while subjects performed a cognitive task. Comparisons between the conventional Gaussian denoising and our proposed approach were presented based on sensitivity, specificity, intensity values, and perimeter of activation regions.

An important note to make here is that even though there exist several other methods in the literature for smoothing images, we restrict to comparisons with the well established and almost unanimously used approach of Gaussian denoising. This is done to emphasize the current assumptions associated with its widespread use, that is, it is a favorable method to follow when applying MNI-template based normalization to get rid of normalization errors, and inter-subject differences in the EPI images acquired for fMRI analysis. As detailed earlier in Section 1.4, the goal of this thesis is not only to propose new methodologies for fMRI preprocessing, but to shed more light on associations between the various parts of the current fMRI preprocessing pipeline and reasons for choosing the approaches in place today.

Towards the end of this thesis, an outlook will be presented on the future of fMRI preprocessing, that I have developed over the past years of research and observations made while pursuing to appropriately modify the way we preprocess fMRI data today.

The next and last methodological chapter on *validation metrics* introduces a new morphological shape metric to compare 3-D connected activation maps. The motivation for this work was the lack of a spatial activation shape comparison metric in the current fMRI literature. It is very difficult to derive a feature that essentially represents the difference in two shapes, specifically activation maps, using a single number. Eventually, the applications of this shape metric were found to be manifold and highlighted with examples in the next

chapter.

Chapter 6: Shape Metrics for FMRI

In functional brain imaging, the underlying shape of an activation region (spatial) determined from statistical analysis is an important characteristic. Ideally, the shape of an fMRI activation map characterizes the anatomical regions in the brain that may be possibly involved in performing certain brain functions. Most fMRI studies involve investigating neural activity in one or more group of subjects and it can be useful to quantify the spatial differences within or across two groups through measuring and comparing shapes of the spatial activation regions. In earlier chapters, the emphasis was on addressing the differences between structure and function through computational methods such as normalization with functional templates.

Following the estimation of the activation component of interest using ICA, it is important to compare its spatial and structural characteristics with that of the ground truth in order to validate the performance of our proposed framework. This chapter contains theory and results explaining new and simple mathematical tools that enable quantification of activation shape between subjects to assist researchers to gain more information about the spatial nature of BOLD fMRI activations. With this objective, two structural metrics are proposed here to quantify the variability in shape composed by a group of voxels after it has been segmented and classified as an activation region.

6.1 Shape Metrics in fMRI

One of the key results obtained from analyzing group data in an fMRI study is to estimate the spatial maps that indicate the locations and magnitudes of brain activity. The neural activity recorded in form of fMRI data sets is usually represented using a t-test or a z-score measure. These maps are derived at a subject level and/or at the group (control or patient) level as a mean map. Depending on the method used for fMRI data analysis, *e.g.* via a

general linear model (GLM) (Section 2.6.1) or ICA (Section 2.6.2), it is possible to obtain multiple spatial maps for a single subject in addition to a group map.

As shown in previous chapters, GLM is a regression method which utilizes a 2-level analysis model to calculate beta weights, contrasts and t-maps for each subject and each condition at the first level and performs a 1-sample t-test on the first level data from all subjects to estimate the group maps for each condition at the second level. On the other hand, ICA is a data-driven method that clusters functionally correlated voxels into various segmented maps, commonly known as functional networks. Unlike the GLM, ICA works independently of a temporal model. Thus, ICA has the ability to derive functional clusters of voxels that may remain uncovered when using GLM. These functional networks may or may not be related to the task but are useful for deriving functional network connectivity, that is, the correlation between different networks in the brain within a subject or across the whole group.

6.2 Spatial Shape Metrics in Computer Vision

Numerous techniques have been introduced in the past to quantify the shape of planar and volumetric objects (see (Tangelder and Veltkamp, 2004, Zhang and Lu, 2001) for a comprehensive survey). The seminal paper by Freeman (1974) introducing chain codes was one of the first methods proposed for quantifying shapes of line drawings and images. Since then, shape representation methods have been grouped as (1) contour-based and (2) region-based methods. Contour-based methods like chain codes, Fourier descriptors (Persoon and Fu, 2007), autoregressive models (Kauppinen et al., 2002), and chain code based shape numbers (Bribiesca and Guzman, 1980) utilize the boundary information which is essentially similar to how humans perceive and compare complex shapes. Region-based methods such as Zernike moments (Kim and Kim, 2000) and grid-based shape measures (Lu and Sajjanhar, 1999) exploit local shape information such as centroid, major and minor axes-based measures. The method proposed in this paper is of the latter class and likely to be less complicated

than most other metrics used to quantify shape.

In this chapter, we introduce a novel weighted metric estimated from a given 2-D shape by utilizing polar distances and orientations of several pixels on its contour. Centroid based measures have been previously utilized in combination with B-splines for applications in object recognition and detection (Gaborski and Paskali, 2007, Saber et al., 2005), but there have only been a few attempts made to quantify the shape of activations in fMRI data (Looi et al., 2010, Scher et al., 2007, Yang and Shan, 2011), and most fMRI studies utilize existing complex shape descriptors. Here, we present a simpler technique that utilizes polar measures of closed 2-D contour(s) that comprise a 3-D shape across multiple axial slices.

6.3 Overview

In functional brain imaging, the underlying shape of an activation region (spatial) determined from statistical analysis is an important characteristic that should be preserved. The shape of the activated regions is usually distorted due to the several preprocessing and analysis steps involved in detecting neural activity and in bringing out the underlying spatial ROI related to the BOLD activation. Most fMRI studies involve investigating neural activity in one or more group of subjects and it can be useful to quantify the spatial differences within or across two groups through measuring and comparing shapes of the spatial activation regions. The primary motivation for devising these metrics is to provide tools that quantify the inter-subject and inter-group shape variation as well as enable researchers to gain more information about the spatial nature of BOLD fMRI activations.

To achieve the aforementioned goals, we present three metrics as illustrated in Figure 6.1:

1. *Centroid-based Polar Shape Metric* (**CPSM**) that utilizes morphology and polar vectors of pixels.

2. *Distance between Centers of mass* (**DCM**) that estimates the centroid distance between two 3-D activation shapes.

3. *Spurious Pixels Ratio* (**SPR**) which depicts the amount of activity in disjoint regions.

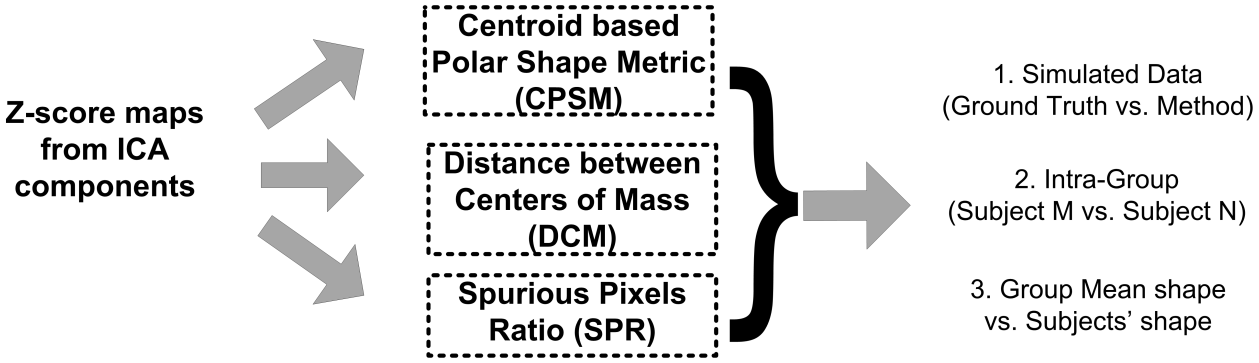

Figure 6.1: A high-level block diagram depicting the three

6.4 Centroid-based Polar Shape Metric (CPSM)

The proposed shape metric is primarily utilized for quantification of shape differences between the spatial components obtained from independent component analysis (ICA) of group functional magnetic resonance imaging (fMRI) data. This metric is applied to measure the difference in shapes of the activation regions obtained from different subjects within a group (healthy controls or patients) or compare spatial effects on activation maps obtained as a result of different fMRI analysis techniques. The parameters comprising the metric are computed for each pixel on the outermost contour (edge) of an activation region for each slice. These parameters are in the form of (r, θ) pairs that may be interpreted as the length and orientation of a vector originating from the centroid of the activation region to the pixel belonging to the boundary contour. Using this information we extract three features that quantify the shape difference between the two shapes under observation. For real fMRI data sets, the reference and observation shapes may be selected in two ways: (a) activation maps from two different subjects or (b) mean activation map compared against subject-wise activations, as obtained from group ICA. However, in the case of simulated fMRI data, the ground truth activation map is considered the reference image, whereas the activation

map resulting from application of different preprocessing (*e.g.* wavelet denoising, Gaussian smoothing) methodologies is taken as the observation image.

In order to compare two shapes, the CPSM metric uses edge maps extracted from the task-positive Z-score component maps obtained through ICA and subsequent thresholding. Following the estimation of Z-score maps, four error measures are utilized to estimate the parent metric value. Additionally, other parameters mentioned above are computed and combined with the parent metric to yield the final CPSM value. Every pixel in a slice $\in R^2$ sub-space and can be described by polar co-ordinates (r, θ) computed with respect to an origin in the same sub-space. This metric records the amount of change in these (r, θ) values (with respect to ground truth) for every pixel belonging to the outermost contour of an activation region highlighted by the component of interest post-ICA. The initial estimates corresponding to a particular slice are obtained in form of MSE values for Euclidean distances and arctangent angles with respect to an origin, that is, the reference Centroid of ground truth map. In order to keep the distance (r) and angle (θ) estimates unbiased, we utilize the centroid of the ground truth (Truth) to compute the distances and angles for the test shapes. A step-by-step algorithmic description for computing CPSM between two different shapes is given here (see Figure 6.2 for an illustration). The simulated data example is utilized where the activation maps for the wICA and sICA methods are compared against the ground truth activation shapes.

STEP 1: Initiate the algorithm with Z^{Edge} maps - Z^{Edge}_{Truth} , Z^{Edge}_{sICA}, and Z^{Edge}_{wICA} as the inputs, derived in the previous chapter for perimeter estimation (see Section 5.6.2 and Figure 5.11. Estimate the variable size vectors containing locations of edge pixels in the i^{th} axial slice: e^i_{Truth} , e^i_{sICA}, and e^i_{wICA}.

STEP 2: Compute the Centroid co-ordinates c^i_{Truth} using the ground truth map Z^i_{Truth} for each axial slice i.

STEP 3: Estimate the Euclidean distance-angle (r, θ) pairs for each pixel in e^i_{Truth} , e^i_{sICA}, and e^i_{wICA} with c^i_{Truth} as the reference centroid for all three edge maps. The resulting

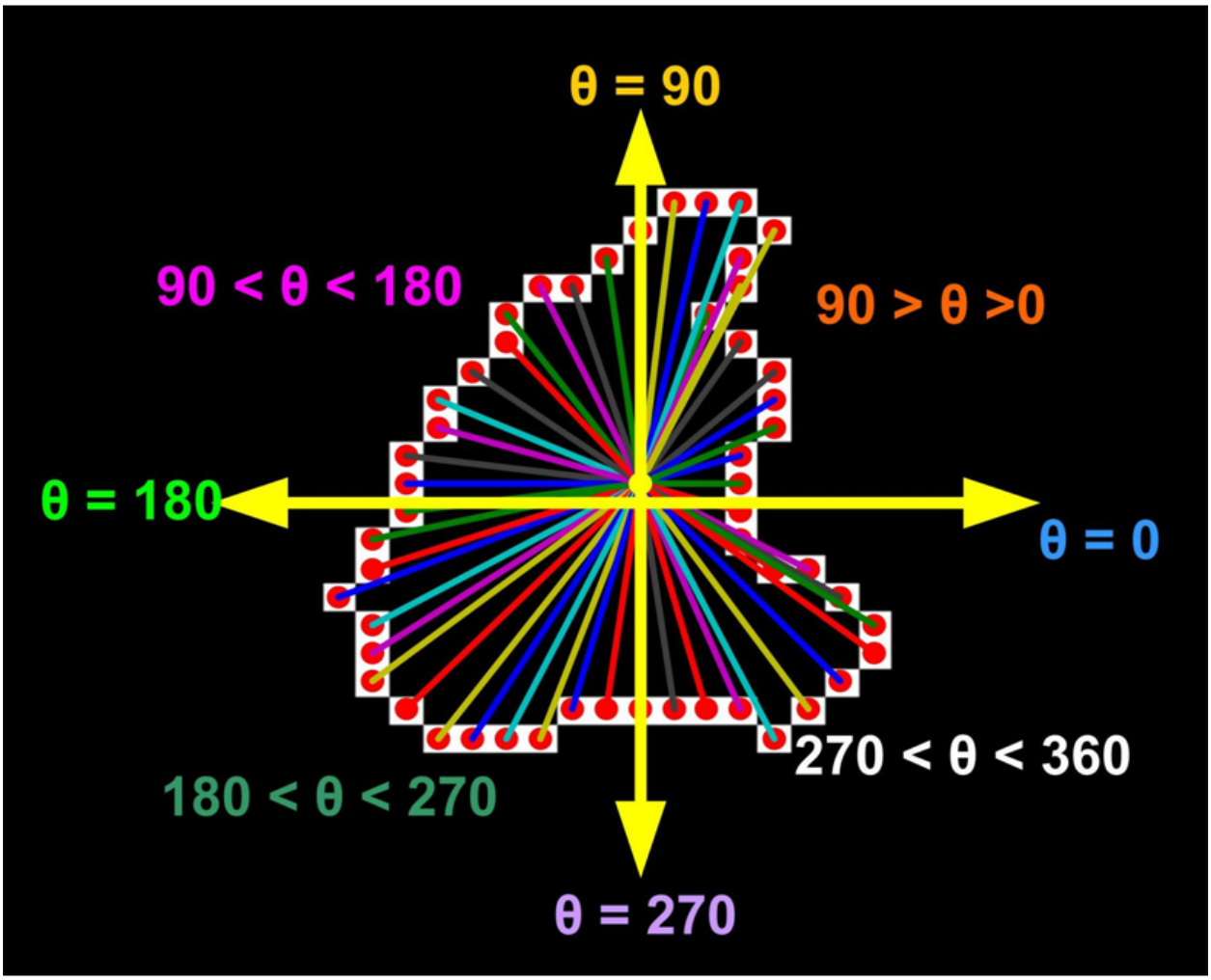

Figure 6.2: Illustration for computation of rotational and translational errors in each quadrant as explained in Steps 3 - 5. Vectors from the Centroid to each pixel are depicted in different colors along with a labeled axes. Various angular quadrants are also labeled to better understand the angular errors and decision criteria.

distance-angle vectors for each axial slice i are stored as $(r^i_{Truth}, \theta^i_{Truth})$, $(r^i_{sICA}, \theta^i_{sICA})$ and $(r^i_{wICA}, \theta^i_{wICA})$.

STEP 4: Locate and count the pixels of e^i_{sICA}, and e^i_{wICA} where the (r, θ) pair matches perfectly with those corresponding to pixels in e^i_{Truth}. The total count is termed as the ***gain*** represented as α^i_{wICA} and α^i_{sICA}.

STEP 5: Locate and count the pixels in e^i_{sICA} and e^i_{wICA} whose r estimates match perfectly with pixels in e^i_{Truth}. As a result, these pixels contribute to rotational (angle) error, given they are in the same angular quadrant (see Figure 6.3). This error primarily accounts for all pixels that have shifted away from the line joining it to the centroid. For example, if a set of corner pixels from ground truth are angularly displaced by an arbitrary angle in the test shape due to smoothing/denoising operations, it may be considered to be a *rotational* error. These errors are recorded in form of MSE values ($\omega^{MSE}_{wICA}(i)$ and $\omega^{MSE}_{sICA}(i)$) for each slice i:

$$\omega^{MSE}_{wICA}(i) = \frac{1}{N_{err}} \sum_{k=1}^{N_{err}} [\theta^i_{wICA}(k) - \theta^i_{Truth}(k)]^2 \tag{6.1}$$

where $k \in (1, 2, 3, ..., N_{err})$ corresponds to the indices of pixels with a rotational error in slice i.

STEP 6: Locate and count the pixels in e^i_{sICA} and e^i_{wICA} whose θ estimates match perfectly with pixels in e^i_{Truth}. Thus, these pixels contribute to translational (distance) errors that may have occurred due a pixel moving along the line joining it to the centroid. These errors are recorded in form of MSE values ($\delta^{MSE}_{wICA}(i)$ and $\delta^{MSE}_{sICA}(i)$) for each slice i:

$$\delta^{MSE}_{wICA}(i) = \frac{1}{N_{err}} \sum_{k=1}^{N_{err}} [r^i_{wICA}(k) - r^i_{Truth}(k)]^2 \tag{6.2}$$

where $k \in (1, 2, 3, ...N_{err})$ and corresponds to the indices of pixels with a translational error in slice i. If a set of corner pixels or pixels in a cusp area in the reference shape are rotated or translated outwards or inwards due to variability in response in different subjects or as a

result of different smoothing operations, then these errors are recorded by the metric through the above explained features.

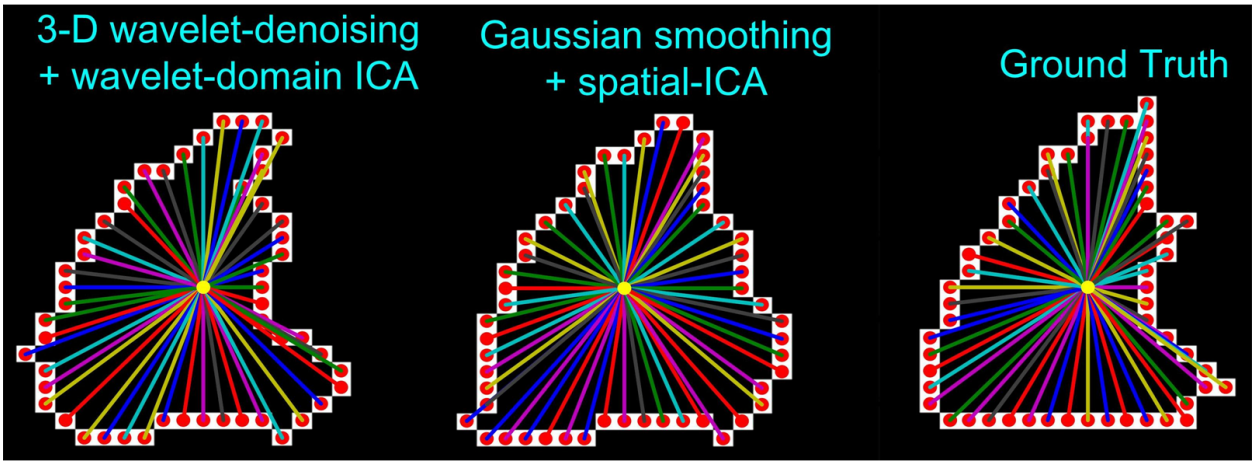

Figure 6.3: **Illustration of difference in shapes and how the distances and angle errors account for this change.** The shapes correspond to slice no. $i = 10$ from e^i_{wICA}, e^i_{sICA} and e^i_{Truth} edge maps. The Centroid location for each slice in the ground truth map was used as the Centroid location in the other two maps.

STEP 7: Count the number of pixels in e^i_{wICA} and e^i_{sICA} that have neither a distance match nor an angle match with any of the pixels in e^i_{Truth}. This count is stored as a *penalty*: β^i_{wICA} or β^i_{sICA}. This error accounts for a large shift of several pixels or addition of a false contour due to smoothing/denoising in some region(s) of the image.

Note: From here on the *Truth* subscript will not appear in any equations as it was absorbed by the MSE equations.

After having obtained four features vectors for each activation volume corresponding to the two methods under comparison - sICA and wICA, we proceed to estimate a weighted combination of these in order to represent the shape of a volume with a single number. We initiate this process by projecting each feature vector to a normalized sub-space by scaling each element with maximum value within that vector, resulting in values ranging between 0 and 1. Further, the normalized feature vectors $\hat{\alpha}^i_{wICA/sICA}$, $\hat{\beta}^i_{wICA/sICA}$, $\hat{\omega}^i_{wICA/sICA}$, and $\hat{\delta}^i_{wICA/sICA}$ are accumulated through a weighted sum across each slice resulting in a metric for each slice (see Eqn. 6.3). This final metric value (CPSM) for the given volume is computed

by summing across the aforementioned weighted metric vector.

$$CPSM = \sum_{k=1}^{N_{slices}} \frac{2\hat{\delta}^i + \hat{\omega}^i + \hat{\beta}^i}{2\hat{\alpha}^i} \tag{6.3}$$

where *CPSM* represents the proposed *Centroid-based Polar Shape Metric*. The above CPSM for a given slice is expected to have a low value when the number of perfect matches ($\hat{\alpha}^i$) is high and the value of the penalty ($\hat{\beta}^i$) is low and there are low values for errors - $\hat{\delta}^i$ and $\hat{\omega}^i$. The coefficients/weights were set based on the significance of the type of error. Perfect matches are always weighted the highest and assigned as the denominator, reducing any bias that could be introduced due to a high number of penalty pixels ($\hat{\beta}^i$) for a given slice.

Next, this metric is texted on the simulated data set(see Section 5.6.1) where the ground truth is well-known. This metric may be also be applied to real data sets depending on the amount of confidence associated with the accuracy of estimated ground truth shapes, even though the exact boundaries of the activation regions in a real fMRI data set are unknown.

Apart from their application for quantifying shape congruence as a result of different processing methods, these metrics may be utilized for measuring and quantifying inter-subject activation shape variability for various group studies. For example, the difference between the spatial characteristics of activation regions may be estimated for subjects belonging to the same group (healthy controls or diseased subjects) on an absolute scale or for quantification of inter-group variability on a relative scale to compare subjects from different groups. The application of CPSM on real fMRI data sets will be presented in later sections of this chapter.

6.5 Simulated fMRI data: CPSM

Previously, simulated data was utilized to test the effects of two approaches sICA and wICA and were repeatedly compared in Section 5.6.2 using ROC curves, and shape perimeter. The MPSM (perimeter metric) primarily focuses on the spread of the contours as a whole whereas

CPSM takes into account the shape of the contour on a pixel-by-pixel basis. This section presents the application of the proposed CPSM metric to quantify the differences between activation regions obtained through the two approaches. CPSM values corresponding to both sets of simulated data - Temporal lobe and Occipital lobe, presented before in Section 5.6.1, are illustrated and discussed below.

6.5.1 Occipital Lobe

The CPSM values for the occipital lobe quantify the differences between the two methods on a pixel-by-pixel basis across 10 random noise frames. A significant and consistent improvement is observed for the w-ICA method with low variance as presented in Figure 6.4. Note that CPSM is estimated using axial geometry only. This is simpler to interpret as most diagnostic analyses are done using axial slices. Although, a more accurate estimate of CPSM may be obtained by using 3-D spherical coordinates for the estimation of the Centroid. In that case, solid angles may be computed for different regions belonging to the surface of 3-D non-rigid activation region.

It can be noted from Figure 6.4 that the level of shape congruence is inversely proportional to the metric values, that is, the metric acquires low values if the shape is more similar to the ground truth and vice versa. The w-ICA method consistently performs better than s-ICA framework and is able to preserve the shape of the activation region while having little effect due to increasing amount of noise across various signal/noise combinations.

6.5.2 Temporal Lobe

The basis for superior performance of the w-ICA over s-ICA is further bolstered through the CPSM values presented in Figure 6.5. The temporal lobe being a large ROI consists of more complex contours across different slices. The edges along these contours were found to be spontaneously varying, thus resulting in larger distortion in shapes as a result of spatial smoothing. A larger shift in voxels in terms of (r, θ) measures is observed, in addition to

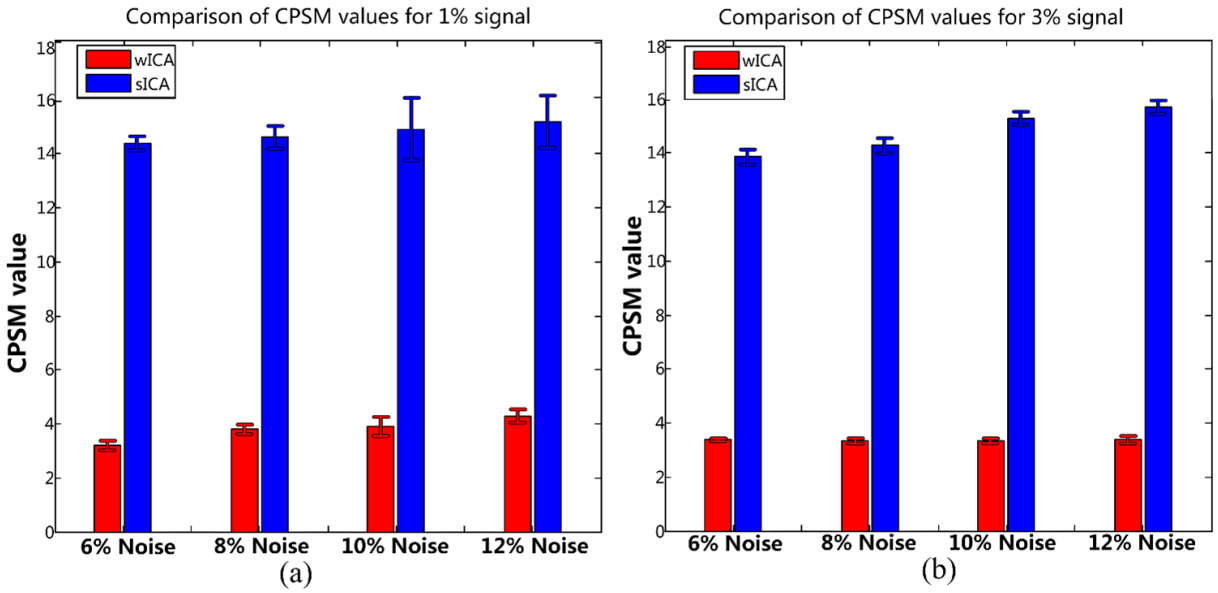

Figure 6.4: **CPSM statistics:** computed and illustrated as the mean and standard errors of $CPSM_{wICA}$(red) and $CPSM_{sICA}$ (blue) across n = 10 observations for every possible combination, that is, for 10 different noise frames: (a) signal = 1%; (b) signal = 3%. The bars are grouped based on different levels of noise (6% to 12%).

greater numbers of voxels being classified as misses which eventually resulted in larger CPSM values for s-ICA framework that employs Gaussian smoothing and ICA in the spatial domain. Low CPSM values were obtained through w-ICA as the wavelets are known to preserve edges and introduce little amounts of spatial smoothing further enabling the generation of better estimates of independent components through ICA being performed in the wavelet domain.

The number of perfect matches or Gain (weighted highest in CPSM) is high in case of a large ROI such as the temporal lobe. This directly results in lower values for CPSM for s-ICA as compared to values observed in case of occipital lobe in Fig. 13. The bars are grouped based on different levels of noise as shown. For 3% signal level, both frameworks show almost no change with increasing noise, whereas larger shape distortion is observed for 1% signal level with increasing level of noise as seen in Figure 6.5.

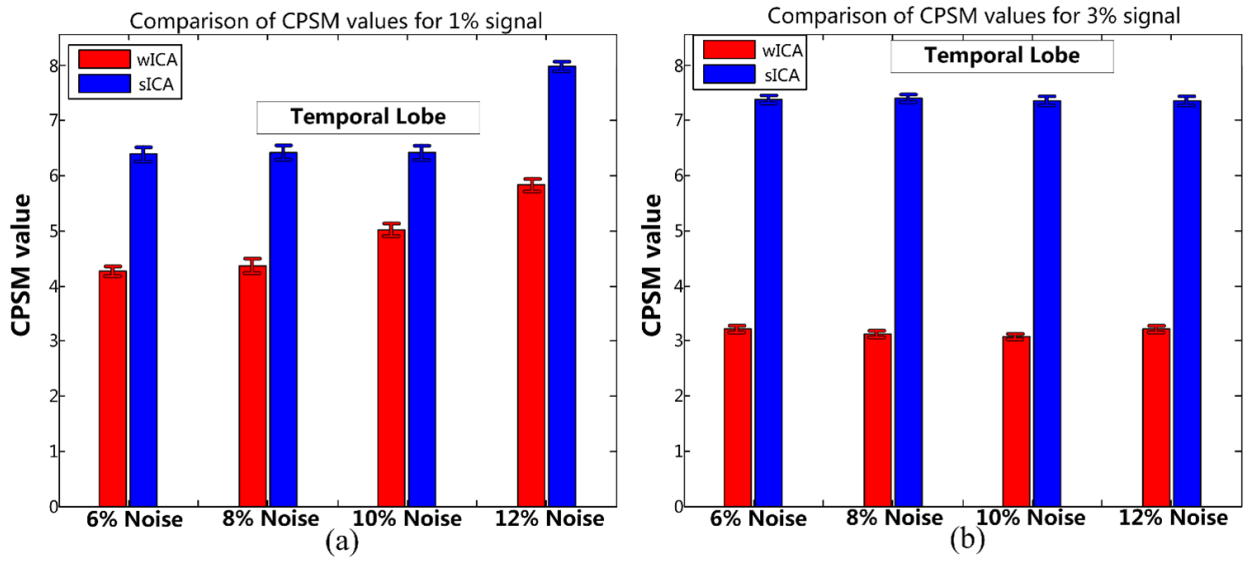

Figure 6.5: $CPSM_TL$ computed for temporal lobe data reported as mean and standard errors of $CPSM_{wICA}$ and $CPSM_{sICA}$ values across 10 noise frames for every possible combination: (a) signal = 1%; (b) signal = 3%.

6.6 Controls vs. Patients: CPSM

The wavelet-based denoising methodology was evaluated using the multi-group data set (HC vs. SZ) in Section 5.6.4 previously. In this section, we present CPSM-based evaluation of activation shapes corresponding to different denoising methodologies applied to data from the same two groups of subjects.

The primary goal of fMRI studies involving patients and controls is to be able quantify inter-group differences as well as differences between subjects within each group. We utilize CPSM to uncover how different each subject's activation is from the group mean. This is essentially useful to identify subjects which are similar or different from the group mean activation. In addition, we apply the metric through two different methods under comparison wICA and sICA as done in Section 5.6.4. The CPSM values set the group's (HC or SZ) mean activation as the reference whereas each subject-wise activation map is considered as the observation image.

As also depicted by comparisons presented in Chapter 5, the CPSM values for the wICA

methodology are consistently lower than the conventional sICA analysis in both groups, as also illustrated in Figures 6.6a and 6.6b. An interesting observation from these results is that there is a high amount of variation in activation shapes in case of controls (HC) as compared to the patients. This signifies that the brains of patients are more similar to each other when presented with this particular stimulus whereas the brains of controls are more different from each other. This diagnostically relevant since we are always trying to identify unique features that define a certain neuro-developmental disorder. It is possible that the patients' brains have ceased to develop after a certain point due to various effects of the illness. This is also consistent with other studies explaining the occurrence of reduced exclusivity in activation patterns amongst patients. In addition, some prior knowledge about behavioral data can be complimentary when attempting to understand such trends. Usually SZ subjects are more cautious about performing a task diligently as compared to the HC subjects. This may be attributed as one of the reasons for such an observation in addition to this study's small population of subjects.

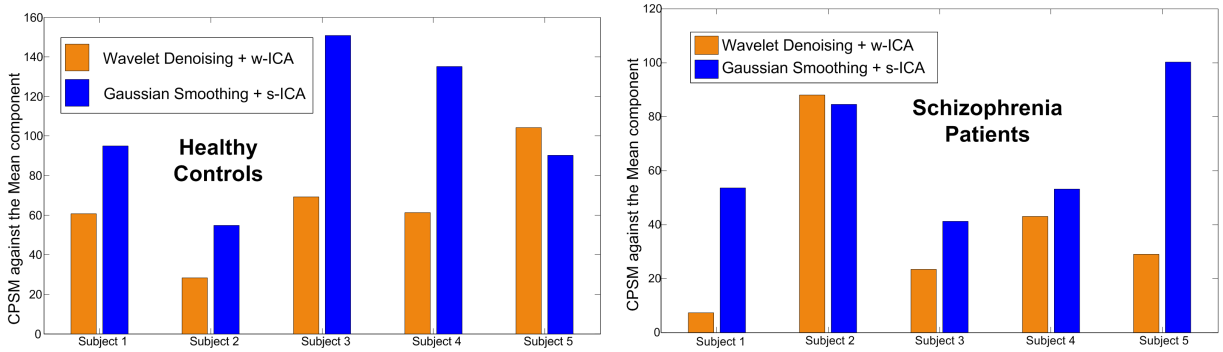

Figure 6.6: **Application of CPSM for Patient data.** Each pair of bars represents the shape difference between the activation map for a subject and the mean activation of that group: (a) Healthy Controls (5 subjects); (b) Schizophrenia patients (5 subjects).

As mentioned above, in contrast to the group data used in this study more interesting differences may be observed when comparing a large group of subjects. This metric may also help in selection of outliers that performed very well and are similar to the mean activation

map or performed poorly and are significantly different from the mean activation.

Lastly, it would be interesting to study resting-state networks using the proposed framework in order to obtain more accurate shapes and sizes of the regions functioning as coherent networks in the brain. This might be an initial step towards improving the statistical power in spatial functional connectivity analysis within large groups of subjects.

6.7 Additional metrics for BOLD-fMRI

As mentioned before, the utility of this metric is manifold and fits well within our preprocessing framework. The initial and probably the sole motivation for devising such a metric was only to compare the performance of different denoising methods through simulated fMRI data sets, that is, when ground truth is available. The topic of inter-subject variability has been discussed widely in literature (Allen et al., 2011) and reflected in the results of various methods presented across the previous chapters of this thesis. It is a well-known fact that everyone's brain is different in form, shape, size and most importantly function and network connectivity. There is known to be large amounts of variability in functional activation boundaries across different subjects. Over the past few years, there has been increased interest in studying the causal and parallel interactions across different regions spread over networks or those comprising a single network for an individual subject . To better quantify the parameters associated with inter-subject variability, we added two different empirical measures - Distance between Centers of Mass (DCM) and Spurious Pixels Ratio (SPR) that account for some of the low-level variations that are usually averaged out when analyzing group-level activations. These mainly act as secondary metrics for CPSM which provides a pixel-by-pixel quantification of shape congruence.

In this section, we illustrate the important role of these two secondary metrics (DCM and SPR) in discriminating between subjects based on activation shape. We also validate the integrity and dependence on CPSM for signifying shape congruence. Even though both these metrics (DCM and SPR) are well known from their common applications in the field of

pattern recognition and image processing, we briefly summarize these below in the interest of clarity. To maintain context, we present the next set of CPSM results in addition to these two new metrics, DCM and SPR on the *Motor-tapping* data set comprising 20 subjects (see Section 2.4.1).

6.7.1 Distance between centers of mass (DCM)

This parameter is estimated for the two 3-D shapes under comparison as the Euclidean distance between the centroids of the 2 shapes under comparison. This measure primarily enables answering questions such as - *is the centroid of activation in a particular subject is anatomically close to the mean activation*; or *how proximal is it to the activation centroid of another subject*. It also allows comparison with the centroid of a known anatomical ROI mask that represents the region that has high likelihood of being activated. This measure can easily be converted to the MNI space in order to locate the exact anatomical coordinates and regions and assist in making detailed inferences about the BOLD activity. The DCM can be simply be represented as:

$$DCM = \sqrt{(X_{Ref} - X_{Obs})^2 + (Y_{Ref} - Y_{Obs})^2 + (Z_{Ref} - Z_{Obs})^2} \tag{6.4}$$

6.7.2 Spurious Pixels Ratio (SPR)

A common problem in handling threshold maps is getting rid of regions/pixels of no interest. Such pixels are usually termed as 'spurious' pixels. Usually, these regions are removed using morphological opening or closing. In this section, we utilize this information by the counting the number of pixels in each of the threshold images under comparison. For example, the mean activation map and each subject's activation map can have different number of regions/pixels that do not belong to the primary activation cluster that is used to measure

CPSM. The ratio may be expressed as:

$$SPR^i = \frac{N^i_{subject}}{N_{mean}}. \tag{6.5}$$

where $N^i_{subject}$ is the number of spurious pixels in the i^{th} subject's activation map and N_{mean} is the number of spurious pixels in the group mean map. This ratio can be greater than 1 in the case $N^i_{subject} > N_{mean}$ which indicates that there were more spurious pixels in the subject's image indicating neural activity elsewhere that may well be worth investigating further for that subject. In Eqn. 6.5, the quantity N_{mean} can be replaced with $N^j_{subject}$ which is the number of spurious pixels in the j^{th} subject's activation map in order to estimate the SPR between two different subjects.

6.8 Motor-tapping Group fMRI: CPSM, DCM, SPR

Frequently, ICA-based fMRI studies typically compare two groups based on their mean maps, but often ignore the variations between individual subject's back-reconstructed ICA activation components and the aggregate maps, which can contain important information. In Figure 6.7a, we present the CPSM results measured by setting the task-positive (motor cortex) group mean component as the reference image and setting each subject's back-reconstructed activation map as the observation image. It is evident from Figure 6.7a, that about 8 out of 20 subjects have a CPSM value = 20. This indicates that the shape of the activation regions in these few subjects is relatively closer to the mean activation map. The lowest CPSM value was obtained for subject 3 = 19 units whereas subject 12 is estimated to be the most different in shape with a CPSM value = 86 units. In order to emphasize the differences in shape, a few slices of the activation maps of two different subjects are overlaid on an anatomical image of the human brain as shown in Figure 6.7b. Significant differences and similarities can be observed in the shapes of subject 12 and subject 3 respectively. There are definitely more 'red' pixels signifying areas that show BOLD activity in subject 12 and are

absent in case of the mean map ('black' pixels). Similarly, the shape of subject 3's activation region is closely related to the shape of the mean activation. Other differences such as shift in centers of mass and activity in spurious or non-task significant areas are accounted for by the distance between centers of mass (DCM) and spurious pixels ratio (SPR) measures.

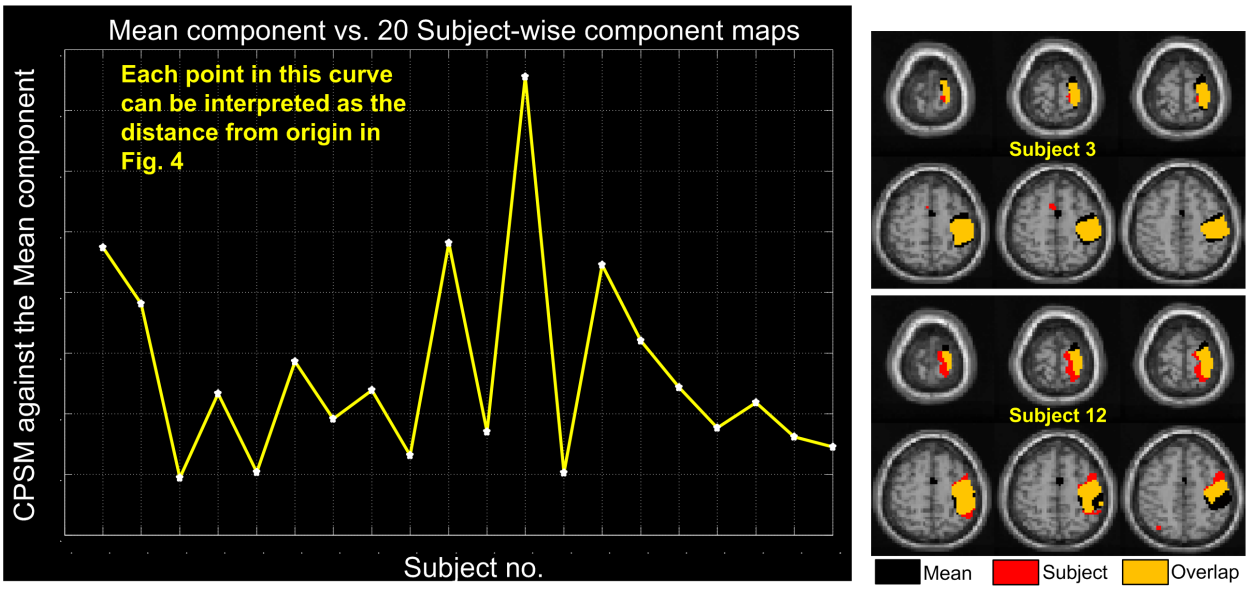

(a) (b)

Figure 6.7: **CPSM: Motor-tapping:** CPSM values obtained by comparing the group mean activations against subject specific maps - (a) Curve showing variation in shape of activation across 20 subjects when compared against the shape of the group mean map. (b) Overlaid maps of subject 3 (lowest CPSM) and subject 12 (highest CPSM) to illustrate the spatial features that result in difference in shape. Note that there are more red voxels (subject activation only) in subject 12 than in subject 3 indicating large variation in activation contours of the former.

Next, we visualize the shape by simultaneously plotting two metrics in a new type of analytical plot. The visualization is known as the *Orbital Graph*. Figure 6.8 is an orbital representation of the variation between different subjects and the mean. The origin in this representation (white circle in the center) signifies the mean activation map (CPSM = 0) and is considered as the reference point for all other subject specific activation maps. In this figure, we incorporated the DCM measure (described as r inset) along with the CPSM values estimated for every subject. Note that circles are arranged in a counter-clockwise manner, increasing from subject 1 to 20. The radius of the colored circles corresponding to

each subject (as annotated) is the scaled DCM value whereas the orbit marked as $0-100$ in steps of 20 represents the number of CPSM units (described as R inset) that the subject is different from the mean. The circles with centers between 0 and 30 correspond to the subjects whose shape is closest to the shape of the mean activation in terms of CPSM's arbitrary but absolute units. This graph provides an overall view of the difference between the mean activation and different subjects. Such an orbital graph can be created with any subject's activation map set as the reference image and compared to other subjects' activation shapes. This graph incorporates the CPSM and the DCM measure into a single method to visualize the variation between various subjects.

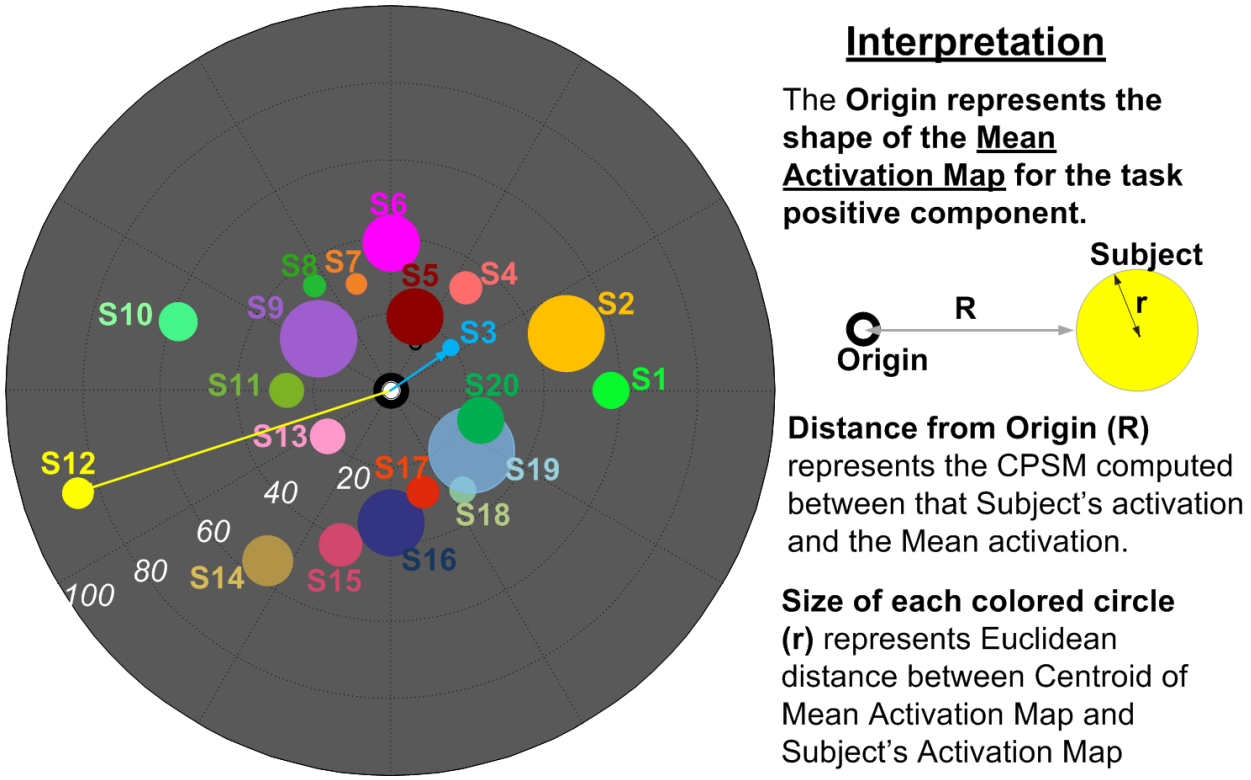

Figure 6.8: An orbital curve showing absolute shape differences across the group versus the mean using CPSM and DCM measures. As explained in the key on the right, farther the circular region, higher the CPSM value (see Figure 6.7). Each circle corresponds to a different subject (arranged in a counter-clockwise manner starting from subject 1 (S1)) whereas the radius of circles represent a scaled DCM measure. A large circle indicates that the activation cluster for that subject was centered at a far away voxel as compared to the activation cluster in the group mean map.

As seen from Figure 6.8, subject 3 has the closest center of mass to the mean center of mass (DCM = 0.6 pixels) whereas subject 19 that corresponds to the largest circle in Figure 6.8 has a DCM value = 3.25 pixels. Even though the CPSM values for subject 3 (19 units) and subject 19 (26 units) are low, the difference between their DCM values can provide significant information relating the activation centers for this particular task positive component. The actual values of the CPSM represented in Figure 6.8 as the location of circles were shown in Figure 6.7a. The next measure presented here is the spurious pixels ratio (SPR) as described

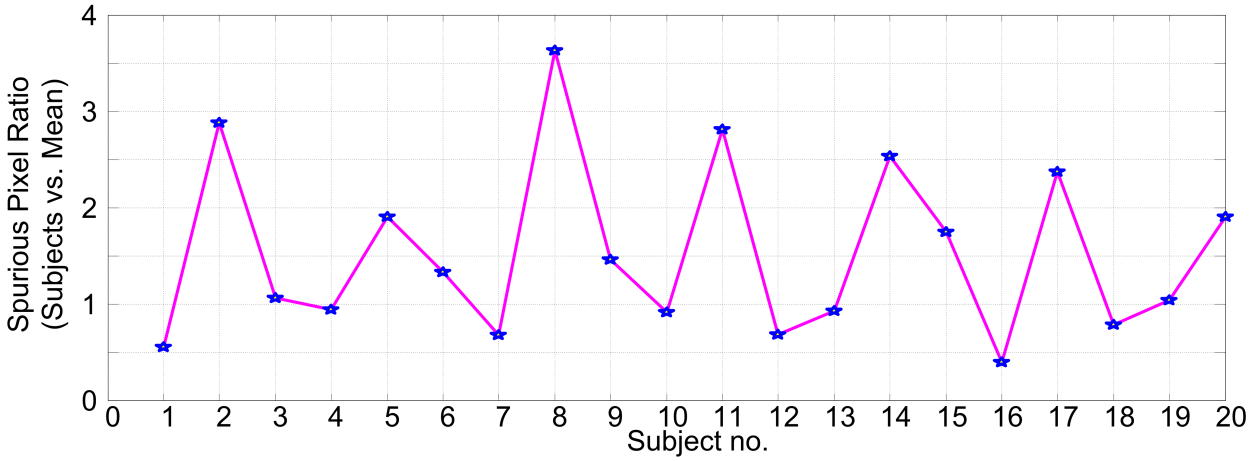

Figure 6.9: Variation in the SPR measure (see Eqn. 6.5) across various subjects. Subjects 2, 5, 8, 11, 14, 17 and 20 have high SPRs indicating that there exist relatively large regions that are not a part of the primary activation region (motor cortex).

in Eqn. 6.5. SPR was computed using the mean activation map and individual subject maps and is presented in Figure 6.9. All subjects that have high SPR values can be considered worth analyzing individually for some interesting task-related activations in regions that are not a part of the motor cortex. Here, the subjects 2, 5, 8, 11, 14, 17 and 20 have very high SPRs indicating large number of non-ROI pixels being active in these subjects in comparison with the non-ROI pixels that are active in the mean component.

6.8.1 Inter-subject CPSM (Subject i vs Subject j

After having quantified the group level mean activation maps with the back-reconstructed maps for individual subjects, we present some subject-to-subject comparisons that are in agreement with the pattern seen in Figures 6.7 and 6.8 when comparing the mean activation with each subject. In Figure 6.10, we present the subject-to-subject CPSM values as a stacked bar plot where each subject (along the x-axis) is compared with every other subject (colored blocks in each bar). The subjects that have a low CPSM value in group comparison show low values here when compared against subjects that had a high CPSM value (see Figure 6.10). Note that, the colored block representing the subject used as reference will be missing from the bar corresponding to the same subject since the metrics are equal to zero when comparing them with each other.

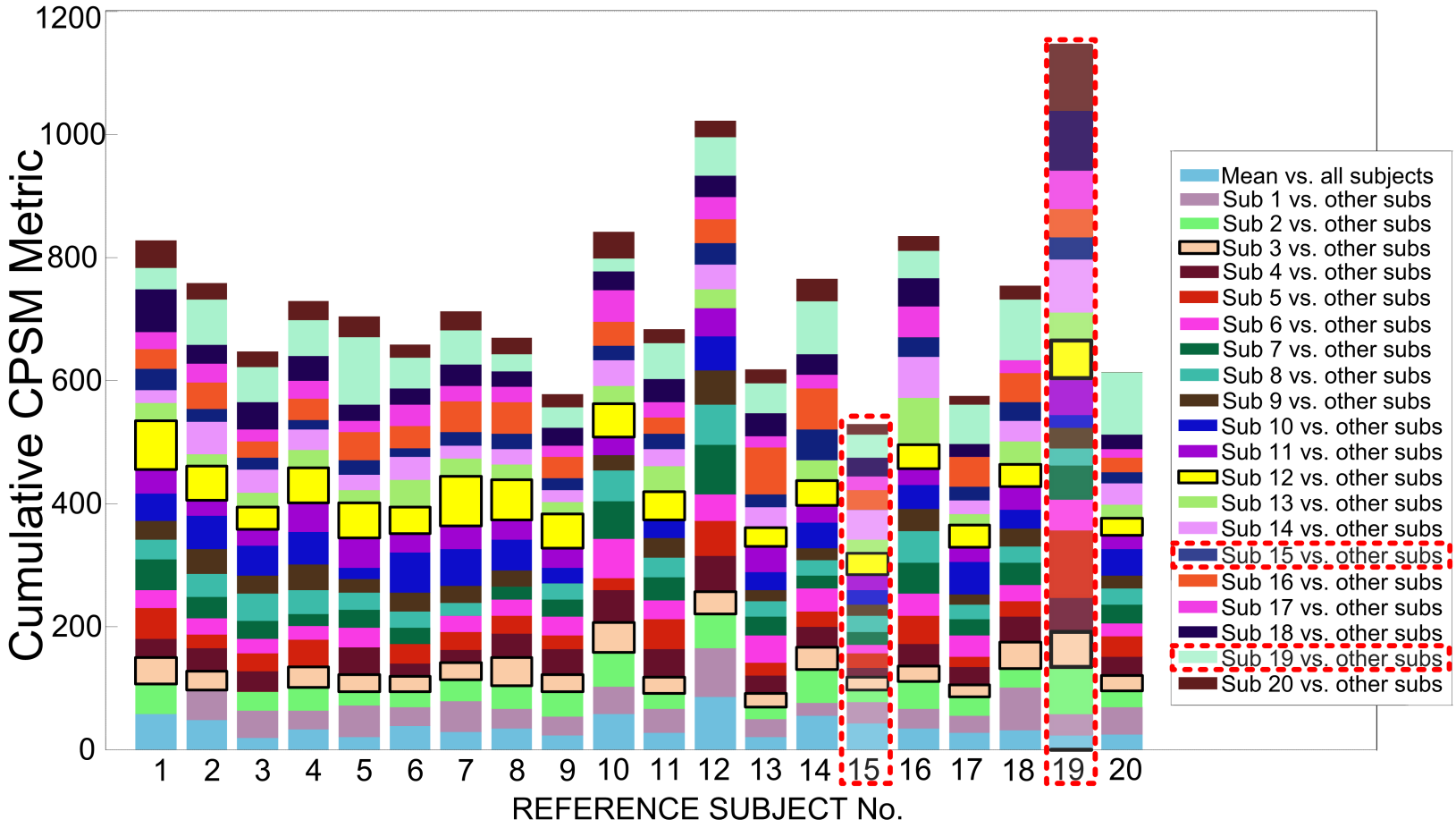

Figure 6.10: Illustration of subject-to-subject variations obtained by comparing each subject's activation shape against every other subject. Each color block (along y axis) represents the CPSM value when compared against the Reference Subject (x-axis). The lowest row of color blocks represent the difference from mean (same information as Figure 6.7a) with subjects 1, 10, 12 and 14 showing large values (see color legend for mean). Note that these subjects are the ones with highest cumulative CPSM values in this graph (tallest bars) subjects suggesting a large overall difference from rest of the subjects.

In Figure 6.10, we summarize the intra-group comparisons where each subject is compared against every other subject on the basis of shape, that is, the CPSM. Note the large size of color blocks corresponding to subjects 3 (beige) and 12 (yellow) as compared to all other subjects. This verifies the observations discussed and illustrated previously in Figures 6.7 and 6.8. The large CPSM measures for subject 19 against other subjects (highlighted in Figure 6.10) may be accounted by the fact that the activation for this subject was the farthest from the mean, thus resulting in high values for the distance parameter (δ^{MSE}), gain (α) and penalty (β) measures that comprise the CPSM metric (see Eqn 6.3). Subjects 1, 10, 12, and 14 are the other subjects that correspond to the high cumulative CPSM values in Figure 6.10. In contrast, the cumulative CPSM values corresponding to subject 15 are lowest, indicating similarity in shape with most other subjects. This is consistent with the peaks seen in Figure 6.7 and the circles lying in the outer orbits in Figure 6.8.

The SPR and DCM measures for within-subject comparisons can be estimated in a similar way but are not presented here due to brevity. When there is a need to compare two or more subjects (and not all subjects) within the same group for some specific differences in activity, researchers might benefit by estimating subject-to-subject differences in SPR and DCM.

6.9 Summary and Applications

The proposed metrics can be utilized in many different ways to quantify changes in activation shapes within and across groups. In addition to the utilities illustrated here, there are other possible uses depending on the data being used for group analysis such as - (1) comparison between different analysis and fMRI pre-processing methods; (2) comparing patient groups and variation in neural activity under different conditions of brain state (while engaged in a cognitive task or while at rest); and lastly (3) using the shape metric as a potential feature in addition to amplitude of fMRI activation, temporal and spectral difference for measuring variability across large scale resting state fMRI group studies.

For real fMRI data, it is typically necessary to track changes in neural activity at a group level and generate useful statistics to make strong comparisons. The proposed shape metric measures could be easily utilized to add to the power of existing statistical measures and measure the changes across subjects within the same group. Another possible application can be to compare various functional networks that co-exist during different states of the brain, that is, while at rest or performing a task. It has been shown that several such networks co-exist within the same group of subjects while they do a task or while at rest (Calhoun et al., 2008). The differences in shapes of these activation regions associated with different networks can be a useful measure to make an estimate of the differences in location of neural activity which in turn can assist in making other unknown inferences about the human brain. Large-scale resting state studies have revealed differences in various functional domains based on various features such as gender, age and ethnicity (Allen et al., 2011, Biswal et al., 2010). The shape metric feature can also reveal significant spatial differences while acting as additional information to the existing set of features.

To summarize, this metric presents a potential feature that would help explain the dynamics of fMRI activity across different subjects in a single study or across different studies. The new metric proposed in this paper may help neuroscience researchers build a better comparison model between subjects based on the shape of their activation regions and also help classify these differences based on other features such as age, sex and ethnicity. This metric can also act as a training feature for design of SVM and neural networks used for separating artifacts from BOLD-related components when using ICA for signal separation. Also, we believe this shape metric will prove to be a useful tool for comparison of different pre-processing methods used for preparing fMRI data for further analysis.

Chapter 7: Summary and Conclusions

In this doctoral dissertation, I developed and presented signal processing methods for functional brain imaging by applying two concepts - Wavelets and Independent Component Analysis (ICA). Both these techniques have been used to decompose a signal into its constituent sub-signals. I have extended them to formulate new methods for denoising volumetric images, normalizing multi-subject fMRI (functional magnetic resonance imaging), and synthesizing spatial templates of brain networks.

In this thesis, I introduced a novel image preprocessing framework that focuses on data-driven approaches and reduces model dependence for fMRI analysis. I achieve this by weaving together two distinct algorithms that benefit from each other: ICA un-mixes the complex fMRI data into multiple components or networks, and wavelets adaptively combine these networks into a single aggregate functional template. This *intelligent* signal processing approach combines information from multiple brain states (at rest or during a task) and forms a stronger foundation for decoding interaction patterns across networks of normal brains as well as that of patients with neurological disorders such as Schizophrenia, Autism, Parkinson's, and Alzheimer's.

I created the ICA-based Functional Normalization (ICA-fNORM), a new framework for spatial normalization of fMRI data from a group of subjects that utilizes their resting state functional maps (default state of the brain) - rather than the structure - as the reference. This provides better functional localization of brain activity and reveals additional relationships between spatial dynamics across various sub-areas of an activation region. I derive these functional templates of the subjects' default brain function using ICA, which separates temporally coherent and maximally independent brain networks as volumetric brain images. Quantitative results from application of the ICA-fNORM method using single-network and multi-network templates were presented in Chapters 3 and 4 respectively. These results show favorable improvements upon current normalization approaches used widely. If the functional

template is constructed from hundreds of subjects and is fine-tuned to small boundary variations, it can serve as a universal functional template of brain function. As a near-future possibility, multiple research labs will be able to generate scanner-specific, study-specific, and population-specific templates of brain function. This could help overcome sources of noise from a single hardware system used repeatedly and can potentially reveal new information about population-based brain function.

After illustrating the advantages of single-network functional templates and functional normalization, the proposed ICA-fNORM approach was advanced through an image fusion methodology. Combination of multiple networks can be considered the next generation functional re-alignment without the need of complicated temporal or high-dimensional warping approaches. Forming functional templates is also possible for normalization of data sets associated with different sessions of the same task performed by a group. This may lead to better realignment understanding of task-related variability within subjects. By demonstrating results from a simple approach for multi-network template fusion, I believe the introduction of functional templates in this thesis lays a good foundation for derive a functionally standard space that can be used to normalize large fMRI data sets. A possible change in general outlook towards data-driven preprocessing can be expected, since the diagnostic importance of our approach was illustrated in form of significant betterment of detection sensitivity, localization of activity and statistical findings on fMRI data from controls and patients. We believe that the proposed method has a lot of potential and can be considered user-ready in its current form for experimentation under various pre-processing scenarios.

Based on the findings presented in previous chapters, the multi-network ideology seems valuable. However, it is still not perfect and the overall theme of combining information from rest and task data can be worrysome to clinical researchers as well as engineers trying to progress the field. The foremost implication being how one interprets each of these temporally coherent networks on their own. Using low-dimensional warping schemes, it is difficult to separate and identify subtle effects of each network on the final fusion template.

The method using single network as a template was first presented as a foundational basis to understand this effect. Having said that, resting state networks are known to have complex interactions across the brain and it is important to carefully choose the robust and task-relevant networks for template fusion and functional normalization. This process of selection may sometimes require multiple iterations to reach an optimal subset of candidates for image fusion. Another point to note is that since the data collected during AOD contains task-related variance, it is difficult to know if the physiologic mechanism behind the patient versus control changes is the same for both paradigms (rest and task). It may be possible that AOD changes are the mixture of the two effects (rest and task), and are only enhanced when resting-state networks are used to normalize the group data.

I have also developed new techniques to apply Wavelet-based denoising to optimize fMRI image quality for improved activation specificity and shape accuracy. The algorithm is spatially adaptive and utilizes inter-scale and intra-scale dependencies in fMRI images without sacrificing resolution or distorting intensity values. This is a flexible smoothing method that is independent of its point of application. That is, it may be applied before or after spatial normalization. This denoising algorithm is able to preserve spatial details (edges, corners, etc.) and 3-D morphology of intensity images while maintaining the homogeneity of the original signal values across an fMRI image sequence. Specifically, this approach exploits a spatially varying threshold estimation scheme, eliminating any need for assumptions about signal or noise distributions. My denoising algorithm utilizes adaptive 3-D edge filters to derive masks for driving a probabilistic signal estimation procedure. This versatile probabilistic approach performs signal detection and estimation as a single step using a priori masks derived from 3-D wavelet sub-bands. The proposed denoising methodology which utilizes an isotropic neighborhood based indicator in combination with prior probabilistic information to achieve a robust estimate of denoised signal. Results indicate a clear advantage of wavelet based methods in terms of achieving shape accuracy in addition to higher specificity and ability to suppress noise. We presented results using simulated data as well as real fMRI

data sets acquired while subjects performed a cognitive task. Comparisons between the conventional Gaussian denoising and our proposed approach were presented based on sensitivity, specificity, intensity values, and perimeter of activation regions. From a diagnostic point of view, the method shows great promise in its ability to assist in decision-making relating to abnormality and bio-markers for functional brain disorders as well as better understanding inter-subject variability in BOLD activation patterns.

Having advocated for application of wavelet transforms for denoising through algorithms and results presented within the thesis, I believe a more optimal outlook will be to view the denoising step from a general angle and leave the field open for a hybrid family of methods. The current assumptions associated with smoothing fMRI data, in general, are largely based on existence of normalization errors, and inter-subject differences in the EPI images acquired for fMRI analysis. Therefore, it may be possible that a hybrid method that performs normalization and registration without adding artefacts that impose the need for smoothing. An even better approach may be to have the ability to simultaneously model and eliminate noise as other preprocessing steps are applied. As detailed earlier in Section 1.4, the goal of this thesis is not only to propose new methodologies for fMRI preprocessing, but to shed more light on associations between the various parts of the current fMRI preprocessing pipeline.

An in-depth study of the effects of different types of denoising placed a irreplacable need for quantitative validation in addition to qualitative analysis. I verified the proposed denoising method against the state-of-the-art using both simulated and real data and successfully published the findings (Khullar et al., 2011b,c,e). I have successfully applied the algorithms to a variety of datasets - including large-scale simulations (Khullar et al., 2011c), single subject data (Khullar et al., 2011b,c) as well as scans of multiple schizophrenia patients (Khullar et al., 2011e). The published results, also presented in this dissertaion, show considerable improvement over existing methods and have proved

viable for uncovering new and improved biomarkers with a reduced number of false positives. I have also made the algorithm freely available as a MATLAB-based software toolbox (`http://mialab.mrn.org/software/waveidiot/index.html`).

I consider the algorithms presented under the context of data-driven prepreprocessing as an intial innovative effort. This ideology, as carried forward, presents a favorable path for this family of data processing techniques to form a strong link between engineers and clinicians. This possible paradigm shift should be seen riding on indispensible facts such as availability of large amounts of data, advanced computational algorithms, and a rapidly increasing interest in the information fusion. I sincerely hope that this work contributes to clarifying the importance and extent of the role played by data-driven fMRI preprocessing in this new age of decoding the mysteries related to the human brain as the most complex self-sustaining system.

7.1 Future Work

Future work associated individually with each component of this thesis was presented at the end of the relevant chapter. In addition, I briefly discuss here some additional directions of future research. This body of work can be seen as precursor to some substantial extensions and improvements forming the future work. In this section, I will highlight the theories that I believe will highly compliment this doctoral thesis while further changing the outlook towards fMRI analysis and the information it provides.

First, a major limitation associated with the principle of using fMRI images for deeply understanding brain function is imposed by the acuquisition system. The magnetic strength of the fMRI scanner governs the resolution of digitized images. High magnetic strength scanners (upto 7 Tesla) that are continuously being tested for safety concerns and quality, are not far from replacing the current generation of 3T machines. However, it may be interesting to apply high resolution imaging to smaller brain regions instead of full-brain snapshot imaging. It is possible that certain complext cognitive tasks engage or activate a certain

region of the brain more intensively as compared to others. The goal of attempting to adapt the methods proposed in this thesis in order to understand the dynamics of various functional boundaries of sub-regions, is not a far-fetched reality. Since, the underlying motivation of all fMRI research is to localize function as accurately as possible, it may not be a bad idea to co-design the algorithms based on certain well thought-out modifications to the acquisition process.

The tremendous success of using ICA for fMRI analysis is closely associated with certain underlying assumptions. The first assumption is that sources in the brain are non-guassian and mixed linearly. Second, in context to group ICA, is that largely the same brain region(s) are engaged during a task across the entire group of individuals. Seen as a *black box* type of approach by most clinicians, it is still unclear whether these assumptions are fully valid. An exciting future extension will be to compare the performance of functional templates formed using blind source separation methods other than ICA. Independent vector analysis (or IVA) is a strong candidate that, in practice does not make assumptions about population wide coherence of region-task association. It will be interesting to use such an approach in conjunction with the template fusion work since the inter-subject variability will be better captured through the warping parameters and may further uncover relationships across functional boundaries that exist in the brain.

Lastly, current fMRI tasks commonly utilized for patient and control analysis are fairly simple since it simplifies separation to engage and modulate distinct brain regions based on exclusive set of functions performed by them. As the field progresses with methodological and hardware improvements, designing complex tasks may become imperative to understand complex functional systems. It may not be uncommon to assign tasks such as solving a puzzle or playing a game through eye-tracking to understand high level systems and their interaction patterns between various regions of the brain. Knowingly so, it may not be unreasonable to assume that different sub regions of the brain may be engaged at different instances during a task. For example, solving a math puzzle over time may involve shift in activation focii across

various sub-regions through different stages of the puzzle. An intuitive method to capture this phenomenon is applying statistical methods over smaller temporal windows of data and studying changes as modulation of resulting statistics and spatial maps of activation.

7.2 Career Agenda

In graduate school, I have been fortunate to collaborate with and learn from researchers in a variety of fields -perceptual image quality, optics, computer vision, brain function, and wearable medical sensing. These collaborations, combined with the wide range of projects I have completed at RIT and at MIT, have led me to my career research goal: to create new algorithms and design low-cost, readily-available imaging systems for personalized wellness that are capable of uncovering interesting information hidden within the captured signal. I will continue collaborating with domain experts to design sensing systems and signal processing algorithms that allow us to develop better understanding of our health and the impact of our environment upon us.

Bibliography

Abou Elseoud, A., Starck, T., Remes, J., Nikkinen, J., Tervonen, O., and Kiviniemi, V. (2010). The effect of model order selection in group PICA. *Human Brain Mapping*, 31(8):1207–1216.

Addison, P. (2002). *The illustrated wavelet transform handbook: Introductory Theory and Applications in Science, Engineering, Medicine and Finance*. Taylor & Francis.

Addison, P., Walker, J., and Guido, R. (2009). Time–frequency analysis of biosignals. *Engineering in Medicine and Biology Magazine, IEEE*, 28(5):14–29.

Allen, E., Erhardt, E., Damaraju, E., Gruner, W., Segall, J., Silva, R., Havlicek, M., Rachakonda, S., Fries, J., and Kalyanam, R. (2011). A baseline for the multivariate comparison of resting-state networks. *Frontiers in Systems Neuroscience*, 5:1–23.

Andersson, J., Hutton, C., Ashburner, J., Turner, R., and Friston, K. (2001). Modeling geometric deformations in EPI time series. *Neuroimage*, 13(5):903–919.

Arbabshirani, M., Havlicek, M., Kiehl, K., Pearlson, G., and Calhoun, V. (2012). Functional network connectivity during rest and task conditions: A comparative study. *Human Brain Mapping*, 34:n–a.

Ardekani, B., Guckemus, S., Bachman, A., Hoptman, M., Wojtaszek, M., and Nierenberg, J. (2005). Quantitative comparison of algorithms for inter-subject registration of 3D volumetric brain MRI scans. *Journal of Neuroscience Methods*, 142(1):67–76.

Argall, B., Saad, Z., and Beauchamp, M. (2006). Simplified intersubject averaging on the cortical surface using suma. *Human Brain Mapping*, 27(1):14–27.

Ashburner, J. and Friston, K. (1999). Nonlinear spatial normalization using basis functions. *Human Brain Mapping*, 7(4):254–266.

Ashburner, J. and Friston, K. (2000). Voxel-based morphometry–the methods. *Neuroimage*, 11(6):805–821.

Azzerboni, B., Carpentieri, M., La Foresta, F., and Morabito, F. (2004). Neural-ICA and wavelet transform for artifacts removal in surface emg. In *Neural Networks, 2004. Proceedings. 2004 IEEE International Joint Conference on*, volume 4, pages 3223–3228. IEEE.

Azzerboni, B., La Foresta, F., Mammone, N., and Morabito, F. (2005). A new approach based on wavelet-ICA algorithms for fetal electrocardiogram extraction. In *European Symposium on Artificial Neural Networks*, pages 193–198. Citeseer.

Bandettini, P., Wong, E., Hinks, R., Tikofsky, R., and Hyde, J. (1992). Time course EPI of human brain function during task activation. *Magnetic Resonance in Medicine*, 25(2):390–397.

Bao, P. and Zhang, L. (2003). Noise reduction for magnetic resonance images via adaptive multiscale products thresholding. *Medical Imaging, IEEE Transactions on*, 22(9):1089–1099.

Beckmann, C. F., DeLuca, M., Devlin, J. T., and Smith, S. M. (2005). Investigations into resting-state connectivity using independent component analysis. *Philosophical Transactions of the Royal Society B: Biological Sciences*, 360(1457):1001–1013.

Biswal, B., Yetkin, F., Haughton, V., and Hyde, J. (1995). Functional connectivity in the motor cortex of resting human brain using echo-planar MRI. *Magnetic Resonance in Medicine*, 34(4):537–541.

Biswal, B. B., Mennes, M., Zuo, X.-N., Gohel, S., Kelly, C., Smith, S. M., Beckmann, C. F., Adelstein, J. S., Buckner, R. L., Colcombe, S., et al. (2010). Toward discovery science of human brain function. *Proceedings of the National Academy of Sciences*, 107(10):4734–4739.

Bloch, I. (1996). Information combination operators for data fusion: A comparative review with classification. *Systems, Man and Cybernetics, Part A: Systems and Humans, IEEE Transactions on*, 26(1):52–67.

Blum, R. and Liu, Z. (2005). *Multi-sensor image fusion and its applications*. CRC.

Boroomand, A., Ahmadian, A., Oghabian, M., Alirezaie, J., and Beckman, C. (2007). An efficient hybrid wavelet-ICA algorithm for analyzing simulated fMRI data in noisy environment. In *IEEE International Symposium on Signal Processing and Information Technology*, pages 408–413, Giza.

Breakspear, M., Brammer, M., Bullmore, T., Das, P., and Williams, L. (2004). Spatiotemporal wavelet resampling for functional neuroimaging data. *Human Brain Mapping*, 23(1):1–25.

Brett, M., Johnsrude, I., and Owen, A. (2002). The problem of functional localization in the human brain. *Nature Reviews Neuroscience*, 3(3):243–249.

Bribiesca, E. and Guzman, A. (—1980—). How to describe pure form and how to measure differences in shapes using shape numbers. *Pattern Recognition*, 12(2):101–112.

Buckheit, J., Chen, S., Donoho, D., Johnstone, I., and Scargle, J. (1995). About WaveLab. Technical report, Stanford University.

Bullmore, E., Long, C., Suckling, J., Fadili, J., Calvert, G., Zelaya, F., Carpenter, T., and Brammer, M. (2001). Colored noise and computational inference in neurophysiological (fMRI) time series analysis: Resampling methods in time and wavelet domains. *Human Brain Mapping*, 12(2):61–78.

Bullmore, E. and Sporns, O. (2009). Complex brain networks: Graph theoretical analysis of structural and functional systems. *Nature Reviews Neuroscience*, 10(3):186–198.

Burt, P. and Kolczynski, R. (1993). Enhanced image capture through fusion. In *Computer Vision, 1993. Proceedings., Fourth International Conference on*, pages 173–182. IEEE.

Calhoun, V. and Adali, T. (2012). Multi-subject independent component analysis of fMRI: A decade of intrinsic networks, default mode, and neurodiagnostic discovery. *Biomedical Engineering, IEEE Reviews in*, 5:60 –73.

Calhoun, V., Adali, T., McGinty, V., Pekar, J., Watson, T., and Pearlson, G. (—2001—a). fMRI activation in a visual-perception task: Network of areas detected using the general linear model and independent components analysis. *Neuroimage*, 14(5):1080–1088.

Calhoun, V., Adali, T., Pearlson, G., and Pekar, J. (2001b). A method for making group inferences from functional MRI data using independent component analysis. *Human Brain Mapping*, 14(3):140–151.

Calhoun, V., Adali, T., Pearlson, G., and Pekar, J. (2001c). Spatial and temporal independent component analysis of functional MRI data containing a pair of task-related waveforms. *Human Brain Mapping*, 13(1):43–53.

Calhoun, V., Adali, T., and Pekar, J. (2004). A method for comparing group fMRI data using independent component analysis: Application to visual, motor and visuomotor tasks. *Magnetic resonance imaging*, 22(9):1181–1191.

Calhoun, V., Eichele, T., and Pearlson, G. (2009a). Functional brain networks in schizophrenia: A review. *Frontiers Human Neuroscience*, 3(17):1–12.

Calhoun, V., Kiehl, K., and Pearlson, G. (2008). Modulation of temporally coherent brain networks estimated using ICA at rest and during cognitive tasks. *Human Brain Mapping*, 29(7):828–838.

Calhoun, V., Liu, J., and Adali, T. (2009b). A review of group ICA for fMRI data and ICA for joint inference of imaging, genetic, and erp data. *NeuroImage*, 45(1):1–10.

Calhoun, V., Sui, J., Kiehl, K., Turner, J., Allen, E., and Pearlson, G. (2011). Exploring the psychosis functional connectome: Aberrant intrinsic networks in schizophrenia and bipolar disorder. *Frontiers in Psychiatry*, 2:1–13.

Calhoun, V. D., Adali, T., Hansen, L. K., Larsen, J., and Pekar, J. J. (2003). ICA of functional MRI data: An overview. In *Proceedings of the International Workshop on Independent Component Analysis and Blind Signal Separation*, pages 281–288.

Carmack, P., Spence, J., Gunst, R., Schucany, W., Woodward, W., and Haley, R. (2004). Improved agreement between Talairach and MNI coordinate spaces in deep brain regions. *NeuroImage*, 22(1):367–371.

Christopoulos, C., Skodras, A., and Ebrahimi, T. (2000). The jpeg2000 still image coding system: An overview. *Consumer Electronics, IEEE Transactions on*, 46(4):1103–1127.

Chumbley, J. and Friston, K. (2009). False discovery rate revisited: FDR and topological inference using Gaussian random fields. *Neuroimage*, 44(1):62–70.

Collins, D. L., Neelin, P., Peters, T. M., and Evans, A. C. (1994). Automatic 3d intersubject registration of MR volumetric data in standardized Talairach space. *Journal of Computer Assisted Tomography*, 18(2):192–205.

Crivello, F., Schormann, T., Tzourio Mazoyer, N., Roland, P., Zilles, K., and Mazoyer, B. (2002). Comparison of spatial normalization procedures and their impact on functional maps. *Human Brain Mapping*, 16(4):228–250.

Damoiseaux, J., Rombouts, S., Barkhof, F., Scheltens, P., Stam, C., Smith, S. M., and Beckmann, C. (2006). Consistent resting-state networks across healthy subjects. *Proceedings of the National Academy of Sciences*, 103(37):13848–13853.

Daubechies, I. (1996). Where do wavelets come from? A personal point of view. *Proceedings of the IEEE*, 84(4):510–513.

De, I. and Chanda, B. (2006). A simple and efficient algorithm for multifocus image fusion using morphological wavelets. *Signal Processing*, 86(5):924–936.

Donoho, D. (1995). De-noising by soft-thresholding. *IEEE Transactions on Information Theory*, 41(3):613–627.

Donoho, D. L. and Johnstone, J. M. (1994). Ideal spatial adaptation by wavelet shrinkage. *Biometrika*, 81(3):425–455.

Dougherty, R., Koch, V., Brewer, A., Fischer, B., Modersitzki, J., and Wandell, B. (2003). Visual field representations and locations of visual areas V1/2/3 in human visual cortex. *Journal of Vision*, 3(10):586–598.

Dubb, A., Gur, R., Avants, B., and Gee, J. (2003). Characterization of sexual dimorphism in the human corpus callosum. *Neuroimage*, 20(1):512–519.

Eltoukhy, H. and Kavusi, S. (2003). Computationally efficient algorithm for multifocus image reconstruction. In *Electronic Imaging 2003*, pages 332–341. International Society for Optics and Photonics.

Erhardt, E., Rachakonda, S., Bedrick, E., Allen, E., Adali, T., and Calhoun, V. (2011). Comparison of multi-subject ICA methods for analysis of fMRI data. *Human Brain Mapping*, 32(12):2075–2095.

Ernst, R. and Anderson, W. (1966). Application of Fourier transform spectroscopy to magnetic resonance. *Review of Scientific Instruments*, 37(1):93–102.

Evans, A., Collins, D., Mills, S., Brown, E., Kelly, R., and Peters, T. (1993). 3D statistical neuroanatomical models from 305 MRI volumes. In *Nuclear Science Symposium and Medical Imaging Conference, 1993., 1993 IEEE Conference Record.*, pages 1813–1817. IEEE.

Filippi, M., Valsasina, P., Misci, P., Falini, A., Comi, G., and Rocca, M. (2012). The

organization of intrinsic brain activity differs between genders: A resting-state fMRI study in a large cohort of young healthy subjects. *Human Brain Mapping*, 34:1–14.

First, M., Spitzer, R., Gibbon, M., Williams, J., Davies, M., Borus, J., Howes, M., Kane, J., Pope Jr, H., and Rounsaville, B. (1995). The structured clinical interview for DSM-III-R personality disorders (SCID-II). Part II: Multi-site test-retest reliability study. *Journal of Personality Disorders*, 9(2):92–104.

Fischl, B., Sereno, M., Tootell, R., and Dale, A. (1999). High-resolution intersubject averaging and a coordinate system for the cortical surface. *Human Brain Mapping*, 8(4):272–284.

Foucher, S., Bénié, G., and Boucher, J. (2001). Multiscale map filtering of sar images. *Image Processing, IEEE Transactions on*, 10(1):49–60.

Fox, M. D., Snyder, A. Z., Vincent, J. L., Corbetta, M., Van Essen, D. C., and Raichle, M. E. (2005). The human brain is intrinsically organized into dynamic, anticorrelated functional networks. *Proceedings of the National Academy of Sciences of the United States of America*, 102(27):9673–9678.

Frackowiak, R. (2004). *Human Brain Function*. Academic Press.

Freeman, H. (1974). Computer processing of line-drawing images. *ACM Computing Surveys (CSUR)*, 6(1):57–97.

Freire, L., Roche, A., and Mangin, J. (2002). What is the best similarity measure for motion correction in fMRI time series? *IEEE transactions on medical imaging*, 21(5):470–484.

Friston, K., Holmes, A., Worsley, K., Poline, J., Frith, C., and Frackowiak, R. (1994). Statistical parametric maps in functional imaging: A general linear approach. *Human Brain Mapping*, 2(4):189–210.

Gabor, D. (1946). Theory of communication. Part 1: The analysis of information. *Electrical*

Engineers-Part III: Radio and Communication Engineering, Journal of the Institution of, 93(26):429–441.

Gaborski, R. and Paskali, J. (2007). A cognitively motivated video detection system. *Journal of Applied Science & Engineering Technology*, 1(0):51–57.

Genovese, C., Lazar, N., and Nichols, T. (2002). Thresholding of statistical maps in functional neuroimaging using the false discovery rate. *Neuroimage*, 15(4):870–878.

Goldman, R., Stern, J., Engel Jr, J., and Cohen, M. (2002). Simultaneous eeg and fMRI of the alpha rhythm. *Neuroreport*, 13(18):2487–2492.

Good, C., Johnsrude, I., Ashburner, J., Henson, R., Friston, K., and Frackowiak, R. (2001a). Cerebral asymmetry and the effects of sex and handedness on brain structure: A voxel-based morphometric analysis of 465 normal adult human brains. *Neuroimage*, 14(3):685–700.

Good, C., Johnsrude, I., Ashburner, J., Henson, R., Friston, K., and Frackowiak, R. (2001b). A voxel-based morphometric study of ageing in 465 normal adult human brains. *Neuroimage*, 14(1):21–36.

Goutsias, J. and Heijmans, H. (2000). Nonlinear multiresolution signal decomposition schemes. i. morphological pyramids. *Image Processing, IEEE Transactions on*, 9(11):1862–1876.

Grachev, I., Berdichevsky, D., Rauch, S., Heckers, S., Kennedy, D., Caviness, V., and Alpert, N. (1999). A method for assessing the accuracy of intersubject registration of the human brain using anatomic landmarks* 1. *Neuroimage*, 9(2):250–268.

Greicius, M., Krasnow, B., Reiss, A., and Menon, V. (2003). Functional connectivity in the resting brain: A network analysis of the default mode hypothesis. *Proceedings of the National Academy of Sciences*, 100(1):253–258.

Gudbjartsson, H. and Patz, S. (1995). The Rician distribution of noisy MRI data. *Magnetic Resonance in Medicine*, 34(6):910–914.

Halgren, E., Marinkovic, K., and Chauvel, P. (1998). Generators of the late cognitive potentials in auditory and visual oddball tasks. *Electroencephalography and Clinical Neurophysiology*, 106(2):156–164.

Hammers, A., Allom, R., Koepp, M., Free, S., Myers, R., Lemieux, L., Mitchell, T., Brooks, D., and Duncan, J. (2003). Three dimensional maximum probability atlas of the human brain, with particular reference to the temporal lobe. *Human Brain Mapping*, 19(4):224–247.

Hammers, A., Koepp, M., Free, S., Brett, M., Richardson, M., Labb, C., Cunningham, V., Brooks, D., and Duncan, J. (2002). Implementation and application of a brain template for multiple volumes of interest. *Human Brain Mapping*, 15(3):165–174.

Harrison, B. J., Pujol, J., López-Solà, M., Hernández-Ribas, R., Deus, J., Ortiz, H., Soriano-Mas, C., Yücel, M., Pantelis, C., and Cardoner, N. (2008). Consistency and functional specialization in the default mode brain network. *Proceedings of the National Academy of Sciences*, 105(28):9781–9786.

He, L. and Greenshields, I. R. (2009). A nonlocal maximum likelihood estimation method for rician noise reduction in MR images. *Medical Imaging, IEEE Transactions on*, 28(2):165–172.

Heijmans, H. and Goutsias, J. (2000). Nonlinear multiresolution signal decomposition schemes. ii. morphological wavelets. *Image Processing, IEEE Transactions on*, 9(11):1897–1913.

Hellier, P., Barillot, C., Corouge, I., Gibaud, B., Le Goualher, G., Collins, D., Evans, A., Malandain, G., Ayache, N., Christensen, G., et al. (2003). Retrospective evaluation of intersubject brain registration. *Medical Imaging, IEEE Transactions on*, 22(9):1120–1130.

Hilton, M., Ogden, T., Hattery, D., Eden, G., and Jawerth, B. (1996). Wavelet denoising of functional MRI data. In *Wavelets in Medicine and Biology*. CRC Press.

Huang, C.-M., Lee, S.-H., Hsiao, I.-T., Kuan, W.-C., Wai, Y.-Y., Ko, H.-J., Wan, Y.-L., Hsu, Y.-Y., and Liu, H.-L. (2010). Study-specific EPI template improves group analysis in functional MRI of young and older adults. *Journal of Neuroscience Methods*, 189(2):257–266.

Huettel, S., Song, A., and McCarthy, G. (2004). *Functional Magnetic Resonance Imaging*. Sinauer Associates Sunderland, MA.

Jang, S., Ahn, S., Yang, D., Lee, D., Kim, D., and Son, S. (2005). Cortical reorganization of hand motor function to primary sensory cortex in hemiparetic patients with a primary motor cortex infarct. *Archives of Physical Medicine and Rehabilitation*, 86(8):1706–1708.

Jansen, M. (2001). *Noise reduction by wavelet thresholding*, volume 161. Springer New York.

Jenkinson, M. (—2003—). Fast, automated, n dimensional phase unwrapping algorithm. *Magnetic Resonance in Medicine*, 49(1):193–197.

Johnson, R., Marchini, J., Smith, S., and Beckmann, C. (2007). Independent component analysis of functional magnetic resonance imaging data using wavelet dictionaries. In *Independent Component Analysis and Signal Separation*, pages 625–632. Springer.

Kadah, Y. M. (2004). Adaptive denoising of event-related functional magnetic resonance imaging data using spectral subtraction. *Biomedical Engineering, IEEE Transactions on*, 51(11):1944–1953.

Kauppinen, H., Seppanen, T., and Pietikainen, M. (2002). An experimental comparison of autoregressive and Fourier-based descriptors in 2D shape classification. *Pattern Analysis and Machine Intelligence, IEEE Transactions on*, 17(2):201–207.

Khullar, S., Michael, A., Correa, N., Adali, T., Baum, S., and Calhoun, V. (2011a). Functional normalization through ICA (ICA-fNORM) with intrinsic networks as functional templates. In *17th Annual Meeting of Organisation for Human Brain Mapping*, Quebec, Canada.

Khullar, S., Michael, A., Correa, N., Adali, T., Baum, S., and Calhoun, V. (2011b). Wavelet-based denoising and independent component analysis for improving multi-group inference in fMRI data. In *IEEE International Symposium on Biomedical Imaging*, Chicago, IL.

Khullar, S., Michael, A., Correa, N., Adali, T., Baum, S., and Calhoun, V. (2011c). Wavelet-based fMRI analysis: 3D denoising, signal separation, and validation metrics. *NeuroImage*, 54(4):2867–2884.

Khullar, S., Michael, A. M., Cahill, N. D., Kiehl, K. A., Pearlson, G., Baum, S. A., and Calhoun, V. D. (2011d). ICA-fNORM: Spatial normalization of fMRI data using intrinsic group-ICA networks. *Frontiers in Systems Neuroscience*, 5:1–18.

Khullar, S., Michael, A. M., Correa, N., Adali, T., Baum, S. A., and Calhoun, V. D. (2011e). Improved 3D wavelet-based de-noising of fMRI data. In *SPIE Medical Imaging*, pages 79624P1–79624P9. International Society for Optics and Photonics.

Kiehl, K., Stevens, M., Laurens, K., Pearlson, G., Calhoun, V., and Liddle, P. (2005). An adaptive reflexive processing model of neurocognitive function: supporting evidence from a large scale (n= 100) fMRI study of an auditory oddball task. *Neuroimage*, 25(3):899–915.

Kim, W. and Kim, Y. (—2000—). A region-based shape descriptor using zernike moments. *Signal Processing: Image Communication*, 16(1-2):95–102.

Kiviniemi, V., Kantola, J., Jauhiainen, J., Hyvärinen, A., and Tervonen, O. (2003). Independent component analysis of nondeterministic fMRI signal sources. *Neuroimage*, 19(2):253–260.

Kubota, T., Ushijima, Y., Okuyama, C., and Nishimura, T. (2006). A region-of-interest template for three-dimensional stereotactic surface projection images: initial application to the analysis of alzheimer's disease and mild cognitive impairment. *Nuclear Medicine Communications*, 27(1):37–44.

Lancaster, J., Woldorff, M., Parsons, L., Liotti, M., Freitas, C., Rainey, L., Kochunov, P., Nickerson, D., Mikiten, S., and Fox, P. (2000). Automated Talairach atlas labels for functional brain mapping. *Human Brain Mapping*, 10(3):120–131.

Lang, M., Guo, H., Odegard, J., Burrus, C., and Wells Jr, R. (1996). Noise reduction using an undecimated discrete wavelet transform. *IEEE Signal Processing Letters*, 3(1):10–12.

Lauterbur, P. et al. (1974). Magnetic resonance zeugmatography. *Pure Appl. Chem*, 40(1-2):149–157.

Lee, J., Lee, D., Kim, J., Kim, Y., Kang, E., Kang, H., Kang, K., Lee, J., Kim, J., Park, H., et al. (2005). Development of korean standard brain templates. *Journal of Korean medical science*, 20(3):483–488.

Li, H., Manjunath, B., and Mitra, S. (1995). Multisensor image fusion using the wavelet transform. *Graphical Models and Image Processing*, 57(3):235–245.

Li, X., Gunturk, B., and Zhang, L. (2008). Image demosaicing: A systematic survey. In *Proc. of SPIE*, volume 6822, pages 68221J–68221J.

Long, C., Brown, E., Manoach, D., and Solo, V. (2004). Spatiotemporal wavelet analysis for functional MRI. *NeuroImage*, 23(2):500–516.

Looi, J., Walterfang, M., Styner, M., Svensson, L., Lindberg, O., Östberg, P., Botes, L., Örndahl, E., Chua, P., Kumar, R., et al. (2010). Shape analysis of the neostriatum in frontotemporal lobar degeneration, alzheimer's disease, and controls. *Neuroimage*, 51(3):970–986.

Lu, G. and Sajjanhar, A. (—1999—). Region-based shape representation and similarity measure suitable for content-based image retrieval. *Multimedia Systems*, 7(2):165–174.

Ma, S., Calhoun, V. D., Eichele, T., Du, W., and Adal, T. (2012). Modulations of functional connectivity in the healthy and schizophrenia groups during task and rest. *NeuroImage*, 62(3):1694–1704.

Mallat, S. (1989). A theory for multiresolution signal decomposition: The wavelet representation. *IEEE Transactions on Pattern Analysis and Machine Intelligence*, 11(7):674–693.

Mallat, S. (1999). *A wavelet tour of signal processing*. Academic Pr.

Malonek, D. and Grinvald, A. (1996). Interactions between electrical activity and cortical microcirculation revealed by imaging spectroscopy: implications for functional brain mapping. *Science*, 272(5261):551–554.

Mazziotta, J., Toga, A., Evans, A., Fox, P., and Lancaster, J. (1995). A probabilistic atlas of the human brain: Theory and rationale for its development:: The international consortium for brain mapping (ICBM). *Neuroimage*, 2(2):89–101.

Mazziotta, J., Toga, A., Evans, A., Fox, P., Lancaster, J., Zilles, K., Woods, R., Paus, T., Simpson, G., Pike, B., et al. (2001). A four-dimensional probabilistic atlas of the human brain. *Journal of the American Medical Informatics Association*, 8(5):401–430.

McKeown, M., Makeig, S., Brown, G., Jung, T., Kindermann, S., Bell, A., and Sejnowski, T. (1998). Analysis of fMRI data by blind separation into independent spatial components. *Human Brain Mapping*, 6(3):160–188.

Mennes, M., Kelly, C., Zuo, X., Di Martino, A., Biswal, B., Castellanos, F., and Milham, M. (2010). Inter-individual differences in resting-state functional connectivity predict task-induced bold activity. *Neuroimage*, 50(4):1690–1701.

Monir, S. and Siyal, M. (2009). Denoising functional magnetic resonance imaging time-series using anisotropic spatial averaging. *Biomedical Signal Processing and Control*, 4(1):16–25.

Mukhopadhyay, S. and Chanda, B. (2001). Fusion of 2D grayscale images using multiscale morphology. *Pattern Recognition*, 34(10):1939–1949.

Nieto-Castanon, A., Ghosh, S., Tourville, J., and Guenther, F. (2003). Region of interest based analysis of functional imaging data. *Neuroimage*, 19(4):1303–1316.

Ogawa, S., Tank, D. W., Menon, R., Ellermann, J. M., Kim, S.-G., Merkle, H., and Ugurbil, K. (1992). Intrinsic signal changes accompanying sensory stimulation: functional brain mapping with magnetic resonance imaging. *Proceedings of the National Academy of Sciences*, 89(13):5951–5955.

Pajares, G. and de la Cruz, J. M. (2004). A wavelet-based image fusion tutorial. *Pattern Recognition*, 37(9):1855 – 1872.

Park, H., Levitt, J., Shenton, M., Salisbury, D., Kubicki, M., Kikinis, R., Jolesz, F., and McCarley, R. (2004). An MRI study of spatial probability brain map differences between first-EPIsode schizophrenia and normal controls. *Neuroimage*, 22(3):1231–1246.

Pekar, J. (2006). A brief introduction to functional MRI. *Engineering in Medicine and Biology Magazine, IEEE*, 25(2):24–26.

Persoon, E. and Fu, K. (—2007—). Shape discrimination using fourier descriptors. *Systems, Man and Cybernetics, IEEE Transactions on*, 7(3):170–179.

Piella, G. (2003). A general framework for multiresolution image fusion: from pixels to regions. *Information Fusion*, 4(4):259–280.

Pizurica, A., Philips, W., Lemahieu, I., and Acheroy, M. (2003). A versatile wavelet domain noise filtration technique for medical imaging. *Medical Imaging, IEEE Transactions on*, 22(3):323–331.

Pizurica, A., Wink, A., Vansteenkiste, E., Philips, W., and Roerdink, B. (2006). A review of wavelet denoising in MRI and ultrasound brain imaging. *Current Medical Imaging Reviews*, 2(2):247–260.

Poline, J., Worsley, K., Evans, A., and Friston, K. (1997). Combining spatial extent and peak intensity to test for activations in functional imaging. *NeuroImage*, 5(2):83–96.

Rachakonda, S., Egolf, E., Correa, N., and Calhoun, V. (2007). Group ICA of fMRI toolbox (gift) manual. Technical report, Mind Research Network.

Rademacher, J., Caviness, V., Steinmetz, H., and Galaburda, A. (1993). Topographical variation of the human primary cortices: implications for neuroimaging, brain mapping, and neurobiology. *Cerebral Cortex*, 3(4):313–329.

Raichle, M. E., MacLeod, A. M., Snyder, A. Z., Powers, W. J., Gusnard, D. A., and Shulman, G. L. (2001). A default mode of brain function. *Proceedings of the National Academy of Sciences*, 98(2):676–682.

Raz, N., Lindenberger, U., Rodrigue, K. M., Kennedy, K. M., Head, D., Williamson, A., Dahle, C., Gerstorf, D., and Acker, J. D. (2005). Regional brain changes in aging healthy adults: general trends, individual differences and modifiers. *Cerebral cortex*, 15(11):1676–1689.

Ripollés, P., Marco-Pallarés, J., de Diego-Balaguer, R., Miró, J., Falip, M., Juncadella, M., Rubio, F., and Rodriguez-Fornells, A. (2012). Analysis of automated methods for spatial normalization of lesioned brains. *NeuroImage*, 60(2):1296–1306.

Rivičre, D., Mangin, J., Papadopoulos-Orfanos, D., Martinez, J., Frouin, V., and Regis, J. (2002). Automatic recognition of cortical sulci of the human brain using a congregation of neural networks. *Medical Image Analysis*, 6(2):77–92.

Robbins, S., Evans, A., Collins, D., and Whitesides, S. (2004). Tuning and comparing spatial normalization methods. *Medical Image Analysis*, 8(3):311–323.

Roland, P., Geyer, S., Amunts, K., Schormann, T., Schleicher, A., Malikovic, A., and Zilles, K. (1997). Cytoarchitectural maps of the human brain in standard anatomical space. *Human Brain Mapping*, 5(4):222–227.

Saber, E., Xu, Y., and Murat Tekalp, A. (2005). Partial shape recognition by sub-matrix matching for partial matching guided image labeling. *Pattern Recognition*, 38(10):1560–1573.

Sabuncu, M., Yeo, B., Van Leemput, K., Vercauteren, T., and Golland, P. (2009). Asymmetric image-template registration. *Medical Image Computing and Computer-Assisted Intervention , MICCAI 2009*, pages 565–573.

Sabuncu, M. R., Singer, B. D., Conroy, B., Bryan, R. E., Ramadge, P. J., and Haxby, J. V. (2010). Function-based intersubject alignment of human cortical anatomy. *Cerebral Cortex*, 20(1):130–140.

Saxe, R., Brett, M., and Kanwisher, N. (2006). Divide and conquer: A defense of functional localizers. *Neuroimage*, 30(4):1088–1096.

Scher, A., Xu, Y., Korf, E., White, L., Scheltens, P., Toga, A., Thompson, P., Hartley, S., Witter, M., Valentino, D., et al. (2007). Hippocampal shape analysis in alzheimers disease: A population-based study. *Neuroimage*, 36(1):8–18.

Sendur, L., Suckling, J., Whitcher, B., and Bullmore, E. (2007). Resampling methods for improved wavelet-based multiple hypothesis testing of parametric maps in functional MRI. *NeuroImage*, 37(4):1186–1194.

Shensa, M. (1992). The discrete wavelet transform: Wedding the A trous and mallat algorithms. *Signal Processing, IEEE Transactions on*, 40(10):2464–2482.

Smith, S. M., Fox, P. T., Miller, K. L., Glahn, D. C., Fox, P. M., Mackay, C. E., Filippi ni, N., Watkins, K. E., Toro, R., Laird, A. R., et al. (2009). Correspondence of the brain's

functional architecture during activation and rest. *Proceedings of the National Academy of Sciences*, 106(31):13040–13045.

Sorg, C., Riedl, V., Mühlau, M., Calhoun, V. D., Eichele, T., Läer, L., Drzezga, A., Förstl, H., Kurz, A., Zimmer, C., et al. (2007). Selective changes of resting-state networks in individuals at risk for alzheimer's disease. *Proceedings of the National Academy of Sciences*, 104(47):18760–18765.

Sporns, O. (2011). The human connectome: A complex network. *Annals of the New York Academy of Sciences*, 1224(1):109–125.

Sporns, O., Chialvo, D., Kaiser, M., Hilgetag, C., et al. (2004). Organization, development and function of complex brain networks. *Trends in cognitive sciences*, 8(9):418–425.

Stehling, M., Turner, R., and Mansfield, P. (1991). Echo-planar imaging: magnetic resonance imaging in a fraction of a second. *Science*, 254(5028):43–50.

Stephan, K. E. and Roebroeck, A. (2012). A short history of causal modeling of fMRI data. *NeuroImage*, 62(2):856 – 863.

Strother, S. (2006). Evaluating fMRI preprocessing pipelines. *Engineering in Medicine and Biology Magazine, IEEE*, 25(2):27–41.

Sweldens, W. (1996). The lifting scheme: A custom-design construction of biorthogonal wavelets. *Applied and computational harmonic analysis*, 3(2):186–200.

Tabelow, K., Polzehl, J., Voss, H., and Spokoiny, V. (2006). Analyzing fMRI experiments with structural adaptive smoothing procedures. *NeuroImage*, 33(1):55–62.

Talairach, J. and Tournoux, P. (1988). *Co-planar stereotaxic atlas of the human brain: 3-Dimensional proportional system - An approach to cerebral imaging*. Thieme.

Tangelder, J. and Veltkamp, R. (2004). A survey of content based 3D shape retrieval methods. In *Shape Modeling Applications, 2004. Proceedings*, pages 145–156. IEEE.

Tenmoto, H., Kudo, M., and Shimbo, M. (1998). Mdl-based selection of the number of components in mixture models for pattern classification. In *Advances in Pattern Recognition*, pages 831–836. Springer.

Thirion, B., Flandin, G., Pinel, P., Roche, A., Ciuciu, P., and Poline, J. (2006). Dealing with the shortcomings of spatial normalization: Multi-subject parcellation of fMRI datasets. *Human Brain Mapping*, 27(8):678–693.

Thompson, P. M., MacDonald, D., Mega, M. S., Holmes, C. J., Evans, A. C., and Toga, A. W. (1997). Detection and mapping of abnormal brain structure with a probabilistic atlas of cortical surfaces. *Journal of Computer Assisted Tomography*, 21(4):567–581.

Toga, A. and Mazziotta, J. (2002). *Brain mapping: The methods*, volume 1. Academic Pr.

Toga, A. and Thompson, P. (2001). Maps of the brain. *The Anatomical Record*, 265(2):37–53.

Tootell, R., Reppas, J., Kwong, K., Malach, R., Born, R., Brady, T., Rosen, B., and Belliveau, J. (1995). Functional analysis of human MT and related visual cortical areas using magnetic resonance imaging. *The Journal of Neuroscience*, 15(4):3215–3230.

Tzourio-Mazoyer, N., Landeau, B., Papathanassiou, D., Crivello, F., Etard, O., Delcroix, N., Mazoyer, B., and Joliot, M. (2002). Automated anatomical labeling of activations in SPM using a macroscopic anatomical parcellation of the MNI MRI single-subject brain. *Neuroimage*, 15(1):273–289.

Unser, M. and Aldroubi, A. (1996). A review of wavelets in biomedical applications. *Proceedings of the IEEE*, 84(4):626–638.

Van De Ville, D., Blu, T., and Unser, M. (2006). Surfing the brain. *IEEE Engineering in Medicine and Biology Magazine*, 25(2):65–78.

Van De Ville, D., Seghier, M., Lazeyras, F., Blu, T., and Unser, M. (2007). WSPM: Wavelet-based statistical parametric mapping. *NeuroImage*, 37(4):1205–1217.

Watson, J. D., Myers, R., Frackowiak, R. S., Hajnal, J. V., Woods, R. P., Mazziotta, J. C., Shipp, S., and Zeki, S. (1993). Area V5 of the human brain: Evidence from a combined study using positron emission tomography and magnetic resonance imaging. *Cerebral Cortex*, 3(2):79–94.

Wink, A. and Roerdink, J. (2004). Denoising functional MR images: A comparison of wavelet denoising and Gaussian smoothing. *IEEE Transactions on Medical Imaging*, 23(3):374–387.

Xu, Y., Weaver, J., Healy, D., and Lu, J. (1994). Wavelet transform domain filters: A spatially selective noise filtration technique. *IEEE Transactions on Image Processing*, 3(6):747–758.

Yang, F. and Shan, Z. (2011). Mapping developmental precentral and postcentral gyral changes in children on magnetic resonance images. *Journal of Magnetic Resonance Imaging*, 33(1):62–70.

Zhang, D. and Lu, G. (2001). Content-based shape retrieval using different shape descriptors: A comparative study. In *IEEE International Conference on Multimedia and Expo*, pages 1139–1142.